

Springer Theses

Recognizing Outstanding Ph.D. Research

Youngjun Lee

Systematic Exploration of Indolizine-Based Small Fluorescent Molecules

Synthesis, Analysis and Application



Springer

Springer Theses

Recognizing Outstanding Ph.D. Research

Aims and Scope

The series “Springer Theses” brings together a selection of the very best Ph.D. theses from around the world and across the physical sciences. Nominated and endorsed by two recognized specialists, each published volume has been selected for its scientific excellence and the high impact of its contents for the pertinent field of research. For greater accessibility to non-specialists, the published versions include an extended introduction, as well as a foreword by the student’s supervisor explaining the special relevance of the work for the field. As a whole, the series will provide a valuable resource both for newcomers to the research fields described, and for other scientists seeking detailed background information on special questions. Finally, it provides an accredited documentation of the valuable contributions made by today’s younger generation of scientists.

Theses are accepted into the series by invited nomination only and must fulfill all of the following criteria

- They must be written in good English.
- The topic should fall within the confines of Chemistry, Physics, Earth Sciences, Engineering and related interdisciplinary fields such as Materials, Nanoscience, Chemical Engineering, Complex Systems and Biophysics.
- The work reported in the thesis must represent a significant scientific advance.
- If the thesis includes previously published material, permission to reproduce this must be gained from the respective copyright holder.
- They must have been examined and passed during the 12 months prior to nomination.
- Each thesis should include a foreword by the supervisor outlining the significance of its content.
- The theses should have a clearly defined structure including an introduction accessible to scientists not expert in that particular field.

More information about this series at <http://www.springer.com/series/8790>

Youngjun Lee

Systematic Exploration of Indolizine-Based Small Fluorescent Molecules

Synthesis, Analysis and Application

Doctoral Thesis accepted by
Seoul National University, Seoul, South Korea

 Springer

Author

Dr. Youngjun Lee
Department of Chemistry, College of
Natural Sciences
Seoul National University
Seoul, South Korea

Supervisors

Prof. Seung Bum Park
Department of Chemistry,
College of Natural Sciences
Seoul National University
Seoul, South Korea

Prof. Seokmin Shin
Department of Chemistry,
College of Natural Sciences
Seoul National University
Seoul, South Korea

ISSN 2190-5053

Springer Theses

ISBN 978-981-13-1644-9

<https://doi.org/10.1007/978-981-13-1645-6>

ISSN 2190-5061 (electronic)

ISBN 978-981-13-1645-6 (eBook)

Library of Congress Control Number: 2018949343

© Springer Nature Singapore Pte Ltd. 2018

This work is subject to copyright. All rights are reserved by the Publisher, whether the whole or part of the material is concerned, specifically the rights of translation, reprinting, reuse of illustrations, recitation, broadcasting, reproduction on microfilms or in any other physical way, and transmission or information storage and retrieval, electronic adaptation, computer software, or by similar or dissimilar methodology now known or hereafter developed.

The use of general descriptive names, registered names, trademarks, service marks, etc. in this publication does not imply, even in the absence of a specific statement, that such names are exempt from the relevant protective laws and regulations and therefore free for general use.

The publisher, the authors, and the editors are safe to assume that the advice and information in this book are believed to be true and accurate at the date of publication. Neither the publisher nor the authors or the editors give a warranty, express or implied, with respect to the material contained herein or for any errors or omissions that may have been made. The publisher remains neutral with regard to jurisdictional claims in published maps and institutional affiliations.

This Springer imprint is published by the registered company Springer Nature Singapore Pte Ltd. The registered company address is: 152 Beach Road, #21-01/04 Gateway East, Singapore 189721, Singapore

Supervisor's Foreword

Fluorescence technique has been an indispensable tool in modern life science, due to its outstanding sensitivity, low cost, and easy of handling. Considering its versatility and tunability, fluorescent organic molecule is an attractive research tool which can be used not only for biological purposes, but also for optical materials, such as organic light-emitting diode (OLED) and dye-sensitized solar cell (DSSC). However, controlling photophysical properties of a given organic fluorophore with a rational prediction is very challenging tasks in many cases.

Dr. Lee's thesis describes multidisciplinary studies on indolizine-based fluorescent molecules including molecular design, organic synthesis, optical property analysis, quantum mechanical calculation, and their biological applications. In each chapter, Dr. Lee constructed a suitable collection of unexplored fluorescent small molecules to elucidate the structure–photophysical property relationship and developed tailored molecular probes on the basis of rational interpretation. These explorations have led to the development of a new microalgae lipid droplet probe, colorful bioorthogonal fluorogenic probes, and a bright mitochondrial probe working under live cell conditions. More importantly, this thesis suggests unprecedented molecular design principles which successfully tackle the problems yet to be solved, such as rational improvement of molar absorptivity, or development of the emission-independent fluorophore–quencher system.

For a couple of decades, harnessing the fluorescent property of an organic fluorophore has been pursued using traditional fluorescent core skeletons including cyanine, BODIPY, rhodamine, fluorescein, and coumarin. But I believe the value of Dr. Lee's thesis lies in a methodical approach to expand our knowledge about the unraveled molecular system and the associated photophysical property on the basis of rational prediction. This thesis will provide useful insights into those who wish to improve and develop unique fluorescent organic materials or optical materials.

Seoul, South Korea
May 2018

Prof. Seung Bum Park

Abstract

Organic fluorophores have been extensively used in the field of molecular biology owing to their excellent photophysical property, suitable cell permeability, and synthetic flexibility. Understanding of the structure–photophysical property relationship of a given fluorophore often paves the road to the development of valuable molecular probes to visualize and transcribe biological networks. This thesis describes in-depth study of an indolizine-based fluorophore, including molecular design, organic synthesis, structure–property analysis, and quantum mechanical interpretation. Chapter 1 explains the fundamental aspects of molecular fluorescence and photophysical parameters, together with a brief illustration of synthesis, general property, structure–photophysical property relationship, and bioapplication of representative organic fluorophores. Chapter 2 deals with fluorescent quantum yield and molecular lipophilicity of indolizine-based Seoul-Fluor system, by analyzing a series of relevant derivatives. Chapter 3 depicts a comprehensive study of tetrazine-embedded bioorthogonal probes, on the basis of well-studied indolizine fluorophore platform. By constructing a systematic series of tetrazine–indolizine conjugates, the usefulness of a newly suggested design strategy for fluorogenic bioorthogonal probes has been demonstrated, compared with conventional FRET- or TBET-based strategies. Chapter 4 discusses a rational approach to enhance molar absorptivity of a given fluorophore, with the guidance of calculated oscillator strength values. An unprecedented fluorophore is logically designed and synthesized, and structure–property relationship study of the novel fluorophore has been also dealt with in detail. Overall, a systematic exploration of an indolizine-based fluorophore has led to the development of a new microalgae lipid droplet probe (in Chap. 2), colorful bioorthogonal fluorogenic probes (in Chap. 3), and a bright mitochondrial probe (in Chap. 4), working under live cell conditions.

Keywords: Indolizine-based fluorophore, Structure–property relationship, Quantum calculation, Bioprobes, Rational design, Bioorthogonal reaction

Student Number: 2012-20285

Acknowledgements

First of all, I would like to express my gratitude to Prof. Seung Bum Park for his professional guidance and continuous support during my Ph.D. course. His tolerance for students and the flexibility in adapting to new research areas have always impressed me, and I have learned from him a lot about how to dealing with research, and how to deliver my idea efficiently. I also thank my dissertation committees, Prof. Jong-In Hong, Prof. Chulbom Lee, and Prof. Donghwan Lee, for their critical discussions and insightful advice. Special thanks must go to my mentor, Prof. Eunha Kim, who has encouraged and inspired me more than any other people, and he always leads me to the right path.

I am so lucky to meet lots of great and talented people in Park's laboratory. My brilliant seniors—Dr. Jongmin Park, Dr. Sanghee Lee, Dr. Minseob Koh, Dr. Jonghoon Kim, and Dr. Donghyun Lim—served as a compass for my graduate student life, and I always tried to follow their footsteps. Also, my good colleges—Dr. Heejun Kim, Dr. Heebom Song, Dr. Jayoung Koo, Dr. Ala Jo—shared lots of fun and great memories, and they are the one who sustained me in my time of hardship. I also thank the current laboratory members for their love and kindness which make me feel I am in the right place.

Lastly, I would like to express my sincere appreciation to my families and good old friends. They are the mainspring of my life and great comfort. Most important of all, I am deeply grateful to my parents for their endless support and love. Without them, I would not be able to grow stronger.

Contents

1	Introduction	1
1.1	Molecular Fluorescence and Photophysical Parameters	1
1.1.1	Molar Absorption Coefficient: $\epsilon(\lambda)$	2
1.1.2	Emission Maxima: λ_{em}	3
1.1.3	Stokes Shift: $\Delta\bar{\nu}$	3
1.1.4	Fluorescent Quantum Yield: Φ_F	4
1.2	Organic Fluorophores	5
1.2.1	Bodipy	6
1.2.2	Coumarin	7
1.2.3	Cyanine	9
1.2.4	Fluorescein	11
1.2.5	Rhodamine	13
1.2.6	Seoul-Fluor (SF)	15
1.3	Aims and Scope of the Thesis	16
	References	18
2	A Comprehensive Studies of an Indolizine-Based Seoul-Fluor System	21
2.1	Structure and Quantum Yield Relationship Study of Seoul-Fluor	21
2.1.1	Introduction	21
2.1.2	Result and Discussion	21
2.1.3	Conclusion	23
2.2	Optimization of SF-Based Lipid Droplet Bioprobes on the Basis of Molecular Lipophilicity	23
2.2.1	Introduction	23
2.2.2	Result and Discussion	24
2.2.3	Conclusion	34
2.3	An Overview of Seoul-Fluor System	34

2.4	Experimental Section	35
2.4.1	General Experimental Information	35
2.4.2	Experimental Procedure	37
2.4.3	Compound Characterization Data	38
	References	41
3	Tetrazine-Containing Colorful Bioorthogonal Probes Based on the Indolizine Core Skeleton	43
3.1	Introduction	43
3.2	Result and Discussion	45
3.2.1	Initial Design and Synthesis	45
3.2.2	Change in Absorption Property of SF _{Tz} 01–05 Upon TCO Cycloaddition Reaction	48
3.2.3	Change in Fluorescence Property of SF _{Tz} 01–05 Upon Cycloaddition Reaction with TCO	49
3.2.4	Reaction Kinetics	51
3.2.5	Rational Expansion of Multicolor SF _{Tz} s Based on a Monochromophoric Strategy	52
3.2.6	TD-DFT Calculation	55
3.2.7	Direct Comparison of Mono- Versus Bichromophoric SF _{Tz} s with Long Emission Wavelength	59
3.2.8	Bioapplication	60
3.3	Conclusion	64
3.4	Experimental Section	64
3.4.1	General Experimental Information	64
3.4.2	Fluorescence Kinetic Measurements	66
3.4.3	Experimental Procedure for Live Cell Fluorescence Image	67
3.4.4	Synthetic Procedure and Characterization of New Compounds	68
	References	83
4	Rational Development of Furoindolizine Core Skeleton Guided by Oscillator Strength	85
4.1	Introduction	85
4.2	Result and Discussion	86
4.2.1	Designing an Unexplored Fluorophore with High Molar Absorptivity	86
4.2.2	Library Construction Based on a Novel Furo[3,2- <i>e</i>] Indolizine Scaffold	89
4.2.3	Photophysical Property Analysis	92
4.2.4	Rational Design of Novel Furoindolizine-Based Fluorescent Compounds and Bioapplication	96
4.3	Conclusion	97

4.4	Experimental Section	97
4.4.1	General Information	97
4.4.2	Experimental Procedure for Live Cell Fluorescence Image	99
4.4.3	Computational Results of Furoindolizine Analogues	102
4.4.4	Prediction of Photophysical Properties for 17, 18 and 19	103
4.4.5	Synthetic Procedure and Compound Characterization	104
	References	120
	Appendix	123

Abbreviations

ACN	Acetonitrile
B3LYP	Becke 3-Parameter (Exchange), Lee, Yang and Parr (correlation; density functional theory)
BODIPY	Boron–dipyrromethene
CAM	Coulomb-attenuating method
D-A	Donor–acceptor
DBU	1,8-Diazabicyclo[5.4.0]undec-7-ene
DCM	Dichloromethane
DDQ	2,3-Dichloro-5,6-dicyano-1,4-benzoquinone
DFT	Density functional theory
DIPEA	<i>N,N</i> -Diisopropylethylamine
DMF	<i>N,N</i> -Dimethylformamide
DMSO	Dimethyl sulfoxide
EDG	Electron donating group
ESI	Electrospray ionization
EWG	Electron withdrawing group
FITC	Fluorescein isothiocyanate
FL _{Tz}	Fluorophore–tetrazine conjugate
FRET	Förster resonance energy transfer
HATU	1-[Bis(dimethylamino)methylene]-1H-1,2,3-triazolo[4,5- <i>b</i>]pyridinium 3-oxid hexafluorophosphate
HOMO	Highest occupied molecular orbital
HPLC	High-performance liquid chromatography
HRMS	High-resolution mass spectrometry
IC	Internal conversion
ICT	Internal charge transfer
iEDDA	Inverse electron demand Diels–Alder
ISC	Intersystem crossing
LD	Lipid droplet
LRMS	Low-resolution mass spectrometry

LUMO	Lowest unoccupied molecular orbital
MeOH	Methanol
NIR	Near-infrared
NMR	Nuclear magnetic resonance
PBS	Phosphate-buffered saline
PeT	Photoinduced electron transfer
Ph	Phenyl
SF	Seoul-Fluor
SF _{Tz}	Seoul-Fluor–tetrazine conjugates
TBET	Through-bond energy transfer
TCO	<i>trans</i> -Cyclooctene
TEA	Triethylamine
TFA	Trifluoroacetic acid
THF	Tetrahydrofuran
TLC	Thin-layer chromatography
TOI	Target of interest
TPP	Triphenylphosphine
Tz	Tetrazine
λ_{abs}	Absorption maximum
λ_{em}	Emission maximum
Φ_{F}	Fluorescence quantum yield
ε	Molar absorption coefficient

List of Figures

Fig. 1.1	<i>Jablonski</i> diagram.	2
Fig. 1.2	Schematic illustration of absorption and emission spectrum with a relatively small (left) and large (right) Stokes shift	4
Fig. 1.3	Examples of structural rigidification inducing enhancement of fluorescent quantum yield.	5
Fig. 1.4	Structures and photophysical properties of BODIPY derivatives. R in B1 represents aliphatic groups, and Ar in B2 is 4-iodophenyl.	7
Fig. 1.5	Structures and photophysical properties of coumarin derivatives.	8
Fig. 1.6	Structures and photophysical properties of cyanine derivatives.	10
Fig. 1.7	Structures and photophysical properties of fluorescein derivatives.	12
Fig. 1.8	Structures and photophysical properties of rhodamine derivatives.	14
Fig. 1.9	Structures and photophysical properties of Seoul-Fluor (SF) derivatives.	17
Fig. 2.1	The correlation between the R ¹ substituents of seoul-fluor and their corresponding quantum yields. a The relationship between Hammett constant values of the R ¹ -substituents and the quantum yields. b The relationship between the HOMO energy level of the R ¹ -substituents and the quantum yield	23
Fig. 2.2	Small molecule-based fluorescent bioprobes for lipid droplets (LDs) in the cellular system. a Chemical structure of LD bioprobes: Nile Red, BODIPY-fatty acid, and SF44. b Schematic diagram of a specific turning-on of fluorescent bioprobe, SF44, in the hydrophobic LDs in mammalian cells	25

Fig. 2.3	General structures of SF44 analogues for specific monitoring of LDs in the biological system. The exact chemical structures of SF44 analogues are illustrated along with their cLogP values	26
Fig. 2.4	The chemical structure of SF44 (a) and one of representative analogues, SF58 (b), and their emission spectra in four different solvent systems (diethyl ether, ethyl acetate, acetonitrile, and methanol) to show their solvatochromism.	27
Fig. 2.5	Fluorescent emission shifts for SF-based analogues in various solvents. Dye concentration was 1 mM	28
Fig. 2.6	Fluorescent images of cellular LDs using SF analogues in HeLa cells. a SF55, b SF56, c SF57, d SF44, e SF58, and f quantified result of (a)–(e). Quantified data was described as a mean value and SD of 20–30 cells. The scale bar represents 20 μm	30
Fig. 2.7	Cell viability results of SF58 against HeLa cells. Various concentration of SF58 was treated to HeLa cells for 12 h. Experiment was performed in triplicate and the results were normalized by DMSO control as 100%	31
Fig. 2.8	A A schematic diagram of biofuel production in green algae and its biomass yield compared to other agricultural feedstocks. B Lipid droplets (LDs) stained by SF44 (in green) a ; fluorescence by chlorophylls (in red) b ; merged image c ; bright-field image d . (C) LDs stained by Nile Red with the gold standard protocol (a , e); LD stained by Nile Red (b , f), SF44 (c , g), and SF58 (d , h) in 2% DMSO at room temperature.	32
Fig. 2.9	Optimization of SF44 for monitoring LDs in <i>chlamydomonas reinhardtii</i> . Various concentration (a) and staining time (b) of SF44 were screened under DMSO 2% at 25 $^{\circ}\text{C}$ in triplicate	33
Fig. 2.10	Fluorescent staining by each analogue in <i>chlamydomonas reinhardtii</i> . a , d , g , j and m are fluorescent images, b , e , h , k and n are DIC images, and c , f , i , l and o are merge images. The final concentration of each analogue is 5 μM under 2% DMSO at room temperature. Scale bar represents 5 μm	33
Fig. 2.11	A LD staining pattern after 25 min incubation with SF58 (5 μM) in the presence of 0.5% (a , b , c), 1% (d , e , f), and 2% DMSO (g , h , i). B Normalized viability of algae in 12 h (a), 24 h (b), and 36 h (c) after the LD image protocol under the optimal condition of SF44 and SF58 and Nile Red (NR).	34
Fig. 2.12	Schematic overview of the structure—photophysical property relationship in seoul-fluor system	35

Fig. 3.1	a Schematic representation of a fluorescence turn-on event of a fluorophore-tetrazine conjugate (FL_{Tz}), induced by bioorthogonal cycloaddition reaction with <i>trans</i> -cyclooctene (TCO). b Bichromophore type FL_{Tz} quenched by dipole-dipole energy transfer (left) or electron-exchange energy transfer (right). c Reported trends of change in fluorescence on/off ratios of FL_{Tz} depending on the emission wavelengths of fluorophores. d Monochromophore type FL_{Tz} , quenched by optically inactive S_0-S_1 transition (dark-state quenching)	44
Fig. 3.2	Molecular structures of Seoul-Fluor (SF) and SF-tetrazine conjugates (SF_{Tz} s)	46
Fig. 3.3	Changes in absorption spectra for Tz-containing molecules before (dashed line) and after (solid line) the reaction with TCO: a 3,6-Dimethyl-1,2,4,5-tetrazine, b $SF_{Tz}01$, c $SF_{Tz}02$, d $SF_{Tz}03$, e $SF_{Tz}04$, f $SF_{Tz}05$. All spectra were measured in an acetonitrile: H_2O (1:1 v/v) mixture at room temperature. The final concentration of dye and TCO was 20 and 200 μM , respectively.	49
Fig. 3.4	Changes in emission spectra for $SF_{Tz}01-SF_{Tz}05$ before (dashed line) and after (solid line) the reaction with TCO: a $SF_{Tz}01$, b $SF_{Tz}02$, c $SF_{Tz}03$, d $SF_{Tz}04$, e $SF_{Tz}05$. All spectra were measured in an acetonitrile: H_2O (1:1 v/v) mixture at room temperature. The final concentration of dye and TCO was 20 and 200 μM , respectively.	50
Fig. 3.5	The linear plots of pseudo first-order rate constant (k_{obs}) for $SF_{Tz}01-05$ versus molar concentration of TCO-NHS-ester, in an acetonitrile: H_2O (1:1 v/v) mixture at 20 $^{\circ}C$. Slopes represent second-order rate constant (k_2) for the corresponding SF_{Tz}	51
Fig. 3.6	a Chemical structure of representative fluorescence on-state SF analogue, SF_{Py} , generated from cycloaddition reaction of $SF_{Tz}02$ with TCO, and Hammett constant values (σ_p) of H, OCH_3 , NH_2 , and NET_2 functional groups. b Calculated HOMO and LUMO energy values (DFT, CAM-B3LYP/6-31G*) of SF_{Py} having H, OCH_3 , NH_2 , and NET_2 groups at the R^1 position. c Changes in the HOMO-LUMO energy gap of SF_{Py} s with corresponding functional groups at the R^1 position.	52
Fig. 3.7	a Chemical structure of a possible fluorescence on-state SF analogue having 4,5-dihydropyridazine moiety, generated from the iEDDA cycloaddition reaction of mono-chromophoric SF_{Tz} s with TCO. b Calculated HOMO and LUMO energy values (DFT, CAM-B3LYP/6-31G*) of $SF_{4,5-dihydroPy}$ s having H, OCH_3 , NH_2 , and NET_2 substituents at	

	the R ¹ position. c Changes in the HOMO-LUMO energy gap of SF _{4,5-dihydroPyS} with corresponding functional groups at the R ¹ position	53
Fig. 3.8	a Molecular structures of SF _{Tz06} (left), SF _{Tz07} (middle), and SF _{Tz08} (right). b Changes in absorption spectra for SF _{Tz06–08} , before (dashed) and after (solid) the reaction with TCO. c Changes in emission spectra for SF _{Tz06–08} , before (dashed) and after (solid) the reaction with TCO.	54
Fig. 3.9	A scatter plot of the inverse of HOMO-LUMO energy gap versus the maximum emission wavelength of SF _{Py02} , SF _{Py06} , SF _{Py07} , and SF _{Py08}	55
Fig. 3.10	A scatter plot of the inverse of HOMO-LUMO energy gap for SF _{4,5-dihydroPyS} versus the experimental maximum emission wavelength of corresponding TCO-SF _{Tz} products	55
Fig. 3.11	a Normalized emission spectra of SF _{Tz02} , SF _{Tz06} , SF _{Tz07} , and SF _{Tz08} after the reaction with TCO. b Photographic images of each compound irradiated at 365 nm, before and after reacting with TCO	56
Fig. 3.12	Molecular orbital distribution, vertical transition energy, and oscillator strength values (<i>f</i>) of SF _{Tz02} , SF _{Tz06} , SF _{Tz07} , and SF _{Tz08} , obtained by TD-DFT calculation (CAM-B3LYP/6-31G*) of corresponding first excited state optimized structures. a Quenched SF _{Tz} compounds before the reaction with TCO. b The fluorogenic SF _{Py} products after the formation of TCO-adducts. The main contributing orbital of S ₀ –S ₁ for each compound is illustrated. H and L stand for HOMO and LUMO, respectively	57
Fig. 3.13	Molecular orbital distribution, vertical transition energy, and oscillator strength values of SF _{4,5-dihydroPy02} , SF _{4,5-dihydroPy06} , SF _{4,5-dihydroPy07} , and SF _{4,5-dihydroPy08} , obtained by TD-DFT (CAM-B3LYP/6-31G*) calculation of corresponding first excited state optimized structures. Only main contributing orbital of S ₀ –S ₁ for each compound is illustrated. H and L stand for HOMO and LUMO, respectively.	59
Fig. 3.14	Molecular structures of SF _{Tz08} , SF _{Tz09} , and SF _{Tz10} for the direct comparison of mono- and bichromophoric design strategies on SF _{Tz} . SF _{Tz08} , SF _{Tz09} , and SF _{Tz10} are designed as long-emission wavelength analogues for the SF _{Tz02} (monochromophoric SF _{Tz}) and SF _{Tz04–05} (bichromophoric SF _{Tz}), respectively	60
Fig. 3.15	Absorption (left) and emission spectra (right) for a SF _{Tz09} and b SF _{Tz10} , before and after the reaction with <i>trans</i> -cyclooctene (TCO). Absorption and emission spectra for	

	SF _{Tz} 09 or SF _{Tz} 10 were obtained in an acetonitrile: H ₂ O (1:1 v/v) or in acetonitrile, respectively	61
Fig. 3.16	Chemical structures and cLogP values of SF _{Tz} 02* and SF _{Tz} 08* (water soluble analogues of SF _{Tz} 02 and SF _{Tz} 08, respectively)	62
Fig. 3.17	Fluorogenic bioorthogonal imaging of innate microtubules with SF _{Tz} in a fixed-cell condition. HeLa human cervical carcinoma cells were treated with DMSO (a, c) or Dox-TCO (b, d) for 1 h. TO-PRO-3 iodide (1 μM) was treated for nucleus staining. After brief washing with PBS, SF _{Tz} 02* (a, b) or SF _{Tz} 08* (c, d) was used to treat the cells (final concentration = 10 μM). Immediately after addition of the probes, the cell images were observed with fluorescence microscope without washing. Selective microtubule staining was further confirmed with immunofluorescence using α-tubulin antibody (g–h). Scale bar, 10 μm	62
Fig. 3.18	Fluorogenic bioorthogonal imaging of mitochondria with SF _{Tz} 02* and SF _{Tz} 08* in live cell conditions without washing steps. HeLa human cervical carcinoma cells were treated with DMSO (a, i) or triphenylphosphonium (TPP)-TCO (10 μM, b, c, e, g, h, j, l) with MitoTracker-Deep Red (f–h, k, l) for 40 min. After brief washing with PBS, SF _{Tz} 02* (a, b, c, e, g, h) or SF _{Tz} 08* (i, j, l) were used to treat the cells (final concentration = 10 μM). Images were immediately observed with fluorescence microscope without washing. (d) Plot intensity values of pixels along a red line in (c) were analyzed with the Image J program. ROI, region of interest	63
Fig. 4.1	Chemical structures of novel furoindolizine-based fluorophores and their calculated oscillator strength values (<i>f</i> values) using TD-DFT calculation at the B3LYP/6-31G* level. R group represents an aliphatic linker moiety	87
Fig. 4.2	A design principle for selecting the functional group positions in the furoindolizine skeleton. a The atomic coefficients in HOMO and LUMO of the core skeleton. b Chemical structure of lactam-embedded furo[3,2- <i>e</i>]indolizine core skeleton. c Calculated oscillator strength <i>f</i> values of the S ₀ –S ₁ transition when incorporated with the phenyl group at each carbon position.	88
Fig. 4.3	Design principles to control the emission wavelength in furoindolizine system	89
Fig. 4.4	Absorption-related photophysical properties of the furoindolizine library. a Schematic graph for the changes in oscillator strength values along with molar absorptivity upon structural modification. b A colored table of the molar	

	absorptivity of synthesized compounds. The darker colors represent higher molar absorptivity. c The average changes in the molar absorptivity upon the introduction of aryl substituents at the R ¹ and R ² positions in comparison with hydrogen.	92
Fig. 4.5	Chemical structures and HOMO and LUMO electron density distribution for a R ¹ EDG (08) and b R ² EDG (15), calculated through DFT at the B3LYP/6-31G(d) level	93
Fig. 4.6	A scattered plot of oscillator strength values and molar absorption coefficients.	93
Fig. 4.7	The calculated oscillator strength values for S ₀ → S ₁ , S ₀ → S ₂ and S ₀ → S ₃ (from top to bottom) using DFT/TDDFT at the B3LYP/6-31G(d) level and reported molar absorption coefficients for benzocoumarin derivatives	94
Fig. 4.8	The relationship between the reported molar absorption coefficients and the calculated oscillator strength values for representative BODIPY derivatives. a Chemical structures of representative BODIPY derivatives. b A table for reported molar absorption coefficients of BODIPY derivatives and the corresponding calculated oscillator strength values for the S ₀ → S ₁ transition. c A scattered plot of oscillator strength values and molar absorption coefficients of BODIPY derivatives	94
Fig. 4.9	a Emission-wavelength changes depending on the R ¹ and R ² functional groups. b Photographic images of the fluorescence emission colors of the representative compounds, irradiated at 365 nm. c A scatter plot of the inverse of the S ₀ -S ₁ energy gap versus the maximum emission wavelength	95
Fig. 4.10	a Rational design of novel furoindolizine-based fluorophores (17 , 18 , and 19) for each filter set of blue, green, and orange, respectively, with enhanced brightness in comparison with original SF analogues (SF09, SF16, and SF20). ^(a) Estimated values; ^(b) Observed values. [R = (CH ₂) ₂ NHBoc] b Chemical structure of Mito-18 and fluorescent live cell images in HeLa human cervical cancer cells stained by MitoTracker Red and Mito-18	96

List of Tables

Table 2.1	Electronic effects of the R ¹ substituents on the quantum yield of seoul-fluors	22
Table 2.2	Photophysical properties of SF44 and its derivatives	29
Table 3.1	Photophysical properties for SF _{Tz} s before and after the Reaction with <i>trans</i> -cyclooctene (TCO)	50
Table 3.2	HOMO and LUMO energy values for SF _{Py} s with variable R ¹ groups	53
Table 3.3	HOMO and LUMO energy values for SF _{4,5-dihydroPy} s with variable R ¹ groups	54
Table 3.4	Photophysical properties for monochromophoric SF _{Tz} s before and after the reaction with TCO.	56
Table 3.5	The TD-DFT calculation data for SF _{Tz} 02, SF _{Tz} 06, SF _{Tz} 07, and SF _{Tz} 08 at the first excited state optimized structures (CAM-B3LYP/6-31G*)	58
Table 3.6	The TD-DFT calculation data for SF _{Py} 02, SF _{Py} 06, SF _{Py} 07, and SF _{Py} 08 at the first excited state optimized structures (CAM-B3LYP/6-31G*)	58
Table 3.7	The TD-DFT calculation data for SF _{4,5-dihydroPy} 02, SF _{4,5-dihydroPy} 06, SF _{4,5-dihydroPy} 07, and SF _{4,5-dihydroPy} 08 at the first excited state optimized structures (CAM-B3LYP/6-31G*)	59
Table 3.8	Photophysical properties of SF _{Tz} s before and after the reaction with TCO.	60
Table 4.1	Previous attempts for extension of the π -conjugated system via incorporating a naphthyl or styryl group at the R ¹ position of indolizine-based SF	87
Table 4.2	Calculated oscillator strength values of the six isomers regarding the S ₀ \rightarrow S ₁ transition.	88

Table 4.3	An optimization table for the palladium-mediated cross-coupling reaction on the furoindolizine-based core skeleton	90
Table 4.4	A list of the compounds in the furoindolizine library with the values of their experimental and theoretical photophysical properties	91

List of Schemes

Scheme 1.1	Synthetic scheme for a representative BODIPY derivative	6
Scheme 1.2	Synthetic scheme for a representative coumarin derivative	7
Scheme 1.3	Synthetic scheme for a representative cyanine derivative	9
Scheme 1.4	Synthetic scheme for a representative fluorescein derivative	11
Scheme 1.5	Synthetic scheme for a representative rhodamine derivative	13
Scheme 1.6	Synthetic scheme for a general seoul-fluor derivative	15
Scheme 2.1	Synthetic scheme for SF44 analogues Reagents and conditions: a trans-4-(Diethylamino)cinnamaldehyde, AcOH, Na ₂ SO ₄ , dichloromethane (DCM), r.t., then NaBH ₄ , MeOH, 0 °C (70%); b Bromoacetyl bromide, triethylamine (TEA), DCM, -78 °C; c 4-acetylpyridine; d 1,8-diazabicyclo[5.4.0]undec-7-ene (DBU), toluene, and DCM (1:1, v/v), then 2,3-dichloro-5,6-dicyano-1,4-benzoquinone (DDQ) (5% for three steps). In case of SF55 and SF56, further deprotection was conducted in quantitative yields	27
Scheme 3.1	Synthetic scheme for SF _{Tz} 01-03	47
Scheme 4.1	Retrosynthetic analysis for the furoindolizine-based skeleton [R = (CH ₂) ₃ NHBoc]	89

Chapter 1

Introduction



1.1 Molecular Fluorescence and Photophysical Parameters

Fluorescence has been at the center of diverse scientific research due to high sensitivity, versatility, and easy accessibility [1]. In principle, fluorescence is an outcome of the energy deactivation process derived from an excited molecule. As shown in *Jablonski* diagram (Fig. 1.1), when the energy of external light is matched with the energy gap between the quantized electronic states of a given molecule, an absorption process occurs within a very short time scale ($10^{-15} \sim 10^{-14}$ s). Then, an excited molecule loses its absorbed energy by collisions with surrounding solvent molecules, so-called vibrational relaxation ($10^{-12} \sim 10^{-10}$ s), leading to the lowest vibrational level of each electronic state. Usually, a molecule with higher lying electronic states (S_2, S_3, \dots) can be stabilized to S_1 state via internal conversion with a time scale of $10^{-11} \sim 10^{-9}$ s, followed by vibrational relaxation toward lowest vibrational level of S_1 state. Finally, the fate of an excited molecule at the lowest lying first excited state results in radiative energy loss (fluorescence, $10^{-10} \sim 10^{-7}$ s), or nonradiative energy loss (quenching). For some molecules, especially with heavy atoms such as iodine, or bromine, intersystem crossing ($10^{-10} \sim 10^{-8}$ s) from singlet to triplet state occurs, resulting in another form of radiative energy loss (phosphorescence, $10^{-4} \sim 10$ s) or nonradiative deactivation process.

Note that the *Jablonski* diagram hypothesizes the electronic environment of the first vertical excited state (Franck-Condon state) and that of fluorescence-emitting state (first excited state after geometry relaxation) would be identical. This ideal description, however, sometimes fails to explain the empirical outcomes from complex molecules. For example, charge transfer molecules often undergo significant structural changes after excitation, which is linked to drastic change in energy levels of excited states [2]. Also, the optical process of every excited molecule varies markedly depending on structures, substituents, and/or surrounded media. In

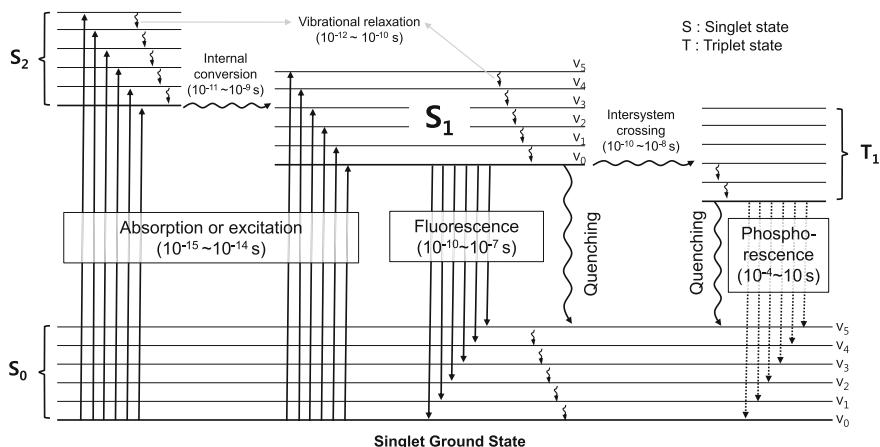


Fig. 1.1 Jablonski diagram

this regard, photophysical parameters can be useful to describe the optical features of a molecule for practical purposes.

1.1.1 Molar Absorption Coefficient: $\epsilon(\lambda)$

Owing to the ultrafast kinetics of absorption processes ($\sim 10^{-15}$ s), the molecular coordinate of an excited molecule is assumed unchanged during the electronic transition (Frank-Condon principle). In fact, absorption ability is one of the key factors governing the fluorescent intensity of a certain fluorophore. As a representative parameter for absorption, molar absorption coefficient (ϵ) defines the intrinsic absorption ability of a certain molecule at any given wavelength. This is an empirical parameter derived from the famous Beer-Lambert law.

$$A = -\log T = \log \frac{I_0}{I} = \epsilon \cdot b \cdot c$$

where A = absorbance, T = transmittance, I_0 = intensity of incident radiation, I = intensity of transmitted radiation, ϵ = molar absorption coefficient ($\text{cm}^{-1}\text{M}^{-1}$), b = path length (cm), c = sample concentration (M).

Another notable absorption parameter is oscillator strength value (f value), which is stemmed from a classical electromagnetic model, where the molecules are considered as oscillating dipoles [3]. Oscillator strength is a dimensionless quantity which represents the transition probability between two electronic states; an f value close to unity refers to strong transition (fully allowed transition), and an f value close to 0 refers to weak transition (forbidden transition). Importantly, the

theoretical oscillator strength value is directly correlated with experimental molar absorption coefficient through a following equation [4].

$$f = \frac{4 \ln 10 \epsilon_0 m c^2}{N_a e^2} \cdot \int \epsilon(\lambda) d\lambda$$

where ϵ_0 = vacuum permittivity, m = mass of an electron, c = speed of light, N_a = Avogadro number, e = charge of an electron.

Some aromatic molecules possessing heteroatoms such as nitrogen or oxygen show very poor molar absorption coefficients and oscillator strength values ($f < 10^3$, $f < 10^{-3}$) at a given wavelength, due to forbidden $n \rightarrow \pi^*$ transition [4]. On the contrary, many aromatic fluorophores with a high degree of conjugation frequently show large molar absorption coefficients (more than $10^4 \sim 10^5$) along with much enhanced oscillator strength values ($f > 10^{-1}$), originated from strong $\pi \rightarrow \pi^*$ transition [4].

1.1.2 Emission Maxima: λ_{em}

In most cases, maximum emission peak (λ_{em}) of a molecule is independent from the wavelength of incident light (Kasha's rule). This is because internal conversion ($\sim 10^{-10}$ s) and vibrational relaxation ($\sim 10^{-12}$ s) normally precede fluorescence process ($\sim 10^{-9}$ s) owing to their superior kinetics. As a general rule, the extension of a π -conjugate system, such as aromatic fusion or olefin insertion, induces bathochromic shift of maximum emission of a molecule, via reducing the energy gap of $\pi - \pi^*$ transition. The substituents on a fluorophore also can promote the shift of a maximum emission peak. For examples, aniline or phenol substitutions on an aromatic system may cause intramolecular charge transfer (ICT), leading to bathochromic shift of maximum emission peaks, concomitant with a broadening effect of overall emission spectra [4].

1.1.3 Stokes Shift: $\Delta\bar{\nu}$

The Stokes shift is defined as the gap between the maximum peak of the first absorption band and the maximum peak of emission. Given that the energy difference between absorption and emission is closely related to deactivation processes of excited states, alterations of Stokes shift with regard to the change of substituents or solvents provide useful information about the excited states of a certain molecule. From a molecular structural point of view, a fluorophore with high symmetry generally shows small Stokes shift, and it is often insensitive to the change in polarity of media [5]. On the other hand, a fluorophore with low symmetry often displays large Stokes shift, along with environmental sensitivity [6]. It is worth

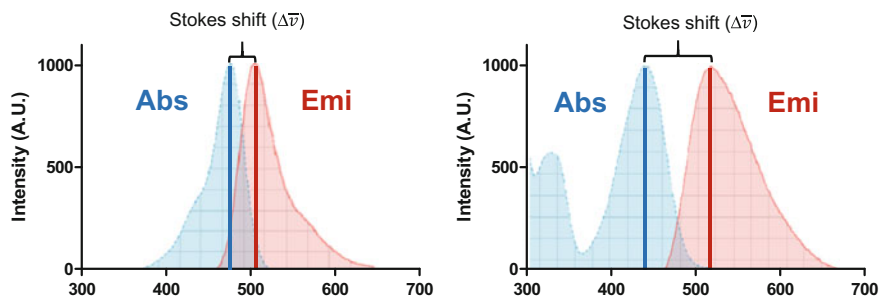


Fig. 1.2 Schematic illustration of absorption and emission spectrum with a relatively small (left) and large (right) Stokes shift

mentioning that drastic change in dipole moment at the excited state often induces increasing Stokes shift of a molecule [7]. The reduced spectral overlap between absorption and emission will guarantee a low chance of self-absorption or self-quenching effect of a given compound, providing a better detection window in the fluorescent microscopy (Fig. 1.2).

1.1.4 Fluorescent Quantum Yield: Φ_F

By definition, fluorescent quantum yield is a ratio of the number of fluorescent molecules to the total number of excited molecules. At the lowest vibrational level of S_1 state, the fluorescence process competes with nonradiative internal conversion ($S_1 \rightarrow S_0$) and intersystem crossing ($S_1 \rightarrow T_1$) pathways. These can be expressed by a following equation [4].

$$\Phi_F = \frac{k_f}{k_f + k_{ic} + k_{isc}} = k_f \cdot \tau$$

where, k_f = rate constant for $S_1 \rightarrow S_0$ fluorescence process, k_{ic} = rate constant for internal conversion $S_1 \rightarrow S_0$, k_{isc} = rate constant for intersystem crossing, τ = life time of S_1 excited state.

But, other factors, such as external conversion by collisions with solvents or oxygen molecules, or electron and energy transfer process also can largely affect the quantum yield of a molecule.

In fact, quantum yield is one of the most important photophysical parameters, determining fluorescent intensity of a fluorophore. Practically, researchers often used a term—product of molar absorption coefficient and quantum yield—to compare the relative brightness of fluorophores [Brightness = $\varepsilon(\lambda) \cdot \Phi_F$] [8]. Quantum yield of a molecule can be enhanced by rigidifying the molecular structure. For example, quantum yield of freely rotatable biphenyl moiety can be markedly improved by a methylene bridge (Fig. 1.3a, $\Phi_F = 0.26 \rightarrow 0.70$) [9]. Also

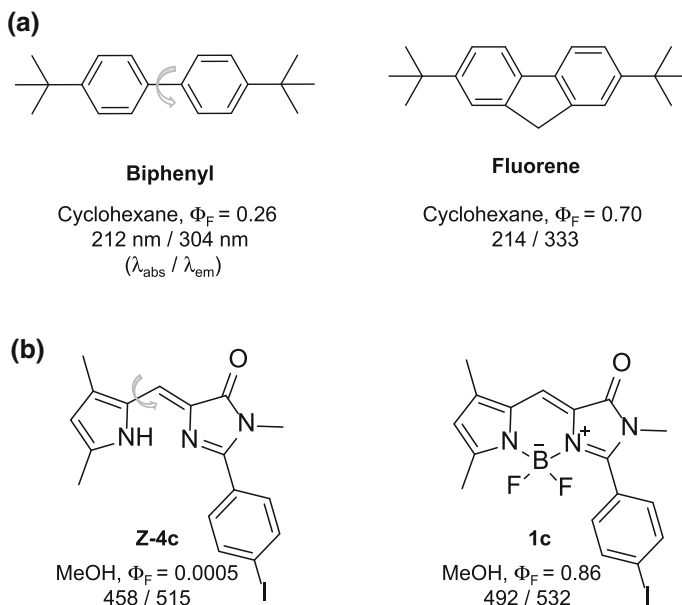


Fig. 1.3 Examples of structural rigidification inducing enhancement of fluorescent quantum yield

many fluorogenic chelators have showed drastic increase in fluorescence after binding with a guest molecule [10], which can be rationalized as the result of enhanced molecular rigidity (Fig. 1.3b). Modification toward inflexible molecular structures reduces the rate constant for internal conversion $S_1 \rightarrow S_0$ (k_{ic}), which is a major nonradiative process, promoting more favorable energy loss through fluorescence deactivation pathway. Also it is known that $\pi - \pi^*$ excited state has a larger fluorescence rate constant (k_f) than that of $n - \pi^*$ excited state [11]. Thus, a molecule with an excited state of the lowest lying an $n - \pi^*$ usually exhibits low fluorescence efficiency, which is the case of most azo compounds [4].

1.2 Organic Fluorophores

In the field of life science, fluorescence proteins, fluorescence nano particles and small organic fluorophores are widely used to visualize and transcribe the biological systems, which have often been linked to clinical diagnosis and drug discovery process [12]. Thanks to the small size (often <1 nm) and suitable photophysical properties, organic fluorophores are heavily used at the cellular, tissue, organ, or even organismal level with superior penetrability [13]. From a molecular design perspective, understanding of the structure-photophysical property relationship of a given fluorophore often paves the road to development of valuable molecular

probes for biological studies. Below is a brief summary of structure and synthesis, general property, structure-photophysical property relationship, and bioapplication of representative organic fluorophores.

1.2.1 Bodipy

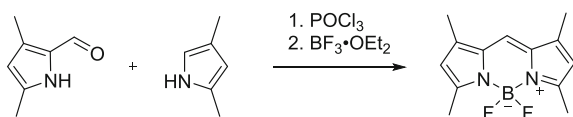
Structure and synthesis. The boron-dipyrromethane (BODIPY) dyes are comprised of endocyclic nitrogen donor and acceptor, with a rigid framework supported by a bridging boron atom. Typically, BODIPY is synthesized by condensation reaction of two equivalents of pyrrole derivatives and an aldehyde derivative, followed by addition of BF_3 [14]. Strong molecular fluorescence appears after the binding of a boron atom [15] (Scheme 1.1).

General property. BODIPY dyes usually shows small Stokes shift, excellent quantum yield, and insensitive fluorescent property to environmental changes. Since the net charge of BODIPY is neutral, it is considered as a lipophilic fluorophore.

Structure-photophysical property relationship. Synthetic flexibility of BODIPY allows researchers to develop a myriad of BODIPY derivatives having diverse photophysical properties [16]. As shown in Fig. 1.4, an extension of π -electron system through *alpha*-position of a BODIPY scaffold allows the bathochromic shift of both absorption and emissions spectrum (**B1** vs. **B2**, **B3**) [16–18]. Notably, nitrogen substituted aza-BODIPY derivatives (**B4**) [19] promote ~ 100 nm bathochromic shifts of absorption and emission spectra compared to that original BODIPY scaffolds, endowing a great advantage for biological applications circumventing auto-fluorescence area. Another interesting example is **B5** and its derivatives, named Keio-Fluor [20], constructed with fused furan rings on the edges of pyrrole rings in a symmetrical manner. By virtue of remarkable enhancement in molar absorption coefficient ($\epsilon \sim 3.0 \times 10^5$) compared to that of a traditional BODIPY ($\epsilon \sim 8.0 \times 10^4$), Keio-Fluors have been recognized as one of the brightest fluorophores ever reported. The *meso*-position of BODIPY is often regarded as an ineffective site for spectral modulations, but modification on it can lead to dynamic changes in fluorescent quantum yield [14, 16]. Therefore, *meso*-modification is highly effective to develop functionalized BODIPY (e.g. indicators for metals, anions, ROS) by triggering fluorescence intensity changes via host-guest chemistry, or specific chemical reactions [14, 16].

Bioapplication. Although the versatility of BODIPY dye encompasses pH indicators, metal and ion sensors, or redox sensors *et cetera* [14, 16], the innate strength of BODIPY dye lies in its excellent light-harvesting ability regardless of surroundings. Thus, BODIPY dyes frequently used as labeling agents in biological systems [21], or

Scheme 1.1 Synthetic scheme for a representative BODIPY derivative



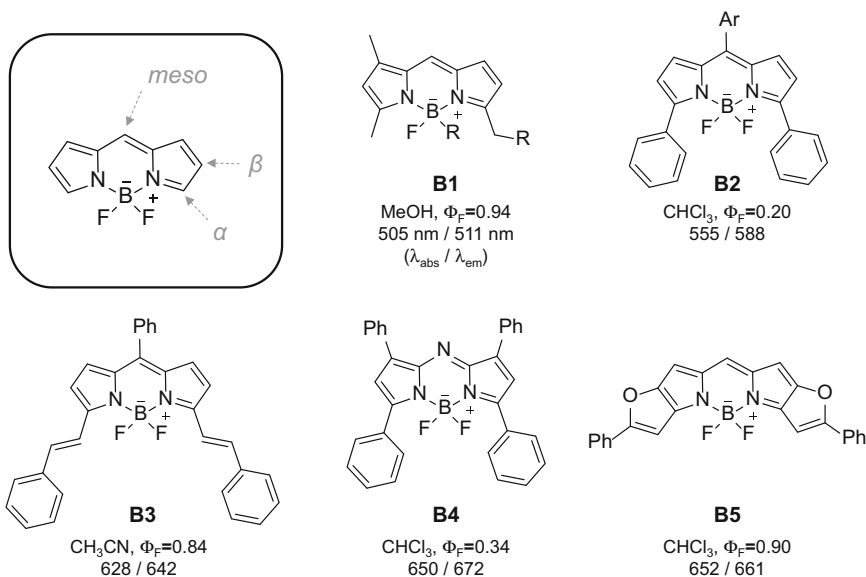
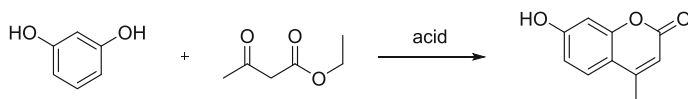


Fig. 1.4 Structures and photophysical properties of BODIPY derivatives. R in **B1** represents aliphatic groups, and Ar in **B2** is 4-iodophenyl

used as conjugates for fluorescence polarization techniques [22]. Also, the lipophilic property of BODIPY can be harnessed to develop staining reagents for lipid membranes [23], or hydrophobic organelles in a specific manner [24].

1.2.2 Coumarin

Structure and synthesis. Coumarin dyes are based on a benzopyrone framework, a privileged structure observed in many natural plants and fruits [25]. Historically, coumarin has received much attention as a pharmacological building block for treatment of various diseases, such as asthma, inflammation, cancer, or depression, *et cetera* [26]. From a structural point of view, coumarin dyes have a compact bicyclic structure along with smaller molecular weight compared to other dye classes. The synthesis of coumarin is usually conducted via the condensation reaction of a phenol derivative and a β -keto ester (or acid) derivative [27] (Scheme 1.2).



Scheme 1.2 Synthetic scheme for a representative coumarin derivative

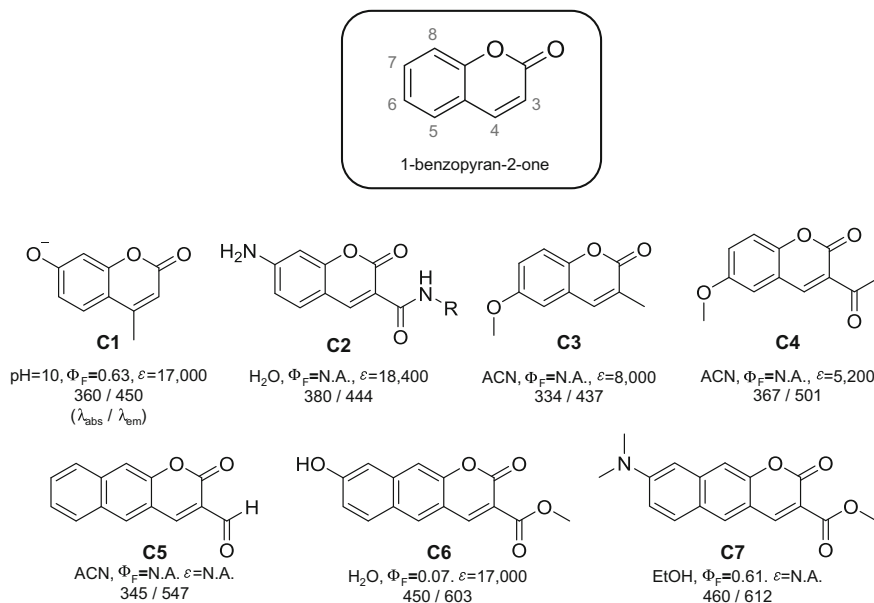


Fig. 1.5 Structures and photophysical properties of coumarin derivatives

General property. To give off meaningful fluorescence, coumarin requires an electron donating group at the 7-position of benzopyrone moiety (Fig. 1.5). Coumarin dyes generally emit blue fluorescence and often show large Stokes shift, originated from charge transfer at the excited state [28]. Chemical stability and cell permeability of coumarin dyes are largely dependent upon substituents [29].

Structure-photophysical property relationship. Despite early discovery, the structure-photophysical property relationship of coumarin has been documented less systematically. As shown in Fig. 1.5, **C1**, 7-hydroxycoumarin, emits blue fluorescence together with decent light-harvesting ability under the basic conditions, forming a phenol anion [30]. Substitution of the hydroxy group to an amine (**C2**) also guarantees good fluorescent property along with much less sensitivity towards pH changes [31]. To promote long wavelength shifts, the extension of the π -electron system or fusion of a benzene ring has also been explored [32–34]. It turns out that π -system elongation through 3-position of a benzopyrone scaffold can lead to effective bathochromic shift of fluorescence, (**C3** vs. **C4**) in many studies [32]. In the case of a benzene fusion, benzo[*g*]coumarin (**C5**) shows the most effective bathochromic shift, compared to other benzocoumarins having different benzo-fused orientations [32, 33]. The introduction of hydroxy or amine groups on the benzo[*g*]coumarin elicits compelling emission shift (**C5** vs. **C6**, **C7**) [32, 34], presumably due to internal charge transfer (ICT) induced by a newly installed electron donating group toward the ketone group of benzo[*g*]coumarin. Notably, many coumarin derivatives show larger Stokes shifts than those of other fluorophores.

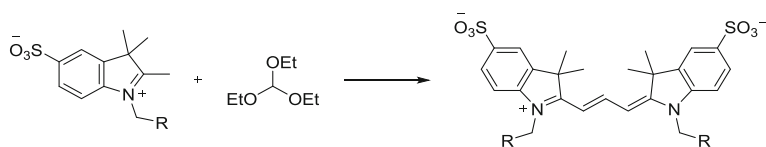
Bioapplication. Based on the important role of an electron donating group at the 7-position of benzopyrone moiety, various electron donating groups were introduced at the 7-position to develop enzyme-responsive latent fluorescence materials [35]. Upon cleavage of masking groups—enzyme substrates—by enzymatic reactions, the electron donating ability at the 7-position of coumarins was restored, concomitant with turn-on fluorescence signals. Also, by combination with long-wavelength fluorophores, coumarin labelings are used to provide multiplexed fluorescence images [36]. However, the mediocre brightness along with short-emission wavelength make them less attractive for biological applications, because they are often overlapped with auto-fluorescence region from biomolecules [37].

1.2.3 Cyanine

Structure and synthesis. Although sometimes, the structure of a cyanine dye is considered limitedly as an indole-based symmetric polymethine scaffold, the cyanine class dye embraces a wide range of molecules containing $R_1N-(CH=CH)_N-CH=N+R_2$ structures. Cyanine dyes have positively charged resonance forms, and a number of polymethine bridges connect donor and acceptor nitrogens with the alternation of single and double bond. The synthesis of cyanine dyes generally requires a condensation reaction between an aldehyde equivalent and activated carbon species. For example, the synthesis of Cy3 dye demands a triethyl orthoformate and two equivalents of indolinium derivatives [38] (Scheme 1.3).

General property. The trademark of cyanine is its outstanding molar absorptivity. Many cyanine dyes exhibit molar absorption coefficient values over 10^5 ($\text{cm}^{-1}\text{M}^{-1}$) along with long-wavelength fluorescence, which places them in primary fluorescent tags for biological applications [39]. The quantum yield of cyanine, however, is inferior to that of rigid fluorophores such as BODIPY or fluorescein, because rotatable polymethinic chains lead to energy loss process through nonradiative internal conversion pathway [40]. It is worth mentioning that cyanine dyes often form aggregates due to strong self-attraction, which can be mitigated by installation of negatively charged sulfonate groups [41] (Fig. 1.6).

Structure-photophysical property relationship. As a representative example, Cy3 consists of three methine bridges emitting yellow-orange fluorescence. The suffix number following 'Cy' identifies the number of methine bridge units for the indole-based cyanine system. Typically, increasing the number of vinylene group in



Scheme 1.3 Synthetic scheme for a representative cyanine derivative

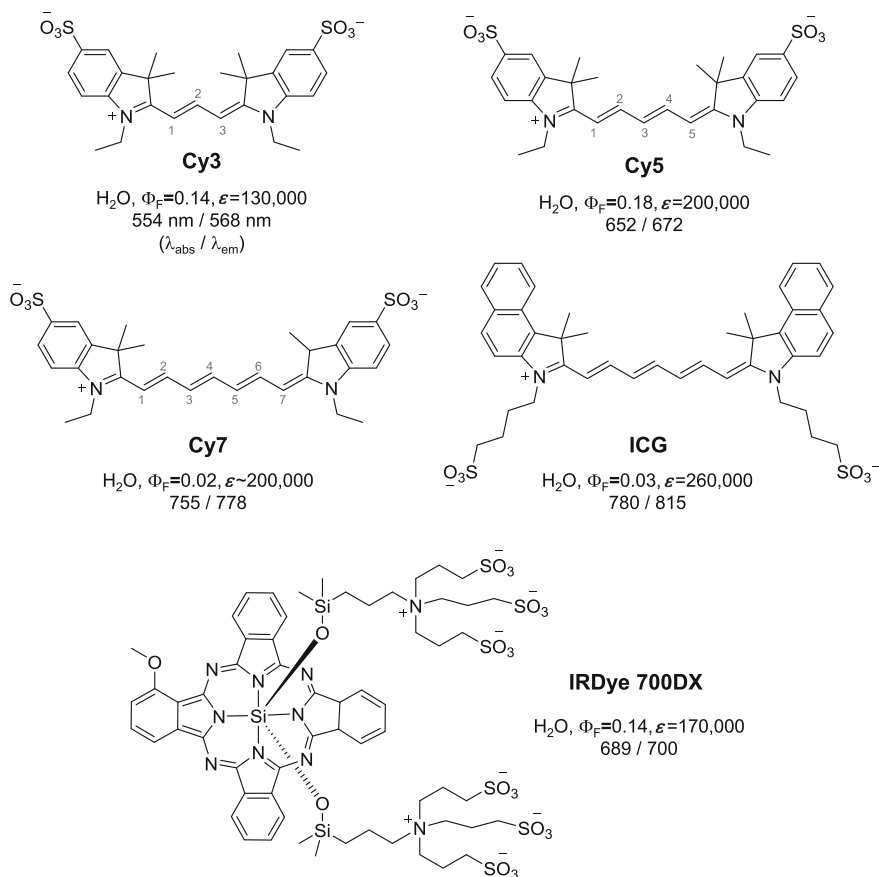


Fig. 1.6 Structures and photophysical properties of cyanine derivatives

the ‘Cy’ system elicits 100 nm bathochromic shift of absorption and emission maxima. For instance, **Cy3**, **Cy5** and **Cy7** exhibit fluorescence emission maxima at 568, 672, and 778 nm, respectively [42]. Fused benzene rings on the indole moiety also can cause 20 ~ 30 nm bathochromic shift, as shown in **ICG** (indocyanine green) [43]. In terms of quantum yield, structural rigidification is valid for cyanine dye class. Phthalocyanine-based **IRDye 700DX** shows higher fluorescent quantum yield (0.14) compared to that of linear polymethine dyes, together with excellent molar absorption coefficient (170,000) at the Near-Infrared (NIR) region [44].

Bioapplication. Cyanine dyes have various advantages for biological researches, such as long-wavelength emission, exceptional light absorbing ability, low toxicity, and excellent biocompatibility [45]. After the development of sulfonated version which ensures minimized self-aggregation along with enhanced solubility [46], the ‘Cy’ class became the number one fluorochrome of choice over the last

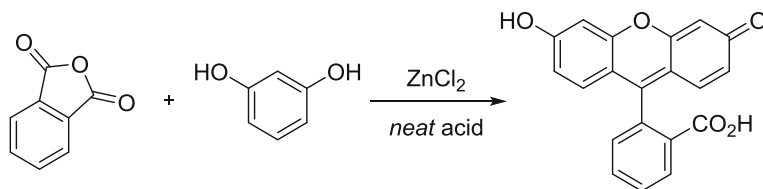
couple of decades [47]. Also, by virtue of adequate spectral overlap, Cy3/Cy5 pair has been applied to numerous FRET experiments to monitor the physical behaviors of proximal biomolecules [47]. Besides, the fact that cyanines show photoblinking property when combined with thiols and laser source, enriches cyanine's utility to super-resolution microscopy technique [48]. However, one should notice that upon binding with target proteins or nucleic acids, the fluorescence intensity of cyanine might increase presumably due to restricted rotation of vinylene groups [49] and this limits the use of cyanine series for some cases [50].

1.2.4 Fluorescein

Structure and synthesis. Fluorescein is one of the most classical fluorophores, and its derivatives have been widely used for biological, medicinal, or industrial purposes [8]. Fluorescein is based on an aromatic xanthene scaffold connected with an adjacent phenyl moiety, and two exocyclic oxygens on the xanthene core create symmetrical 'push-pull' resonance structure. Frequently, the synthesis of a fluorescein involved a condensation reaction between a phthalic anhydride and two equivalents of resorcinol, with an aid of ZnCl_2 under neat acid conditions [51]. (Scheme 1.4.)

General property. The sodium salt form of fluorescein has fairly good solubility under basic aqueous conditions, and it shows high molar absorptivity and excellent quantum yields. Fluorescein can be changed from mono- to di-anionic form around pKa value of 6.4 [51], and the di-anionic form emits the brightest fluorescence property. As shown in Fig. 1.7, the most intriguing character of fluorescein is its equilibrium between a lactone (closed, nonfluorescent) and a quinoid form (open, fluorescent). By using this structural changes, turn-on fluorescent sensors triggered by external stimuli such as light or enzymes have been largely explored [52].

Structure-photophysical property relationship. By introducing a fused benzene ring, drastic bathochromic shift of absorption and emission spectra of fluorescein can be achieved, as a compensation for reduced light harvesting ability. As shown in Fig. 1.7, an asymmetrical structure, **F2** (seminaphtofluorescein, SNAFL) presents interesting photophysical properties different from its mother molecule **F1**; for instance, pKa values, emission spectra, and Stokes shift [53]. For symmetric **F3** (naphthofluorescein), it displays more red-shifted spectra along with



Scheme 1.4 Synthetic scheme for a representative fluorescein derivative

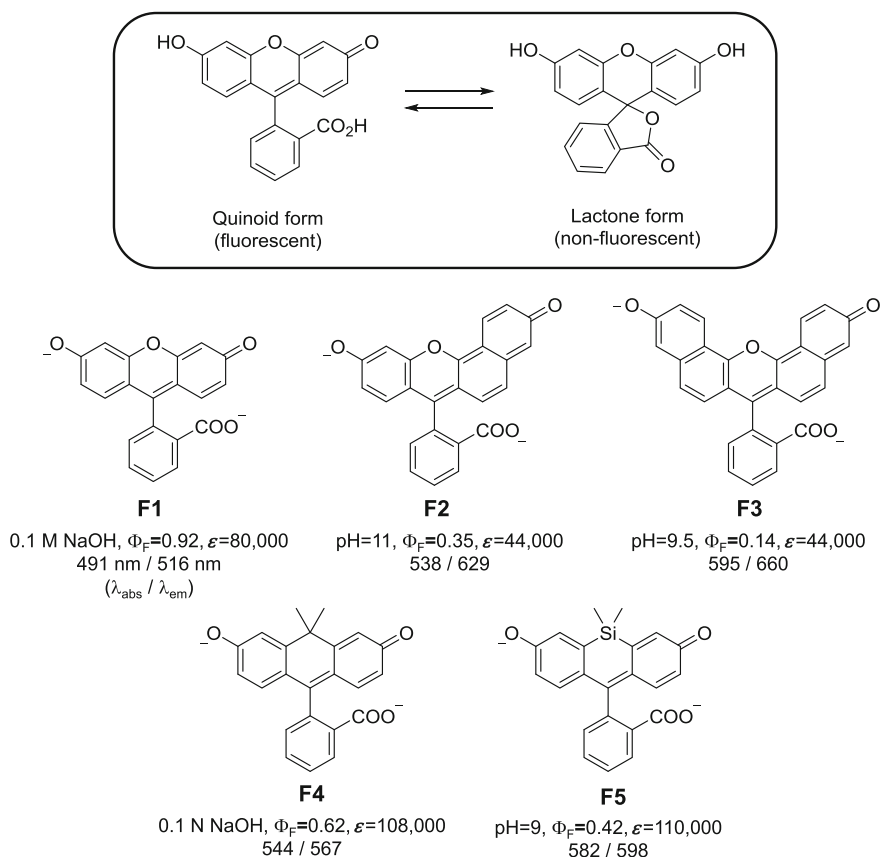


Fig. 1.7 Structures and photophysical properties of fluorescein derivatives

inferior fluorescent quantum yield to that of **F1** and **F2** [54]. Interestingly, atomic replacement at the center of xanthen moiety produces large bathochromic shift of absorption and emission spectra. For examples, **F4** (carbofluorescein) exhibits around 50 nm shift [55] and **F5** (sila-fluorescein) records around 80 nm shift [56] of both in absorption and emission, compared to those of **F1**. Throughout many studies, the phenyl moiety on the xanthen core is served as recognition sites for metals or ions, producing PeT process between the electronically decoupled phenyl moiety and the xanthen fluorescent core [57].

Bioapplication. Since fluorescein derivatives have multiple states of ionic equilibrium together with variable pKa values, they are frequently used for chromophoric pH indicators [58]. For the cellular imaging purposes, good water solubility and excellent brightness of fluorescein derivatives enable researchers to develop various enzyme reporters, metal or ion indicators and bright conjugates for biomolecules [8, 52, 57]. For diagnosis purpose, fluorescein diacetate is approved by FDA as an fluorescent angiography agent to exam retinal blood vessels [58].

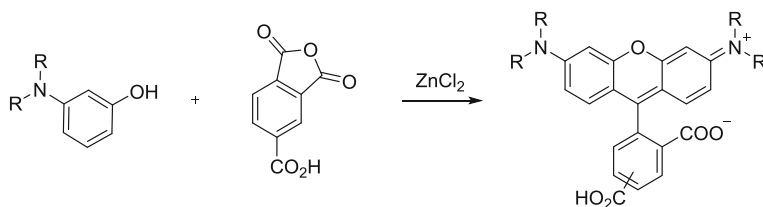
However, relatively high photobleaching rate of fluorescein derivatives often problematic for long-term imaging of cellular systems [58]. Also, low brightness under a pH value less than 6, limits its usage as a fluorescence reporter, especially in the acidic cellular environments [59].

1.2.5 Rhodamine

Structure and synthesis. The molecular structure of rhodamine is almost identical with fluorescein, except the exocyclic heteroatom is nitrogen. The synthesis of rhodamine requires a condensation reaction between a phthalic anhydride derivative and two equivalents of 3-aminophenol with an aid of a lewis acid under the neat conditions [60]. A carboxyl group attached to a phthalic anhydride is often used for further bioconjugation. However, it generates hard-to-separate isomeric mixtures (3-carboxyphenyl or 4-carboxyphenyl), unlike easily separable fluorescein isomeric mixtures [61]. In this regard, many commercial vendors handle rhodamine products as isomeric mixtures. (Scheme 1.5.)

General property. Although the synthetic accessibility is limited compared to fluorescein, general photophysical properties of rhodamines are superior to that of fluorescein analogues. Most of rhodamine derivatives have low pH-sensitivity and high photobleaching resistance, which are important advantages for developing practical bioimaging agents [62]. On top of that, modifiable aromatic amines on the xanthene scaffold endow better flexibility in fluorescence spectrum [63]. Rhodamine also has an open/closed equilibrium, and the control of this spirocycle formation has been major interests for the many researchers in the development of useful turn-on fluorescent sensors respond to a stimulus of interest.

Structure-photophysical property relationship. Normally, the alkylation of aromatic amines on the xanthene core leads to bathochromic shifts of absorption and emission spectra of rhodamine, concomitant deterioration of fluorescent quantum yield (**R1** vs. **R2**) [8]. After a molecular excitation, the C–N bond rotation on the xanthene core is considered as a major culprit for nonradiative deactivation process [64]. In this context, synthetic chemists tried to freeze the rotatable C–N bonds. As shown in Fig. 1.8, the tethered derivative **R3**, well-known as Texas Red, usually gives off brighter fluorescence compared to alkyl substituted (untethered) rhodamine



Scheme 1.5 Synthetic scheme for a representative rhodamine derivative

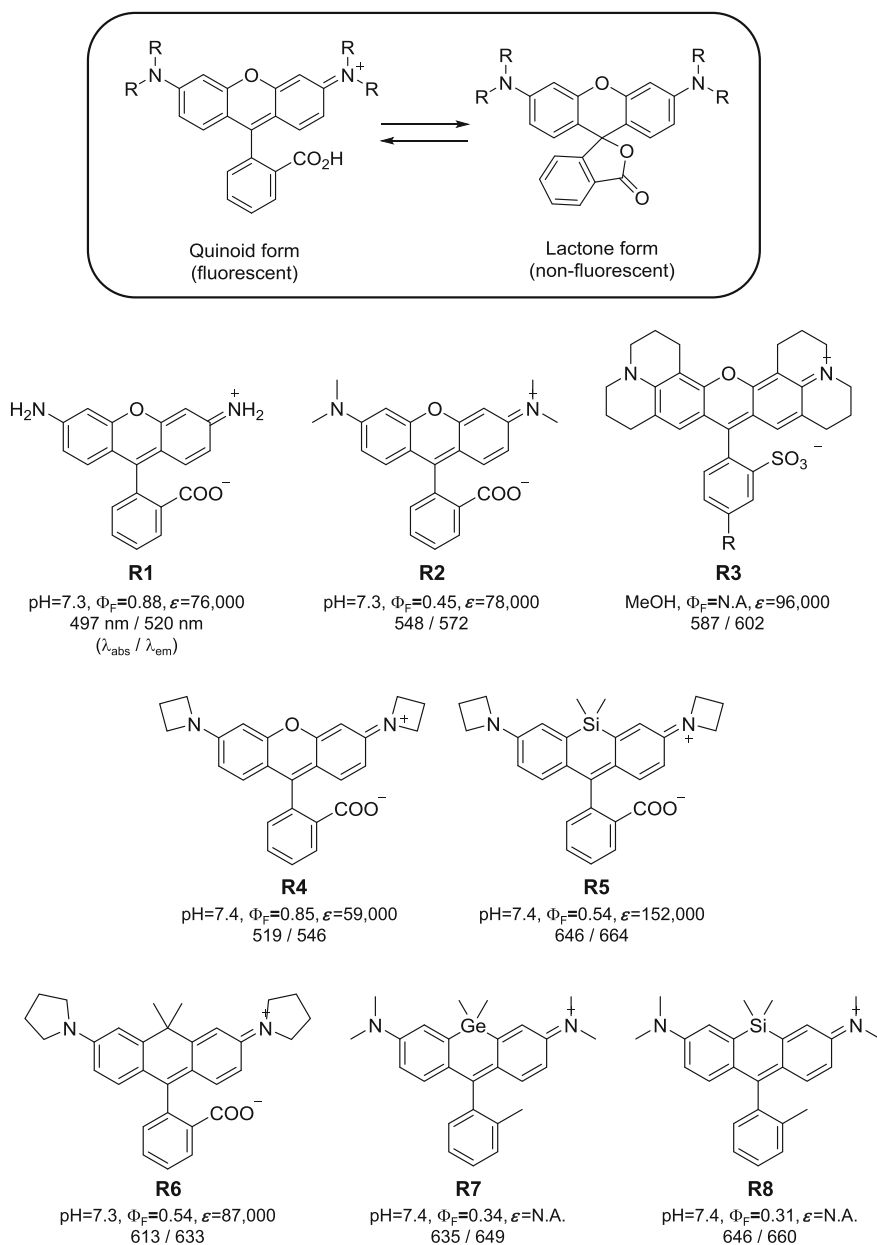


Fig. 1.8 Structures and photophysical properties of rhodamine derivatives

derivatives [65]. Interestingly, recent progresses reveal that introducing three-membered or four-membered rings on the aniline part is an effective strategy to preserve the fluorescent quantum yields of rhodamines (**R2** vs. **R4**, and **R8** vs. **R5**)

[66]. Authors rationalized that small ring-type alkyl substituents on the aromatic amines could mitigate nonfluorescent TICT (twisted internal charge transfer) process, due to minimized steric hindrance between the xantheno moiety and adjacent cyclic amine substituents. Another structural modification, atomic replacement strategy, is also valid to the rhodamine moiety. The substitution of oxygen to carbon (**R6**), germanium (**R7**) or silicon bridge (**R8**) displays effective bathochromic shift of emission and absorption maxima, together with relatively well-conserved light harvesting ability [67].

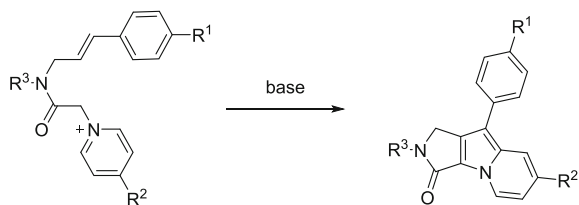
Bioapplication. The excellent fluorescence property, pH insensitivity, and biocompatibility of rhodamines have led to development of a number of fluorescent bioconjugates for in vitro and in vivo applications [68]. In recent years, silicon-rhodamines derivatives have received great attention as practical in vivo imaging agents, due to NIR fluorescence along with excellent cell permeability [69]. Besides, rhodamine derivatives are frequently used for super-resolution microscopy technique [70], due to their excellent photostability. By taking advantage of the spirocyclic open/closed equilibrium of rhodamine derivatives, Urano and co-workers reported brilliant spontaneous super-resolution materials, which do not require invasive external sources, such as intensive light or additive molecules [71].

1.2.6 Seoul-Fluor (SF)

Structure and synthesis. A novel in-house fluorophore, namely Seoul-Fluor (SF), is based on a γ -lactam embedded indolizine scaffold along with a phenyl moiety affixed to the main fluorophore [72]. The SF has three variable groups; the R^1 and R^2 are connected with π -electron system of indolizine, and the R^3 is normally consisted with aliphatic chains. The key synthetic step for the formation of the γ -lactam embedded indolizine is intramolecular 1,3 dipolar cycloaddition between an azomethine ylide and a substituted olefin, which are initially derived from the pyridines and cinnamaldehyde derivatives, respectively [72]. The combinatorial approach allows researchers to construct the systematic molecular library, which segues into solid understanding of the structure-photophysical property relationship of the SF system [73]. (Scheme 1.6.)

General property. The uniqueness of SF lies in its variability in substituents, which induce dramatic changes in optical, chemical, and physical properties. Optical property of SFs are mainly controlled by the R^1 and R^2 groups, and

Scheme 1.6 Synthetic scheme for a general seoul-fluor derivative



physicochemical property is highly dependent on the constituents of the R³ groups [72–74]. For some derivatives, especially the one with an electron donating group (EDG) at the R¹ position, show strong charge transfer character, which in turn elicits the environmental sensitivity of SF analogues [75].

Structure-photophysical property relationship. By virtue of systematic SF library via a combinatorial approach, the structure-photophysical property relationship of SFs has been relatively well-explored. As shown in Fig. 1.9, changing the R² group from electron-donating group (EDG) to electron-withdrawing group (EWG) (SF02, SF03, and SF04) induces effective bathochromic shift both in absorption and emission spectra [73]. Besides, the position of R² group turned out to be critical for emission and quantum yield; the EWG at the 7-position of indolizine shows the most red-shifted, and the highest quantum yield value compared to EWG at the 6-, or 8-position [73]. In the case of R¹ group, changing from EWG to EDG elicits drastic bathochromic shifts (SF04, SF12, SF16, and SF24), which is an opposite effect from the R² group. Also, *-para* substituted R¹ groups commonly exhibit the most pronounced substitution effect, presumably better accessibility to the π -electron system of indolizine fluorophore [73]. It should be emphasized that, emission maxima of SFs are well-matched with calculated energy gaps ($\Delta\epsilon$ V) between HOMO and LUMO, which can be harnessed to design the novel SF-based probes with a desirable emission wavelength [73].

Bioapplication. By taking advantage of environmental sensitivity and lipophilicity, SF44, a representative SF derivative, has been developed as a specific lipid droplet (LD)—an important hydrophobic organelle closely related with cardiovascular complications and type 2 diabetes—staining reagent [75]. Internal charge transfer (ICT) character of SF44 allows washing-free visualization of LDs in the live cell conditions, which leads to a practical application for high-contents screening [76]. Also, amines or carboxyl groups embedded SF derivatives show drastic fluorescence alteration in response to pH changes, which have led to development of colorful pH sensors [77]. Furthermore, by introducing an enzyme substrate at the R¹ group, a SF-based bioprobe (S/BP) for protein tyrosine kinases has also been developed with high specificity [78].

1.3 Aims and Scope of the Thesis

This thesis describes in-depth studies of indolizine-based fluorescent molecules, including molecular design, organic synthesis, optical property analysis, and quantum calculation. Herein, rational development of molecular probes and biological applications will be followed. Specific aims and scope of research described in this thesis include:

1. To synthesize unexplored fluorescent small molecules in a systematic manner
2. To elucidate structure-property relationship of indolizine-based fluorophore on the basis of quantum mechanical approaches

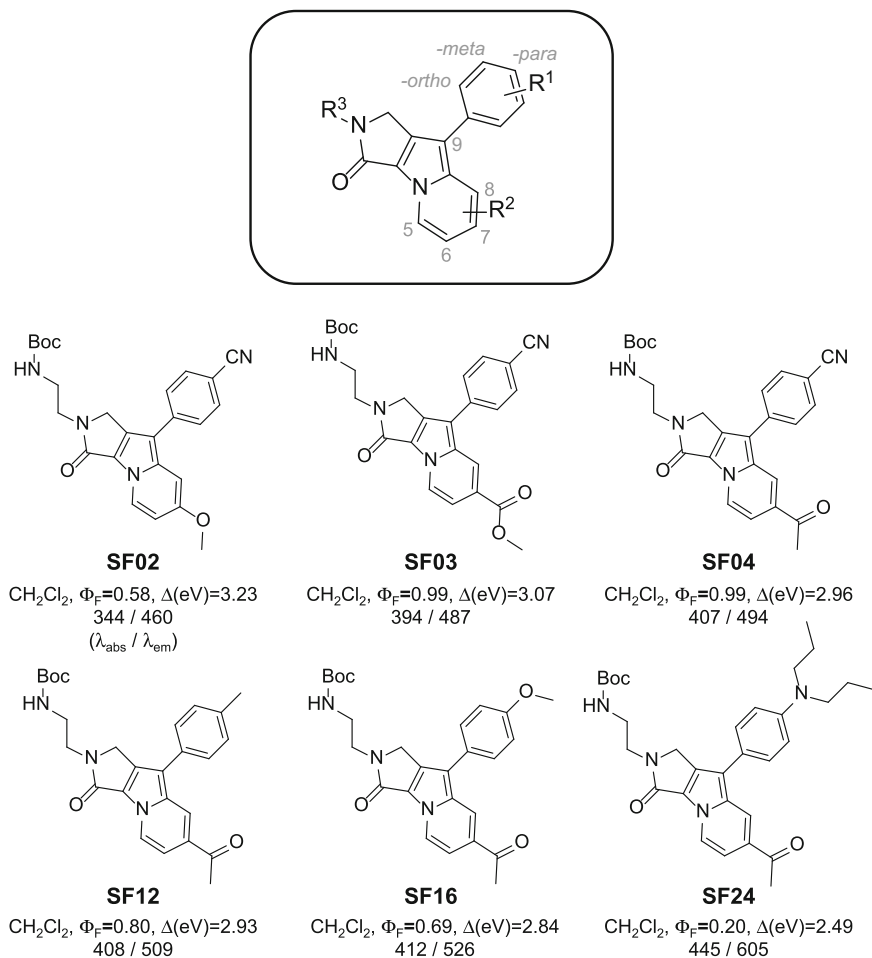


Fig. 1.9 Structures and photophysical properties of Seoul-Fluor (SF) derivatives

3. To develop tailored molecular probes for biological studies
4. To demonstrate a novel design strategy for fluorogenic bioorthogonal probes
5. To suggest a rational design principle for enhancing molecular absorptivity

According to these goals, each chapter contains the following research subjects.

Chapter 2 describes continuous efforts to understand the relationship between the photophysical property and molecular structure of the Seoul-Fluor system. Quantum yield and molecular lipophilicity have been explored with regards to the structural modifications.

Chapter 3 deals with a novel approach for tetrazine containing bioorthogonal probes having excellent turn-on fluorescent ratios, regardless of emission wavelengths. On the basis of well-studied indolizine fluorophore platform, design

principle, synthesis, photophysical property analysis and quantum mechanical interpretations are discussed. Finally, bioorthogonal applications for the live cell imaging has been followed.

Chapter 4 depicts a rational design strategy to secure an unexplored fluorophore having enhanced molar absorptivity. With the guidance of calculated oscillator strength values, a systematic library construction and structure-property relationship study have been dealt with in detail. The direct comparison between Seoul-Fluor and newly suggested furoindolizine derivatives are also presented, along with bioapplication for visualizing live cell mitochondria.

References

1. Lakowicz JR (2006) Principles of fluorescence spectroscopy, 3rd edn. Springer-Verlag, New York
2. Zachariasse KA, Grobys M, von der Haar Th, Hebecker A, Il'ichev Yu V, Jiang Y-B, Morawski O, Kühnle W (1996) *J Photoch Photobio A: Chem* 102:59–70
3. Turro NJ (1991) Modern molecular photochemistry. University Science Books, Mill Valley, CA
4. Valeur B, Berberan-Santos MN (2012) Molecular fluorescence, 2nd edn. Wiley-VCH, Weinheim, Germany
5. Brahme A (2014) Comprehensive biomedical physics, 1st edn. Elsevier, Amsterdam, Netherlands
6. (a) Er JC, Tang MK, Chia CG, Liew H, Vendrell M, Chang Y-T (2013) *Chem Sci* 4:2168–2176. (b) Yang L, Liu Y, Zhou X, Wu Y, Ma C, Liu W, Zhang C (2016) *Dyes Pigment* 126:232–238
7. Wu Y-Y, Chen Y, Gou G-Z, Mu W-H, Lv X-J, Du M-L, Fu W-F (2012) *Org Lett* 14:5226–5229
8. Lavis LD, Raines RT (2008) *ACS Chem Biol* 3:142–155
9. Kauffman JM, Litak PT, Novinski JA, Kelley CJ, Ghiorghis A, Qin Y (1995) *J Fluoresc* 5:295–305
10. (a) Wu L, Burgess K (2008) *J Am Chem Soc* 130:4089–4096. (b) Kowser Z, Rayhan U, Rahman S, Georghiou PE, Yamato T (2017) *Tetrahedron* 73:5418–5424
11. Skoog DA, Holler FJ, Crouch SR (2007) Principle of instrumental analysis, 6th edn. Thomson Brooks/Cole, Belmont, CA
12. (a) Urano Y, Asanuma D, Hama Y, Koyama Y, Barrett T, Kamiya M, Nagano T, Watanabe T, Hasegawa A, Choyke PL, Kobayashi H (2009) *Nat Med* 15:104–109. (b) Nagano T (2010) *Proc Jpn Acad Ser B* 86:837–847
13. Hong G, Antaris AL, Dai H (2017) *Nat Biomed Eng* 1:0010
14. Boens N, Leen V, Dehaen W (2012) *Chem Soc Rev* 41:1130–1172
15. Yoshino J, Kano N, Kawashima T (2013) *Dalt Trans* 42:15826–15834
16. Loudet A, Burgess K (2007) *Chem Rev* 107:4891–4932
17. Johnson I (1998) *Histochem J* 30:123–140
18. Rurack K, Kollmannsberger M, Daub J (2001) *New J Chem* 25:289–292
19. Killoran J, Allen L, Gallagher JF, Gallagher WM, O'Shea DF (2002) *Chem Commun* 24:1862–1863
20. (a) Umezawa K, Nakamura Y, Makino H, Citterio D, Suzuki K (2008) *J Am Chem Soc* 130:1550–1551. (b) Umezawa K, Matsui A, Nakamura Y, Citterio D, Suzuki K (2009) *Chem-A Eur J* 15:1096–1106
21. (a) Xie S-X, Petrache G, Schneider E, Ye Q-Z, Bernhardt G, Seifert R, Buschauer A (2006) *Bioorg Med Chem Lett* 16:3886–3890. (b) Middleton RJ, Briddon SJ, Cordeaux Y, Yates AS, Dale CL, George MW, Baker JG, Hill SJ, Kellam B (2007) *J Med Chem* 50:782–793

22. (a) Chen C-S, Chen W-NU, Zhou M, Arttamangkul S, Haugland RP (2000) *J Biochem Biophys Methods* 42:137–151. (b) Dubach JM, Vinegoni C, Mazitschek R, Fumene Feruglio P, Cameron LA, Weissleder R (2014) *Nat Commun* 5:3946
23. Klymchenko AS, Kreder R (2014) *Chem Biol* 21:97–113
24. Cirulis JT, Strasser BC, Scott JA, Ross GM (2012) *Cytom Part A* 81(A): 618–626
25. Rao AV, Rao LG (2015) *Phytochemicals—Isolation, Characterisation and Role in Human Health*. InTech, Rijeka, Croatia
26. Medina FG, Marrero JG, Macias-Alonso M, Gonzalez MC, Cordova-Guerrero I, Teissier Garcia AG, Osegueda-Robles S (2015) *Nat Prod Rep* 32:1472–1507
27. Katritzky A (1995) *Advances in Heterocyclic Chemistry*, 1st edn. Academic Press, London, UK
28. Liu X, Cole JM, Waddell PG, Lin T-C, Radia J, Zeidler A (2012) *J Phys Chem A* 116:727–737
29. (a) Zhao Y, Zheng Q, Dakin K, Xu K, Martinez ML, Li W-H (2004) *J Am Chem Soc* 126:4653–4663. (b) Galkin A, Fallarero A, Vuorela PM (2009) *J Pharm Pharmacol* 61:177–184. (c) Dragojević S, Šunjić V, Bencetić-Mihaljević V, Ralić J, Mesić M, Elenkov IJ, Sučić AF, Klonek AČ, Lerman L, Ilijaš M, Gabelica-Marković V, Malnar I (2011) *J Pharm Biomed Anal* 54:37–47. (d) Dekić B, Samaržija-Jovanović S, Jovanović V, Dekić V, Radulović N, Simonović R, Marinović-Cincović M (2014) *J Therm Anal Calorim* 115:1619–1626
30. Sun W-C, Gee KR, Haugland RP (1998) *Bioorg Med Chem Lett* 8:3107–3110
31. Jin X, Uttamapinant C, Ting AY (2011) *ChemBioChem* 12:65–70
32. Murata C, Masuda T, Kamochi Y, Todoroki K, Yoshida H, Nohta H, Yamaguchi M, Takadate A (2005) *Chem Pharm Bull* 53:750–758
33. Tasiar M, Kim D, Singha S, Krzeszewski M, Ahn KH, Gryko DTJ (2015) *Mater. Chem. C* 3:1421–1446
34. (a) Kim I, Kim D, Sambasivan S, Ahn KH (2012) *Asian J Org Chem* 1:60–64. (b) Kim D, Xuan QP, Moon H, Jun YW, Ahn KH (2014) *Asian J Org Chem* 3:1089–1096
35. (a) Gee KR, Sun W-C, Bhalgat MK, Upson RH, Klaubert DH, Latham KA, Haugland RP (1999) *Anal Biochem* 273:41–48. (b) Wegener D, Wirsching F, Riestler D, Schwienhorst A (2003) *Chem Biol* 10:61–68. (c) Lavis LD, Chao T-Y, Raines RT (2006) *ChemBioChem* 7:1151–1154
36. (a) Stack EC, Wang C, Roman KA, Hoyt CC (2014) *Methods* 70:46–58. (b) Zhao M, Li Y, Peng L (2014) *Opt Express* 22:10221
37. Weissleder R (2001) *Nat Biotechnol* 19:316–317
38. Panigrahi M, Dash S, Patel S, Mishra BK (2012) *Tetrahedron* 68:781–805
39. Mishra A, Behera RK, Behera PK, Mishra BK, Behera GB (2000) *Chem Rev* 100:1973–2011
40. Upadhyayula S, Nuñez V, Espinoza EM, Larsen JM, Bao D, Shi D, Mac JT, Anvari B, Vullev VI (2015) *Chem Sci* 6:2237–2251
41. Mujumdar SR, Mujumdar RB, Grant CM, Waggoner AS (1996) *Bioconjug Chem* 7:356–362
42. Waggoner A (1995) *Methods Enzymol* 246:362–373
43. (a) Philip R, Penzkofer A, Bäuml W, Szeimies RM, Abels C (1996) *J Photochem Photobiol A Chem* 96:137–148. (b) Yuan B, Chen N, Zhu Q (2004) *J Biomed Opt* 9:497–503. (c) Russin TJ, Altinoğlu Eİ, Adair JH, Eklund PC (2010) *J Phys Condens Matter* 22:334217
44. Peng X, Draney DR, Volcheck WM, Bashford GR, Lamb DT, Grone DL, Zhang Y, Johnson CM (2006) *Proc SPIE-Int Soc Opt Eng* 6097E:1–12
45. Sun W, Guo S, Hu C, Fan J, Peng X (2016) *Chem Rev* 116:7768–7817
46. Mujumdar RB, Ernst LA, Mujumdar SR, Waggoner AS (1989) *Cytometry* 10:11–19
47. Levitus M, Ranjit S (2011) *Q Rev Biophys* 44:123–151
48. (a) Bates M, Blosser TR, Zhuang X (2005) *Phys Rev Lett* 94:108101. (b) Bates M, Huang B, Dempsey GT, Zhuang X (2007) *Science* 317:1749–1753. (c) Dempsey GT, Bates M, Kowtoniuk WE, Liu DR, Tsien RY, Zhuang X (2009) *J Am Chem Soc* 131:18192–18193
49. Chaires JB, Graves D (2013) *Quadruplex Nucleic Acids*. Springer, Berlin Heidelberg

50. Gruber HJ, Hahn CD, Kada G, Riener CK, Harms GS, Ahrer W, Dax TG, Knaus HG (2000) *Bioconjug Chem* 11:696–704
51. Sun W-C, Gee KR, Klaubert DH, Haugland RP (1997) *J Org Chem* 62:6469–6475
52. Chen X, Pradhan T, Wang F, Kim JS, Yoon J (2012) *Chem Rev* 112:1910–1956
53. (a) Whitaker JE, Haugland RP, Prendergast FG (1991) *Anal Biochem* 194:330–344. (b) Azuma E, Nakamura N, Kuramochi K, Sasamori T, Tokitoh N, Sagami I, Tsubaki K (2012) *J Org Chem* 77:3492–3500
54. Lee LG, Berry GM, Chen C-H (1989) *Cytometry* 10:151–164
55. Grimm JB, Sung AJ, Legant WR, Hulamm P, Matlosz SM, Betzig E, Lavis LD (2013) *ACS Chem Biol* 8:1303–1310
56. Egawa T, Koide Y, Hanaoka K, Komatsu T, Terai T, Nagano T (2011) *Chem Commun* 47:4162–4164
57. Zheng H, Zhan X-Q, Bian Q-N, Zhang X-J (2013) *Chem Commun* 49:429–447
58. Johnson I, Spence MTZ (2010) *Molecular probes handbook, a guide to fluorescent probes and labeling technologies*, 11th edn. Life Technologies Inc, Eugene, OR
59. Garman AJ (1997) *Non-radioactive labelling: a practical introduction*, 1st edn. Academic Press, San Diego
60. Khanna PL, Ullman EF (1980) *Anal Biochem* 108:156–161
61. Lavis LD, Raines RT (2014) *ACS Chem Biol* 9:855–866
62. Beija M, Afonso CAM, Martinho JMG (2009) *Chem Soc Rev* 38:2410–2433
63. Yuan L, Lin W, Zheng K, He L, Huang W (2013) *Chem Soc Rev* 42:622–661
64. Schäfer FP (1977) *Dye lasers*, 2nd edn. Springer-Verlag, Berlin
65. (a) Lefevre C, Kang HC, Haugland RP, Malekzadeh N, Arttamangkul S, Haugland RP (1996) *Bioconjug Chem* 7:482–489. (b) Grimm JB, Lavis LD (2011) *Org Lett* 13:6354–6357
66. (a) Grimm JB, English BP, Chen J, Slaughter JP, Zhang Z, Revyakina A, Patel R, Macklin JJ, Normanno D, Singer RH, Lionnet T, Lavis LD (2015) *Nat Methods* 12:244–250. (b) Liu X, Qiao Q, Tian W, Liu W, Chen J, Lang MJ, Xu ZJ (2016) *Am Chem Soc* 138:6960–6963
67. (a) Koide Y, Urano Y, Hanaoka K, Terai T, Nagano T (2011) *ACS Chem Biol* 6:600–608. (b) Grimm JB, Sung AJ, Legant WR, Hulamm P, Matlosz SM, Betzig E, Lavis LD (2013) *ACS Chem Biol* 8:1303–1310
68. Panchuk-Voloshina N, Haugland RP, Bishop-Stewart J, Bhalgat MK, Millard PJ, Mao F, Leung W-Y, Haugland RP (1999) *J Histochem Cytochem* 47:1179–1188
69. (a) Koide Y, Urano Y, Hanaoka K, Piao W, Kusakabe M, Saito N, Terai T, Okabe T, Nagano T (2012) *J Am Chem Soc* 134:5029–5031. (b) Lukinavicius G, Umezawa K, Olivier N, Honigsmann A, Yang G, Plass T, Mueller V, Reymond L, Corrêa IR, Luo Z-G, Schultz C, Lemke EA, Heppenstall P, Eggeling C, Manley S, Johnsson K (2013) *Nat Chem* 5:132–139
70. (a) Belov VN, Bossi ML, Fölling J, Boyarskiy VP, Hell SW (2009) *Chem-A Eur J* 15:10762–10776. (b) Butkevich AN, Mitronova GY, Sidenstein SC, Klocke JL, Kamin D, Meineke DNH, D’Este E, Kraemer PT, Danzl JG, Belov VN, Hell SW (2016) *Angew Chem Int Ed* 55:3290–3294
71. Uno S, Kamiya M, Yoshihara T, Sugawara K, Okabe K, Tarhan MC, Fujita H, Funatsu T, Okada Y, Tobita S, Urano Y (2014) *Nat Chem* 6:681–689
72. Kim E, Koh M, Ryu J, Park SB (2008) *J Am Chem Soc* 130:12206–12207
73. Kim E, Koh M, Lim BJ, Park SB (2011) *J Am Chem Soc* 133:6642–6649
74. Kim E, Park SB (2009) *Chem Asian J* 4:1646–1658
75. Kim E, Lee S, Park SB (2012) *Chem Commun* 48:2331–2333
76. Lee S, Kim E, Park SB (2013) *Chem Sci* 4:3282–3287
77. Kim E, Lee S, Park SB (2011) *Chem Commun* 47:7734–7736
78. Jeong MS, Kim E, Kang HJ, Choi EJ, Cho AR, Chung SJ, Park SB (2012) *Chem Commun* 48:6553–6555

Chapter 2

A Comprehensive Studies of an Indolizine-Based Seoul-Fluor System



2.1 Structure and Quantum Yield Relationship Study of Seoul-Fluor¹

2.1.1 Introduction

Fluorescent quantum yield is one of the most important photophysical properties, governing the brightness of a given fluorescent molecule [1]. Understanding the relationship between the structure and the quantum yield of a certain fluorophore system often elicits the rational design of novel turn-on fluorescent biosensors [2]. Although there are dozens of reported fluorophore systems [3], only a few studies have systematically elucidated the change of fluorescent quantum yields from a structural point of view [4].

Seoul-Fluor (SF), a combinatorial fluorophore system based on the indolizine scaffold, shows an interesting emission property, covering a full range of visible area, by simple change of two functional groups (R^1 and R^2 groups) [5]. On top of that, the emission wavelength of Seoul-Fluors can be predicted by computational analysis of the energy gaps between HOMO and LUMO [6]. In this section, a special attention was focused on the relationship between the structure and the fluorescent quantum yield of Seoul-Fluor system, which is an important theme for developing on/off switchable fluorescent sensors [7].

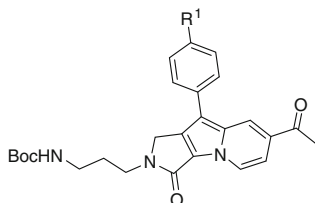
2.1.2 Result and Discussion

With systematic derivatives of Seoul-Fluor in hands via a palladium mediated cross-coupling reaction [8], the correlation between the chemical structure of

¹[*Angew. Chem. Int. Ed.* **2014**, 53, 1346–1350.] Reproduced by permission of Wiley VCH.

Seoul-Fluors and their quantum yields has been investigated. The R² group of Seoul-Fluor was fixed with an acetyl moiety due to its superior photophysical properties, such as higher quantum yield, and more red-shifted fluorescent emission, compared to other functional groups [6]. Preliminarily, it was observed that the R¹ substituents exhibit variable fluorescent intensity, depending on their electronic property [6]. Considering a systematic variation of the electronic richness of the R¹ substituent, nine Seoul-Fluor derivatives were selected based on the Hammett constant values [9]. Also, by using a density functional theory (DFT) calculation, the energy level of HOMO at the R¹ group was calculated as a computable indicator of the electron density for the R¹ substituted phenyl moiety. As shown in Table 2.1, a systematic decrease in the quantum yield values from 0.63 (**09**) to 0.00 (**01**) was observed, as the electron density of the R¹ phenyl group decreases from a cyano to a diethylamino- moiety. Also, two quantifiable electronic parameters, the Hammett constant value and computable HOMO energy level of R¹ phenyl moiety, show a positive correlation with experimental quantum yields of nine derivatives (Fig. 2.1), which enables rational prediction of fluorescent quantum yield for unexplored SF-based molecules. The dramatic changes in quantum yield values can be rationalized by photoinduced electron transfer (PeT) phenomenon, which is one of the major mechanisms of fluorescence quenching; an electron

Table 2.1 Electronic effects of the R¹ substituents on the quantum yield of seoul-fluors



Compound	R ¹	σ^a	E _{HOMO} ^b	Φ_F^c
01	NEt ₂	-0.72	-0.160	0.00
02	NH ₂	-0.66	-0.169	0.03
03	OH	-0.37	-0.200	0.12
04	OCH ₃	-0.27	-0.195	0.20
05	CH ₃	-0.17	-0.215	0.38
06	H	+0.00	-0.227	0.50
07	F	+0.06	-0.225	0.47
08	CF ₃	+0.54	-0.249	0.64
09	CN	+0.66	-0.247	0.63

^aThe Hammett constants of the R¹ substituents. ^bCalculated energies in hartree of the HOMO level of the phenyl moieties. ^cAbsolute fluorescence quantum yields in methanol.

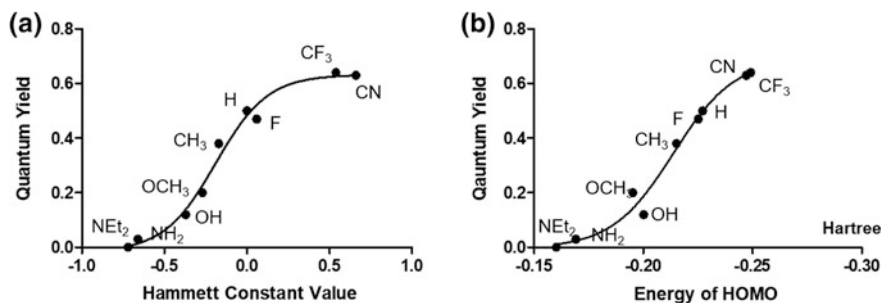


Fig. 2.1 The correlation between the R^1 substituents of seoul-fluor and their corresponding quantum yields. **a** The relationship between Hammett constant values of the R^1 -substituents and the quantum yields. **b** The relationship between the HOMO energy level of the R^1 -substituents and the quantum yield

transfer from a donor (R^1 -substituted phenyl) to its acceptor (indolizine fluorophore) [10]. Later, by using electron paramagnetic resonance (EPR) spectroscopy, radical signals were further confirmed for nonfluorescent **01** compounds under irradiation at 365 nm, as a signature event of the PeT process [11].

2.1.3 Conclusion

This section described a structure-quantum yield relationship study by using a series of Seoul-Fluor derivatives. The quantum yield of Seoul-Fluor can be changed by systematic alteration of the electronic richness at the R^1 phenyl substituents, which can be quantified by the Hammett constant values and the calculated HOMO energy level. On the basis of this result, the rational development of Seoul-Fluor based turn-on fluorescent sensors is highly expected.

2.2 Optimization of SF-Based Lipid Droplet Bioprobes on the Basis of Molecular Lipophilicity²

2.2.1 Introduction

Lipid droplets (LDs) are subcellular organelles containing neutral lipids such as triacylglycerols or cholesteryl esters surrounded by a phospholipid monolayer [12]. Even though, in earlier times, LDs were considered to be an inert aggregate of neutral lipids for simple storage purpose [13], recent studies have demonstrated that

²[*Mol. BioSyst.*, **2013**, 9, 952–956] Reproduced by permission of The Royal Society of Chemistry.

the LD is a dynamic organelle and that it is involved in various physiological processes, including lipid metabolism, which is closely associated with cardiovascular complications and type 2 diabetes [14]. Therefore, the monitoring of LD accumulation could serve as a powerful tool for biomedical research and early diagnosis of various human diseases [15]. Additionally, in recent years, LDs have received significant attention from the biofuel research community as an alternative source of fuel [16]. Particularly, LDs present in microalgae have an excellent potential for the development of highly efficient fuel from biomaterials [17].

With the increasing importance of LDs, recent investigations have focused on the development of highly-sensitive and easy-to-handle fluorescent bioprobes such as Nile Red and BODIPY-fatty acid (Fig. 2.2 [18], for visualizing the accumulation of LDs in biological systems. Previously, Park's group have reported a full-color tunable and predictable novel fluorescent skeleton, namely, Seoul-Fluor [5, 6]. Through combinatorial synthesis followed by complete spectroscopic characterization of SF analogues, the correlation between their photophysical properties and chemical structure was successfully demonstrated, particularly regarding the electronic natures of substituents on the indolizine core skeleton. Consequently, SF44, a Seoul-Fluor-based bioprobe for LDs was developed by utilizing the unique photophysical property of SFs [19]. As shown in Fig. 2.2, the turning-on of specific fluorescent signals of SF44 in the LD was observed, which caused by a drastic enhancement of its quantum yield and hypsochromic shift in the hydrophobic environment. This solvatochromism of SF44 could sufficiently quench the fluorescent signals with concomitant bathochromic shifts in the polar environment such as cytoplasm and liquid media, presumably due to internal charge transfer (ICT) process from the electron-donating diethyl amino group to the electron-accepting acetyl group [19]. Using the fluorogenic character of SF44, specific visualization of the hydrophobic organelles, LDs, was possible in mammalian cells with excellent sensitivity without any washing procedure.

2.2.2 *Result and Discussion*

Design and synthesis. As a continuation of previous bioprobe research, an extended study to understand the relationship between LDs and the specific staining ability of SF44 was conducted at the molecular level. Owing to the inherent hydrophobic nature of LDs, it is hypothesized that although the molecular lipophilicity would be one of the predominant issues for specific LD targeting, it could be in conflict with the other desired physical properties of bioprobes, including cell permeability and solubility in aqueous media. To examine this hypothesis, a series of SF44 analogues were designed with varying lipophilicities. Two substituents of SF44, namely, dialkylamine and acetyl moiety, were retained in those analogues because the ICT process between the two groups are essential for switching-on the fluorescence signal in LDs.

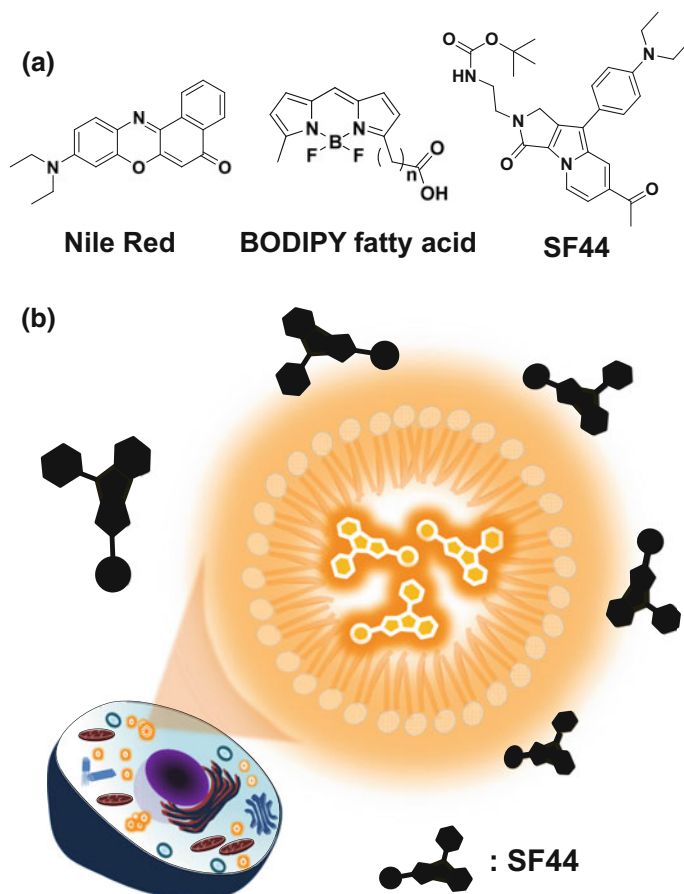


Fig. 2.2 Small molecule-based fluorescent bioprobes for lipid droplets (LDs) in the cellular system. **a** Chemical structure of LD bioprobes: Nile Red, BODIPY-fatty acid, and SF44. **b** Schematic diagram of a specific turning-on of fluorescent bioprobe, SF44, in the hydrophobic LDs in mammalian cells

Four analogues of SF44 were designed and synthesized by simple changes in R^3 groups (Fig. 2.3). The lipophilicity of SF analogues was tuned via systematic changes at the R^3 position of SF44 analogues, guided by the cLogP value [20]. The original LD bioprobe, SF44, has a cLogP value of 5.50, and its analogues have a range of cLogP values from 2.87 (SF55), 3.93 (SF56), 4.64 (SF57), to 6.21 (SF58). In fact, it was previously reported that the photophysical property of the dimethylamino group was almost identical to that of diethylamino group [19]. Therefore, SF55 was designed to have a dimethylamino group instead of the diethylamino group present in other SF44 analogues, in order to have a low cLogP value for the clear linearity of cLogP. All the designed analogues were synthesized using intramolecular 1,3-dipolar cycloaddition of β,γ -unsaturated amide with

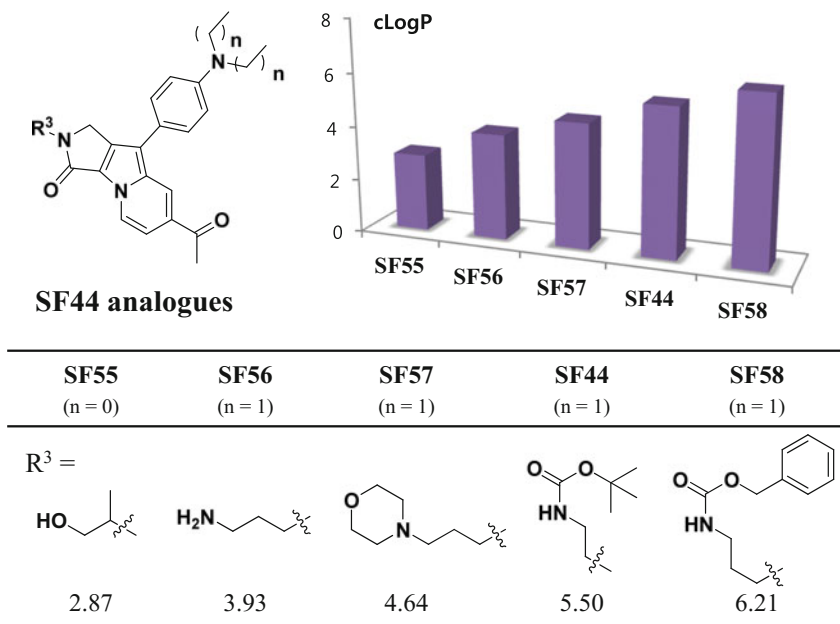
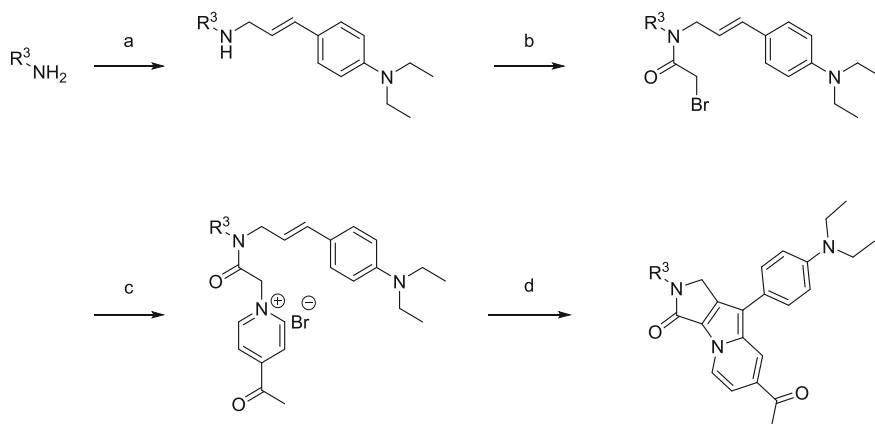


Fig. 2.3 General structures of SF44 analogues for specific monitoring of LDs in the biological system. The exact chemical structures of SF44 analogues are illustrated along with their cLogP values

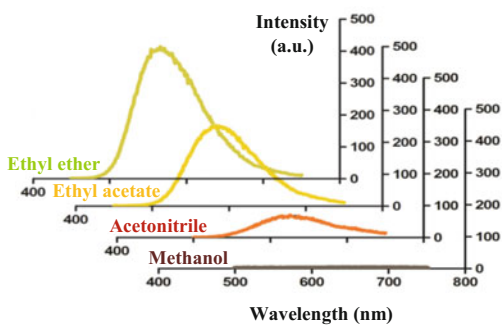
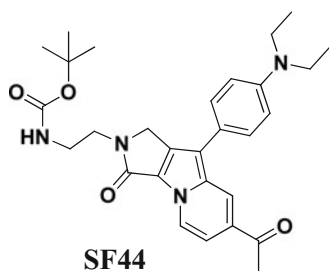
azomethine ylide in toluene in the presence of 1,8-diazabicyclo[5.4.0]undec-7-ene (DBU) to yield the desired SF skeleton, namely, 1,2-dihydropyrrolo-[3,4-β]indolizin-3-one, varying the R³ group in a one-pot fashion (Scheme 2.1).

Photophysical property. Subsequent to the synthesis of all SF44 analogues, their photophysical properties were investigated in various solvent systems of varying polarity—from the nonpolar diethyl ether to polar methanol, with gradually increasing polarities to confirm the solvatochromism-based fluorescent turn-on signals in the nonpolar environment. As shown in Figs. 2.4, 2.5 and Table 2.2, analogues showed fairly similar patterns of excitation and emission wavelengths in four different solvent systems, even in case of the dimethylamino group-containing SF55 (Fig. 2.5). Moreover, the quantum efficiencies of SF44 analogues decreased significantly as the solvent polarity increased, indicating that all the five analogues would glow brighter in the hydrophobic environment, which is essential for the specific monitoring of LDs having a turn-on signal. It was confirmed that the simple changes of R³ group would not affect the fluorescent character of SF44 analogues based on their photophysical properties.

Application for mammalian cells. The LD-specific staining ability of SF44 analogues within a range of lipophilicities was tested on human cervical cancer HeLa cells. Remarkably, as all SF44 analogues have a turn-on property in the hydrophobic area, the LD staining pattern can be easily acquired by standard



(a)



(b)

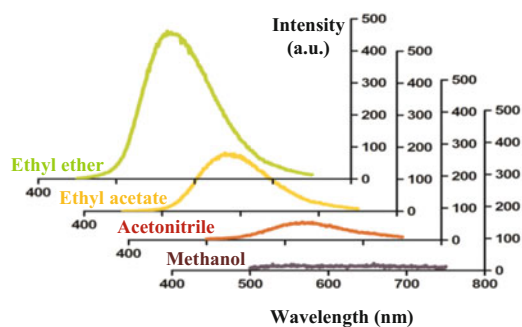
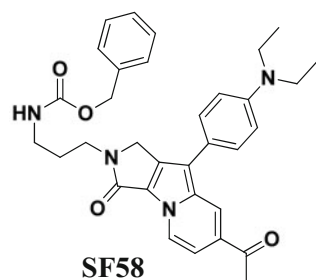


Fig. 2.4 The chemical structure of SF44 (a) and one of representative analogues, SF58 (b), and their emission spectra in four different solvent systems (diethyl ether, ethyl acetate, acetonitrile, and methanol) to show their solvatochromism

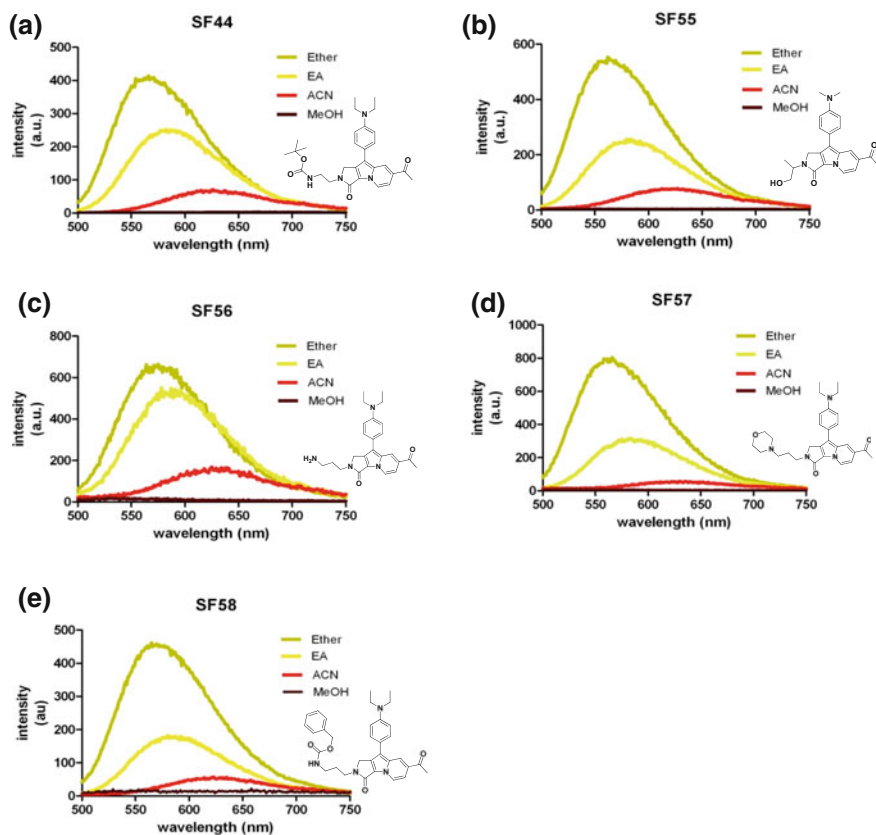


Fig. 2.5 Fluorescent emission shifts for SF-based analogues in various solvents. Dye concentration was 1 mM

fluorescent microscopy without any washing and fixation steps. Unlike other commercial LD probes, this simple procedure of SF-based LD bioprobe is the big advantage in image-based LD monitoring. As shown in Fig. 2.6, the side-by-side comparison of each SF analogue in the cell-based imaging experiment demonstrated that the analogues with relatively low cLogP values (SF55, SF56, and SF57) displayed less efficient LD staining than those with cLogP values over 5 (SF44 and SF58). In the quantification data, amongst the cellular images stained by each LD bioprobe (Fig. 2.6f), SF56 showed a slightly higher fluorescent intensity than its fluorescent image. This discrepancy might be due to the nonspecific staining of SF56 throughout the whole cytoplasm, resulting in blurring of the cellular fluorescent image by SF56, which could mislead in the quantification in the image analysis software. Among the SF analogues, SF44 and SF58 showed excellent specificity and brightness in the stained cellular image. The most lipophilic analogue, SF58, showed a marginal improvement in the LD staining pattern compared

Table 2.2 Photophysical properties of SF44 and its derivatives

	SF44			SF55			SF56			SF57			SF58		
	$\lambda_{\text{ex}}^{\text{a}}$	$\lambda_{\text{em}}^{\text{b}}$	$\Phi_{\text{F}}^{\text{c}}$	λ_{ex}	λ_{em}	Φ_{F}	λ_{ex}	λ_{em}	Φ_{F}	λ_{ex}	λ_{em}	Φ_{F}	λ_{ex}	λ_{em}	Φ_{F}
Ethyl ether (34.5) ^d	438	573	0.30	431	570	0.30	433	575	0.30	430	566	0.30	430	565	0.30
Ethyl acetate (38.1)	437	583	0.22	430	580	0.21	436	580	0.21	438	584	0.21	438	580	0.23
Acetonitrile (45.6)	455	626	0.09	438	627	0.09	438	625	0.08	440	630	0.07	440	623	0.09
Methanol (55.4)	n.d. ^e	n.d.	<0.01	n.d.	n.d.	<0.01	n.d.	n.d.	<0.01	n.d.	n.d.	0.05	n.d.	n.d.	<0.01

^aExcitation wavelength; ^bEmission wavelength; ^cQuantum yield; ^dSolvent polarity represented as E_{T} value; ^eNot detected due to low fluorescent intensity

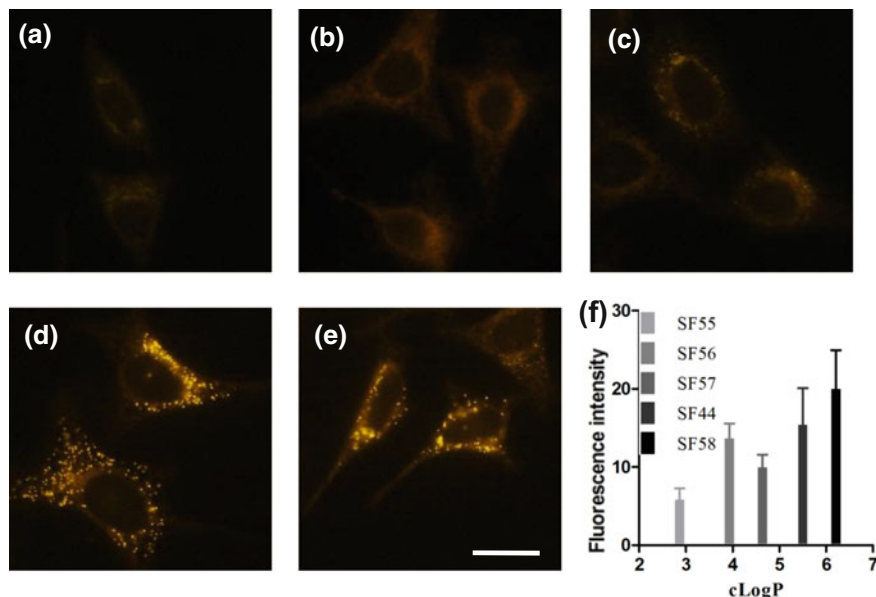


Fig. 2.6 Fluorescent images of cellular LDs using SF analogues in HeLa cells. **a** SF55, **b** SF56, **c** SF57, **d** SF44, **e** SF58, and **f** quantified result of (a)–(e). Quantified data was described as a mean value and SD of 20–30 cells. The scale bar represents 20 μm

to SF44, mainly because of the enhanced lipophilicity to improve LD accumulation ability as a compensation for low cell permeability. For a practical application in bioimaging, SF58 was tested for its cytotoxicity in HeLa cells; notably, no influence on the cell viability was observed up to a concentration of 20 μM (Fig. 2.7).

Application for microorganisms. On successful acquisition of LD-specific systems attention directed toward the practical application in the field of biofuel research, where LD monitoring can be used as a measure of efficiency levels of biological carbon fixation [21]. Recently, biofuels have received growing public and scientific attention owing to the high demands for energy security. Among various organisms, microalgae have been recognized as one of the most promising alternative biomass source [22]. As shown in Fig. 2.8, microalgae are photosynthetic microorganisms that play an instrumental role in converting natural materials such as water and carbon dioxide into carbon-rich lipids with oxygen as a byproduct. The biomass productivity of microalgae is more than 100-fold better than that of agricultural crops such as soy bean and corns [23]. In addition, the production of biodiesel from high-lipid containing microalgae, cultivated using waste CO_2 from power plants, can offer an alternative solution for CO_2 mitigation as well as high biomass productivity (Fig. 2.8A). However, biofuel research using microalgae is limited because of the lack of a proper system for monitoring the production of lipid content in microalgae, which has a direct correlation to the formation of LDs [24]. Currently, the gold standard for monitoring LDs in

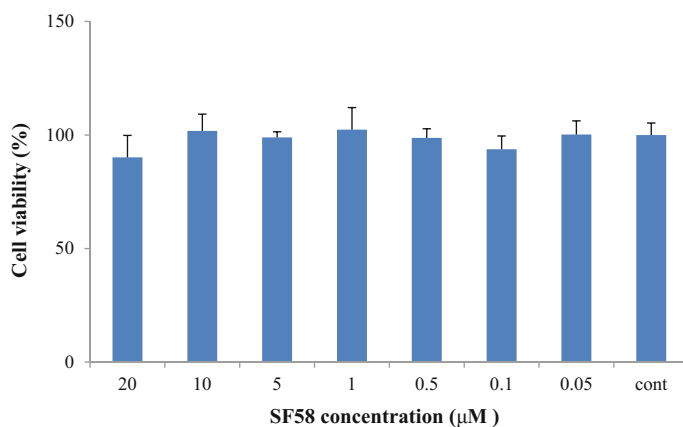


Fig. 2.7 Cell viability results of SF58 against HeLa cells. Various concentration of SF58 was treated to HeLa cells for 12 h. Experiment was performed in triplicate and the results were normalized by DMSO control as 100%

microalgae involves a 10 min incubation of microalgae at 40 °C with Nile Red (0.5 µg/mL) in 20% dimethyl sulfoxide (DMSO) [25]. However, because microalgae cannot survive this harsh protocol using Nile Red, it is not possible to pursue the screening process via the random genetic mutations of microalgae and the subsequent selection of a single microalga with high efficiency in the production of LDs using fluorescence-assisted cell sorting (FACS) technology [26]. To overcome this limitation in biofuel research using microalgae, the five SF-based LD bioprobes were tested against *Chlamydomonas reinhardtii* (CC-503), a single-celled green alga with well-studied genetics, a short doubling time, and well-understood physiology. At the outset, the imaging condition optimization for algal LD staining was conducted, and it comprises a 25 min incubation of 5 µM SF44 with 2% DMSO at room temperature after a systematic variation of the probe concentration and incubation time (Fig. 2.9). As shown in Fig. 2.8B, SF44 specifically stained algal LDs (colored in green) without any overlap of auto-fluorescent signals from chlorophyll (colored in red). Then, the LD staining pattern in algae was tested with all five SF-based LD bioprobes using the optimized imaging conditions, and the best staining of algal LD was displayed by both SF44 and SF58 (Fig. 2.10). It is worth mentioning that Nile Red showed a significant reduction in fluorescence signal in algal LDs when the DMSO concentration of incubation media was changed from 20 to 2% (Fig. 2.8C). Moreover, the increase in Nile Red concentration did not improve the fluorescence signal of algal LDs as the fluorescence signal by Nile Red reached plateaued at a concentration of 0.5 µg/mL and decreased on further increasing its concentration [25].

Unlike Nile Red—the current gold standard of LD staining in algae, SF44 and SF58 showed efficient LD staining under the condition similar to its physiological conditions. As shown in Fig. 2.11A, the specific LD staining ability by SF58 was

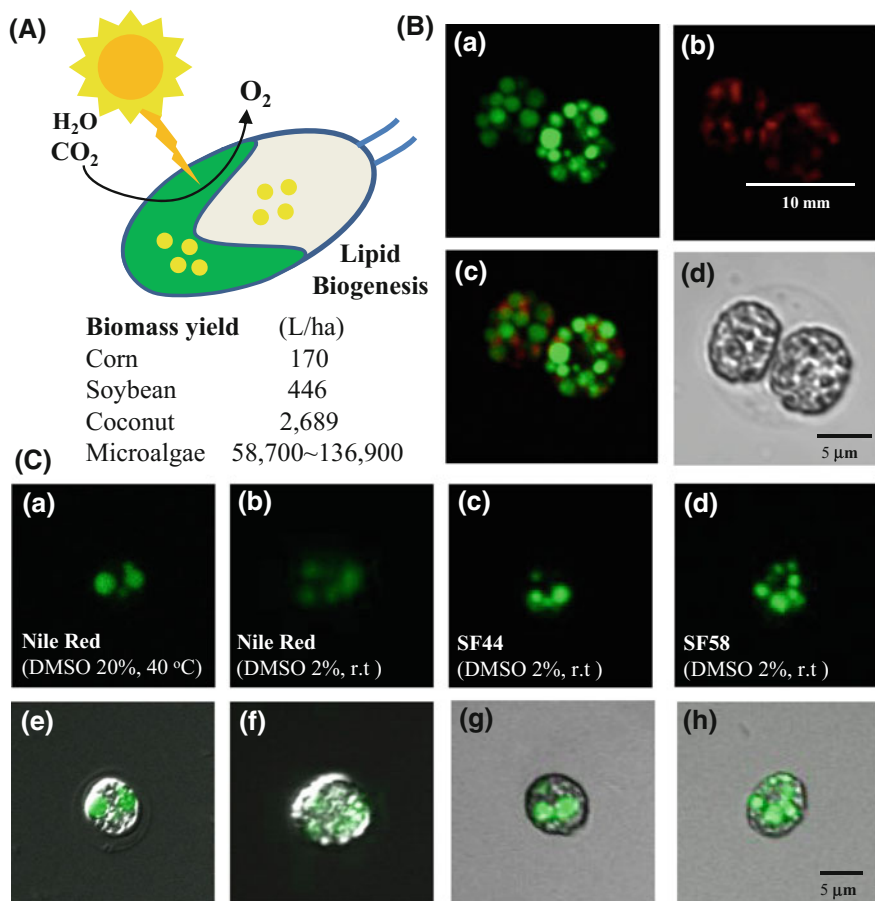


Fig. 2.8 **A** schematic diagram of biofuel production in green algae and its biomass yield compared to other agricultural feedstocks. **B** Lipid droplets (LDs) stained by SF44 (in green) **a**; fluorescence by chlorophylls (in red) **b**; merged image **c**; bright-field image **d**. **(C)** LDs stained by Nile Red with the gold standard protocol (**a**, **e**); LD stained by Nile Red (**b**, **f**), SF44 (**c**, **g**), and SF58 (**d**, **h**) in 2% DMSO at room temperature

observed even in presence of 0.5 or 1% DMSO, but imaging protocol was set to 2% DMSO, because some algal LDs were not homogeneously stained with 0.5% DMSO (Fig. 2.11A, white arrow). The potential applicability of SF-based LD monitoring in biofuel research could be demonstrated on examination of algal viability after exposure to the optimized imaging protocol for SF44 and SF58 (25 min incubation at room temperature with 2% DMSO), as well as Nile Red (10 min incubation at 40 °C with 20% DMSO). The SF44 and SF58-treated algae showed no sign of retardation in cell viability after 12, 24, and 36 h (Fig. 2.11B) as

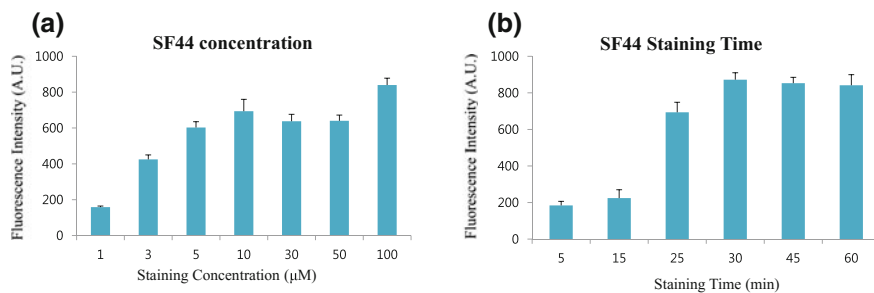


Fig. 2.9 Optimization of SF44 for monitoring LDs in *chlamydomonas reinhardtii*. Various concentration (a) and staining time (b) of SF44 were screened under DMSO 2% at 25 °C in triplicate

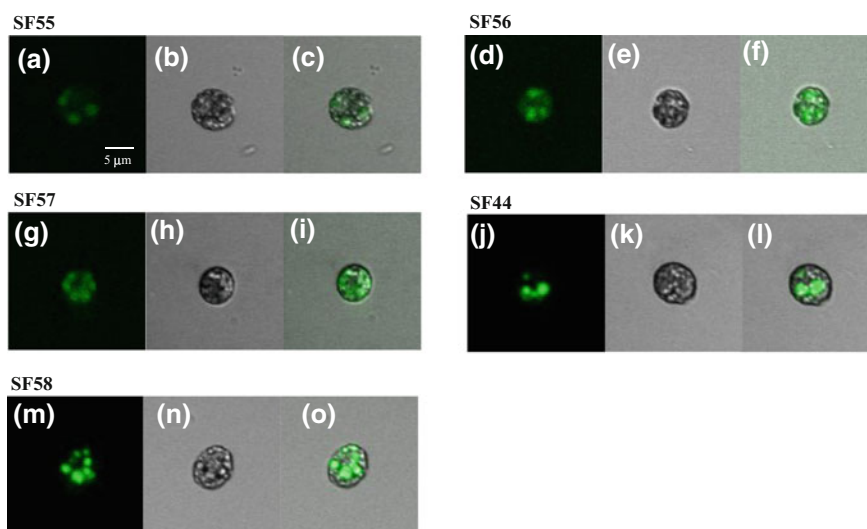


Fig. 2.10 Fluorescent staining by each analogue in *chlamydomonas reinhardtii*. a, d, g, j and m are fluorescent images, b, e, h, k and n are DIC images, and c, f, i, l and o are merge images. The final concentration of each analogue is 5 μM under 2% DMSO at room temperature. Scale bar represents 5 μm

opposed to the Nile Red-treated algae which showed a significant reduction in viability. On the basis of this observation, it could be stated that, compared to the gold standard LD-staining protocol with Nile Red, SF44 and SF58 can robustly stain the algal LDs with excellent specificity; moreover their treatment condition is non-invasive and non-cytotoxic enough to be applied to FACS-assisted selection of desired algae in a continuous manner.

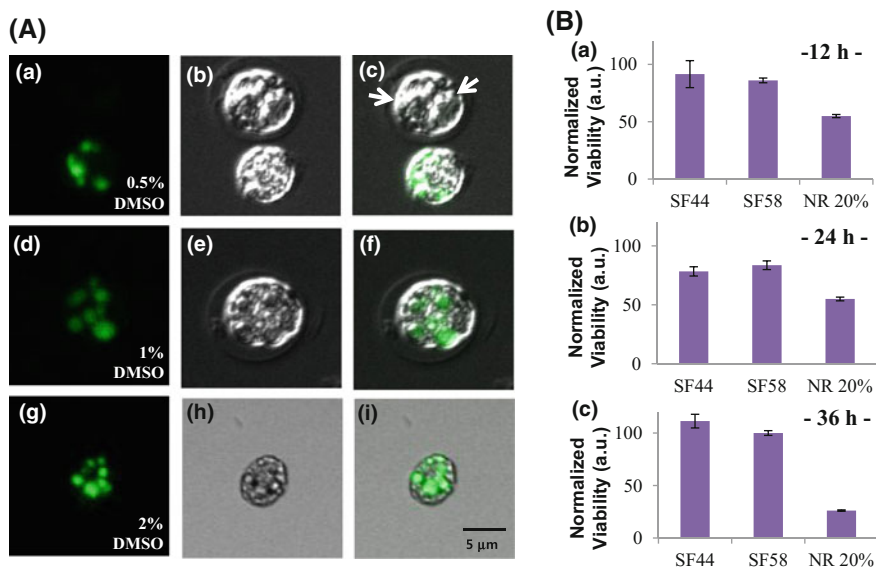


Fig. 2.11 A LD staining pattern after 25 min incubation with SF58 (5 μM) in the presence of 0.5% (a, b, c), 1% (d, e, f), and 2% DMSO (g, h, i). **B** Normalized viability of algae in 12 h (a), 24 h (b), and 36 h (c) after the LD image protocol under the optimal condition of SF44 and SF58 and Nile Red (NR)

2.2.3 Conclusion

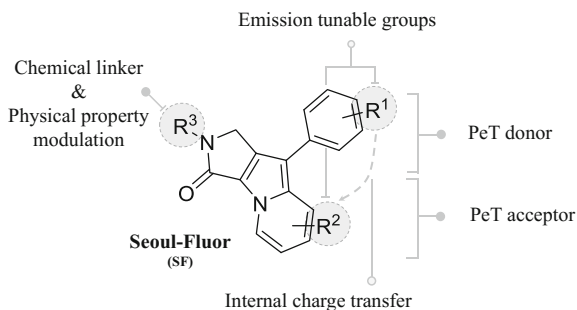
As a continuation of molecular level study for Seoul-Fluor and SF-based LD bioprobe (SF44), a series of SF44 analogues was designed and synthesized along with a linear range of lipophilicity, guided by cLogP values. Among five SF44 analogues, SF44 and SF58 were identified as SF-based LD bioprobes owing to their efficiency in specific LD staining in HeLa cells. Furthermore, the application of SF-based LD bioprobes to the field of biofuel research was explored using microalgae. Unlike the conventional LD bioprobe, Nile Red, the specific LD staining in algae with SF44 and SF58 was demonstrated under the non-invasive imaging conditions.

2.3 An Overview of Seoul-Fluor System³

Since the original discovery of an indolizine-based novel fluorophore [5], a series of studies on understanding and developing SF-based fluorescent materials has been pursued [6, 19]. Through the previous reports [27] and recent studies from this

³[*Acc. Chem. Res.* **2015**, *48*, 538 – 547] Reproduced by permission of ACS Publications, direct link: <http://pubs.acs.org/doi/abs/10.1021/ar500370v>.

Fig. 2.12 Schematic overview of the structure—photophysical property relationship in seoul-fluor system



chapter [28], it has been demonstrated that the SF system has (i) tunable and predictable emission wavelength covering a full visible-color range; [6] (ii) controllable quantum yield via photoinduced electron transfer phenomenon; [28b] and (iii) environment sensitive fluorogenic properties that can be modified through intramolecular charge transfer processes [19] (Fig. 2.12).

From a structural perspective, the SF is built on an indolizine-based fluorescent platform with three different positions, R^1 , R^2 , and R^3 , to introduce various substituents. Specifically, the R^1 -substituted aryl moiety is an important part for emission tunability; an EDG on the R^1 position can produce drastic red-shifts in emission wavelengths. Also, three-dimensional geometry of the R^1 -substituted aryl group is considered to be relatively tilted from the planar framework of the indolizine core structure. The electronic nature of substituents at the R^2 position is considered as a major control tower for modulating π -electrons of indolizine core; the incorporation of an EWG at the R^2 position causes bathochromic shifts and internal charge transfer (ICT) throughout indolizine π -system. The electronic property of the R^3 group is orthogonal to indolizine's fluorescent property, therefore the R^3 groups can be utilized as aliphatic linkers to attach various biomolecules. In addition, the R^3 group can be harnessed to modulate the physicochemical properties of a given SF probe such as solubility, lipophilicity or cell permeability.

2.4 Experimental Section

2.4.1 General Experimental Information

The density functional theory (DFT) calculation in Sect. 2.1 was performed using the Materials Studio® 4.2 program (Accelrys Software Inc.). A generalized gradient approximation (GGA) for the exchange correlation function of Perdew, Burke, and Ernzerhof (PBE) was used together with double numerical with polarization basis set (DNP), which is implemented in DMol3.

^1H and ^{13}C NMR spectra in Sect. 2.2 were recorded on Agilent 400-MR (Agilent Technologies) and Varian Inova-500 (Varian Associates), and chemical shifts were

measured in ppm downfield from internal tetramethylsilane (TMS) standard. Multiplicity was indicated as follows: s (singlet); d (doublet); t (triplet); q (quartet); m (multiplet); dd (doublet of doublet); dt (doublet of triplet); br s (broad singlet), etc. Coupling constants were reported in Hz. Routine mass analyses were performed on LC/MS system equipped with a reverse phase column (C-18, 50 × 2.1 mm, 5 μm) and photodiode array detector using electron spray ionization (ESI) or atmospheric pressure chemical ionization (APCI). The identity of desired fluorescence compounds were further confirmed by high-resolution mass spectrometry (HRMS). The HRMS analyses were conducted at the Mass Spectrometry Laboratory of Seoul National University by direct injection on a JEOL JMS 600 W spectrometer using electron impact (EI) or chemical ionization (CI), and JEOL JMS AX505WA spectrometer using fast atom bombardment (FAB) method. Excitation maxima and emission maxima were measured by Cary Eclipse Fluorescence spectrophotometer (Varian Associates) and absolute fluorescent quantum yield of all compounds in this chapter was measured by QE-1000 (OTSUKA Electronics). Triethylamine, diisobutylaluminium hydride, 1,8-diazabicyclo[5.4.0]undec-7-ene (DBU), sodium borohydride, bromoacetyl bromide, sodium hydride, 4-acetyl pyridine, 2,3-dichloro-5,6-dicyano-1,4-benzoquinone (DDQ), trifluoroacetic acid, acetic acid, anhydrous dimethyl formamide (DMF) were purchased from Sigma-Aldrich and Tokyo Chemical Industry Co., LTD. The progress of reaction was monitored using thin-layer chromatography (TLC) (silica gel 60, F₂₅₄ 0.25 mm), and components were visualized by observation under UV light (254 and 365 nm) or by treating the TLC plates with anisaldehyde, KMnO₄, and ninhydrin followed by heating. Solvents were purchased from commercial vendors and used without further purification. Distilled water was polished by ion exchange and filtration. Biochemical reagents were purchased from Sigma-Aldrich. Ez-cytox kit was purchased from Daeil Co. and was used for the cell viability test. Commercial dyes Nile Red were purchased from Invitrogen.

Fluorescence microscope and analysis program for Bio-Imaging experiment.

Fluorescence microscopy studies for mammalian LDs were conducted with Olympus Inverted Microscope Model IX71, equipped for epi-illumination using a halogen bulb (Philips No. 7724). Emission signal of each experiments were observed at two spectral setting: green channel, using a 450–480 band pass exciter filter, a 500 nm center wavelength chromatic beam splitter, a 515 nm-long pass barrier filter (Olympus filter set U-MWB2); and red channel using a 510–550 band pass exciter filter, a 570 nm center wavelength chromatic beam splitter, a 590 nm-long pass barrier filter (Olympus filter set U-MWG2). Emission signals of each experiment were detected with 12.5 M pixel recording digital color camera (Olympus, DP71) Algae study was carried out using a FluoView FV1000 confocal laser scanning unit with Olympus Inverted Microscope Model IX81 and Confocal PMT detector, equipped for Multi-line Ar Laser (488 nm). Fluorescence images were analyzed and quantified by Image-Pro Plus[®] 6.2 program, and all graphs were figured by GraphPad Prism 5. Algal figures were processed by IMARIS software (Bitplane). The quantified data are processed via the mean measurement of 40–50 cells from at least three different independent experiments and SEM.

Cell culture

HeLa cell line was obtained from American Type Culture Collection. HeLa cells were cultured in RPMI 1640 [GIBCO, Invitrogen] supplemented with heat-inactivated 10% (v/v) fetal bovine serum [GIBCO, Invitrogen] and 1% (v/v) antibiotic-antimycotic solution [GIBCO, Invitrogen]. Cells were maintained in a humidified atmosphere of 5% CO₂ incubator at 37 °C, and cultured in 100 mm cell culture dish [CORNING]. *Chlamydomonas reinhardtii* cell was obtained from Chlamydomonas Resource Center. Chlamydomonas cell strain number was CC-503 cw 92 mt + . Cell was cultured in 500 mL glass flask with stir incubator at 25 °C and normal atmosphere. Algae logarithmic phase was maintained with tris-acetate-phosphate (TAP) medium, and then cell grown under nitrogen privation condition media in 6 days.

2.4.2 Experimental Procedure

Image-based screening of SF44 analogues with HeLa cells.

HeLa cells were treated for 15 min with 5 μM solutions of series of Seoul-Fluor-based bioprobes in RPMI media, supplemented with 10% (v/v) FBS and 1% (v/v) antibiotic-antimycotic solution. Without media washing, fluorescent images of stained cells were captured using fluorescence microscopy and their fluorescent intensity were determined from the region of interest (ROI) and was quantified by Image-Pro Plus[®] 6.2 program

Image-based screening of SF44 analogues with *chlamydomonas reinhardtii*.

Nitrogen-starved cells for 6 days (density 2.4×10^6 cells/ml) were treated with 5 μM solution of series of Seoul-Fluor-based bioprobe in 2% DMSO solution. Nitrogen starvation facilitates the formation of lipid droplets in microalgae. After 25 min incubation, microalga were observed by Z-depth-controlled image captured in confocal fluorescent microscopy.

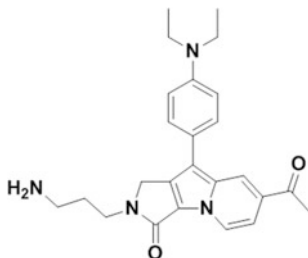
In Vitro cytotoxicity test.

Cell viability was measured by the EZ-Cytox assay kit, and the experimental procedure was based on the manufacturer's manual. HeLa cells were cultured into 96-well plates at a density of 3×10^3 cells/well for 24 h, followed by the treatment of compounds in various concentrations. After 12 h of incubation with increasing concentration, 10 μL of WST-1 solution, (2-(4-nitrophenyl)-5-(2-sulfophenyl)-3-[4-(4-sulfophenylazo)-2-sulfophenyl]-2H-tetrazolium disodium salt, was added to each well, and plates were incubated for an additional 1 h at 37 °C. To measure the viability in microalgae, cells were seeded in 96 well plate and treated with series of Seoul-Fluor-based bioprobes or Nile Red. Final concentration of fluorescent probe was 5 μM (Seoul-Fluor-based bioprobes) in 2% DMSO solution or 0.1 μg/mL (Nile Red) in 20% DMSO solution. After 12, 24 and 36 h incubation, cell viability was measured by identical protocol for assay with HeLa cells. The resulting signal was observed after 90 min incubation at 25 °C. Absorbance in 455 nm was

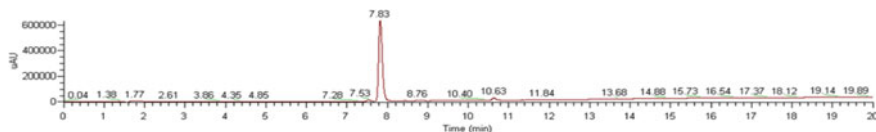
measured by microplate reader. The percentage of cell viability was calculated by following formula: % cell viability = (mean absorbance in test wells)/(mean absorbance in control well) \times 100. Each experiment was performed in triplicate.

2.4.3 Compound Characterization Data

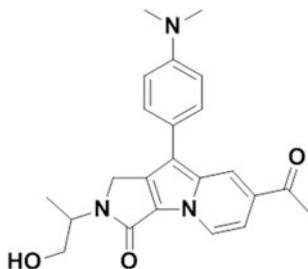
7-Acetyl-9-(4-(dimethylamino)phenyl)-2-(1-hydroxypropan-2-yl)-1*H*-pyrrolo[3,4- β]indolizin-3(2*H*)-one (SF55)



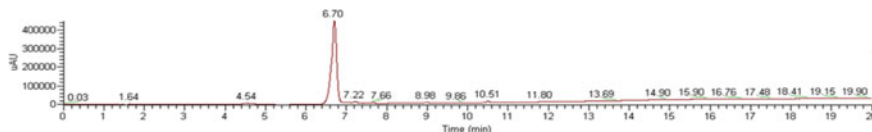
^1H NMR (500 MHz, CDCl_3) δ 8.46 (dd, $J = 1.0, 7.5$ Hz, 1H), 8.33 (s, 1H), 7.42 (d, $J = 8.5$ Hz, 2H), 7.19 (dd, $J = 1.5, 7.0$ Hz, 1H), 6.86 (dd, $J = 2.0, 7.0$ Hz, 2H), 4.52 (q, $J = 16.5$ Hz, 2H), 4.41 (m, 1H), 3.92–3.75 (m, 2H), 3.03 (s, 6H), 2.57 (s, 3H), 1.35 (d, $J = 7.0$ Hz, 3H); ^{13}C NMR (125 MHz, CDCl_3) δ 195.7, 162.4, 134.5, 134.1, 128.4, 124.5, 122.9, 121.8, 121.5, 114.8, 113.3, 113.2, 109.2, 70.7, 65.6, 50.9, 43.8, 40.7, 26.2, 15.5; HRMS (FAB): m/z calcd for $\text{C}_{23}\text{H}_{25}\text{N}_3\text{O}_3$ $[\text{M}]^+$: 391.1896; found: 391.1893.



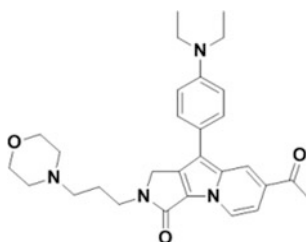
7-Acetyl-2-(3-aminopropyl)-9-(4-(diethylamino)phenyl)-1*H*-pyrrolo[3,4- β]indolizin-3(2*H*)-one (SF56)



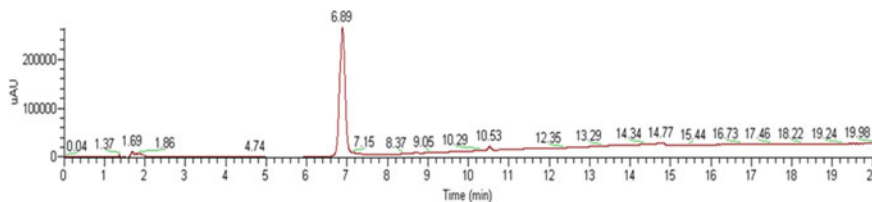
^1H NMR (400 MHz, CDCl_3) δ 8.51 (dd, $J = 0.8, 7.2$ Hz, 1H), 8.39 (s, 1H), 7.41 (d, $J = 9.2$ Hz, 2H), 7.23 (dd, $J = 1.8, 7.4$ Hz, 1H), 6.81 (d, $J = 9.2$ Hz, 2H), 4.48 (s, 2H), 3.71 (t, $J = 6.8$ Hz, 2H), 3.43 (q, $J = 7.1$ Hz, 4H), 2.77 (t, $J = 6.6$ Hz, 2H), 2.60 (s, 3H), 1.82 (pentet, $J = 6.7$ Hz, 2H), 1.23 (t, $J = 7.0$ Hz, 6H); ^{13}C NMR (100 MHz, CDCl_3) δ 195.6, 161.8, 146.8, 134.0, 133.9, 128.7, 128.3, 124.4, 122.8, 122.0, 120.2, 115.0, 112.2, 109.1, 46.5, 44.4, 40.1, 39.0, 32.3, 26.0, 12.7; HRMS (FAB): m/z calcd for $\text{C}_{25}\text{H}_{31}\text{N}_4\text{O}_2$ $[\text{M} + \text{H}]^+$ 419.2447, found 419.2445.



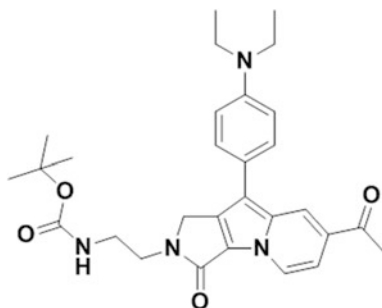
7-Acetyl-9-(4-(diethylamino)phenyl)-2-(3-morpholinopropyl)-1H-pyrrolo [3,4- β]indolizin-3(2H)-one (SF57)



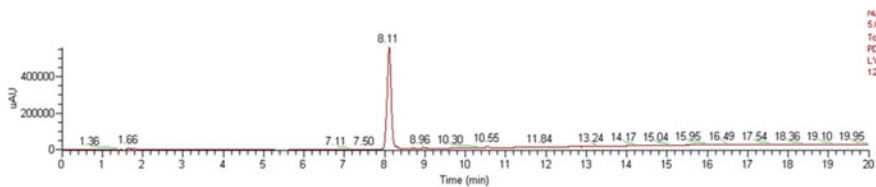
^1H NMR (500 MHz, CDCl_3) δ 8.57 (d, $J = 7.5$ Hz, 1H), 8.38 (s, 1H), 7.73 (d, $J = 8.5$ Hz, 2H), 7.68 (d, $J = 8.5$ Hz, 2H), 7.36 (d, $J = 7.0$ Hz, 1H), 4.58 (s, 2H), 4.00–3.90 (m, 4H), 3.75 (t, $J = 6$ Hz, 2H), 3.62 (q, $J = 6.5$ Hz, 4H), 3.52 (d, $J = 11$ Hz, 2H), 3.13 (t, $J = 8$ Hz, 2H), 2.88 (br s, 2H), 2.65 (s, 3H), 2.24 (pentet, $J = 7.1$ Hz, 2H), 1.23 (t, $J = 7.0$ Hz, 6H); ^{13}C NMR (125 MHz, CDCl_3) δ 195.4, 161.9, 136.0, 135.7, 135.3, 135.2, 130.4, 129.2, 125.0, 123.5, 122.3, 120.4, 112.1, 110.3, 63.8, 55.1, 53.4, 52.3, 46.1, 39.6, 26.2, 23.1, 10.4; HRMS (FAB): m/z calcd for $\text{C}_{29}\text{H}_{37}\text{N}_4\text{O}_3$ $[\text{M} + \text{H}]^+$ 489.2866, found 489.2864.



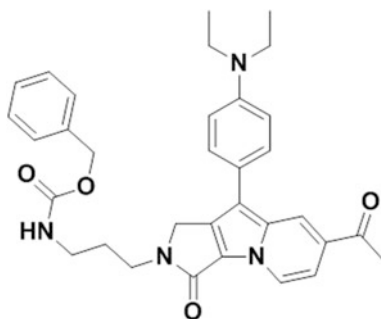
***tert*-Butyl (2-(7-acetyl-9-(4-(diethylamino)phenyl)-3-oxo-1H-pyrrolo[3,4- β]indolizin-2(3H)-yl)ethyl)carbamate (SF44)**



^1H NMR (500 MHz, CDCl_3) δ 8.50 (dd, $J = 1.0, 7.5$ Hz, 1H), 8.39 (s, 1H), 7.41 (d, $J = 9.0$ Hz, 2H), 7.23 (dd, $J = 1.7, 7.2$ Hz, 1H), 6.81 (d, $J = 9.0$ Hz, 2H), 4.97 (br s, 1H), 4.56 (s, 2H), 3.73 (t, $J = 5.7$ Hz, 2H), 3.45–3.41 (m, 6H), 2.60 (s, 3H), 1.35 (s, 9H), 1.23 (t, $J = 7.0$ Hz, 6H); ^{13}C NMR (125 MHz, CDCl_3) 195.6, 162.2, 156.3, 146.8, 134.3, 133.9, 128.6, 128.2, 124.3, 122.4, 122.0, 120.1, 115.0, 112.3, 108.9, 79.5, 47.3, 44.5, 43.1, 39.8, 28.4, 26.0, 12.7; HRMS (FAB): m/z calcd for $\text{C}_{29}\text{H}_{36}\text{N}_4\text{O}_4$ $[\text{M}]^+$ 504.2737, found 504.2743.

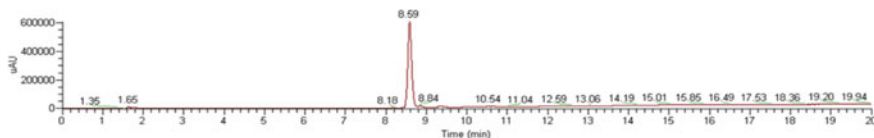


Benzyl (3-(7-acetyl-9-(4-(diethylamino)phenyl)-3-oxo-1H-pyrrolo[3,4- β]indolizin-2(3H)-yl)propyl)carbamate (SF58)



^1H NMR (500 MHz, CDCl_3) δ 8.47 (dd, $J = 0.75, 7.3$ Hz, 1H), 8.38 (s, 1H), 7.40 (d, $J = 9$ Hz, 2H), 7.37–7.26 (m, 5H), 7.22 (dd, $J = 1.5, 7.0$ Hz, 1H), 6.81 (d, $J = 9$ Hz, 2H), 5.82 (br s, $J = 5.75$ Hz, 1H), 5.10 (s, 2H), 4.47 (s, 2H), 3.68 (t, 6 Hz,

2H), 3.43 (q, $J = 7.2$ Hz, 4H), 3.23 (t, $J = 5.8$ Hz, 2H), 2.60 (s, 3H), 1.84 (pentet, $J = 5.75$ Hz, 2H), 1.23 (t, $J = 7.0$ Hz, 6H); ^{13}C NMR (75 MHz, CDCl_3) δ 195.9, 162.5, 156.9, 147.1, 137.1, 134.5, 134.3, 129.0, 128.77, 128.75, 128.3, 128.0, 124.8, 122.7, 122.3, 120.3, 115.4, 112.6, 109.5, 66.9, 47.0, 44.8, 40.3, 37.9, 28.9, 26.3, 13.0; HRMS (FAB) m/z calcd for $\text{C}_{33}\text{H}_{36}\text{N}_4\text{O}_4$ $[\text{M}]^+$ 552.2737, found 552.2744.



References

1. de Silva AP, Gunaratne HQN, Gunnlaugsson T, Huxley AJM, McCoy CP, Rademacher JT, Rice TE (1997) *Chem Rev* 97:1515–1566
2. Yao S, Belfield KD (2012) *Eur J Org Chem* 3199–3217
3. Lavis LD, Raines RT (2008) *ACS Chem Biol* 3:142–155
4. (a) Miura T, Urano Y, Tanaka K, Nagano T, Ohkubo K, Fukuzumi S (2003) *J Am Chem Soc* 125:8666–8671. (b) Ueno T, Urano Y, Setsukinai K, Takakusa H, Kojima H, Kikuchi K, Ohkubo K, Fukuzumi S, Nagano T (2004) *J Am Chem Soc* 126:14079–1408. (c) Urano Y, Kamiya M, Kanda K, Ueno T, Hirose K, Nagano T (2005) *J Am Chem Soc* 127:4888–4894. (d) Ueno T, Urano Y, Kojima H, Nagano T, *J Am Chem Soc* 128:10640–10641
5. Kim E, Koh M, Ryu J, Park SB (2008) *J Am Chem Soc* 130:12206–12207
6. Kim E, Koh M, Lim BJ, Park SB (2011) *J Am Chem Soc* 133:6642–6649
7. Uchiyama S, Kimura K, Gota C, Okabe K, Kawamoto K, Inada N, Yoshihara T, Tobita S (2012) *Chem—A Eur J* 18:9552–9563
8. (a) Chen X, Engle KM, Wang D, Yu J (2009) *Angew Chem* 121:5196–5217; *Angew Chem Int Ed* 48:5094–5115. (b) Dupont J, Consorti CS, Spencer J (2005) *Chem Rev* 105:2527–2572. (c) Cho SH, Kim JY, Kwak J, Chang S (2011) *Chem Soc Rev* 40:5068–5083. (d) Lyons TW, Sanford MS (2010) *Chem Rev* 110:1147–1169
9. Hansch C, Leo A, Taft RW (1991) *Chem Rev* 91:165–195
10. Kollmannsberger M, Rurack K, Resch-Genger U, Daub J (1998) *J Phys Chem A* 102:10211–10220
11. Martino DM, van Willigen H, Spitler MT (1997) *J Phys Chem B* 101:8914–8919
12. Murphy J (2001) *Prog Lipid Res* 40:325–438
13. Farese RV Jr, Walther TC (2009) *Cell* 139:855–860
14. (a) den Boer M, Voshol PJ, Kuipers F, Havekes LM, Romijn JA (2004) *Arterioscler Thromb Vasc Biol* 24:644–649. (b) Paul A, Chan L, Bickel PE (2008) *Curr Hypertens Rep* 10:461–466. (c) Greenberg AS, Coleman RA, Kraemer FB, McManaman JL, Obin MS, Puri V, Yan Q-W, Miyoshi H, Mashek DG (2011) *J Clin Invest* 121:2102–2110
15. Straub BK, Herpel E, Singer S, Zimbelmann R, Breuhahn K, Goepfinger SM, Warth A, Koch JL, Longgerich T, Heid H, Schirmacher P (2010) *Modern Pathol* 23:480–492
16. Walther TC, Farese RV Jr (2009) *Biochim Biophys Acta* 1791:459–466
17. Wijffels RH, Barbosa MJ (2010) *Science* 329:796–799

18. (a) Lee JH, So J-H, Jeon JH, Choi EB, Lee Y-R, Chang Y-T, Kim C-H, Bae MA, Ahn JH (2011) *Chem Commun* 47:7500–7502. (b) Greenspan P, Mayer EP, Fowler SD (1985) *J Cell Biol* 100:965–973
19. Kim E, Lee S, Park SB (2012) *Chem Commun* 48:2331–2333
20. Ghose AK, Viswanadhan VN, Wendoloski JJ (1998) *J Phys Chem A* 102:3762–3772
21. Siaux M, Cuiné S, Cagnon C, Fessler B, Nguyen M, Carrier P, Beyly A, Beisson F, Triantaphylidès C, Beisson YL, Peltier G (2011) *BMC Biotechnol* 11:7
22. Beer LL, Boyd ES, Peters JW, Posewitz MC (2009) *Curr Opin Biotechnol* 20:264–271
23. Chisti Y (2007) *Biotechnol Adv* 25:294–306
24. Bertozzini E, Galluzzi L, Penna A, Magnani M (2011) *J Microbiol Methods* 87:17–23
25. Chen W, Zhang C, Song L, Sommerfeld M, Hu Q (2009) *J Microbiol Methods* 77:41–47
26. (a) Montero MF, Aristizábal M, Reina GG (2011) *J Appl Phycol* 23:1053–1057. (b) Hanagata N, Takeuchi T, Fukuju Y, Barnes DJ, Karube I (1992) *Phytochemistry* 31:3345–3348
27. (a) Kim E, Lee S, Park SB (2011) *Chem Commun* 47:7734–7736. (b) Jeong MS, Kim E, Kang HJ, Choi EJ, Cho AR, Chung SJ, Park SB (2012) *Chem Commun* 48:6553–6555. (c) Choi EJ, Park SB (2015) *Org Biomol Chem* 13:5202–5208
28. (a) Lee Y, Na S, Lee S, Jeon NL, Park SB (2013) *Mol Biosyst* 9:952–956. (b) Choi EJ, Kim E, Lee Y, Jo A, Park SB (2014) *Angew Chem Int Ed* 53:1346–1350

Chapter 3

Tetrazine-Containing Colorful Bioorthogonal Probes Based on the Indolizine Core Skeleton



3.1 Introduction¹

Fluorescent imaging techniques have revolutionized the way to understand biological systems at the nanoscopic, [1] microscopic, [2] and macroscopic levels [3]. To date, fluorescent proteins and immunofluorescence techniques have been most widely used for imaging a target of interest (TOI) [4]. However, the requirement of genetic engineering, fixation, cell membrane penetration or other treatment conditions makes these techniques unsuitable for imaging of innate proteins under a live cell environment, especially for primary cells or clinical samples. An alternative method is making fluorescent conjugate, which binds specifically to the TOI protein [5]. The simplest approach for fluorescent conjugate is the direct coupling of fluorochromes to ligands of TOI proteins, but this approach can reduce the binding affinity of ligand-fluorochrome probes or redirect these probes to off-target proteins in a nonspecific manner [6]. Moreover, extensive washing is required to remove an excess amount of fluorescent conjugates to get a higher signal-to-noise ratio. By taking advantage of bioorthogonal chemistry (highly specific and working in aqueous conditions), [7] researchers now can develop exquisite ligands for protein bioimaging with a minimal perturbation of original binding affinity, due to the much smaller size of bioorthogonal tags for the ligand modification compared to that of direct fluorophore ligation [8].

Among various bioorthogonal reactions, recent advances in inverse electron-demand Diels-Alder (iEDDA) reaction received enormous attention because of its superior kinetics and specificity under physiological conditions [9]. Based on the dual functionality of tetrazine (Tz), a bioorthogonal reactive group [10] as well as a fluorescence quencher, [10e, f] fluorophore-Tz conjugate (FL_{Tz}) has been at the center of attention [8b, 11]. FL_{Tz}s can selectively react with *trans*-cyclooctene (TCO)—ligand complex via iEDDA reaction as a simultaneous

¹[*J. Am. Chem. Soc.* **2018**, *140*, 974–983] Reproduced by permission of ACS Publications.

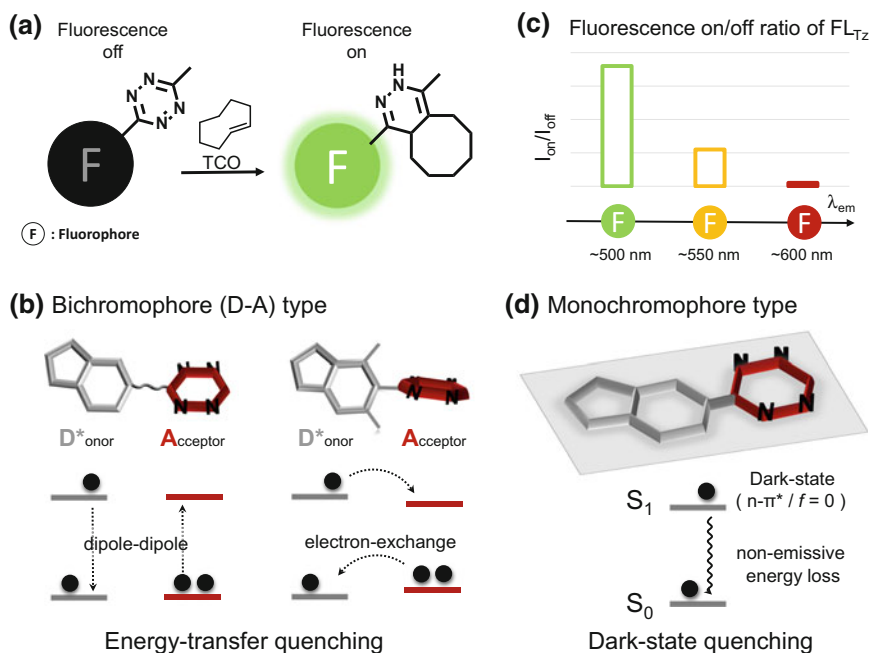


Fig. 3.1 **a** Schematic representation of a fluorescence turn-on event of a fluorophore-tetrazine conjugate (FL_{Tz}), induced by bioorthogonal cycloaddition reaction with *trans*-cyclooctene (TCO). **b** Bichromophore type FL_{Tz} quenched by dipole-dipole energy transfer (left) or electron-exchange energy transfer (right). **c** Reported trends of change in fluorescence on/off ratios of FL_{Tz} depending on the emission wavelengths of fluorophores. **d** Monochromophore type FL_{Tz} , quenched by optically inactive $\text{S}_0\text{-S}_1$ transition (dark-state quenching)

bioorthogonal fluorogenic reaction, which allows fluorescence imaging of multiple intracellular proteins [8a, 12] under live cell conditions without washing steps (Fig. 3.1a).

Up to now, several approaches have been pursued to generate the FL_{Tz} having better turn-on efficiency with a wider range of fluorescent emission wavelengths [9]. From a molecular architectural point of view, the earlier version of FL_{Tz} has aliphatic linkers between the fluorophore (donor) and Tz (acceptor) for simple conjugation, [11a] and the fluorescence of FL_{Tz} is assumed to be quenched by transferring the fluorophore's excited energy to the Tz quencher via a long-range dipole-dipole interaction, also known as fluorescent resonance energy transfer (FRET) (Fig. 3.1b, left) [13]. A few years later, a new type of molecular design emerged via direct conjunction of Tz to the π -conjugation system of flat organic fluorophores in an out-of-plane shape, due to the steric hindrance from adjacent substituents, [11b–d] which is known as through-bond energy transfer (TBET) strategy [14]. Considering the close proximity ($<10 \text{ \AA}$) between the donor (D) and acceptor (A) along with electronically decoupled structures, an excited donor of a TBET pair most likely transfer its energy to the Tz quencher via a short-range

electron-exchange mechanism (Fig. 3.1b, right) [15]. Although FRET- and TBET-based strategies were successfully applied to several fluorochromes for the development of fluorogenic FL_{Tz} s, a significant decrease in fluorescence turn-on/off ratios at longer emission wavelengths is a problem yet to be solved (Fig. 3.1c). Therefore, there is a high demand in alternative molecular design strategies for FL_{Tz} having a high turn-on/off ratios independent of the FL_{Tz} 's emission wavelength, to succeed in high-quality multiplex fluorescent imaging of TOI proteins in live cells.

This chapter describes the development of SF_{Tz} , a new series of FL_{Tz} fluorogenic probes using an emission-tunable Seoul-Fluor (SF) fluorescent core skeleton [16] via monochromophoric design strategy (Fig. 3.1d). Based on understanding of the structure-photophysical property relationship on SF system (Chap. 2), SF_{Tz} analogues were designed through Tz modification at the R^1 , R^2 , or R^3 position of SF with or without aliphatic linker for the direct comparison of TBET-, FRET-based, or monochromophoric FL_{Tz} s. SF_{Tz} s have fast reaction kinetics with TCO in aqueous conditions and turn-on/off ratios up to 1000-fold with full-visible-color emission ranges. With SF_{Tz} s in hands innate microtubules and mitochondria were successfully visualized using TCO-ligand complexes in live cell conditions without washing steps. To the best of my knowledge, the results described in this chapter would be the first report about FL_{Tz} turn-on probes with a single core skeleton covering a full range of visible color, for the washing-free fluorescent live cell imaging of innate TOI proteins and intracellular organelles.

3.2 Result and Discussion

3.2.1 Initial Design and Synthesis

Many of blue or green color-emitting FL_{Tz} s showed a remarkable turn-on/off ratio by taking advantage of a donor-acceptor (D-A) type bichromophoric design strategy [11b–d]. However, orange, red, or far-red emitting FL_{Tz} s suffered drastic deterioration of their on/off ratio, [11a, c, f] which suggests that the turn-on/off efficiency of D-A type FL_{Tz} pairs is highly dependent on the emission energy of donor fluorophores [17]. Considering absorption maxima (λ_{abs}) of Tz (acceptor) is around 500–550 nm, [18b] the fluorophores (donor) with emission wavelength (λ_{em}) longer than 500–550 nm (smaller energy than Tz's absorption) inevitably have a lower efficiency of transferring their excited energy to higher lying energy state of Tz. This inefficient energy transfer causes residual background fluorescence from the long-wavelength FL_{Tz} , resulting in severely decreased fluorescence on/off ratios than that of short-wavelength FL_{Tz} . To overcome this wavelength-dependent quenching efficiency, this chapter envisioned an alternative molecular design approach, the monochromophoric strategy, which features strong electronic coupling between Tz and fluorophores for the development of superdark FL_{Tz} .

Many Tz derivatives, even with multiple aromatic groups, are known to be nonfluorescent [18]. Once excited, Tz derivatives should undergo nonradiative energy decay process due to the lowest lying dark-state at S_1 (dark-state quenching), [19] presumably originated from nonradiative $n \rightarrow \pi^*$ transition [20]. In this context, I hypothesized that unlike previous energy-transfer quenching in D-A type (bichromophoric) FL_{Tz} system, which is sensitive to the donor's energy level, monochromophoric FL_{Tz} system would have inherent $n \rightarrow \pi^*$ transition stemming from Tz, and it could allow highly efficient dark-state quenching independent from the donor's energy level. After the spontaneous iEDDA reaction of Tz with TCO, irreversible releases of two nitrogen atoms from Tz would cause significant changes in nonbonding orbitals of monochromophoric FL_{Tz} system. Subsequently, the lowest lying nonradiative $n \rightarrow \pi^*$ transition might vanish in this state, which allows fluorescence turn-on via an optically active $\pi \rightarrow \pi^*$ transition originating from the embedded fluorophores after iEDDA reaction. To prove this hypothesis, a series of FL_{Tz} derivatives sharing a single core skeleton—indolizine based Seoul Fluor—was designed and synthesized to minimize other factors from resulting in structural differences.

Owing to its full-color tunable fluorescence property and synthetic versatility, the SF scaffold can be an ideal fluorophore system to test above molecular design strategy. For the systematic comparison of each design strategy of FL_{Tz} with the SF scaffold, three distinct modification sites, the R^1 , R^2 , and R^3 positions of the SF scaffold were selected. As shown in Fig. 3.2, $SF_{Tz}01$ and $SF_{Tz}02$ were designed to

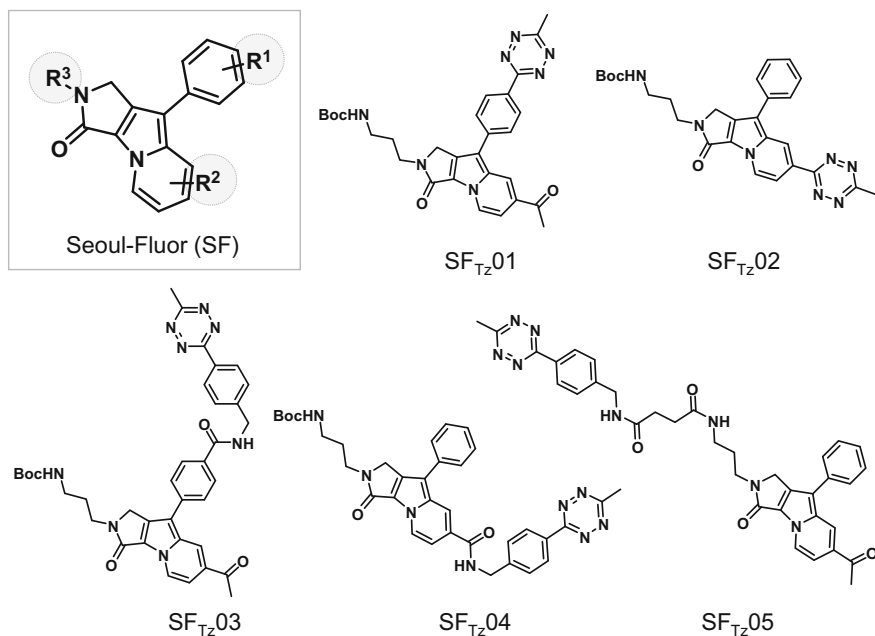
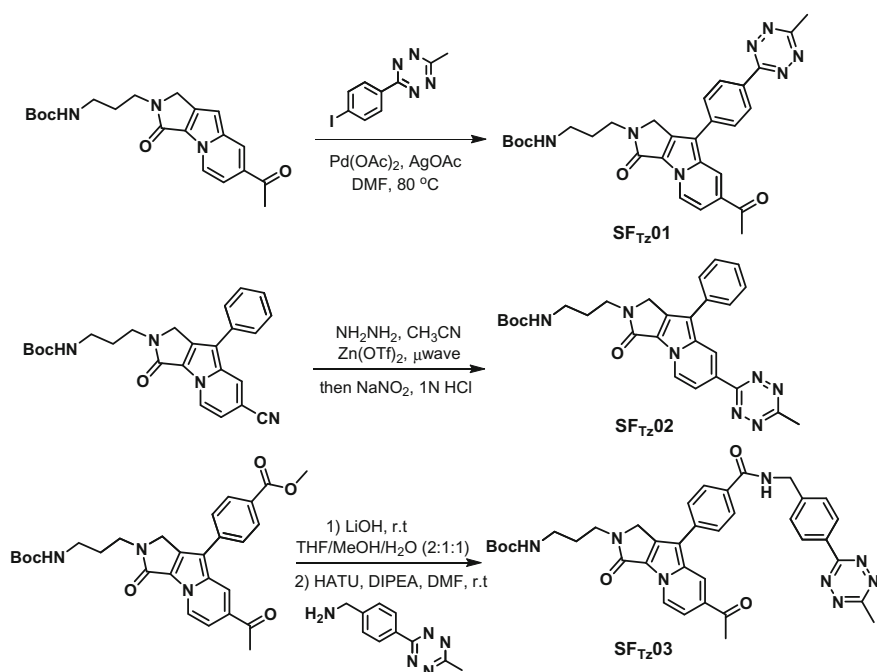


Fig. 3.2 Molecular structures of Seoul-Fluor (SF) and SF-tetrazine conjugates ($SF_{Tz}S$)

incorporate the Tz chromophore without aliphatic linkers at the R¹ and R² positions, respectively. For SF_{Tz}01, a Tz-containing aryl moiety at the R¹ position can be geometrically tilted from the indolizine π -system, [16d] leading to decoupling of the π -systems between the indolizine and Tz, which is a hallmark of a TBET-based FL_{Tz}. Special attention was paid toward the molecular architecture of SF_{Tz}02, because the π -conjugation systems of two chromophores, indolizine and Tz, can be strongly coupled with each other due to the negligible rotational barrier of the single-bond between indolizine and Tz. Thus, SF_{Tz}02 might behave as a monochromophoric FL_{Tz}. In the case of SF_{Tz}03–05, Tz was introduced on the SF scaffold through aliphatic linkers at the R¹, R², and R³ positions, respectively, as analogues of FRET-based FL_{Tz}s.

For the synthesis of SF_{Tz}01 (Scheme 3.1), palladium-mediated C–H activation was utilized on the indolizine scaffold. Tz moiety at the R¹ position was introduced in the presence of 3-(4-iodophenyl)-6-methyl-1,2,4,5-tetrazine and Pd(OAc)₂ with AgOAc [16d]. SF_{Tz}02 was prepared via direct conversion of nitrile group at the R² position of indolizine moiety into Tz under the microwave irradiation using NH₂NH₂, acetonitrile, and Zn(OTf)₂, followed by acid-mediated oxidation step with NaNO₂ [21]. In cases of SF_{Tz}03, SF_{Tz}04, and SF_{Tz}05, carboxyl acid moiety at the R¹, R², or R³ positions of corresponding SF's was coupled with Tz moiety containing aliphatic amine, 4-(6-methyl-1,2,4,5-tetrazin-3-yl)benzylamine, with an



Scheme 3.1 Synthetic scheme for SF_{Tz}01–03

aid of HATU and DIPEA. The final SF_{Tz} products were thoroughly purified by preparative high-performance liquid chromatography before checking their photophysical properties.

3.2.2 *Change in Absorption Property of SF_{Tz}01–05 Upon TCO Cycloaddition Reaction*

To investigate the effect of the molecular design on the electronic orthogonality between indolizine and Tz, absorption spectra of SF_{Tz}s were checked before and after the bioorthogonal reaction with TCO. Before the reaction with TCO, two different absorption peaks around 400–420 nm and 500–550 nm were observed from SF_{Tz}01, SF_{Tz}03, SF_{Tz}04 and SF_{Tz}05 (Fig. 3.3, dashed line). On the contrary, SF_{Tz}02 has an absorption peak around 400–420 nm, but indistinguishable absorption maxima around 500–550 nm (Fig. 3.3c, dashed line). Considering Tz analogues generally have a distinct weak absorption peak around 500–550 nm (Fig. 3.3a, dashed line), [18b, 20] this observation indicates that SF_{Tz}02 has stronger coupled states between SF and Tz than others. More clearly, the electronic orthogonality of SF_{Tz} analogues could be confirmed by analyzing absorption changes after iEDDA reaction with TCO. If Tz and fluorophore have two independent and electronically decoupled states, the cycloaddition reaction of SF_{Tz} with TCO will cause independent dissipation of absorption peak around 500–550 nm, which is originated from Tz's absorption, while most of absorption patterns in other wavelength ranges should be intact. On the other hand, if Tz and indolizine are strongly coupled and act as a single chromophore, the iEDDA reaction with TCO will lead to an overall hypsochromic shift in absorption spectra due to the reduction of π -conjugation length. After the bioorthogonal reaction with TCO, SF_{Tz}01, SF_{Tz}03, SF_{Tz}04, and SF_{Tz}05 showed marginal to negligible changes in absorption spectra except for a clear disappearance of absorption around 500–550 nm (Fig. 3.3, inset graphs). As described earlier, FRET-based SF_{Tz}03–SF_{Tz}05 were constructed via the conjugation of two chromophores, indolizine and Tz, with aliphatic linkers. Therefore, electronically decoupled states between SF and Tz were expected, which leads to negligible changes in absorption spectra of SF_{Tz}03–SF_{Tz}05 after iEDDA reaction. In the case of TBET-based SF_{Tz}01, the hypothesis that Tz moiety at the R¹ position is geometrically tilted and electronically decoupled from π -system of indolizine, was strongly supported by marginal changes in absorption spectrum of SF_{Tz}01 after the iEDDA reaction. These observations confirmed that SF_{Tz}01 and SF_{Tz}03–SF_{Tz}05 have electronically decoupled π -systems between the two chromophores. On the other hand, drastic overall changes of SF_{Tz}02 in the absorption spectra and hypsochromic shift of the absorption maximum (from 415 to 386 nm) upon TCO treatment clearly indicate that monochromophoric molecular design of SF_{Tz}02 results in strong electronic coupling between two chromophores, indolizine and Tz. Collectively, the electronic

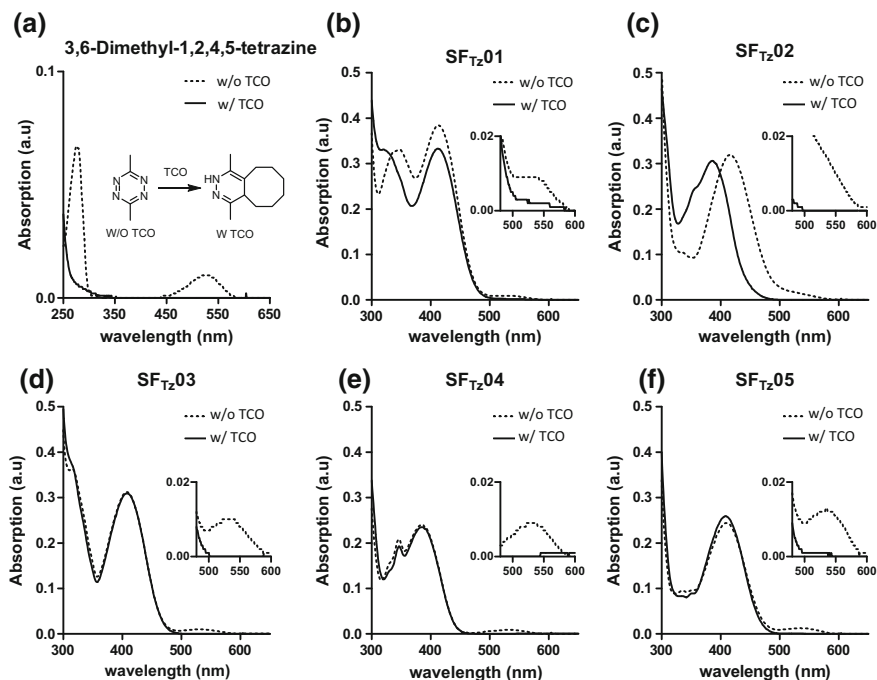


Fig. 3.3 Changes in absorption spectra for Tz-containing molecules before (dashed line) and after (solid line) the reaction with TCO: **a** 3,6-Dimethyl-1,2,4,5-tetrazine, **b** SF_{Tz}01, **c** SF_{Tz}02, **d** SF_{Tz}03, **e** SF_{Tz}04, **f** SF_{Tz}05. All spectra were measured in an acetonitrile: H₂O (1:1 v/v) mixture at room temperature. The final concentration of dye and TCO was 20 and 200 μM, respectively

orthogonality of π -conjugation system between Tz and indolizine is highly dependent on the applied molecular design strategies.

3.2.3 Change in Fluorescence Property of SF_{Tz}01–05 Upon Cycloaddition Reaction with TCO

Next, fluorescence changes of SF_{Tz}01–05 were investigated by comparing the emission spectra before and after (when reaching the maximum intensity in fluorescence) reacting with TCO. Interestingly, the strong electronically coupled SF_{Tz}02 results in remarkable enhancement of turn-on/off ratios via complete dark-state quenching (Fig. 3.4b). As shown in Table 3.1, SF_{Tz}02 showed a completely quenched fluorescence property (quantum yield: 0.2%), while others showed residual fluorescence (quantum yield: up to 4%) before reaction with TCO. Consequently, the residual off-state fluorescence of those FRET- or TBET-type SF_{Tz}S lead to a moderate on/off enhancement (10–70 fold) for SF_{Tz}01 and SF_{Tz}03–05,

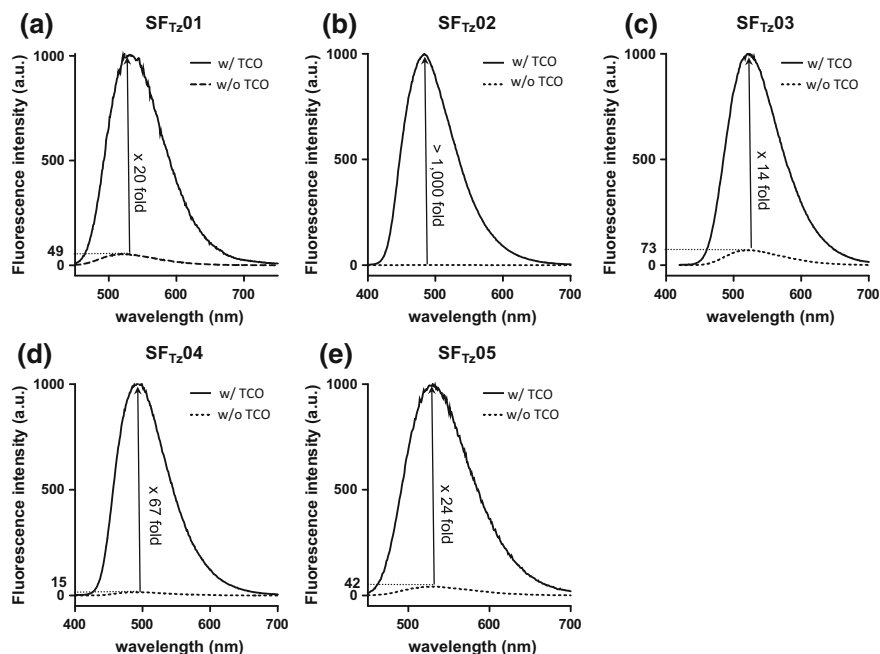


Fig. 3.4 Changes in emission spectra for SF_{Tz}01–SF_{Tz}05 before (dashed line) and after (solid line) the reaction with TCO: **a** SF_{Tz}01, **b** SF_{Tz}02, **c** SF_{Tz}03, **d** SF_{Tz}04, **e** SF_{Tz}05. All spectra were measured in an acetonitrile: H₂O (1:1 v/v) mixture at room temperature. The final concentration of dye and TCO was 20 and 200 μM, respectively

Table 3.1 Photophysical properties for SF_{Tz}s before and after the Reaction with *trans*-cyclooctene (TCO)

Probe	$\Phi_{\text{off}}^{\text{a}}$	k_2^{b} (M ⁻¹ s ⁻¹)	$\lambda_{\text{ex}}^{\text{c}}$ (nm)	$\lambda_{\text{em}}^{\text{d}}$ (nm)	$\Phi_{\text{on}}^{\text{e}}$	fold (on/off) ^f
SF _{Tz} 01	0.011	21	416	532	0.168	20
SF _{Tz} 02	0.002	24	375	484	0.683	>1000
SF _{Tz} 03	0.042	15	401	522	0.583	14
SF _{Tz} 04	0.012	15	375	493	0.616	67
SF _{Tz} 05	0.017	8.5	401	530	0.325	24

^{a,e} Φ_{off} and Φ_{on} denote absolute quantum yield of the SF_{Tz} and SF_{Py} form, respectively.

^bSecond-order rate constant measured at 20 °C. ^cThe largest excitation maxima at the given maximal emission wavelength. ^dMaximal emission wavelength. ^fFluorescence intensity increase measured upon reaction with TCO. All experimental data were measured an acetonitrile:H₂O (1:1 v/v) mixture. The final concentration of dye and TCO was 20 and 200 μM, respectively

but superdark quenching of SF_{Tz}02 lead to an exceptional enhancement, more than 1000-fold, of the fluorescence on/off signal. This result suggests that mono- chromophoric design strategy can generate a series of effectively quenched fluorophores by direct conjugation of Tz to the π -conjugated core structure of fluorophore, which

prompted me to develop a colorful series of monochromophoric SF_{Tz}s with ensured quenching efficiency even at a longer emission wavelength.

3.2.4 Reaction Kinetics

Next, the reaction kinetics of the SF_{Tz} series were evaluated by tracking the change in fluorescence intensity over time, after treatment with TCO. As shown in Table 3.1 and Fig. 3.5, the entire SF_{Tz} series showed fast reaction kinetics ($k_2 = \sim 10 \text{ M}^{-1}\text{s}^{-1}$) in 1:1 acetonitrile/water condition, which is comparable with widely used bioorthogonal reactions, such as copper-catalyzed azide-alkyne cycloadditions (CuAAC, $>10 \text{ M}^{-1}\text{s}^{-1}$) [22] or photo-click cycloadditions ($<60 \text{ M}^{-1}\text{s}^{-1}$) [22b, 23].

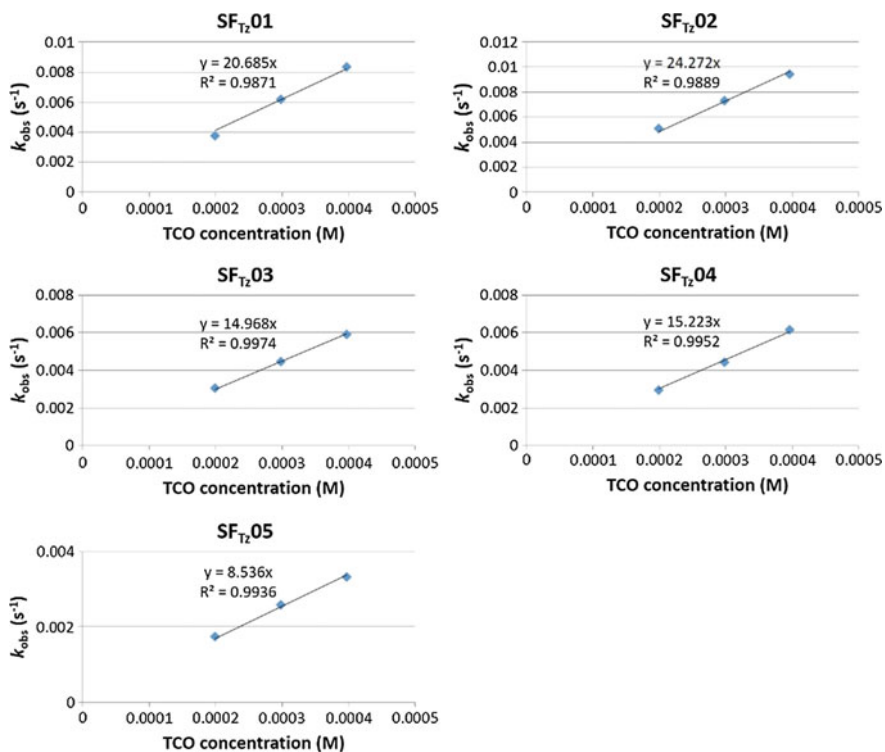


Fig. 3.5 The linear plots of pseudo first-order rate constant (k_{obs}) for SF_{Tz}01–05 versus molar concentration of TCO-NHS-ester, in an acetonitrile: H₂O (1:1 v/v) mixture at 20 °C. Slopes represent second-order rate constant (k_2) for the corresponding SF_{Tz}

3.2.5 Rational Expansion of Multicolor SF_{Tz}s Based on a Monochromophoric Strategy

Based on accumulated knowledge about emission modularity of SF, [16b] a series of SF_{Tz}02 analogues were designed to span a wide emission range simply by changing the electronic nature of substituents at the R¹ position of monochromophoric SF_{Tz}. As shown in Fig. 3.6a, the electron-donating substituents were introduced guided by the Hammett constant [24] [methoxy ($\sigma_p = -0.27$), amino (-0.66), and diethylamino group (-0.72)] at the R¹ position of SF_{Py}—the corresponding iEDDA reaction product of SF_{Tz} with TCO having a 1,4-dihydropyridazine moiety—to induce a bathochromic shift of the emission wavelength of SF_{Tz}-TCO adducts. The trend in emission wavelength changes of SF_{Py} analogues was predicted by density functional theory (DFT) calculation at the CAM-B3LYP/6-31G* level. It is worth mentioning that during the continuous monitoring of the fluorogenic reaction for SF_{Tz}02 with TCO using mass spectroscopy, a progressive disappearance of the mass peak of SF_{Tz}02 was observed until the fluorescence signal reached to maximum, along with the gradual emergence of a new mass peak, which is matched with that of two different types of SF_{Tz}-TCO adducts, 1,4- and 4,5-dihydropyridazine forms. In this chapter, the 1,4-dihydropyridazine isomer will be mainly considered as a representative fluorogenic SF_{Py} on the basis of previous reports [11a, b, g]. As shown in Fig. 3.6b, electron-donating groups at the R¹ position can raise the energy level of the highest occupied molecular orbital (HOMO) more than that of the lowest unoccupied

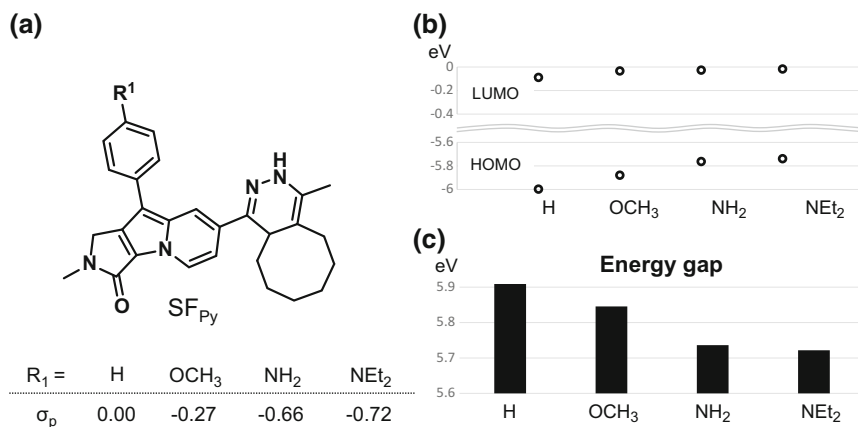


Fig. 3.6 **a** Chemical structure of representative fluorescence on-state SF analogue, SF_{Py}, generated from cycloaddition reaction of SF_{Tz}02 with TCO, and Hammett constant values (σ_p) of H, OCH₃, NH₂, and NEt₂ functional groups. **b** Calculated HOMO and LUMO energy values (DFT, CAM-B3LYP/6-31G*) of SF_{Py} having H, OCH₃, NH₂, and NEt₂ groups at the R¹ position. **c** Changes in the HOMO-LUMO energy gap of SF_{Py}s with corresponding functional groups at the R¹ position

Table 3.2 HOMO and LUMO energy values for SF_{Py}s with variable R¹ groups

R ¹	HOMO (eV)	LUMO (eV)	E _{gap} (eV)
H	-5.997	-0.088	5.909
OCH ₃	-5.879	-0.033	5.846
NH ₂	-5.762	-0.026	5.736
NEt ₂	-5.738	-0.017	5.722

molecular orbital (LUMO). Therefore, the substitution of methoxy, amino and diethylamino groups results in the reduced HOMO-LUMO energy gap of the SF system (Fig. 3.6c and Table 3.2), which is expected to induce a bathochromic shift of emission wavelength compared to that of SF_{Tz}02. The similar trend of HOMO-LUMO energy gaps was also observed in 4,5-dihydropyridazine form as SF_{Py} analogues, according to the changes of substituents at the R¹ position (Fig. 3.7 and Table 3.3).

Accordingly, SF_{Tz}06 (R¹ = methoxy; calculated energy gap = 5.846 eV), SF_{Tz}07 (amino; 5.736 eV), and SF_{Tz}08 (diethylamino; 5.722 eV) were synthesized to generate a multicolor set of bioorthogonal SF_{Tz} probes (Fig. 3.8a). The synthetic procedure for these analogues was identical to that of SF_{Tz}02 (see experimental section). With these new analogues in hand, their electronic orthogonality between indolizine and Tz was evaluated first, by checking the changes in absorption spectra, before and after TCO treatment (Fig. 3.8b). Similar to SF_{Tz}02, all three compounds showed distinct hypsochromic shifts of absorption maxima

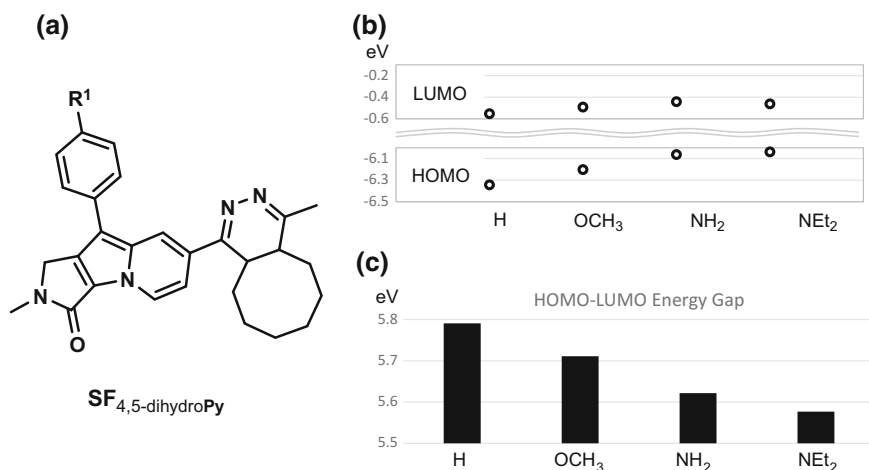


Fig. 3.7 a Chemical structure of a possible fluorescence on-state SF analogue having 4,5-dihydropyridazine moiety, generated from the iEDDA cycloaddition reaction of mono-chromophoric SF_{Tz}s with TCO. b Calculated HOMO and LUMO energy values (DFT, CAM-B3LYP/6-31G*) of SF_{4,5-dihydroPy}s having H, OCH₃, NH₂, and NEt₂ substituents at the R¹ position. c Changes in the HOMO-LUMO energy gap of SF_{4,5-dihydroPy}s with corresponding functional groups at the R¹ position

Table 3.3 HOMO and LUMO energy values for SF_{Tz}4,5-dihydroPy_s with variable R¹ groups

R ¹	HOMO (eV)	LUMO (eV)	E _{gap} (eV)
H	-6.343	-0.552	5.791
OCH ₃	-6.202	-0.491	5.711
NH ₂	-6.063	-0.441	5.622
NEt ₂	-6.038	-0.461	5.577

(425 → 393, 436 → 399, and 457 → 409 nm for SF_{Tz}06, SF_{Tz}07, and SF_{Tz}08, respectively), which clearly suggested strong electronic coupling between Tz and the indolizine aromatic π -system. Upon the reaction with TCO, newly synthesized SF_{Tz}s showed decent reaction kinetics ($>10 \text{ M}^{-1}\text{s}^{-1}$), similar to that of SF_{Tz}02. Emission maxima of SF_{Tz}06 (505 nm), SF_{Tz}07 (562 nm), and SF_{Tz}08 (581 nm) were well matched with DFT calculation (Figs. 3.9 and 3.10), and the resulting monochromophoric SF_{Tz}s, including SF_{Tz}02, cover blue to orange visible-color emission (Table 3.4 and Fig. 3.11). The most remarkable achievement of the monochromophoric SF_{Tz} system is the complete quenching of residual fluorescence at the off-state, regardless of emission wavelength (Fig. 3.8c and Table 3.4). Due to

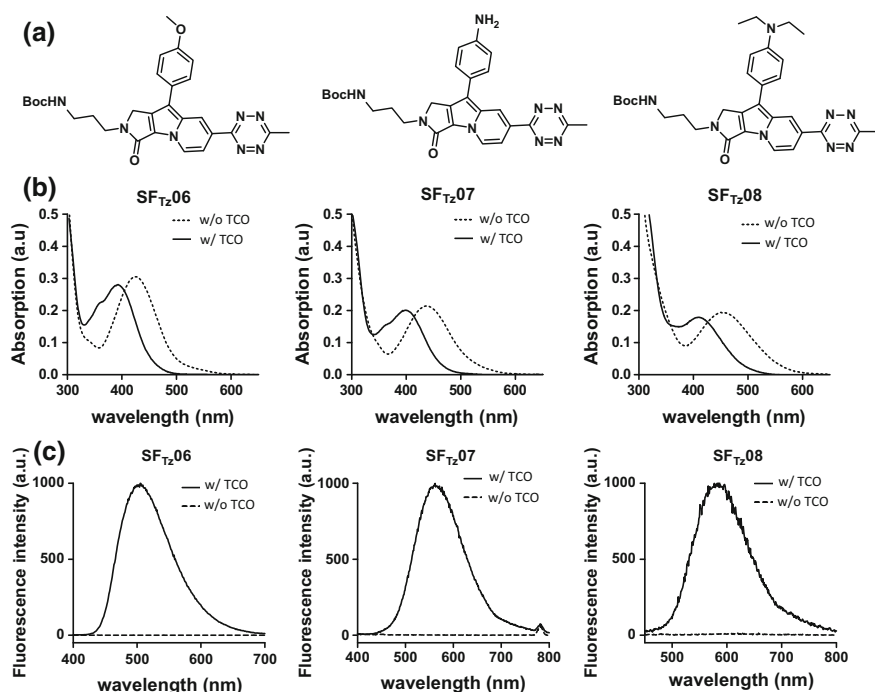


Fig. 3.8 **a** Molecular structures of SF_{Tz}06 (left), SF_{Tz}07 (middle), and SF_{Tz}08 (right). **b** Changes in absorption spectra for SF_{Tz}06–08, before (dashed) and after (solid) the reaction with TCO. **c** Changes in emission spectra for SF_{Tz}06–08, before (dashed) and after (solid) the reaction with TCO

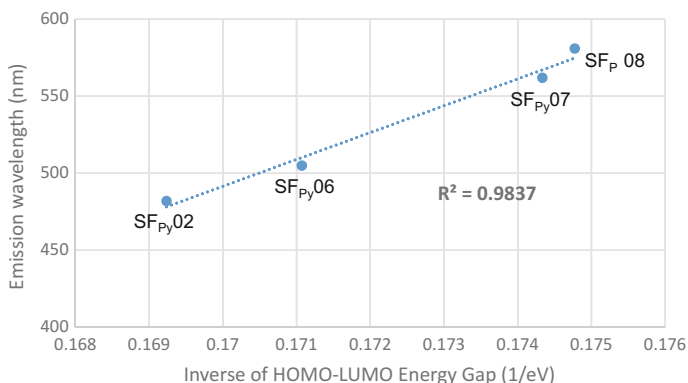


Fig. 3.9 A scatter plot of the inverse of HOMO-LUMO energy gap versus the maximum emission wavelength of SF_{Py}02, SF_{Py}06, SF_{Py}07, and SF_P08

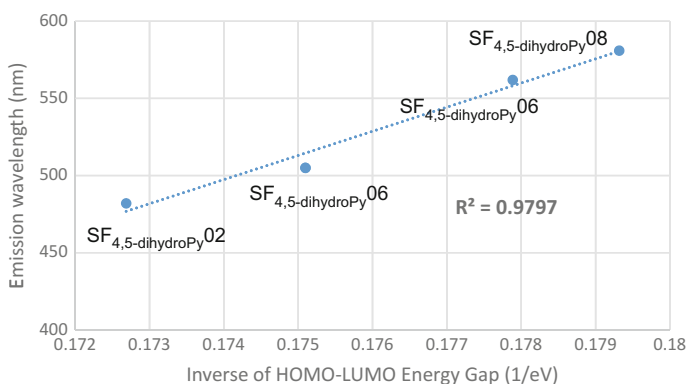


Fig. 3.10 A scatter plot of the inverse of HOMO-LUMO energy gap for SF_{4,5-dihydroPy}S versus the experimental maximum emission wavelength of corresponding TCO-SF_{Tz} products

complete dark-state quenching, the fluorescence on/off ratios of all monochromophoric SF_{Tz}S showed remarkable triple or quadruple-digit-fold enhancement (600–1000 fold), independent from their emission wavelength, even in the case of SF_{Tz}08, with an emission wavelength of >580 nm (Table 3.4).

3.2.6 TD-DFT Calculation

To decipher the fluorescence turn-on mechanism and photophysical property of SF_{Tz}02 and its analogues (SF_{Tz}06–08), time-dependent (TD)-DFT calculations (CAM-B3LYP/6-31G^{*}) was conducted with energy-minimized conformers of

Table 3.4 Photophysical properties for monochromophoric SF_{Tz}S before and after the reaction with TCO

Probe	$\Phi_{\text{off}}^{\text{a}}$	k_2^{b} (M ⁻¹ s ⁻¹)	$\lambda_{\text{ex}}^{\text{c}}$ (nm)	$\lambda_{\text{em}}^{\text{d}}$ (nm)	$\Phi_{\text{off}}^{\text{e}}$	Fold (on/off) ^f
SF _{Tz} 02	0.002	24	375	484	0.683	>1000
SF _{Tz} 06	0.001	23	383	505	0.485	>1000
SF _{Tz} 07	0.002	22	390	562	0.064	>600
SF _{Tz} 08	0.001	22	401	581	0.045	>600

^{a,e} Φ_{off} and Φ_{on} denote absolute quantum yield of SF_{Tz} and SF_{Pz} form, respectively. ^bSecond-order rate constant measured at 20 °C. ^cThe largest excitation maxima at the given maximal emission wavelength. ^dMaximal emission wavelength. ^fFluorescence intensity increase measured upon reaction with TCO. All experimental data were measured in an acetonitrile:H₂O (1:1 v/v) mixture. The final concentration of dye and TCO was 20 μ M and 200 μ M, respectively

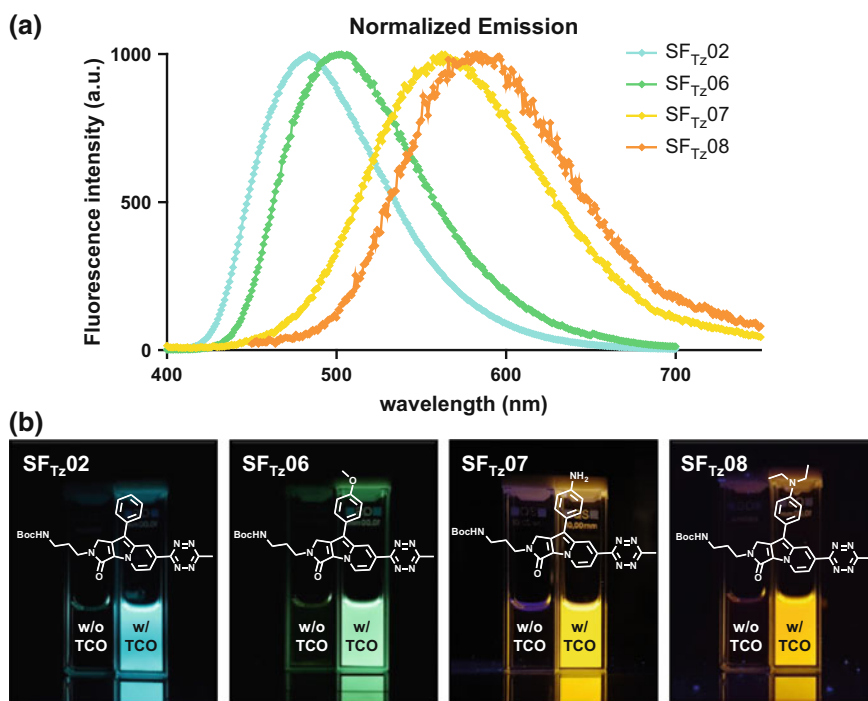


Fig. 3.11 **a** Normalized emission spectra of SF_{Tz}02, SF_{Tz}06, SF_{Tz}07, and SF_{Tz}08 after the reaction with TCO. **b** Photographic images of each compound irradiated at 365 nm, before and after reacting with TCO

SF_{Tz}S, and their corresponding iEDDA reaction products having the 1,4-dihydropyridazine form (SF_{Pz}). The major concern was the probability of optical S₀–S₁ transition at the lowest-lying first singlet excited state, which is known as the most important electronic state for fluorescence phenomenon

according to Kasha's rule [25]. In this regard, geometry optimization of the first excited state for monochromophoric SF_{Tz}s and SF_{Py}s was conducted. Then, molecular orbitals and oscillator strength values (f) [26]—the optical transition probability—between S₀ and S₁ states were investigated using quantum mechanical calculations. As shown in Fig. 3.12a and Table 3.5, the dominant orbitals contributing to S₀–S₁ transition of all monochromophoric SF_{Tz}s were expected to have an n → π* type transition [20]. Based on the orbital distribution of the lowest first excited state of all SF_{Tz}s, it was confirmed that nonbonding orbitals from the nitrogen atom-rich Tz significantly contribute to the n → π* transition within the molecule. On top of that, the f values for all SF_{Tz}s are very close to zero, suggesting that optical transition between S₀ and S₁ is almost forbidden [26]. Therefore, low optical transition possibility for S₀–S₁ transition strongly indicates that monochromophoric SF_{Tz}s would lose their excited energy via nonradiative decay process. Note that this is a completely different quenching mechanism from TBET- or FRET-based systems, whose quenching performance is governed by energy

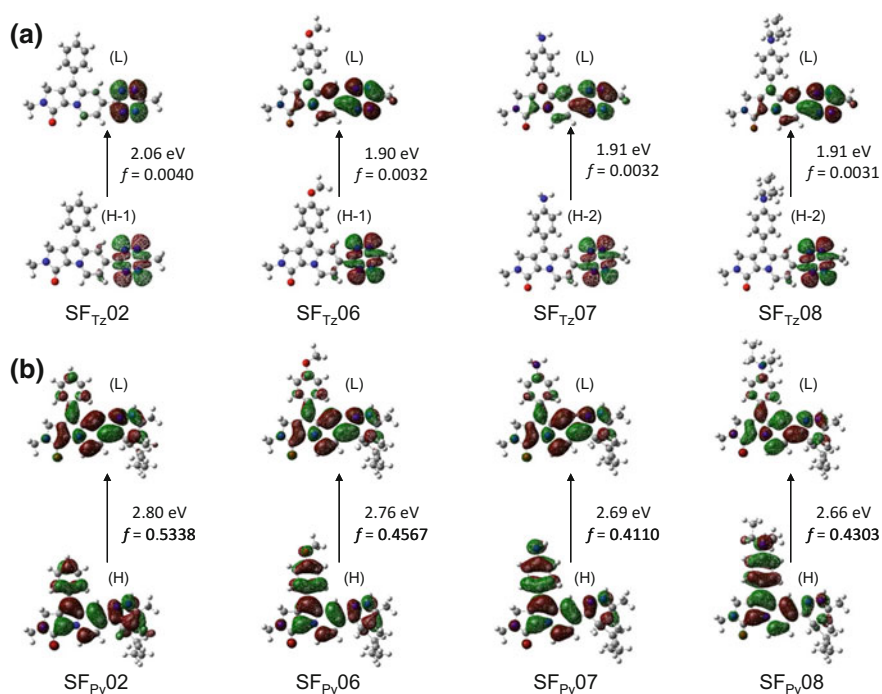


Fig. 3.12 Molecular orbital distribution, vertical transition energy, and oscillator strength values (f) of SF_{Tz}02, SF_{Tz}06, SF_{Tz}07, and SF_{Tz}08, obtained by TD-DFT calculation (CAM-B3LYP/6-31G*) of corresponding first excited state optimized structures. **a** Quenched SF_{Tz} compounds before the reaction with TCO. **b** The fluorogenic SF_{Py} products after the formation of TCO-adducts. The main contributing orbital of S₀–S₁ for each compound is illustrated. H and L stand for HOMO and LUMO, respectively

Table 3.5 The TD-DFT calculation data for SF_{Tz}02, SF_{Tz}06, SF_{Tz}07, and SF_{Tz}08 at the first excited state optimized structures (CAM-B3LYP/6-31G^{*})

	f^a	E (eV) ^b	Transitions ^c	CI expansion coefficient ^d
SF _{Tz} 02	0.0040	2.0611	HOMO-1 → LUMO	+0.70199
SF _{Tz} 06	0.0032	1.9023	HOMO-1 → LUMO	-0.64297
			HOMO-1 → LUMO + 1	+0.29035
SF _{Tz} 07	0.0032	1.9082	HOMO-2 → LUMO	-0.64244
			HOMO-2 → LUMO + 1	+0.28410
SF _{Tz} 08	0.0031	1.9069	HOMO-2 → LUMO	+0.64439
			HOMO-2 → LUMO + 1	-0.28748

^aOscillator strength values for S₀-S₁ transition. ^bVertical transition energy for S₀-S₁. ^cOrbital transitions involved in S₀-S₁. ^dCI expansion coefficients (orbital contribution)

Table 3.6 The TD-DFT calculation data for SF_{Py}02, SF_{Py}06, SF_{Py}07, and SF_{Py}08 at the first excited state optimized structures (CAM-B3LYP/6-31G^{*})

	f^a	E (eV) ^b	Transitions ^c	CI expansion coefficient ^d
SF _{Py} 02	0.5338	2.7953	HOMO → LUMO	0.69207
SF _{Py} 06	0.4567	2.7550	HOMO → LUMO	0.69155
SF _{Py} 07	0.4110	2.6865	HOMO → LUMO	0.68901
SF _{Py} 08	0.4303	2.6627	HOMO → LUMO	0.68444

^aOscillator strength values for S₀-S₁ transition. ^bVertical transition energy for S₀-S₁. ^cOrbital transitions involved in S₀-S₁. ^dCI expansion coefficients (orbital contribution)

transfer efficiency from the excited fluorophore to the electronically decoupled Tz quencher. After the cycloaddition reaction of SF_{Tz} with TCO, removal of two nitrogen atoms as well as extinction of the aromatic system of Tz might cause a huge transformation of nonbonding orbitals of SF_{Tz}. Therefore, the optically inactive $n \rightarrow \pi^*$ transition at the lowest lying state is no longer valid after iEDDA reaction, but the $\pi \rightarrow \pi^*$ transition becomes the most important transition between the S₀ and S₁ states in all SF_{Py}s (Fig. 3.12b and Table 3.6). Besides, f values for the S₀-S₁ transition in SF_{Py}s (from 0.41 to 0.53) are significantly higher than that of the S₀-S₁ transition in SF_{Tz}s (from 0.0031 to 0.0040). In other words, radiative energy loss of excited fluorophores becomes “allowed” after iEDDA reaction and it makes SF_{Py}s fluorescent. Almost identical results were observed in the case of the 4,5-dihydropyridazine isomer as SF_{Py}s (Fig. 3.13 and Table 3.7). In summary, computational calculation indicates that direct incorporation of Tz to SF makes the optically inactive $n \rightarrow \pi^*$ transition (low f value) the major S₀-S₁ transition for SF_{Tz}s, which quenches the fluorescence process of chromophores. Destruction of Tz in SF_{Tz}s, induced by bioorthogonal iEDDA reaction with TCO, makes the optically active $\pi \rightarrow \pi^*$ transition dominant (high f value) for the S₀-S₁ transition in SF_{Py}s, which turns on the molecules’ fluorescence.

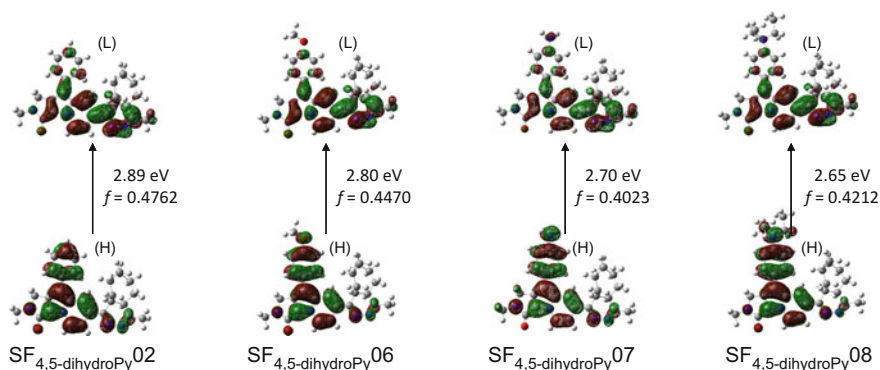


Fig. 3.13 Molecular orbital distribution, vertical transition energy, and oscillator strength values of SF_{4,5-dihydroPy02}, SF_{4,5-dihydroPy06}, SF_{4,5-dihydroPy07}, and SF_{4,5-dihydroPy08}, obtained by TD-DFT (CAM-B3LYP/6-31G*) calculation of corresponding first excited state optimized structures. Only main contributing orbital of S₀-S₁ for each compound is illustrated. H and L stand for HOMO and LUMO, respectively

Table 3.7 The TD-DFT calculation data for SF_{4,5-dihydroPy02}, SF_{4,5-dihydroPy06}, SF_{4,5-dihydroPy07}, and SF_{4,5-dihydroPy08} at the first excited state optimized structures (CAM-B3LYP/6-31G*)

	f^a	E (eV) ^b	Transitions ^c	CI expansion coefficient ^d
SF _{4,5-dihydroPy02}	0.4762	2.8889	HOMO → LUMO	0.68218
SF _{4,5-dihydroPy06}	0.4470	2.7995	HOMO → LUMO	0.68522
SF _{4,5-dihydroPy07}	0.4023	2.7003	HOMO → LUMO	0.68364
SF _{4,5-dihydroPy08}	0.4212	2.6495	HOMO → LUMO	0.68034

^aOscillator strength values for S₀-S₁ transition. ^bVertical transition energy for S₀-S₁. ^cOrbital transitions involved in S₀-S₁. ^dCI expansion coefficients (orbital contribution)

3.2.7 Direct Comparison of Mono- Versus Bichromophoric SF_{Tz}s with Long Emission Wavelength

Next, the direct comparison of the mono- versus bichromophoric design strategy was pursued by analyzing the turn-on/off ratios at the longer emission wavelength. For the comparison with SF_{Tz}08, the representative long wavelength compound for monochromophoric SF_{Tz}, an electron-donating diethylamino group was simply introduced at the R¹ position of SF_{Tz}04 and SF_{Tz}05 to yield SF_{Tz}09 and SF_{Tz}10, respectively, as representative long-wavelength bichromophoric SF_{Tz}s (Fig. 3.14). It turns out that after TCO treatment, electronically decoupled bichromophoric systems, SF_{Tz}09–10, showed noticeable depreciation of turn-on/off ratios (67 → 30-fold for SF_{Tz}04 → SF_{Tz}09 and 24 → 3-fold for SF_{Tz}05 → SF_{Tz}10) as the fluorophore's emission coverage was shifted to the longer emission area (Tables 3.1 and 3.8, Figs. 3.4 and 3.15). On the contrary, monochromophoric design strategy allowed SF_{Tz}08 to preserve compelling turn-on/off efficiency (over

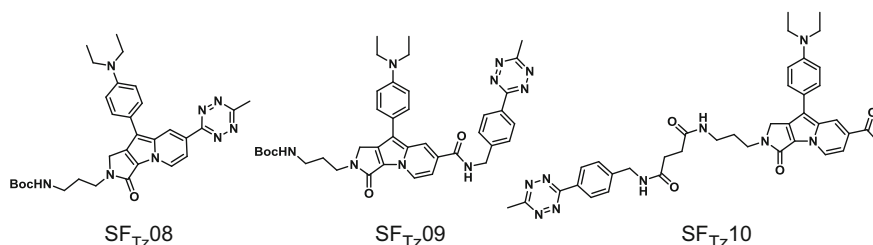


Fig. 3.14 Molecular structures of SF_{Tz}08, SF_{Tz}09, and SF_{Tz}10 for the direct comparison of mono- and bichromophoric design strategies on SF_{Tz}. SF_{Tz}08, SF_{Tz}09, and SF_{Tz}10 are designed as long-emission wavelength analogues for the SF_{Tz}02 (monochromophoric SF_{Tz}) and SF_{Tz}04–05 (bichromophoric SF_{Tz}), respectively

Table 3.8 Photophysical properties of SF_{Tz}s before and after the reaction with TCO

Probe	$\Phi_{\text{off}}^{\text{a,c}}$	k_2^{b} ($\text{M}^{-1}\text{s}^{-1}$)	$\lambda_{\text{ex}}^{\text{c}}$ (nm)	$\lambda_{\text{em}}^{\text{d}}$ (nm)	$\Phi_{\text{on}}^{\text{e}}$	Fold (on/off) ^f
SF _{Tz} 08	0.001	22	401	581	0.045	>600
SF _{Tz} 09	0.005	15	418	608	0.016	30
SF _{Tz} 10	0.013	1.2	438	625	0.028	3

^{a,c} Φ_{off} and Φ_{on} denote absolute quantum yield of SF_{Tz} and SF_{Py} form, respectively. ^bSecond-order rate constant measured at 20 °C. ^cThe largest excitation maxima at the given maximal emission wavelength. ^dMaximal emission wavelength. ^fFluorescence intensity increase measured upon reaction with TCO. Experimental data were measured in an acetonitrile:H₂O (1:1 v/v) mixture for SF_{Tz}08 and SF_{Tz}09, and in acetonitrile for SF_{Tz}10. The final concentration of dye and TCO was 20 μM and 200 μM, respectively

600 fold), comparable to that of SF_{Tz}02 (over 1000 fold), at the long emission area. The slight reduction in turn-on/off ratios of SF_{Tz}08 might originate from the innate low quantum yield of its fluorogenic form. Collectively, this comparison experiment demonstrated the unique advantage of monochromophoric design strategy, which guarantees excellent fluorescence off/on ratio, independent from the emission wavelength of fluorophores. By taking advantage of wavelength-independent quenching mechanism, different from conventional energy-transfer type quenching (FRET or TBET), monochromophoric approach could provide a robust and generally applicable molecular design strategy for the development of multicolor bioorthogonal fluorogenic probes with high turn-on ratios.

3.2.8 Bioapplication

Lastly, SF_{Tz}02 and SF_{Tz}08 were applied for cellular imaging to demonstrate the usefulness of SF_{Tz}s as multicolor bioorthogonal fluorogenic imaging probes. For the practical usage of SF_{Tz} probes, the R³ position of SF system—proven as orthogonal to the fluorescence property [16c, e]—was changed by introducing a

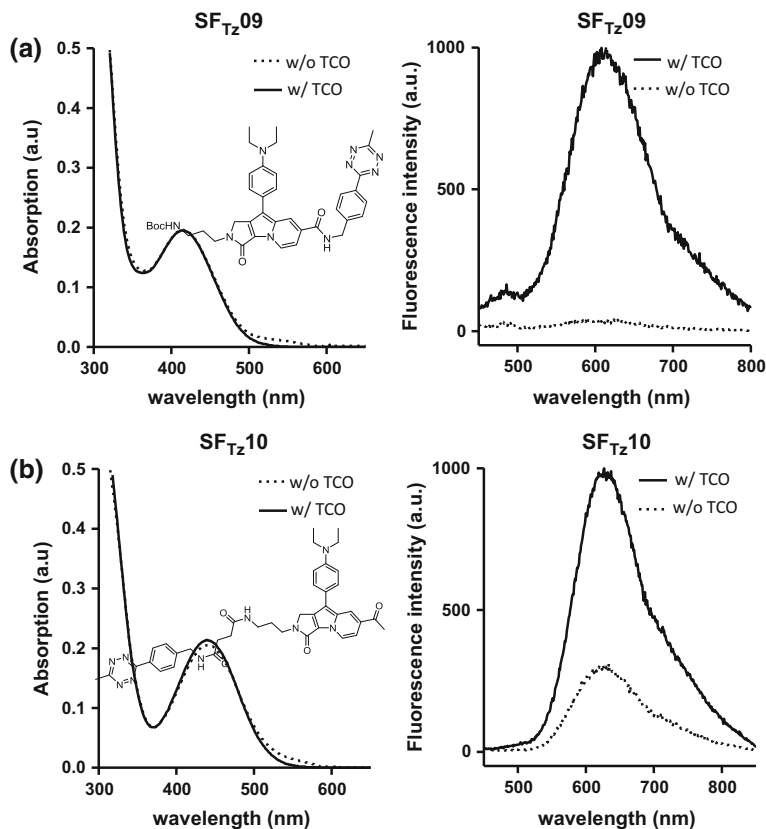


Fig. 3.15 Absorption (left) and emission spectra (right) for **a** SF_{Tz}09 and **b** SF_{Tz}10, before and after the reaction with *trans*-cyclooctene (TCO). Absorption and emission spectra for SF_{Tz}09 or SF_{Tz}10 were obtained in an acetonitrile: H₂O (1:1 v/v) or in acetonitrile, respectively

water soluble moiety such as piperazine and carboxyl group to yield SF_{Tz}02* and SF_{Tz}08*, respectively (Fig. 3.16). Then, Docetaxel-TCO conjugate (Dox-TCO) was firstly used for fluorescent bioimaging of microtubules (Fig. 3.17). HeLa human cervical carcinoma cells were fixed and incubated with Dox-TCO for 1 h and washed briefly with PBS. Immediately after the addition of SF_{Tz}02* or SF_{Tz}08* to the cells, bright cytoplasmic fluorescent signal was generated and the intracellular fluorescent images resembled typical spindle structures of microtubules (Fig. 3.17b, d). Control experiments confirmed that there is a negligible background signal inside the cells and no background signal outside of the cells even with longer exposure time (Fig. 3.17a, c). Therefore, a sharp contrast in fluorescent signal between cytoplasmic and outside of fixed cells could be achieved without washing steps to remove excess SF_{Tz} probes. Further immunofluorescence with α -tubulin antibody confirmed the specific staining of microtubules with Dox-TCO/SF_{Tz}s (Fig. 3.17f, g, h). Considering the importance of mitochondrial phenotyping,

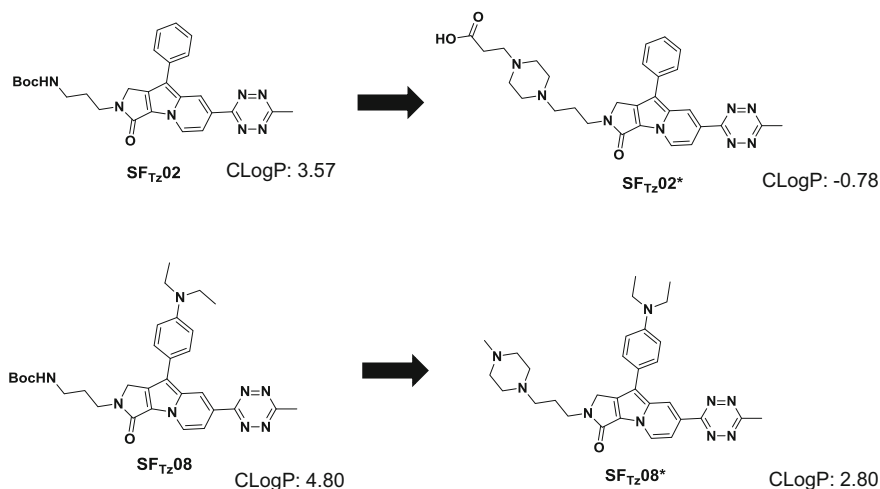


Fig. 3.16 Chemical structures and cLogP values of SF_{Tz}02* and SF_{Tz}08* (water soluble analogues of SF_{Tz}02 and SF_{Tz}08, respectively)

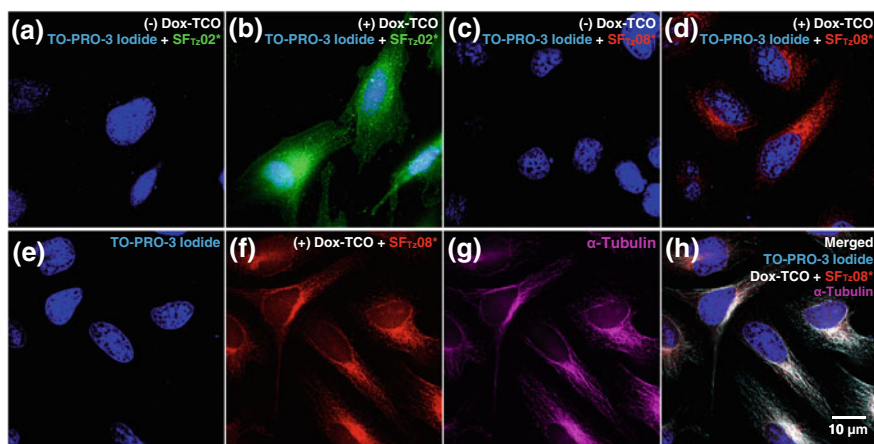


Fig. 3.17 Fluorogenic bioorthogonal imaging of innate microtubules with SF_{Tz} in a fixed-cell condition. HeLa human cervical carcinoma cells were treated with DMSO (a, c) or Dox-TCO (b, d) for 1 h. TO-PRO-3 iodide (1 μM) was treated for nucleus staining. After brief washing with PBS, SF_{Tz}02* (a, b) or SF_{Tz}08* (c, d) was used to treat the cells (final concentration = 10 μM). Immediately after addition of the probes, the cell images were observed with fluorescence microscope without washing. Selective microtubule staining was further confirmed with immunofluorescence using α-tubulin antibody (g–h). Scale bar, 10 μm

[27] the SF_{Tz}s were then used in fluorescence imaging of mitochondria in live cells (Fig. 3.18). After 1 h incubation in the presence or absence of triphenylphosphonium (TPP)-TCO, HeLa cells were washed and treated with SF_{Tz}02* or SF_{Tz}08*.

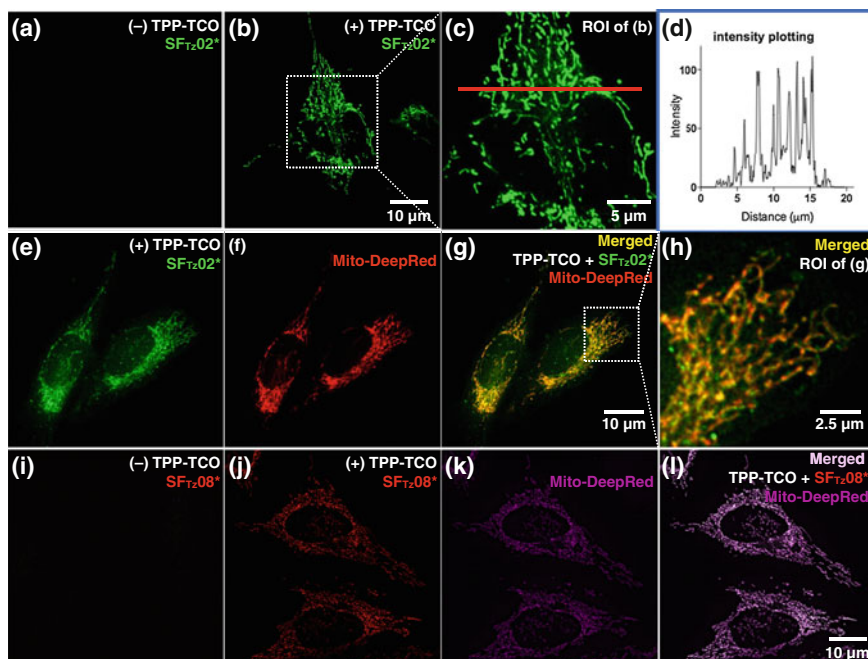


Fig. 3.18 Fluorogenic bioorthogonal imaging of mitochondria with SF_{Tz}02* and SF_{Tz}08* in live cell conditions without washing steps. HeLa human cervical carcinoma cells were treated with DMSO (a, i) or triphenylphosphonium (TPP)-TCO (10 μM, b, c, e, g, h, j, l) with MitoTracker-Deep Red (f–h, k, l) for 40 min. After brief washing with PBS, SF_{Tz}02* (a, b, c, e, g, h) or SF_{Tz}08* (i, j, l) were used to treat the cells (final concentration = 10 μM). Images were immediately observed with fluorescence microscope without washing. (d) Plot intensity values of pixels along a red line in (c) were analyzed with the Image J program. ROI, region of interest

In the absence of TPP-TCO, no specific staining of mitochondria nor background signal was observed, even without washing steps (Fig. 3.18a, i). On the other hand, TPP-TCO/SF_{Tz}02* or TPP-TCO/SF_{Tz}08* treatment produced crisp fluorescent mitochondrial images with an exceptional resolution (Fig. 3.18b, e, j). Plot intensity values of pixels along a red line (Fig. 3.18c, d) revealed a sharp contrast between mitochondrion and other areas, which validated complete fluorescence quenching of SF_{Tz}s under the physiological culture-media condition (zero intensity was observed in the extracellular area). To confirm the selectivity of TPP-TCO/SF_{Tz}02* and TPP-TCO/SF_{Tz}08* for mitochondria, HeLa cells were cotreated with commercially available mitochondria staining dye, MitoTracker Deep Red, and excellent colocalization of the signal between MitoTracker Deep Red and SF_{Tz}02* or SF_{Tz}08* was observed. Together, highly efficient and selective fluorescent staining of intracellular TOI protein and intracellular organelles was possible without multiple washing steps using SF_{Tz}s in live cell conditions.

3.3 Conclusion

In summary, the monochromophoric design strategy enables the development of fluorogenic probe SF_{TzS}, having an extraordinary turn-on/off ratios covering the full visible color range, for the live cell imaging via rapid and catalyst-free bioorthogonal reaction. Strong electronic coupling between the SF core and Tz chromophore causes dark-state quenching, which is completely different from conventional FRET- or TBET-type energy transfer mechanism. Wavelength independent dark-state quenching enables efficient widening of the emission color range of SF_{TzS}, validating generality and robustness of this monochromophoric strategy. The applicability of SF_{TzS} as bioorthogonal fluorescent probes was successfully demonstrated by imaging of TOI proteins and subcellular organelles in live cell conditions without washing steps.

When applying this monochromophoric strategy, a dihydropyridazine moiety—product of TCO–Tz reaction—will directly affect the π -electronic system of the resulting fluorophores after the TCO–FL_{Tz} reaction. Considering photophysical properties of our monochromophoric probes, this group would act like an electron withdrawing group (EWG). Therefore, our monochromophoric strategy will be suitable for fluorophores having specific positions, where an EWG is essential to exhibit fluorescent properties. In this regard, the EWG position of charge-transfer-type fluorophores, such as nitrobenzoxadiazole (NBD), acedan, or coumarin derivatives, might be a potential candidate for tetrazine incorporation. The monochromophoric design strategy will be useful to provide highly reliable and generally applicable method for the development of bioorthogonal fluorogenic probes with excellent turn-on/off ratios in vitro and in vivo.

3.4 Experimental Section

3.4.1 General Experimental Information

a. Compound characterization

¹H and ¹³C NMR spectra were recorded on an Agilent 400-NMR [Agilent Technologies], Varian Inova-500 [Varian Associates], and AVANCETM 600 [Bruker]. Chemical shifts were reported in parts per million (δ) and calibrated using internal tetramethylsilane (TMS) standard or residual undeuterated solvent for ¹H NMR spectra (CD₂Cl₂ 5.32 ppm; DMSO-*d*₆ 2.50 ppm; pyridine-*d*₅ 7.22 ppm) and for ¹³C NMR spectra (DMSO-*d*₆ 39.52 ppm; CDCl₃ 77.16 ppm, CD₂Cl₂ 53.84 ppm). Multiplicity was indicated as follows: s (singlet); d (doublet); t (triplet); q (quartet); quin (quintet); m (multiplet); dd (doublet of doublet); dt (doublet of triplet); br s (broad singlet), br d (broad doublet) etc. Coupling constants were reported in Hz. Low resolution mass spectrometry (LRMS) was obtained by LCMS-2020 [Shimadzu]. High resolution mass spectrometry (HRMS) of final

compounds was further confirmed by Ultra High Resolution ESI Q-TOF mass spectrometer [Bruker] from *Organic Chemistry Research Center* at Sogang University.

b. Photophysical properties

Absorption spectra were measured by UV-VIS spectrophotometer UV-1650PC [Shimadzu]. Emission spectra and kinetic data were measured by Cary Eclipse Fluorescence spectrophotometer [Varian Associates] and absolute quantum yield was measured by QE-2000 [Otsuka Electronics].

c. Materials

All chemicals were purchased from Sigma-Aldrich, Tokyo Chemical Industry Co., Ltd, ThermoFisher Scientific, or Click Chemistry Tools and used without further purification unless otherwise specified. The progress of reaction was monitored using thin-layer chromatography (TLC) (silica gel 60, F₂₅₄ 0.25 mm), and components were visualized by observation under UV light (254 and 365 nm) or by treating the TLC plates either with *p*-anisaldehyde, KMnO₄, or ninhydrin followed by heating. Solvents were purchased from commercial vendors and used without further purification. Mouse anti-alpha tubulin monoclonal antibody [#3873] was purchased from Cell Signaling Technology. Rhodamine-tagged goat Anti-mouse IgG (H+L) secondary antibody [31660], TO-PRO™-3 Iodide [T3605], and MitoTracker™ Deep Red FM [M22426] were purchased from Thermo Scientific. RPMI 1640 medium, fetal bovine serum (FBS), and antibiotic-antimycotic solution were purchased from Gibco, Invitrogen. Phosphate-buffered saline (PBS) buffer was purchased from WELGENE. HeLa human cervical cancer cell line was obtained from Korean Cell Line Bank. Dyes, docetaxel-TCO (Dox-TCO), and triphenylphosphonium (TPP)-TCO probe were prepared in dimethyl sulfoxide (DMSO) solution before fluorescence imaging. DMSO, paraformaldehyde, and Triton X-100 were purchased from Sigma-Aldrich. Nunc™ Lab-Tek™ II chambered coverglass was purchased from Thermo Scientific. 100-mm culture dish was purchased from CORNING.

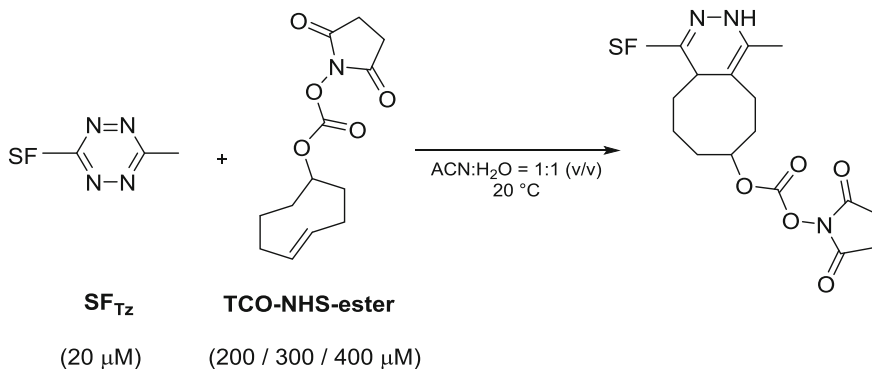
d. Quantum mechanical calculations

All quantum mechanical calculations were performed in Gaussin09 W. The ground state structures were optimized using density functional theory (DFT) at the CAM-B3LYP/6-31G* level. Frequency were checked after ground state geometry optimization to verify the stability of calculated molecular geometry. Energy levels of the highest occupied molecular orbital (HOMO) and the lowest unoccupied molecular orbital (LUMO) were calculated with the optimized ground state molecular geometry. Vertical transition energy and oscillator strength values (*f*) were calculated through time-dependent density functional theory (TD-DFT) at the CAM-B3LYP/6-31G* level, with optimized first-excited state molecular geometry. In all calculations, the substituent at the R³ position of SF_{TzS} was fixed as a methyl group to minimize the calculation cost.

e. Fluorescence microscopy

Fluorescence imaging experiment was performed with DeltaVision Elite imaging system from GE Healthcare. Objective lenses were equipped with Olympus IX-71 inverted microscope with PLAN APO 60×/Oil (PLAPON60×O), 1.42 NA, WD 0.15 mm sCMOS camera. InSightSSI fluorescence illumination module was equipped within the system. Imaging was performed with four-color standard filter set [GE Healthcare, 52-852113-003]. For live cell imaging, CO₂ supporting chamber with an objective air heater was installed with the system. Images were analyzed with SoftWorks program supported by GE Healthcare and ImageJ software by National Institutes of Health.

3.4.2 Fluorescence Kinetic Measurements



SF_{TzS} and a TCO sample were prepared as 5 mM, and 100 mM DMSO stocks, respectively. To a solution of 20 μM SF_{TzS} in a quartz cuvette (2.5 mL, CH₃CN:H₂O = 1:1) at 20 °C, was added 10, 15, or 20 fold excess of TCO-NHS-ester (total DMSO volume was less than 1%), with a vigorous agitation using a Pasteur pipette. SF_{TzS} were excited at the corresponding largest λ_{ex}, and fluorescence signal was recorded over every two seconds at λ_{em} of each SF_{Tz}. *k*_{obs} values were calculated from GraphPad Prism 5 software, using the one phase exponential association equation.

3.4.3 *Experimental Procedure for Live Cell Fluorescence Image*

a. Cell culture

HeLa human cervical cancer cells were cultured in RPMI 1640 medium supplemented with 10% (v/v) fetal bovine serum (FBS) and 1% (v/v) antibiotic-antimycotic solution. Cells were maintained in 100-mm cell culture dish, in 5% CO₂ incubator at 37 °C with humidified atmosphere.

b. Dox-TCO fluorescence imaging

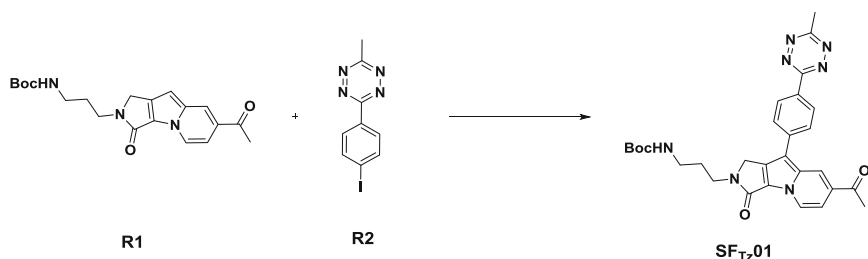
HeLa cell was seeded in NuncTM Lab-TekTM II chambered cover-glass and maintained for 1 day. For imaging after fixation, media was aspirated and washed with PBS. Then, cell was incubated with 4% (m/v) paraformaldehyde solution at room temperature for 15 min. 4% (m/v) paraformaldehyde solution was then aspirated and cell was washed with PBS for 3 times. For cell permeabilization, 0.1% (v/v) Triton X-100 in PBS solution were treated at room temperature for 10 min. Solution was then removed and cell was washed with PBS for 3 times. Then, 5~10 μM docetaxel-TCO were treated at room temperature for 1 h, or at 4 °C overnight. After brief washing with PBS, TO-PRO-3 Iodide was treated for nucleus staining. Cells were finally washed with PBS for 3 times and imaging was carried out immediately after SF_{Tz}02* or SF_{Tz}08* (10 μM) treatment.

For the co-localization imaging with alpha-tubulin, media was aspirated and washed with PBS. Then, cell was incubated with 4% (m/v) paraformaldehyde solution at room temperature for 15 min. 4% (m/v) paraformaldehyde solution was then aspirated and cell was washed with PBS for 3 times. For cell permeabilization, 0.1% (v/v) Triton X-100 solution in PBS were treated at room temperature for 10 min. 2% (m/v) BSA solution was treated and incubated at room temperature for 1 h. Solution was then removed and primary antibody diluted in 1% (m/v) BSA solution (1:400) was co-treated with 10 μM docetaxel-TCO at 4 °C overnight. Primary antibody solution was removed and sample was washed with PBS for 3 times. Secondary antibody diluted in 1% (m/v) BSA solution (1:200) was treated at room temperature for 1 h. For the secondary antibody, rhodamine-tagged goat anti-mouse IgG (H+L) secondary antibody was treated. After 1 h, antibody solution was aspirated and sample was washed with PBS for 3 times. After brief washing with PBS, TO-PRO-3 Iodide was treated for nucleus staining. Cells were finally washed with PBS and imaging was carried out immediately after SF_{Tz}02* or SF_{Tz}08* (10 μM) treatment. SF_{Tz}02* fluorescence was visualized using DAPI/FITC filter set, SF_{Tz}08* fluorescence was visualize using DAPI/TRITC filter set, TO-PRO-3 Iodide fluorescence was visualized using Cy5/Cy5 filter set, and alpha-tubulin immunofluorescence was visualized using TRITC/TRITC filter set. DAPI (Excitation: 390/18 nm, Emission: 435/48 nm); FITC (Excitation: 475/28 nm, Emission: 525/48 nm); TRITC (Excitation: 542/27 nm, Emission: 597/45 nm); Cy5 (Excitation: 632/22, Emission: 679/34). Images were analyzed and merged with SoftWorks deconvolution software and ImageJ software.

c. TPP-TCO imaging

HeLa cell was seeded in Nunc™ Lab-Tek™ II chambered coverglass and maintained for 1 day. TPP-TCO (10 μM) and MitoTracker™ Deep Red (50 nM) were treated 40 min. Then, cell was washed with PBS, followed by SF_{Tz}02* or SF_{Tz}08* (10 μM) treatment. For live cell imaging, DeltaVision chamber was maintained in 37 °C with 5% CO₂ for at least 2 h prior to imaging. Imaging was performed right after SF_{Tz}02* or SF_{Tz}08* treatment. SF_{Tz}02* fluorescence was visualized using DAPI/FITC filter set, SF_{Tz}08* fluorescence was visualized using DAPI/TRITC filter set, and MitoTracker™ Deep Red fluorescence was visualized using Cy5/Cy5 filter set. DAPI (Excitation: 390/18 nm, Emission: 435/48 nm); FITC (Excitation: 475/28 nm, Emission: 525/48 nm); TRITC (Excitation: 542/27 nm, Emission: 597/45 nm); Cy5 (Excitation: 632/22, Emission: 679/34). Images were analyzed and merged with SoftWorks deconvolution software and ImageJ software.

3.4.4 Synthetic Procedure and Characterization of New Compounds

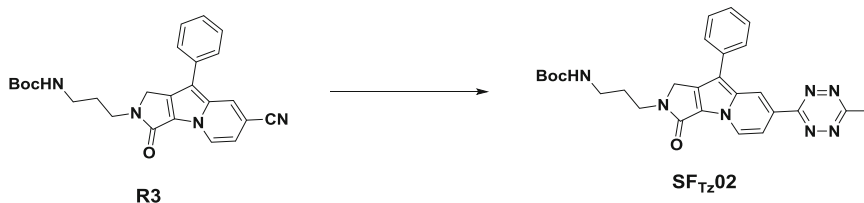


Compound SF_{Tz}01: **R1**² (93.0 mg, 250 μmol), **R2**³ (224 mg, 751 μmol), palladium acetate (11.2 mg, 50.0 μmol), and silver acetate (125 mg, 751 μmol) were dissolved in 2.5 mL of *N,N*-dimethylformamide (DMF). The reaction mixture was stirred at 80 °C for overnight. The crude reaction mixture was then filtered through Celite and concentrated under reduced pressure. The crude product was purified by silica-gel flash column chromatography [toluene:ethyl acetate(EtOAc) = 1:1] to afford **SF_{Tz}01** (7.7 mg, 5.7% yield) as an orange solid; ¹H NMR (400 MHz, CDCl₃) δ 8.72 (d, *J* = 8.2 Hz, 2H), 8.62 (d, *J* = 7.4 Hz, 1H), 8.49 (s, 1H), 7.77 (d, *J* = 8.6 Hz, 2H), 7.35 (d, *J* = 7.0 Hz, 1H), 5.32 (br s, 1H, NH), 4.60 (s, 2H), 3.72 (t, *J* = 6.3 Hz, 2H), 3.20 (m, 2H), 3.13 (s, 3H), 2.66 (s, 3H), 1.88 (t, *J* = 6.1 Hz, 2H), 1.43 (s, 9H); ¹³C NMR (100 MHz, CDCl₃) δ 195.4, 167.2, 163.8, 161.7, 156.1, 137.9, 135.3, 135.0, 130.0, 129.9, 128.8, 127.9, 125.0, 123.2, 120.9, 112.9, 110.1,

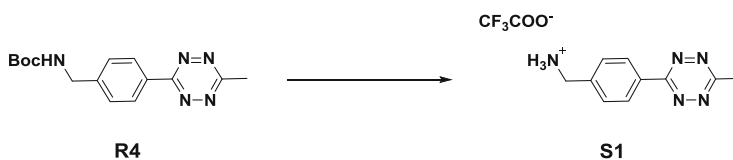
²Angew. Chem. Int. Ed. **2014**, 53, 1346–1350.

³Org. Biomol. Chem. **2014**, 12, 4177–4185.

79.2, 46.8, 40.2, 37.3, 28.8, 28.4, 26.2, 21.2; HRMS (ESI) m/z calcd for $C_{29}H_{31}N_7NaO_4$ $[M+Na]^+$: 564.2330, found: 564.2331.



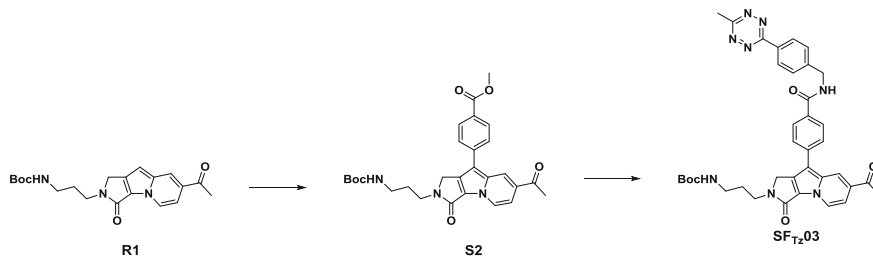
Compound SF_{Tz}02: A reaction mixture of **R3**¹ (64.5 mg, 150 μ mol), acetonitrile (391 μ L, 7.49 mmol), zinc trifluoromethanesulfonate (27.2 mg, 74.9 μ mol), and hydrazine monohydrate (728 μ L, 15.0 mmol) in microwave reaction vial (10 mL) was irradiated under microwaves at 80 $^{\circ}$ C (100 W) with magnetic stirring for 0.5 h. After cooled down to room temperature, sodium nitrite (517 mg, 7.49 mmol) in 1 mL of water was added followed by slow addition of 1 N HCl until pH value reached at 3 (caution! toxic nitrogen oxide gas evolved!). Then, the resulting residue was washed with saturated $NaHCO_3$ aqueous solution, extracted with CH_2Cl_2 , dried over anhydrous Na_2SO_4 , and concentrated. The crude product was purified by normal-phase preparative HPLC using a linear gradient of methanol (1–4%) in CH_2Cl_2 with a flow rate of 5 ml/min to afford **SF_{Tz}02** (16.7 mg, 22.3% yield) as a red solid; 1H NMR (400 MHz, $CDCl_3$) δ 9.16 (s, 1H), 8.69 (d, J = 7.4 Hz, 1H), 7.87 (d, J = 7.4 Hz, 1H), 7.59 (d, J = 7.4 Hz, 2H), 7.50 (t, J = 7.6 Hz, 2H), 7.35 (t, J = 7.3 Hz, 1H), 5.39 (br s, 1H, NH), 4.53 (s, 2H), 3.70 (t, J = 6.3 Hz, 2H), 3.20 (m, 2H), 3 s.10 (s, 3H), 1.86 (quin, J = 6.3 Hz, 2H), 1.44 (s, 9H); ^{13}C NMR (100 MHz, $CDCl_3$) δ 167.0, 163.2, 162.0, 156.2, 135.6, 135.2, 133.6, 129.4, 127.6, 127.0, 125.6, 124.2, 122.8, 119.8, 113.8, 109.2, 79.2, 46.8, 40.2, 37.4, 28.9, 28.6, 21.3; HRMS (ESI) m/z calcd for $C_{27}H_{29}N_7NaO_3$ $[M+Na]^+$: 522.2224, found: 522.2225.



Compound S1: **R4**⁴ (45.9 mg, 152 μ mol) and trifluoroacetic acid (TFA, 300 μ L, 3.92 mmol) were dissolved in CH_2Cl_2 (1.2 mL). The reaction mixture was stirred at room temperature for 2 h. The solvent was removed in vacuo to afford **S1** (quantitative yield) as a red solid. Resulting product was used for next step without further purification; 1H NMR (400 MHz, $DMSO-d_6$) δ 8.51 (d, J = 8.2 Hz, 2H),

⁴Chem. Commun. 2014, 50, 9557–9560.

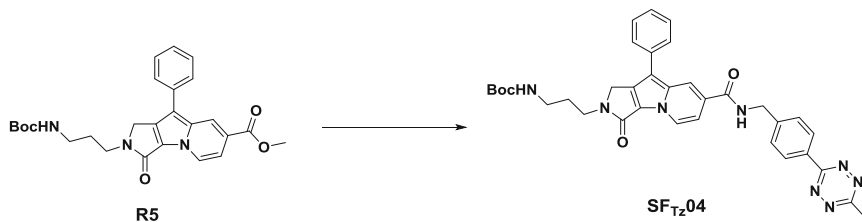
8.41 (br s, 3H, NH), 7.74 (d, $J = 8.2$ Hz, 2H), 4.20 (br s, 2H), 3.01 (s, 3H); ^{13}C NMR (100 MHz, DMSO- d_6) δ 167.3, 163.0, 138.4, 132.0, 129.8, 127.6, 42.0, 20.9; LRMS (ESI) m/z calcd for $\text{C}_{10}\text{H}_{12}\text{N}_5$ $[\text{M}]^+$: 202.1, found: 202.1.



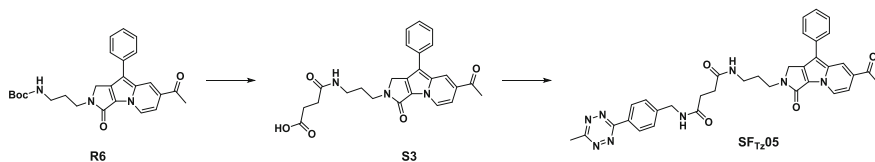
Compound S2: A suspension of **R1**¹ (114 mg, 308 μmol), methyl 4-iodobenzoate (242 mg, 924 μmol), palladium acetate (13.8 mg, 61.6 μmol), and silver acetate (154 mg, 924 μmol) in DMF (3 mL) was stirred at 80 °C for overnight. The reaction mixture was then filtered through Celite and concentrated under reduced pressure. The crude product was purified by silica-gel flash column chromatography (toluene:EtOAc = 2:1–1:2) to afford **S2** (56.1 mg, 36.0% yield) as a yellow solid; ^1H NMR (400 MHz, CDCl_3) δ 8.60 (d, $J = 7.0$ Hz, 1H), 8.43 (s, 1H), 8.17 (d, $J = 8.2$ Hz, 2H), 7.62 (d, $J = 8.2$ Hz, 2H), 7.33 (d, $J = 7.0$ Hz, 1H), 5.32 (br s, 1H, NH), 4.55 (s, 2H), 3.97 (s, 3H), 3.70 (t, $J = 6.0$ Hz, 2H), 3.18 (m, 2H), 2.63 (s, 3H), 1.87–1.84 (m, 2H), 1.43 (s, 9H); ^{13}C NMR (100 MHz, CDCl_3) δ 195.5, 166.8, 161.8, 156.2, 138.4, 135.3, 135.1, 130.8, 130.0, 128.4, 127.2, 125.0, 123.3, 121.0, 113.0, 110.2, 79.3, 52.4, 46.8, 40.3, 37.4, 28.9, 28.6, 26.3; LRMS (ESI) m/z calcd for $\text{C}_{28}\text{H}_{32}\text{N}_3\text{O}_6$ $[\text{M}+\text{H}]^+$: 506.2, found: 506.2.

Compound SF_{Tz}03: A reaction mixture of **S2** (43.3 mg, 85.7 μmol), and lithium hydroxide monohydrate (10.8 mg, 257 μmol) in tetrahydrofuran (0.6 mL), methanol (0.3 mL), and water (0.3 mL) was stirred at room temperature for 3 h. The reaction mixture was then washed with saturated NH_4Cl aqueous solution, extracted with CH_2Cl_2 , dried over anhydrous Na_2SO_4 , and concentrated. The resulting solid, *N*-[(dimethylamino)-1H-1,2,3-triazolo-[4,5-*b*]pyridin-1-ylmethylene]-*N*-methyl-4 *N*-oxide (HATU, 65.1 mg, 171 μmol), and *N,N*-diisopropylethylamine (DIPEA, 74.6 μL , 428 μmol) were dissolved in DMF (1.2 mL). After the solution was stirred for 0.5 h at room temperature, **S1** (40.5 mg, 128 μmol) was added to the solution and stirred at room temperature for additional 2 h. The crude product was purified by silica-gel flash column chromatography (CH_2Cl_2 :MeOH = 20:1) followed by washing with EtOAc for several times, and dried *in vacuo* to afford **SF_{Tz}03** (21 mg, 36% yield) as a red solid; ^1H NMR (500 MHz, CD_2Cl_2) δ 8.59–8.57 (m, 3H), 8.44 (s, 1H), 7.98 (d, $J = 8.3$ Hz, 2H), 7.68 (d, $J = 8.3$ Hz, 2H), 7.63 (d, $J = 8.3$ Hz, 2H), 7.32 (dd, $J = 7.3, 1.5$ Hz, 1H), 6.75 (t, $J = 5.8$ Hz, 1H, NH), 5.36 (br s, 1H, NH), 4.80 (d, $J = 5.9$ Hz, 2H), 4.54 (s, 2H), 3.67 (t, $J = 6.4$ Hz, 2H), 3.10 (m, 2H), 3.07 (s, 3H), 2.60 (s, 3H), 1.81 (quin, $J = 6.3$ Hz, 2H), 1.41 (s, 9H); ^{13}C NMR (100 MHz, CDCl_3 :MeOD- d_4 = 10:1, v/v) δ 196.1, 167.6, 167.3, 163.9, 161.9,

156.6, 143.5, 137.0, 135.4, 135.1, 132.2, 130.8, 129.7, 128.5, 128.34, 128.26, 127.4, 124.9, 122.9, 120.9, 113.1, 110.2, 79.4, 46.8, 43.7, 40.4, 37.5, 28.7, 28.4, 26.3, 21.1; HRMS (ESI) m/z calcd for $C_{37}H_{38}N_8NaO_5$ $[M+Na]^+$: 697.2857, found: 697.2860.



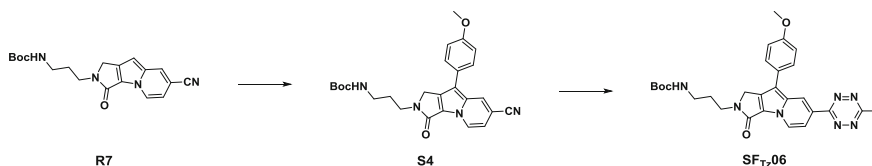
Compound SF_{Tz}04: A reaction mixture of **R5**¹ (39.2 mg, 84.6 μ mol), lithium hydroxide monohydrate (10.6 mg, 254 μ mol), tetrahydrofuran (0.6 mL), methanol (0.3 mL), and water (0.3 mL) was stirred at room temperature for 1 h. The reaction mixture was then washed with saturated NH_4Cl aqueous solution, extracted with EtOAc, dried over anhydrous Na_2SO_4 , and concentrated. The resulting solid, **S1** (40.0 mg, 127 μ mol), HATU (64.3 mg, 169 μ mol), and DIPEA (73.7 μ L, 423 μ mol) were dissolved in DMF (0.9 mL). The mixture was stirred at room temperature for 2 h. After the solvent was removed under reduced pressure, the crude product was purified by silica-gel flash column chromatography (CH_2Cl_2 :MeOH = 20:1) to afford **SF_{Tz}04** (37.6 mg, 70.2% yield) as a pink solid; ¹H NMR (500 MHz, CD_2Cl_2) δ 8.57 (d, J = 7.3 Hz, 1H), 8.54 (d, J = 8.3 Hz, 2H), 8.34 (s, 1H), 7.60–7.56 (m, 4H), 7.48 (t, J = 7.8 Hz, 2H), 7.31 (t, J = 7.3 Hz, 2H), 7.12 (dd, J = 7.1, 1.7 Hz, 1H), 6.79 (t, J = 5.9 Hz, 1H, NH), 5.41 (br s, 1H, NH), 4.76 (d, J = 5.9 Hz, 2H), 4.49 (s, 2H), 3.64 (t, J = 6.4 Hz, 2H), 3.13–3.10 (m, 2H), 3.06 (s, 3H), 1.79 (quin, J = 6.4 Hz, 2H), 1.40 (s, 9H); ¹³C NMR (100 MHz, $CDCl_3$:MeOD- d_4 = 10:1, v/v) δ 167.3, 166.4, 163.9, 162.4, 156.6, 143.6, 135.34, 135.29, 133.5, 130.8, 129.2, 128.5, 128.2, 127.5, 126.8, 126.3, 124.7, 121.5, 119.4, 112.7, 109.7, 79.4, 46.8, 43.8, 40.4, 37.5, 28.7, 28.4, 21.1; HRMS (ESI) m/z calcd for $C_{35}H_{36}N_8NaO_4$ $[M+Na]^+$: 655.2752, found: 655.2755.



Compound S3: A suspension of **R6**¹ (42 mg, 94 μ mol) and 12 N HCl (100 μ L, 1.2 mmol) in CH_2Cl_2 (1 mL) was stirred at room temperature for 2 h, and solvent was then concentrated under reduced pressure. The resulting crude solid, succinic anhydride (14.1 mg, 141 μ mol), and triethylamine (65.4 μ L, 469 μ mol) were dissolved in CH_2Cl_2 (1 mL). The mixture was stirred at room temperature for overnight. The crude mixture was then directly purified by silica-gel flash column chromatography (CH_2Cl_2 :MeOH = 10:1 with 1% acetic acid) to afford **S3** (36 mg,

86% yield) as a yellow solid; ^1H NMR (500 MHz, $\text{DMSO-}d_6$) δ 8.55 (d, $J = 7.3$ Hz, 1H), 8.47 (s, 1H), 7.90 (t, $J = 5.3$ Hz, 1H, NH), 7.73 (d, $J = 7.3$ Hz, 2H), 7.54 (t, $J = 7.6$ Hz, 2H), 7.36 (t, $J = 7.2$ Hz, 1H), 7.31 (d, $J = 7.3$ Hz, 1H), 4.70 (s, 2H), 3.52 (t, $J = 7.1$ Hz, 2H), 3.11–3.08 (m, 2H), 2.64 (s, 3H), 2.42 (t, $J = 7.1$ Hz, 2H), 2.31 (t, $J = 7.1$ Hz, 3H), 1.77 (quin, $J = 6.8$ Hz, 2H); ^{13}C NMR (100 MHz, $\text{DMSO-}d_6$) δ 195.7, 174.0, 171.0, 160.3, 135.3, 133.5, 133.2, 129.3, 128.7, 127.3, 126.7, 124.2, 122.6, 121.3, 113.0, 109.5, 46.2, 40.3, 36.3, 30.1, 29.3, 28.2, 26.2; LRMS (ESI) m/z calcd for $\text{C}_{25}\text{H}_{26}\text{N}_3\text{O}_5$ $[\text{M}+\text{H}]^+$: 448.2, found: 448.1.

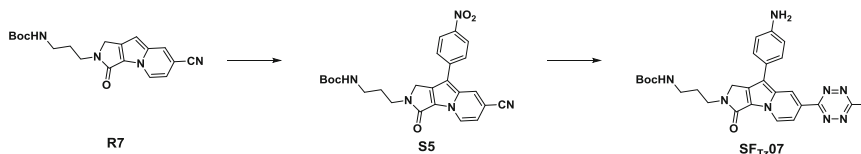
Compound SF_{Tz}05: A suspension of **S3** (33 mg, 74 μmol), **S1** (35 mg, 110 μmol), HATU (56 mg, 150 μmol), and DIPEA (64 μL , 370 μmol) in DMF (1 mL) was stirred at room temperature for 2 h. The crude reaction mixture was directly purified by silica-gel flash column chromatography ($\text{CH}_2\text{Cl}_2:\text{MeOH} = 20:1$) to afford **SF_{Tz}05** (23 mg, 49% yield) as an orange solid; ^1H NMR (500 MHz, pyridine- d_5) δ 9.41 (t, $J = 5.9$ Hz, 1H, NH), 8.66 (d, $J = 7.3$ Hz, 1H), 8.60 (d, $J = 7.8$ Hz, 2H), 8.57 (s, 1H), 7.77 (d, $J = 7.3$ Hz, 2H), 7.67 (d, $J = 8.3$ Hz, 2H), 7.60–7.57 (m, 2H), 7.44–7.40 (m, 2H), 4.78 (d, $J = 5.9$ Hz, 2H), 4.39 (s, 2H), 3.79 (t, $J = 7.0$ Hz, 2H), 3.63–3.60 (m, 2H), 3.05–3.03 (m, 2H), 2.99–2.95 (m, 5H), 2.61 (s, 3H), 2.06 (quin, $J = 6.8$ Hz, 2H); ^{13}C NMR (100 MHz, $\text{CDCl}_3:\text{MeOD-}d_4 = 10:1$, v/v) δ 196.3, 173.1, 173.0, 167.2, 163.9, 162.2, 143.5, 135.2, 134.9, 133.3, 130.6, 129.43, 129.38, 128.3, 128.1, 127.6, 127.1, 124.7, 122.5, 121.5, 114.4, 109.8, 46.8, 43.1, 40.5, 36.4, 31.73, 31.66, 28.3, 26.1, 21.1; HRMS (ESI) m/z calcd for $\text{C}_{35}\text{H}_{34}\text{N}_8\text{NaO}_4$ $[\text{M}+\text{Na}]^+$: 653.2595, found: 653.2599.



Compound S4: A suspension of **R7**¹ (181.5 mg, 512 μmol), 4-iodoanisole (360 mg, 1.54 mmol), palladium acetate (23 mg, 102 μmol), and silver acetate (256 mg, 1.54 mmol) in DMF (5 mL) was stirred at 80 $^{\circ}\text{C}$ for 4 h. The crude reaction mixture was then filtered through Celite and concentrated under reduced pressure. The crude product was purified by silica-gel flash column chromatography (toluene:EtOAc = 2:1) to afford **S4** (80 mg, 34% yield) as a solid; ^1H NMR (400 MHz, CDCl_3) δ 8.55 (d, $J = 7.4$ Hz, 1H), 8.09 (s, 1H), 7.41 (d, $J = 8.6$ Hz, 2H), 7.04 (d, $J = 8.6$ Hz, 2H), 6.77 (d, $J = 7.0$ Hz, 1H), 5.29 (br s, 1H, NH), 4.49 (s, 2H), 3.88 (s, 3H), 3.68 (t, $J = 6.3$ Hz, 2H), 3.17 (q, $J = 6.0$ Hz, 2H), 1.84 (quin, $J = 6.3$ Hz, 2H), 1.42 (s, 9H); ^{13}C NMR (100 MHz, CDCl_3) δ 161.6, 159.0, 156.1, 134.7, 133.5, 128.7, 125.8, 125.3, 125.0, 123.3, 118.5, 114.9, 113.6, 111.1, 102.7, 79.1, 55.4, 46.5, 40.2, 37.3, 28.7, 28.4; LRMS (ESI) m/z calcd for $\text{C}_{26}\text{H}_{29}\text{N}_4\text{O}_4$ $[\text{M}+\text{H}]^+$: 461.2, found: 461.1.

Compound SF_{Tz}06: A reaction mixture of **S4** (33.4 mg, 72.5 μmol), acetonitrile (190 μL , 3.63 mmol), zinc trifluoromethanesulfonate (13.2 mg, 36.3 μmol), and

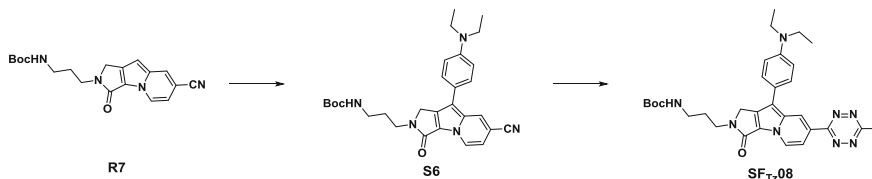
hydrazine monohydrate (352 μL , 7.25 mmol) in microwave reaction vial (10 mL) was irradiated under microwaves at 80 $^{\circ}\text{C}$ (100 W) with magnetic stirring for 0.5 h. After cooled down to room temperature, sodium nitrite (250 mg, 3.63 mmol) in 1 ml of water was added followed by slow addition of 1 N HCl until pH value reached at 3 (caution! toxic nitrogen oxide gas evolved!). Then, the resulting residue was washed with brine, extracted with CH_2Cl_2 , and dried over anhydrous Na_2SO_4 . After concentrated under reduced pressure, the crude product was purified by normal-phase preparative HPLC using a gradient of methanol (1–10%) in CH_2Cl_2 with a flow rate of 5 ml/min to afford **SF_{Tz}06** (7.0 mg, 18% yield) as a red solid; ^1H NMR (400 MHz, CDCl_3) δ 9.12 (s, 1H), 8.69 (d, $J = 7.4$ Hz, 1H), 7.86 (dd, $J = 7.2, 1.2$ Hz, 1H), 7.53 (d, $J = 8.6$ Hz, 2H), 7.05 (d, $J = 8.6$ Hz, 2H), 5.39 (br s, 1 H, NH), 4.51 (s, 2H), 3.89 (s, 3H), 3.70 (t, $J = 6.3$ Hz, 2H), 3.19 (q, $J = 5.9$ Hz, 2H), 3.09 (s, 3H), 1.85 (quin, $J = 6.3$ Hz, 2H), 1.43 (s, 9H); ^{13}C NMR (100 MHz, CDCl_3) δ 166.8, 163.1, 162.0, 158.6, 156.1, 135.3, 134.6, 128.7, 125.9, 125.4, 123.6, 122.5, 119.8, 114.8, 113.6, 108.9, 79.1, 55.4, 46.6, 40.1, 37.2, 28.7, 28.4, 21.2; HRMS (ESI) m/z calcd for $\text{C}_{28}\text{H}_{31}\text{N}_7\text{NaO}_4$ [$\text{M}+\text{Na}$] $^+$: 552.2330, found: 552.2330.



Compound S5: A suspension of **R7**¹ (126 mg, 356 μmol), 1-iodo-4-nitro-benzene (266 mg, 1.07 mmol), palladium acetate (16.0 mg, 71.1 μmol), and silver acetate (178 mg, 1.07 mmol) in DMF (3.6 mL) was stirred at 80 $^{\circ}\text{C}$ for 2 h. The reaction mixture was then filtered through a short bed of silica gel with EtOAc and concentrated under reduced pressure. The crude product was purified by silica-gel flash column chromatography (toluene:EtOAc = 1:1) to afford **S5** (134 mg, 283 μmol , 79.5% yield) as a yellow solid; ^1H NMR (400 MHz, CDCl_3) δ 8.68 (d, $J = 7.4$ Hz, 1H), 8.37 (d, $J = 8.6$ Hz, 2H), 8.21 (s, 1H), 7.67 (d, $J = 9.0$ Hz, 2H), 6.94 (d, $J = 7.4$ Hz, 1H), 5.18 (br s, 1H, NH), 4.59 (s, 2H), 3.71 (t, $J = 6.5$ Hz, 2H), 3.19 (q, $J = 6.1$ Hz, 2H), 1.88 (quin, $J = 6.3$ Hz, 2H), 1.43 (s, 9H); ^{13}C NMR (100 MHz, CDCl_3) δ 161.1, 156.0, 146.3, 139.6, 135.7, 134.1, 127.6, 125.9, 125.0, 124.8, 124.3, 117.8, 112.2, 111.2, 105.1, 79.3, 46.6, 40.3, 37.4, 28.8, 28.4; LRMS (ESI) m/z calcd for $\text{C}_{25}\text{H}_{26}\text{N}_5\text{O}_5$ [$\text{M}+\text{H}$] $^+$: 476.2, found: 476.2.

Compound SF_{Tz}07: A reaction mixture of **S5** (40 mg, 84 μmol), hydrazine monohydrate (409 μL , 8.41 mmol), acetonitrile (220 μL , 4.21 mmol), and zinc trifluoromethanesulfonate (15.3 mg, 42.1 μmol) in a microwave reaction vial (10 ml) was irradiated under microwaves at 80 $^{\circ}\text{C}$ (100 W) with magnetic stirring for 1.5 h. After cooled down to room temperature, sodium nitrite (290 mg, 4.21 mmol) in 0.5 mL of water was added followed by slow addition of 1 N HCl until pH value reached 3 (caution! toxic nitrogen oxide gas evolved!). Then, the resulting residue was washed with saturated NaHCO_3 aqueous solution, extracted

with CH_2Cl_2 , dried over anhydrous Na_2SO_4 , and concentrated. The crude product was purified by normal-phase preparative HPLC using a linear gradient of methanol (0.1–10%) in CH_2Cl_2 with a flow rate of 5 ml/min to afford **SF_{Tz}07** (2 mg, 5% yield) as a reddish brown solid; ^1H NMR (400 MHz, CDCl_3) δ 9.13 (s, 1H), 8.67 (d, $J = 7.4$ Hz, 1H), 7.84 (dd, $J = 7.4, 1.6$ Hz, 1H), 7.41 (d, $J = 8.2$ Hz, 2H), 6.83 (d, $J = 8.6$ Hz, 2H), 5.39 (br s, 1H, NH), 4.50 (s, 2H), 3.81 (br s, 2H, NH_2), 3.70 (t, $J = 6.3$ Hz, 2H), 3.19 (q, $J = 6.2$ Hz, 2H), 3.09 (s, 3H), 1.84 (quin, $J = 6.2$ Hz, 2H), 1.43 (s, 9H); ^{13}C NMR (150 MHz, CDCl_3) δ 166.7, 163.2, 162.0, 156.1, 145.5, 135.2, 134.4, 128.7, 125.4, 123.6, 123.3, 122.4, 120.1, 115.8, 114.2, 108.8, 79.1, 46.6, 40.1, 37.3, 28.7, 28.4, 21.2; HRMS (ESI) m/z calcd for $\text{C}_{27}\text{H}_{30}\text{N}_8\text{NaO}_3$ [$\text{M} + \text{Na}$] $^+$: 537.2333, found: 537.2335.

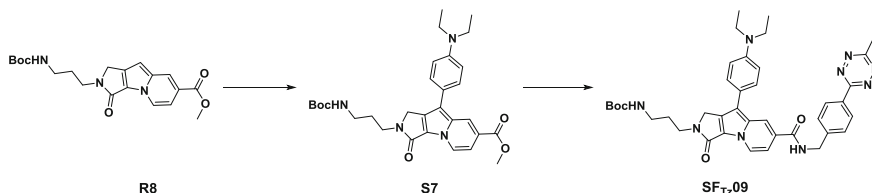


Compound S6: **R7**¹ (368.4 mg, 895 μmol), *N,N*-diethyl-4-iodoaniline⁵ (739 mg, 2.69 mmol), palladium acetate (40.2 mg, 179 μmol), and silver acetate (488 mg, 2.69 mmol) were dissolved in DMF (9 mL). The mixture was stirred at 80 °C for overnight. The reaction mixture was filtered through a short bed of silica gel with EtOAc and concentrated under reduced pressure. The crude reaction mixture was purified by silica-gel flash column chromatography (toluene:EtOAc = 10:1) to afford **S6** (147.5 mg, 29.5% yield) as a reddish brown solid; ^1H NMR (400 MHz, CDCl_3) δ 8.51 (d, $J = 7.4$ Hz, 1H), 8.12 (s, 1H), 7.34 (d, $J = 8.6$ Hz, 2H), 6.78 (d, $J = 9.0$ Hz, 2H), 6.72 (dd, $J = 7.0, 1.2$ Hz, 1H), 5.34 (br s, 1H, NH), 4.48 (s, 2H), 3.68 (t, $J = 6.2$ Hz, 2H), 3.42 (q, $J = 7.0$ Hz, 4H), 3.17 (q, $J = 6.0$ Hz, 2H), 1.83 (quin, $J = 6.3$ Hz, 2H), 1.43 (s, 9H), 1.22 (t, $J = 7.0$ Hz, 6H); ^{13}C NMR (100 MHz, CDCl_3) δ 161.8, 156.2, 147.1, 134.3, 133.3, 128.7, 126.4, 125.2, 123.2, 119.2, 118.9, 114.7, 112.3, 110.9, 101.9, 79.2, 46.7, 44.5, 40.3, 37.4, 28.8, 28.5, 12.7; LRMS (ESI) m/z calcd for $\text{C}_{29}\text{H}_{36}\text{N}_5\text{O}_3$ [$\text{M} + \text{H}$] $^+$: 502.3, found: 502.2.

Compound SF_{Tz}08: A reaction mixture of **S6** (60.2 mg, 120 μmol), acetonitrile (313 μL , 6.00 mmol), zinc trifluoromethanesulfonate (21.8 mg, 60.0 μmol), and hydrazine monohydrate (583 μL , 12.0 mmol) in microwave reaction vial (10 mL) was irradiated under microwaves at 100 °C (40 W) with magnetic stirring for 1.5 h. After cooled down to room temperature, NaNO_2 was added followed by slow addition of 1 N HCl until pH value reached at 3 (caution! toxic nitrogen oxide gas evolved!). Then, the resulting residue was washed with saturated NaHCO_3 aqueous solution, extracted with CH_2Cl_2 , dried over anhydrous Na_2SO_4 , and concentrated. The crude product was purified by silica-gel flash column chromatography

⁵Helv. Chim. Acta 2010, 93, 587–594.

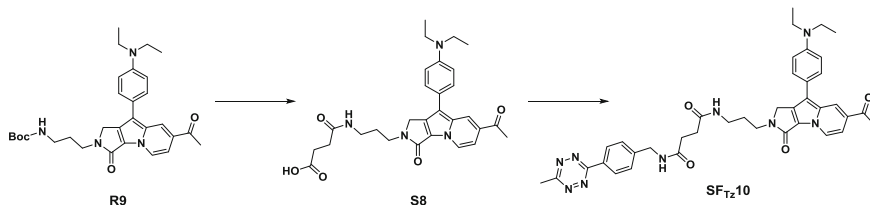
(CH₂Cl₂:EtOAc = 8:1) to afford **SF_{Tz}08** (11.8 mg, 17.2% yield) as a reddish brown solid; ¹H NMR (400 MHz, CD₂Cl₂) δ 9.15 (s, 1H), 8.65 (d, *J* = 7.0 Hz, 1H), 7.81 (d, *J* = 7.4 Hz, 1H), 7.48 (d, *J* = 8.6 Hz, 2H), 6.83 (d, *J* = 8.2 Hz, 2H), 5.46 (br s, 1H, NH), 4.51 (s, 2H), 3.67 (t, *J* = 6.3 Hz, 2H), 3.43 (q, *J* = 6.8 Hz, 4H), 3.14 (q, *J* = 6.0 Hz, 2H), 3.05 (s, 3H), 1.81 (quin, *J* = 6.3 Hz, 2H), 1.42 (s, 9H), 1.21 (t, *J* = 7.0 Hz, 6H); ¹³C NMR (100 MHz, CDCl₃) δ 166.6, 163.2, 162.1, 156.1, 146.7, 135.0, 134.1, 128.6, 125.3, 122.9, 122.4, 120.4, 120.1, 114.6, 112.2, 108.6, 79.0, 46.7, 44.5, 40.0, 37.2, 28.7, 28.4, 21.2, 12.7; HRMS (ESI) *m/z* calcd for C₃₁H₃₈N₈NaO₃ [M+Na]⁺: 593.2959, found: 593.2960.



Compound S7: A suspension of **R8**¹ (129 mg, 333 μmol), *N,N*-diethyl-4-iodo-aniline⁴ (275 mg, 999 μmol), palladium acetate (15.0 mg, 66.6 μmol), and silver acetate (167 mg, 999 μmol) in DMF (3.5 mL) was stirred at 80 °C for overnight. The reaction mixture was then filtered through a short bed of silica gel with EtOAc and concentrated under reduced pressure. The crude product was purified by silica-gel flash column chromatography (toluene:EtOAc = 1:1) to afford **S7** (37 mg, 21% yield) as a reddish solid; ¹H NMR (400 MHz, CDCl₃) δ 8.54 (s, 1H), 8.51 (d, *J* = 7.4 Hz, 1H), 7.41 (d, *J* = 8.6 Hz, 2H), 7.23 (dd, *J* = 7.0, 1.6 Hz, 1H), 6.79 (d, *J* = 8.6 Hz, 2H), 5.41 (br s, 1H, NH), 4.47 (s, 2H), 3.93 (s, 3H), 3.68 (t, *J* = 6.3 Hz, 2H), 3.42 (q, *J* = 7.0 Hz, 4H), 3.17 (q, *J* = 5.9 Hz, 2H), 1.82 (quin, *J* = 6.2 Hz, 2H), 1.42 (s, 9H), 1.22 (t, *J* = 7.0 Hz, 6H); ¹³C NMR (100 MHz, CDCl₃) δ 166.1, 162.1, 156.1, 146.7, 134.4, 133.9, 128.6, 124.2, 122.7, 122.1, 121.1, 120.1, 114.2, 112.2, 110.3, 79.0, 52.3, 46.6, 44.4, 40.0, 37.2, 28.7, 28.4, 12.7; LRMS (ESI) *m/z* calcd for C₃₀H₃₉N₄O₅ [M+H]⁺: 535.3, found: 535.2.

Compound SF_{Tz}09: A reaction mixture of **S7** (26.7 mg, 49.9 μmol), lithium hydroxide monohydrate (6.3 mg, 150 μmol), tetrahydrofuran (THF, 300 μL), MeOH (150 μL), and H₂O (150 μL) was stirred at room temperature for 2 h. The mixture was then washed with saturated NH₄Cl aqueous solution, extracted with EtOAc, dried over anhydrous Na₂SO₄, and concentrated. The resulting solid, **S1** (23.6 mg, 74.9 μmol), HATU (38.0 mg, 100 μmol), and DIPEA (43.5 μL, 250 μmol) were dissolved in DMF (0.5 mL). The mixture was stirred at room temperature for 2 h. After the solvent was removed under reduced pressure, the crude product was purified by silica-gel flash column chromatography (CH₂Cl₂:MeOH = 20:1) to afford **SF_{Tz}09** (32.9 mg, 93.6% yield) as a brown solid; ¹H NMR (400 MHz, CDCl₃) δ 8.54 (d, *J* = 8.2 Hz, 2H), 8.48 (d, *J* = 7.4 Hz, 1H), 8.31 (s, 1H), 7.56 (d, *J* = 8.2 Hz, 2H), 7.36 (d, *J* = 9.0 Hz, 2H), 7.04 (d, *J* = 7.0 Hz, 1H), 6.80–6.74 (m, 3H), 5.39 (br s., 1H, NH), 4.77 (d, *J* = 5.9 Hz, 2H), 4.44 (s, 2H), 3.65

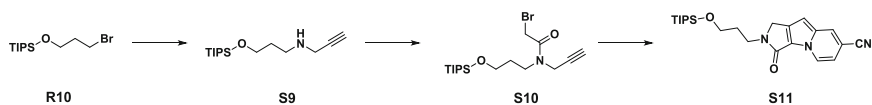
(t, $J = 6.1$ Hz, 2H), 3.39 (q, $J = 7.0$ Hz, 4H), 3.15 (d, $J = 5.9$ Hz, 2H), 3.08 (s, 3H), 1.80 (quin, $J = 6.3$ Hz, 2H), 1.42 (s, 9H), 1.19 (t, $J = 6.8$ Hz, 6H); ^{13}C NMR (100 MHz, $\text{CDCl}_3:\text{MeOD}-d_4 = 10:1$, v/v) δ 167.3, 166.7, 164.0, 162.6, 156.7, 146.7, 143.7, 134.8, 134.6, 130.7, 128.6, 128.5, 128.2, 125.2, 124.5, 121.1, 120.3, 119.9, 113.5, 112.5, 109.3, 79.4, 46.9, 44.5, 43.8, 40.4, 37.5, 28.7, 28.4, 21.1, 12.6; HRMS (ESI) m/z calcd for $\text{C}_{39}\text{H}_{46}\text{N}_9\text{O}_4$ $[\text{M}+\text{H}]^+$: 704.3667, found: 704.3669.



Compound S8: A suspension of **R9**¹ (45 mg, 87 μmol), and TFA (200 μL , 2.61 mmol) in CH_2Cl_2 (0.9 mL) was stirred at room temperature for 3 h. The resulting residue was then washed with saturated NaHCO_3 aqueous solution, extracted with CH_2Cl_2 , dried over anhydrous Na_2SO_4 , and concentrated. The resulting solid, succinic anhydride (13.0 mg, 130 μmol), and triethylamine (60.5 μL , 433 μmol) were dissolved in CH_2Cl_2 (900 μL). The mixture was stirred at room temperature for 1 h. The crude reaction mixture was directly purified by silica-gel flash column chromatography ($\text{CH}_2\text{Cl}_2:\text{MeOH} = 10:1$ with 1% acetic acid) to afford **S8** (35.3 mg, 78.5% yield) as a red solid; ^1H NMR (400 MHz, CDCl_3) δ 8.49 (d, $J = 7.0$ Hz, 1H), 8.40 (s, 1H), 7.43 (br s, 2H), 7.25 (d, $J = 6.7$ Hz, 1H), 6.84 (br s, 2H), 4.51 (s, 2H), 3.66 (t, $J = 6.5$ Hz, 2H), 3.45 (d, $J = 5.9$ Hz, 4H), 3.27 (t, $J = 6.1$ Hz, 2H), 2.68–2.65 (m, 2H), 2.61 (s, 3H), 2.56–2.52 (m, 2H), 1.86 (quin, $J = 6.2$ Hz, 2H), 1.24 (t, $J = 7.0$ Hz, 6H); ^{13}C NMR (100 MHz, $\text{CDCl}_3:\text{MeOD}-d_4 = 10:1$, v/v) δ 196.3, 175.3, 173.0, 162.5, 147.1, 134.5, 129.1, 128.8, 128.3, 125.4, 124.6, 122.3, 119.9, 115.4, 112.5, 109.4, 46.9, 44.6, 40.4, 36.2, 31.1, 29.9, 28.2, 26.1, 12.5; LRMS (ESI) m/z calcd for $\text{C}_{29}\text{H}_{35}\text{N}_4\text{O}_5$ $[\text{M}+\text{H}]^+$: 519.3, found: 519.1.

Compound SF_{Tz}10: A suspension of **S8** (26 mg, 50 μmol), **S1** (23.7 mg, 75.2 μmol), HATU (38.1 mg, 100 μmol), and DIPEA (43.7 μL , 251 μmol) in DMF (500 μL) was stirred at room temperature for 2 h. Solvent was then removed under reduced pressure and the crude product was purified by silica-gel flash column chromatography ($\text{CH}_2\text{Cl}_2:\text{MeOH} = 20:1$) to afford **SF_{Tz}10** (26 mg, 74% yield) as a red solid; ^1H NMR (400 MHz, CDCl_3) δ 8.45–8.37 (m, 2H), 8.37 (s, 1H), 7.45 (d, $J = 8.2$ Hz, 2H), 7.36 (d, $J = 8.6$ Hz, 2H), 7.24 (d, $J = 7.0$ Hz, 1H), 7.03–6.99 (m, 2H), 6.79 (d, $J = 8.6$ Hz, 2H), 4.55 (d, $J = 5.9$ Hz, 2H), 4.44 (s, 2H), 3.64 (t, $J = 6.1$ Hz, 2H), 3.43 (q, $J = 7.0$ Hz, 4H), 3.29 (q, $J = 5.6$ Hz, 2H), 3.04 (s, 3H), 2.67 (m, 4H), 2.61 (s, 3H), 1.84–1.78 (m, 2H), 1.23 (t, $J = 7.0$ Hz, 6H); ^{13}C NMR (100 MHz, CDCl_3) δ 195.5, 172.4, 172.3, 167.1, 163.7, 162.2, 146.7, 143.4, 134.1, 133.9, 130.6, 128.54, 128.46, 128.2, 127.9, 124.3, 122.04, 121.99, 119.8, 115.0, 112.2, 109.2, 46.7, 44.4, 43.2, 39.9, 35.8, 32.0, 28.3, 26.0, 21.1, 12.7; HRMS

(ESI) m/z calcd for $C_{39}H_{43}N_9NaO_4$ $[M+Na]^+$: 724.3330, found: 724.3333.



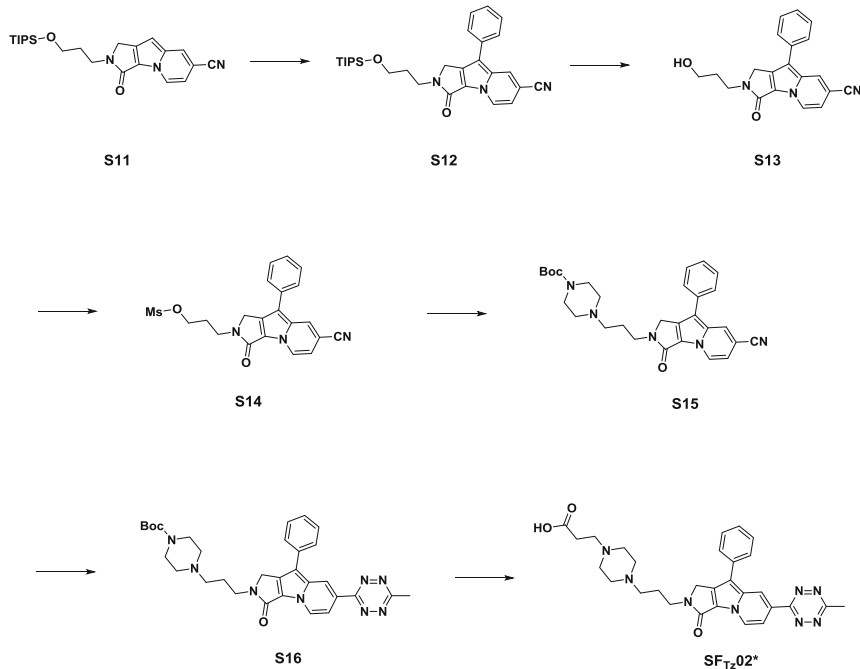
Compound S9: A suspension of **R10**⁶ (11.7 g, 39.5 mmol), propargylamine (12.7 mL, 198 mmol), and potassium carbonate (10.9 g, 79.0 mmol) in acetonitrile (100 mL) was stirred at 80 °C for overnight. Solvent was then removed under reduced pressure and the resulting residue was washed with saturated $NaHCO_3$ aqueous solution, extracted with EtOAc, dried over anhydrous Na_2SO_4 , and concentrated. The crude product was then purified by silica-gel flash column chromatography (hexane:EtOAc = 2:1–1:1) to afford **S9** (8.47 g, 79.5% yield) as a yellow oil; 1H NMR (400 MHz, $CDCl_3$) δ 3.79 (t, J = 6.1 Hz, 2H), 3.42 (d, J = 2.3 Hz, 2H), 2.82 (t, J = 6.8 Hz, 2H), 2.19 (t, J = 2.3 Hz, 1H), 1.74 (quin, J = 6.4 Hz, 2H), 1.12–1.03 (m, 21H); ^{13}C NMR (100 MHz, $CDCl_3$) δ 82.5, 71.2, 62.3, 46.4, 38.4, 32.9, 18.2, 12.1; LRMS (ESI) m/z calcd for $C_{15}H_{32}NO$ $[M+H]^+$: 270.2, found: 270.2.

Compound S10: To a solution of bromoacetyl bromide (5.5 mL, 62 mmol) and dry triethylamine (13 mL, 94 mmol) in dry CH_2Cl_2 (200 mL) was slowly added a dry CH_2Cl_2 (100 mL) containing **S9** (8.4 g, 31 mmol) for 5 min at -78 °C under argon atmosphere and the reaction mixture was stirred at -78 °C for 1 h. The crude mixture was then washed with saturated brine, extracted with CH_2Cl_2 , dried over anhydrous Na_2SO_4 , and concentrated. The crude product was purified by silica-gel flash column chromatography (hexane:EtOAc = 5:1–3:1) to afford **S10** (10.3 g, 85% yield) as a yellow oil; 1H NMR (70:30 mixture of rotamers, * denote minor rotamer peaks, 500 MHz, $CDCl_3$) δ 4.22 (d, J = 2.4 Hz, 2H), 4.20* (d, J = 2.4 Hz, 2H), 4.00 (s, 2H), 3.94* (s, 2H), 3.76–3.72 (m, 2H), 3.67 (t, J = 7.1 Hz, 2H), 3.58* (t, J = 7.1 Hz, 2H), 2.33* (t, J = 2.4 Hz, 1H), 2.22 (t, J = 2.4 Hz, 1H), 1.89–1.81 (m, 2 H), 1.14–1.05 (m, 21 H); ^{13}C NMR (125 MHz, $CDCl_3$) δ 166.9, 78.5, 73.2*, 72.3, 60.6*, 59.6, 45.1, 44.7*, 38.8*, 35.1, 31.5, 30.6*, 26.4*, 26.1, 18.2, 12.1*, 12.0; LRMS (ESI) m/z calcd for $C_{17}H_{33}BrNO_2Si$ $[M+H]^+$: 390.2, found: 390.2.

Compound S11: A suspension of **S10** (3.41 g, 8.73 mmol) and 4-cyanopyridine (1.09 g, 10.5 mmol) in acetonitrile (45 mL) was stirred at 80 °C for overnight. The reaction mixture was then cooled down to room temperature, copper iodide (1.66 g, 8.73 mmol) and potassium carbonate (3.62 g, 26.2 mmol) were added, and reaction mixture was stirred at room temperature for 4 h. The solvent was removed under reduced pressure, and the mixture was filtered through a short bed of silica gel with EtOAc. After concentration, the crude product was purified by silica-gel flash column chromatography (hexane:EtOAc = 4:1) to afford **S11** (700 mg, 19.5% yield) as a white solid; 1H NMR (500 MHz, $DMSO-d_6$) δ 8.50 (d, J = 7.3 Hz, 1H),

⁶*J. Am. Chem. Soc.* **2014**, *136*, 12762–12770.

8.33 (s, 1H), 6.98 (dd, $J = 7.1, 1.7$ Hz, 1H), 6.79 (s, 1 H), 4.44 (s, 2H), 3.72 (t, $J = 6.0$ Hz, 2H), 3.57 (t, $J = 7.3$ Hz, 2H), 1.82 (quin, $J = 6.8$ Hz, 2H), 1.04–0.97 (m, 21 H); ^{13}C NMR (125 MHz, DMSO- d_6) δ 160.1, 137.2, 136.5, 126.9, 124.6, 123.4, 118.5, 111.0, 101.0, 98.5, 60.8, 46.1, 39.7, 31.5, 17.8, 11.4; LRMS (ESI) m/z calcd for $\text{C}_{23}\text{H}_{34}\text{N}_3\text{O}_2\text{Si}$ $[\text{M}+\text{H}]^+$: 412.2, found: 412.2.



Compound S12: A suspension of **S11** (300 mg, 729 μmol), iodobenzene (245 μL , 2.19 mmol), palladium acetate (32.7 mg, 146 μmol), and silver acetate (365 mg, 2.19 mmol) in DMF (7.5 mL) was stirred at 80 $^{\circ}\text{C}$ for overnight. The reaction mixture was then filtered through a short bed of silica gel with EtOAc and concentrated under reduced pressure. The crude product was purified by silica-gel flash column chromatography (toluene:EtOAc = 10:1) to afford **S12** (195 mg, 54.9% yield) as a yellow solid; ^1H NMR (500 MHz, CDCl_3) δ 8.60 (d, $J = 7.3$ Hz, 1H), 8.16 (s, 1H), 7.50 (d, $J = 4.4$ Hz, 4H), 7.39–7.35 (m, 1H), 6.80 (dd, $J = 7.1, 1.2$ Hz, 1H), 4.57 (s, 2H), 3.81 (t, $J = 6.0$ Hz, 2H), 3.74 (t, $J = 7.2$ Hz, 2H), 1.94 (quin, $J = 6.7$ Hz, 2H), 1.11–1.04 (m, 21H); ^{13}C NMR (100 MHz, CDCl_3) δ 161.2, 135.2, 133.6, 133.0, 129.5, 127.7, 127.4, 125.9, 125.5, 124.2, 118.6, 113.7, 111.3, 103.1, 61.0, 47.1, 40.7, 32.1, 18.2, 12.1; LRMS (ESI) m/z calcd for $\text{C}_{29}\text{H}_{38}\text{N}_3\text{O}_2\text{Si}$ $[\text{M}+\text{H}]^+$: 488.3, found: 488.3.

Compound S13: To a solution of **S12** (595 mg, 1.22 mmol) in tetrahydrofuran (3.3 mL), was added tetra-*n*-butylammonium fluoride (TBAF) solution (1.0 M in THF, 1.8 mL, 1.8 mmol) at 0 $^{\circ}\text{C}$. The reaction mixture was stirred at 0 $^{\circ}\text{C}$ for

1.5 h. The crude product was directly purified by silica-gel flash column chromatography (CH_2Cl_2 :MeOH = 20:1) to afford **S13** (376.4 mg, 93.1% yield) as a green-yellow solid; ^1H NMR (400 MHz, $\text{DMSO}-d_6$) δ 8.53 (d, J = 7.0 Hz, 1H), 8.47 (s, 1H), 7.67 (d, J = 7.4 Hz, 2H), 7.49 (t, J = 7.6 Hz, 2H), 7.35 (t, J = 7.4 Hz, 1H), 7.04 (dd, J = 7.0, 1.2 Hz, 1H), 4.68 (s, 2H), 4.53 (t, J = 5.0 Hz, 1H, OH), 3.58 (t, J = 7.0 Hz, 2H), 3.48 (q, J = 5.7 Hz, 2H), 1.79 (quin, J = 6.7 Hz, 2H); ^{13}C NMR (100 MHz, $\text{DMSO}-d_6$) δ 160.0, 135.3, 132.55, 132.53, 129.2, 127.3, 126.8, 125.9, 125.0, 123.3, 118.5, 112.5, 111.5, 102.3, 58.4, 46.3, 39.8, 31.4; LRMS (ESI) m/z calcd for $\text{C}_{20}\text{H}_{18}\text{N}_3\text{O}_2$ $[\text{M}+\text{H}]^+$: 332.1, found: 332.1.

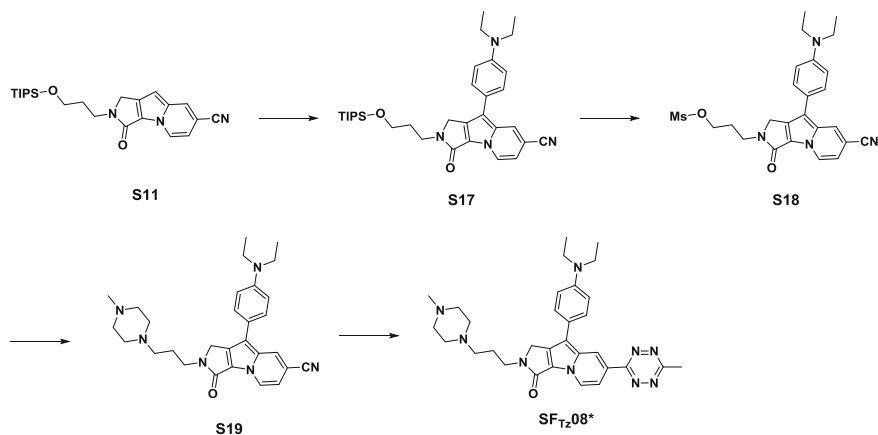
Compound S14: A suspension of **S13** (356 mg, 1.07 mmol), methanesulfonic anhydride (281 mg, 1.61 mmol), and anhydrous triethylamine (749 μL , 5.37 mmol) in anhydrous CH_2Cl_2 (4 mL) was stirred at room temperature for 2.5 h under Ar. The crude reaction mixture was then directly purified by silica-gel flash column chromatography (CH_2Cl_2 :MeOH = 20:1) to afford **S14** (441 mg, 100% yield) as a yellow solid; ^1H NMR (400 MHz, CDCl_3) δ 8.57 (d, J = 7.0 Hz, 1H), 8.15 (s, 1H), 7.53–7.48 (m, 4H), 7.40–7.36 (m, 1H), 6.81 (d, J = 7.4 Hz, 1H), 4.56 (s, 2H), 4.33 (t, J = 6.1 Hz, 2H), 3.76 (t, J = 6.7 Hz, 2H), 3.06 (s, 3H), 2.18 (quin, J = 6.4 Hz, 2H); ^{13}C NMR (100 MHz, CDCl_3) δ 161.3, 135.1, 133.7, 132.6, 129.4, 127.5, 127.4, 125.7, 125.4, 123.3, 118.3, 113.7, 111.3, 103.3, 67.3, 46.9, 39.7, 37.5, 28.6; LRMS (ESI) m/z calcd for $\text{C}_{21}\text{H}_{20}\text{N}_3\text{O}_4\text{S}$ $[\text{M}+\text{H}]^+$: 410.1, found: 410.0.

Compound S15: A suspension of **S14** (439 mg, 1.07 mmol), 1-Boc-piperazine (399 mg, 2.14 mmol), and triethylamine (449 μL , 3.22 mmol) in DMF (3 mL) was stirred at 50 °C for overnight. The crude reaction mixture was then directly purified by silica-gel flash column chromatography (CH_2Cl_2 :MeOH = 5:1) to afford **S15** (391 mg, 73% yield) as a yellow solid; ^1H NMR (500 MHz, CDCl_3) δ 8.60 (d, J = 7.4 Hz, 1H), 8.17 (s, 1H), 7.53–7.49 (m, 4H), 7.39–7.37 (m, 1H), 6.81 (dd, J = 7.1, 1.7 Hz, 1H), 4.53 (s, 2H), 3.67 (t, J = 7.1 Hz, 2H), 3.41 (t, J = 4.8 Hz, 4H), 2.44 (t, J = 7.3 Hz, 2H), 2.38–2.36 (m, 4H), 1.89 (quin, J = 7.2 Hz, 2H), 1.46 (s, 9H); ^{13}C NMR (100 MHz, CDCl_3) δ 161.1, 154.7, 135.0, 133.5, 132.8, 129.4, 127.5, 127.3, 125.7, 125.4, 123.8, 118.4, 113.6, 111.2, 103.1, 79.6, 55.7, 53.0, 46.6, 43.9, 41.4, 28.4, 26.1; LRMS (ESI) m/z calcd for $\text{C}_{29}\text{H}_{34}\text{N}_5\text{O}_3$ $[\text{M}+\text{H}]^+$: 500.3, found: 500.1.

Compound S16: A reaction mixture of **S15** (80 mg, 160 μmol), acetonitrile (418 μL , 8.01 mmol), hydrazine monohydrate (778 μL , 16.0 mmol), and zinc trifluoromethanesulfonate (29.1 mg, 80.1 μmol) in microwave reaction vial (10 mL) was irradiated under microwaves at 90 °C (30 W) with magnetic stirring for 1 h. After cooled down to room temperature, sodium nitrite (552 mg, 8.01 mmol) in 2 mL of water was added followed by slow addition of 1 N HCl until pH value reached at 3 (caution! toxic nitrogen oxide gas evolved!). Then, the resulting residue was washed with saturated NaHCO_3 aqueous solution, extracted with CH_2Cl_2 , dried over anhydrous Na_2SO_4 , and concentrated. The crude product was purified by normal-phase preparative HPLC using a linear gradient of methanol (0.1–10%) in CH_2Cl_2 with a flow rate of 5.5 ml/min to afford **S16** (18 mg, 20% yield) as a red solid; ^1H NMR (400 MHz, CDCl_3) δ 9.15 (s, 1H), 8.70 (d, J =

7.4 Hz, 1H), 7.86 (d, $J = 7.4$ Hz, 1H), 7.60 (d, $J = 7.8$ Hz, 2H), 7.51 (t, $J = 7.4$ Hz, 2H), 7.35 (t, $J = 7.2$ Hz, 1H), 4.55 (s, 2H), 3.69 (t, $J = 6.8$ Hz, 2H), 3.45 (br s, 4H), 3.09 (s, 3H), 2.52–2.44 (m, 6H), 1.96–1.92 (m, 2H), 1.45 (s, 9H); ^{13}C NMR (100 MHz, CDCl_3) δ 166.8, 163.1, 161.5, 154.7, 135.4, 135.0, 133.5, 129.3, 127.5, 126.8, 125.5, 124.0, 123.0, 119.7, 113.6, 109.0, 79.7, 55.7, 53.0, 46.8, 43.1, 41.3, 28.4, 26.0, 21.2; LRMS (ESI) m/z calcd for $\text{C}_{31}\text{H}_{37}\text{N}_8\text{O}_3$ $[\text{M}+\text{H}]^+$: 569.3, found: 569.2.

Compound $\text{SF}_{\text{Tz}}\mathbf{02}^*$: A suspension of **S16**, 3-bromopropanoic acid (4.8 mg, 32 μmol), and DIPEA (28 μL , 160 μmol), in DMF (160 μL) was stirred at 50 $^\circ\text{C}$ for 2 h. The crude product was directly purified by reverse-phase preparative HPLC using a linear gradient of acetonitrile (5–100%) in water with 1% TFA to afford the TFA salts of $\text{SF}_{\text{Tz}}\mathbf{02}^*$ (5.7 mg, 47% yield) as a red solid; ^1H NMR (400 MHz, $\text{CDCl}_3:\text{MeOD}-d_4 = 10:1$, v/v) δ 9.15 (s, 1H), 8.67 (d, $J = 7.4$ Hz, 1H), 7.87 (d, $J = 7.4$ Hz, 1H), 7.64 (d, $J = 7.4$ Hz, 2H), 7.52 (t, $J = 7.6$ Hz, 2H), 7.36 (t, $J = 7.5$ Hz, 1H), 4.60 (s, 2H), 3.72 (t, $J = 6.5$ Hz, 2H), 3.31 (br s, 8 H), 3.20–3.11 (m, 4H), 3.07 (s, 3H), 2.70 (t, $J = 6.8$ Hz, 2H), 2.18–2.11 (m, 2H); ^{13}C NMR (100 MHz, $\text{CDCl}_3:\text{MeOD}-d_4 = 10:1$, v/v) δ 172.8, 167.5, 163.4, 162.5, 136.2, 136.0, 133.8, 129.6, 127.9, 127.2, 125.9, 124.9, 122.5, 119.9, 114.0, 109.6, 54.9, 52.9, 50.5, 49.8, 47.2, 40.5, 30.1, 24.1, 21.3; HRMS (ESI) m/z calcd for $\text{C}_{29}\text{H}_{33}\text{N}_8\text{O}_3$ $[\text{M}+\text{H}]^+$: 541.2670, found: 541.2674.



Compound **S17**: A suspension of **S11** (368.4 mg, 895 μmol), *N,N*-diethyl-4-iodo-aniline⁴ (739 mg, 2.69 mmol), palladium acetate (40.2 mg, 179 μmol), and silver acetate (448 mg, 2.69 mmol) in DMF (9 mL) was stirred at 80 $^\circ\text{C}$ for overnight. The reaction mixture was then filtered through a short bed of silica gel with EtOAc and concentrated under reduced pressure. The crude product was purified by flash column chromatography (silica gel, toluene:EtOAc = 10:1) to afford **S17** (147.5 mg, 29.5% yield) as a red solid; ^1H NMR (400 MHz, CDCl_3) δ 8.52 (d, $J = 7.0$ Hz, 1H), 8.13 (s, 1H), 7.35 (d, $J = 9.0$ Hz, 2H), 6.78 (d, $J = 8.6$ Hz, 2H), 6.71 (dd, $J = 7.2$, 1.4 Hz, 1H), 4.52 (s, 2H), 3.81 (t, $J = 5.9$ Hz, 2H), 3.72 (t,

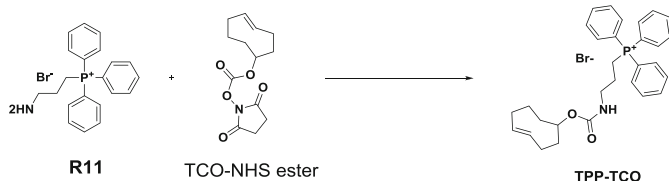
$J = 7.2$ Hz, 2H), 3.42 (q, $J = 7.0$ Hz, 4H), 1.93 (quin, $J = 6.6$ Hz, 2H), 1.22 (t, $J = 7.0$ Hz, 6H), 1.12–1.03 (m, 21H); ^{13}C NMR (100 MHz, CDCl_3) δ 161.3, 146.9, 134.2, 133.0, 128.6, 126.3, 125.1, 123.7, 119.4, 118.9, 114.4, 112.2, 110.6, 101.6, 60.9, 47.0, 44.4, 40.5, 32.1, 18.0, 12.6, 12.0; LRMS (ESI) m/z calcd for $\text{C}_{33}\text{H}_{47}\text{N}_4\text{O}_2\text{Si}$ $[\text{M}+\text{H}]^+$: 559.4, found: 559.4.

Compound S18: To a solution of **S17** (134.4 mg, 240.5 μmol) in tetrahydrofuran (2.5 mL), was added TBAF solution (1.0 M in THF, 361 μL , 361 μmol) at 0 $^\circ\text{C}$. The reaction mixture was stirred at 0 $^\circ\text{C}$ for 1 h and then washed with saturated brine, extracted with EtOAc, dried over anhydrous Na_2SO_4 , and concentrated. The resulting solid, methanesulfonic anhydride (126 mg, 722 μmol), and anhydrous triethylamine (168 μL , 1.20 mmol) were dissolved in anhydrous CH_2Cl_2 (2.5 mL) under Ar. The mixture was stirred at room temperature for 4 h. The crude mixture was directly purified by flash column chromatography (silica gel, CH_2Cl_2 :MeOH = 40:1) to afford **S18** (116 mg, 100% yield) as a yellow solid; ^1H NMR (400 MHz, CDCl_3) δ 8.50 (d, $J = 7.0$ Hz, 1H), 8.12 (s, 1H), 7.34 (d, $J = 8.6$ Hz, 2H), 6.79 (d, $J = 8.6$ Hz, 2H), 6.73 (dd, $J = 7.2$, 1.4 Hz, 1H), 4.52 (s, 2H), 4.33 (t, $J = 6.1$ Hz, 2H), 3.75 (t, $J = 6.7$ Hz, 2H), 3.42 (q, $J = 7.0$ Hz, 4H), 3.05 (s, 3H), 2.17 (quin, $J = 6.5$ Hz, 2H), 1.22 (t, $J = 7.0$ Hz, 6H); ^{13}C NMR (100 MHz, CDCl_3) δ 161.7, 147.1, 134.4, 133.4, 128.8, 126.4, 125.3, 123.1, 119.2, 118.8, 114.7, 112.3, 111.0, 102.1, 67.5, 47.1, 44.6, 39.8, 37.6, 28.8, 12.7; LRMS (ESI) m/z calcd for $\text{C}_{25}\text{H}_{29}\text{N}_4\text{O}_4\text{S}$ $[\text{M}+\text{H}]^+$: 481.2, found: 481.2.

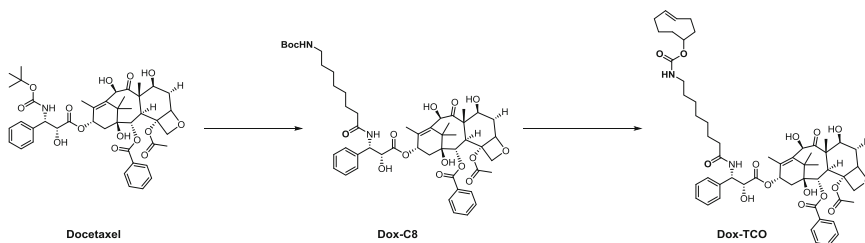
Compound S19: A suspension of **S18** (54.0 mg, 112 μmol), 1-methylpiperazine (62 μL , 562 μmol), and potassium carbonate (46.6 mg, 337 μmol) in anhydrous DMF (1.2 mL) was stirred at 50 $^\circ\text{C}$ for overnight. The reaction mixture was then directly purified by flash column chromatography (silica gel, CH_2Cl_2 :MeOH = 5:1) to afford **S19** (38.1 mg, 70% yield) as a yellow solid; ^1H NMR (400 MHz, CDCl_3) δ 8.52 (d, $J = 7.4$ Hz, 1H), 8.14 (s, 1H), 7.35 (d, $J = 8.6$ Hz, 2H), 6.79 (d, $J = 8.6$ Hz, 2H), 6.72 (d, $J = 7.4$ Hz, 1H), 4.49 (s, 2H), 3.65 (t, $J = 7.0$ Hz, 2H), 3.42 (q, $J = 7.0$ Hz, 4H), 2.47–2.43 (m, 10H), 2.29 (s, 3H), 1.92–1.85 (m, 2H), 1.22 (t, $J = 7.0$ Hz, 6H); ^{13}C NMR (125 MHz, CDCl_3) δ 161.4, 147.1, 134.3, 133.2, 128.7, 126.4, 125.2, 123.6, 119.4, 118.9, 114.5, 112.3, 110.8, 101.8, 55.8, 55.2, 53.2, 46.8, 46.1, 44.5, 41.6, 26.3, 12.8; LRMS (ESI) m/z calcd for $\text{C}_{29}\text{H}_{37}\text{N}_6\text{O}$ $[\text{M}+\text{H}]^+$: 485.3, found: 485.3.

Compound SF_{Tz}08*: A reaction mixture of **S19** (15.2 mg, 31.3 μmol), acetonitrile (82 μL , 1.6 mmol), zinc trifluoromethanesulfonate (5.7 mg, 16 μmol), and hydrazine monohydrate (152 μL , 3.13 mmol) in microwave reaction vial (10 ml) was irradiated under microwaves at 100 $^\circ\text{C}$ (40 W) with magnetic stirring for 1.5 h. After cooled down to room temperature, sodium nitrite (43.3 mg, 627 μmol) in 1 mL of water was added followed by slow addition of 1N HCl until pH value reached 3 (caution! toxic nitrogen oxide gas evolved!). Then, the resulting residue was washed with saturated NaHCO_3 aqueous solution, extracted with CH_2Cl_2 , dried over anhydrous Na_2SO_4 , and concentrated. The crude product was purified by reverse-phase preparative HPLC using a linear gradient of acetonitrile (5–100%) in water with 1% of TFA to afford the

TFA salts of **SF_{Tz}08*** (6.5 mg, 31% yield) as a reddish brown solid; NMR spectra were recorded after basic work-up using saturated NaHCO₃ aqueous solution, ¹H NMR (400 MHz, CDCl₃) δ 9.17 (s, 1H), 8.66 (d, *J* = 7.5 Hz, 1H), 7.81 (d, *J* = 7.5 Hz, 1H), 7.47 (d, *J* = 8.6 Hz, 2H), 6.81 (d, *J* = 8.6 Hz, 2H), 4.52 (s, 2H), 3.67 (t, *J* = 7.0 Hz, 2H), 3.43 (q, *J* = 7.0 Hz, 4H), 3.07 (s, 3H), 2.47 (m, 10H), 2.28 (s, 3H), 1.90 (quin, *J* = 7.1 Hz, 2H), 1.23 (t, *J* = 7.0 Hz, 6H); ¹³C NMR (100 MHz, CDCl₃) δ 166.5, 163.2, 161.6, 146.7, 134.9, 134.1, 128.6, 125.3, 122.9, 122.7, 120.4, 120.2, 114.5, 112.3, 108.5, 55.8, 55.1, 53.2, 46.8, 46.0, 44.5, 41.4, 26.3, 21.1, 12.7; HRMS (ESI) *m/z* calcd for C₃₁H₄₀N₉O [M+H]⁺: 554.3350, found: 554.3351.



Compound TPP-TCO: A suspension of **R11**⁷ (5.0 mg, 12 μmol), TCO-NHS ester (6.7 mg, 25 μmol), and triethylamine (17 μL, 120 μmol) in DMF (200 μL) was stirred at room temperature for 15 min. The crude product was directly purified by reverse-phase preparative HPLC using a linear gradient of acetonitrile (5–100%) in water with 1% TFA to afford **TPP-TCO** (5.5 mg, 80% yield) as transparent oil; HRMS (ESI) *m/z* calcd for C₃₀H₃₅NO₂P+ [M]⁺: 472.2400, found: 472.2402



Dox-C8 and **Dox-TCO** were prepared by a modified procedure of a reported paper.⁸

Compound Dox-C8: Docetaxel (152 mg, 188 μmol) were dissolved in formic acid (6 mL, 159 mmol) and the reaction mixture was stirred at room temperature for 1 h. Formic acid was then removed under reduced pressure. To a resulting solid (52 mg) in DMF (1 mL) was added 8-(*tert*-butoxycarbonylamino)octanoic acid (35.8 mg, 138 μmol), TSTU (41.5 mg, 138 μmol), and DIPEA (120 μL, 690 μmol). The mixture was stirred at 60 °C for 2 days. The crude product was directly purified by reverse-phase preparative HPLC using a linear gradient of

⁷Chem. Commun. **2016**, 52, 12330–12333.

⁸Nat. Methods **2014**, 11, 731–733.

acetonitrile (5–100%) in water with 1% TFA to afford **Dox-C8** (19.1 mg, 29.2% yield) as a white solid; LRMS (ESI) m/z calcd for $C_{51}H_{69}N_2O_{15}$ $[M+H]^+$: 949.5, found: 949.2.

Compound Dox-TCO: Dox-C8 (8.1 mg, 8.5 μ mol) were dissolved in formic acid (200 μ L, 5.30 mmol) and the reaction mixture was stirred at room temperature for 1 h. Formic acid was removed under reduced pressure. To a resulting solid (7.6 mg) in DMF (200 μ L), were added TCO-NHS Ester (4.6 mg, 17 μ mol), and triethylamine (12 μ L, 85 μ mol). The mixture was stirred room temperature for 1 h. The crude product was directly purified by reverse-phase preparative HPLC using a linear gradient of acetonitrile (5–100%) in water with 1% TFA to afford **Dox-TCO** (5.8 mg, 67% yield) as a white solid; HRMS (ESI) m/z calcd for $C_{55}H_{72}N_2NaO_{15}$ $[M+Na]^+$: 1023.4825, found: 1023.4830.

References

1. (a) Fernández-Suárez M, Ting AY (2009) *Nat Rev Mol Cell Biol* 9:929–943. (b) Hell SW (2009) *Nat Methods* 6:24–32
2. (a) Lavis LD, Raines RT (2008) *ACS Chem Biol* 3:142–155. (b) Lavis LD, Raines RT (2014) *ACS Chem Biol* 9, 855–866. (c) Dean KM, Palmer AE (2014) *Nat Chem Biol* 10:512–523
3. (a) Weissleder R (2001) *Nat Biotechnol* 19:316–317. (b) Ntziachristos V, Ripoll J, Wang LV, Weissleder R (2005) *Nat Biotechnol* 23:313–320
4. (a) Chudakov DM, Matz MV, Lukyanov S, Lukyanov KA (2010) *Physiol Rev* 90:1103–1163. (b) Odell ID, Cook D (2013) *J Invest Dermatol* 133:e4
5. (a) van Dam GM, Themelis G, Crane LMA, Harlaar NJ, Pleijhuis RG, Kelder W, Sarantopoulos A, de Jong JS, Arts HJG, van der Zee AGJ, Bart J, Low PS, Ntziachristos V (2011) *Nat Med* 17:1315–1319. (b) Choi HS, Gibbs SL, Lee JH, Kim SH, Ashitate Y, Liu F, Hyun H, Park G, Xie Y, Bae S, Henary M, Frangioni JV (2013) *Nat Biotechnol* 31:148–153. (c) Xue L, Karpenko IA, Hiblot J, Johnsson K (2015) *Nat Chem Biol* 11:917–923. (d) Kim E, Yang KS, Kohler RH, Dubach JM, Mikula H, Weissleder R (2015) *Bioconjug Chem* 26:1513–1518. (e) Lee MM, Gao Z, Peterson BR (2017) *Angew Chem Int Ed* 56:6927–6931
6. Kim E, Yang KS, Giedt RJ, Weissleder R (2014) *Chem Commun* 50:4504–4507
7. (a) Sletten EM, Bertozzi CR (2009) *Angew Chem Int Ed* 48:6974–6998. (b) Patterson DM, Nazarova LA, Prescher JA (2014) *ACS Chem Biol* 9:592–605
8. (a) Reiner T, Earley S, Turetsky A, Weissleder R (2010) *ChemBioChem* 11:2374–2377. (b) Cserép GB, Herner A, Kele P (2015) *Methods Appl Fluoresc* 3:042001
9. Oliveira BL, Guo Z, Bernardes GJL (2017) *Chem Soc Rev* 46:4895–4950
10. (a) Blackman ML, Royzen M, Fox JMJ (2008) *Am Chem Soc* 130:13518–13519. (b) Devaraj NK, Weissleder R, Hilderbrand SA (2008) *Bioconjug Chem* 19:2297–2299. (c) Taylor MT, Blackman ML, Dmitrenko O, Fox JMJ (2011) *Am Chem Soc* 133:9646–9649. (d) Knall A-C, Slugovc C (2013) *Chem Soc Rev* 42:5131–5142. (e) Selvaraj R, Fox JM (2013) *Curr Opin Chem Biol* 17:753–760. (f) Mayer S, Lang K (2017) *Synthesis* 49:830–848
11. (a) Devaraj NK, Hilderbrand S, Upadhyay R, Mazitschek R, Weissleder R (2010) *Angew Chem Int Ed* 49:2869–2872. (b) Carlson JCT, Meimetus LG, Hilderbrand SA, Weissleder R (2013) *Angew Chem Int Ed* 52:6917–6920. (c) Wu H, Yang J, Šečkutè J, Devaraj NK (2014) *Angew Chem Int Ed* 53:5805–5809. (d) Meimetus LG, Carlson JCT, Giedt RJ, Kohler RH, Weissleder R (2014) *Angew Chem Int Ed* 53:7531–7534. (e) Knorr G, Kozma E, Herner A, Lemke EA, Kele P (2016) *Chem Eur J* 22:8972–8979. (f) Wiczorek A, Werther P, Euchner J,

- Wombacher R (2017) *Chem Sci* 8:1506–1510. (g) Kozma E, Estrada Girona G, Paci G, Lemke EA, Kele P (2017) *Chem Commun* 53:6696–6699
12. (a) Budin G, Yang KS, Reiner T, Weissleder R (2011) *Angew Chem Int Ed* 50:9378–9381. (b) Yang KS, Budin G, Reiner T, Vinegoni C, Weissleder R (2012) *Angew Chem Int Ed* 51:6598–6603
 13. (a) Förster T (1948) *Ann Phys* 2:55–75; Förster T (1959) *Disc Faraday Soc* 27:7–17
 14. (a) Jiao G-S, Thoresen LH, Burgess KJ (2003) *Am Chem Soc* 125:14668–14669. (b) Bandichhor R, Petrescu AD, Vespa A, Kier AB, Schroeder F, Burgess KJ (2006) *Am Chem Soc* 128:10688–10689
 15. (a) Dexter DLJ (1953) *Chem Phys* 21:836–850. (b) Otsuki J, Kanazawa Y, Kaito A, Islam D-MS, Araki Y, Ito O (2008) *Chem Eur J* 14:3776–3784. (c) Hurenkamp JH (2008) Tuning energy transfer between chromophores switchable molecular photonic systems. Ph.D. Thesis, University of Groningen
 16. (a) Kim E, Koh M, Ryu J, Park SBJ (2008) *Am Chem Soc* 130:12206–12207. (b) Kim E, Koh M, Lim BJ, Park SBJ (2011) *Am Chem Soc* 133:6642–6649. (c) Lee Y, Na S, Lee S, Jeon NL, Park SB (2013) *Mol BioSyst* 9:952–956. (d) Choi EJ, Kim E, Lee Y, Jo A, Park SB (2014) *Angew Chem Int Ed* 53:1346–1350. (e) Kim E, Lee Y, Lee S, Park SB (2015) *Acc Chem Res* 48:538–547
 17. (a) Anslyn EV, Dougherty DA (2005) *Modern physical organic chemistry*, University Science Books, Sausalito, CA. (b) Turro NJ, Ramamurthy V, Scaiano JC (2008) *Principles of molecular photochemistry: an introduction*, 1st edition, University Science Books, Sausalito, CA
 18. (a) Gong Y-H, Miomandre F, Méallet-Renault R, Badré S, Galmiche L, Tang J, Audebert P, Clavier G (2009) *Eur J Org Chem* 6121–6128. (b) Clavier G, Audebert P (2010) *Chem Rev* 110:3299–3314
 19. Escudero D (2016) *Acc Chem Res* 49:1816–1824
 20. Plugge M, Alain-Rizzo V, Audebert P, Brouwer AM (2012) *J Photochem Photobiol A Chem* 234:12–20
 21. Yang J, Karver MR, Li W, Sahu S, Devaraj NK (2012) *Angew Chem Int Ed* 51:5222–5225
 22. (a) Presolski SI, Hong V, Cho S-H, Finn MGJ (2010) *Am Chem Soc* 132:14570–14576. (b) Lang K, Chin JW (2014) *ACS Chem Biol* 9:16–20
 23. (a) Song W, Wang Y, Qu J, Lin QJ (2008) *Am Chem Soc* 130:9654–9655. (b) Song W, Wang Y, Qu J, Madden MM, Lin Q (2008) *Angew Chem Int Ed* 47:2832–2835. (c) Yu Z, Pan Y, Wang Z, Wang J, Lin Q (2012) *Angew Chem Int Ed* 51:10600–10604
 24. Hansch C, Leo A, Taft RW (1991) *Chem Rev* 91:165–195
 25. (a) Kasha M (1950) *Disc Faraday Soc* 9:14–19. (b) Klán P, Wirz J (2009) *Photochemistry of organic compounds: from concepts to practice*, Wiley-Blackwell
 26. (a) Hilborn RC (1982) *Am J Phys* 50:982–986. (b) Lee Y, Jo A, Park SB (2015) *Angew Chem Int Ed* 54:15689–15693. (c) Valeur B, Berberan-Santos MN (2012) *Molecular fluorescence: principles and applications*, second edition, Wiley-VCH, Weinheim
 27. Alirol E, Martinou JC (2006) *Oncogene* 25:4706–4716

Chapter 4

Rational Development of Furoindolizine Core Skeleton Guided by Oscillator Strength



4.1 Introduction¹

Molar absorptivity (ϵ) is an intrinsic property of every chemical entity, and it represents how well the entity absorbs light at any given wavelength [1]. From a synthetic point of view, the development of a new design strategy that allows for the predictable enhancement of the molar absorptivity of a species is highly valuable—with benefits spanning from aiding in the development of light-harvesting materials, such as dye-sensitized solar cells (DSSC), to various types of fluorescent materials [2]. However, very few papers have reported the successful improvement of molar absorptivity of particular initial compounds [3] because the prime strategy, an extension of the π -conjugated systems of these compounds, does not always guarantee increased molar absorptivity, and some instances have even been shown to have negligible or opposite effects [4]. To the best of my knowledge, there was no scientific report pursuing the rational design of organic fluorophores with enhanced molar absorptivity.

Fluorescent organic dyes are a class of emissive materials with high sensitivity, selectivity, accessibility, and ease of use, making them first-class monitoring tools in molecular biology and life sciences [5]. However, only a limited number of fluorophores, such as cyanine, BODIPY, fluorescein, and rhodamine, have been repeatedly used in the majority of research, mainly owing to their innate brightness, which in turn is associated with their excellent molar absorptivity [6]. Therefore, a rational improvement of molar absorptivity is in high demand for the development of distinctive organic fluorophores in various practical uses. To address this issue, a molecular design approach using oscillator strength value (or f value) [1, 7] has been described in this chapter. Oscillator strength is a physical parameter that represents the “allowedness” of an electron transition [8] and can be tuned through the incorporation of various functional groups [9]. To conduct a case study

¹[*Angew. Chem. Int. Ed.*, **2015**, *54*, 15689–15693] Reproduced by permission of Wiley VCH.

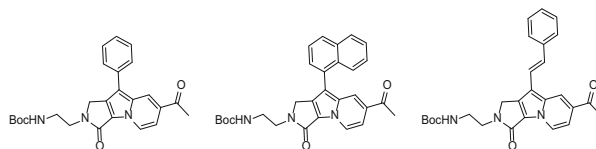
regarding the relationship between calculated oscillator strength value and experimental molar absorptivity, a novel fluorophore was designed starting from an indolizine-based Seoul-Fluor (SF) scaffold, [10] to enhance its molar absorptivity, guided by the computable oscillator strength value.

4.2 Result and Discussion

4.2.1 *Designing an Unexplored Fluorophore with High Molar Absorptivity*

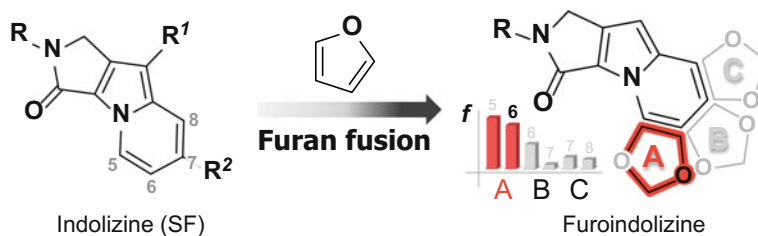
Previously, a marginal enhancement of molar absorptivity was observed when incorporated naphthyl or styryl groups in SF (Table 4.1) [11]. Therefore, the introduction of a heteroaromatic ring was envisioned to extend the π -conjugated system of indolizine scaffold, because the electronic nature of initial fluorophores can be significantly transformed by the inductive or resonance effects of the newly introduced heteroatom [12]. Of the potential heteroaromatic rings, fusion of a furan ring was preferred, after considering the remarkable molar absorptivity enhancement of BODIPY reported by Suzuki et al. [13]. Given that the SF system is based on the lactam-embedded indolizine moiety, combining a furan ring with the SF's indolizine can generate six different furoindolizine isomers, depending on the fused position between the five- and six- membered rings and the arrangement of the atomic oxygen in the furan (Fig. 4.1). Without any challenging or time-consuming efforts to synthesize all possible candidates, time-dependent density functional theory (TD-DFT) calculation was performed at the B3LYP/6-31G* level to obtain the oscillator strength values of six isomers, thereby estimating the “transition allowedness” from the S_0 to the S_1 state of each core skeleton (see Table 4.2). This result indicates that placing the furan at the “A” position would have the highest f value, potentially implying the highest molar absorptivity. Of the two cores at “A,” the “A-6” was selected to generate an unprecedented furoindolizine core skeleton for the in depth structure-photophysical property (SPPR) study, owing to its greater synthetic accessibility.

To construct a library set covering a wide range of molar absorptivity and emission wavelengths, the positions for the incorporation of the R^1 and R^2 groups were strategically chosen, as based on the quantum-mechanical calculations. First, the R^1 position was selected on the basis of the electron density in the highest occupied molecular orbital (HOMO) in comparison with that in the lowest unoccupied molecular orbital (LUMO), using TD-DFT calculations (Fig. 4.2a). Following previous studies, [10b] it was hypothesized that the electron-donating group (EDG), existing on the carbon with the much larger atomic coefficient in HOMO than that in LUMO, would induce a smaller energy gap—bathochromic shifts of fluorescence emission wavelength—as it would preferentially elevate the energy level of HOMO over that of LUMO (Fig. 4.3) [14]. In the same manner, the

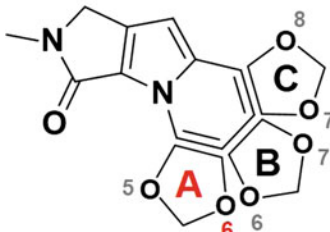
Table 4.1 Previous attempts for extension of the π -conjugated system via incorporating a naphthyl or styryl group at the R¹ position of indolizine-based SF

R ¹ substituents		Phenyl	Naphthyl	Styryl
ϵ^a		13,000 (at 403 nm)	14,000 (at 396 nm)	14,000 (at 424 nm)
f value ^b	S ₀ →S ₁	0.2552 (393 nm)	0.2596 (392 nm)	0.3098 (437 nm)
	S ₀ →S ₂	0.0003 (346 nm)	0.0570 (347 nm)	0.0005 (350 nm)
	S ₀ →S ₃	0.0007 (317 nm)	0.0043 (345 nm)	0.1994 (339 nm)

^aExperimental data of the largest absorption maxima and molar absorption coefficients measured in CH₂Cl₂. ^bCalculated oscillator strength values for S₀→S₁, S₀→S₂ and S₀→S₃, respectively (from top to bottom).

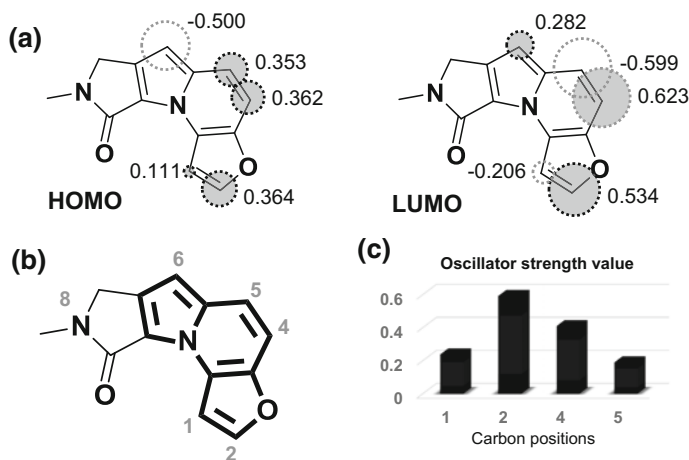
**Fig. 4.1** Chemical structures of novel furoindolizine-based fluorophores and their calculated oscillator strength values (f values) using TD-DFT calculation at the B3LYP/6-31G* level. R group represents an aliphatic linker moiety

electron-withdrawing group (EWG), existing on the carbon with the larger atomic coefficient in the LUMO, would induce selective reduction of the LUMO's energy level, causing a smaller energy gap. Accordingly, the C6 atom was selected as the position for the R¹ group, leaving the C2, C4, and C5 atoms as potential sites for the R² group (Fig. 4.2b). Next, the latent R² position was carefully assessed via the calculated oscillator strength values to enhance their molar absorptivity. As shown in Fig. 4.2c, it was the C2 site that demonstrated the highest f value when a phenyl group was virtually incorporated. Given all these considerations, the construction of

Table 4.2 Calculated oscillator strength values of the six isomers regarding the $S_0 \rightarrow S_1$ transition


Ring	Oxygen	$f_{(S_0 \rightarrow S_1)}$
A	5	0.2739
	6	0.2348
B	6	0.1317
	7	0.0233
C	7	0.0622
	8	0.0501

Furoindolizine

**Fig. 4.2** A design principle for selecting the functional group positions in the furoindolizine skeleton. **a** The atomic coefficients in HOMO and LUMO of the core skeleton. **b** Chemical structure of lactam-embedded furo[3,2-*e*]indolizine core skeleton. **c** Calculated oscillator strength f values of the $S_0 \rightarrow S_1$ transition when incorporated with the phenyl group at each carbon position

a fluorescent library was pursued based on the novel furo[3,2-*e*]indolizine core skeleton with the R^1 group at the C6 position and the R^2 group at the C2 position. The R^1 and R^2 groups were diversified to phenyl moieties with an EDG and an EWG in order to investigate the effects of the electronic changes on the furoindolizine core skeleton. Additionally, previous observation leads to select the N8 position of lactam ring as the linker site for further chemical conjugation, since it allowed minimal perturbation of photophysical property [10a, c].

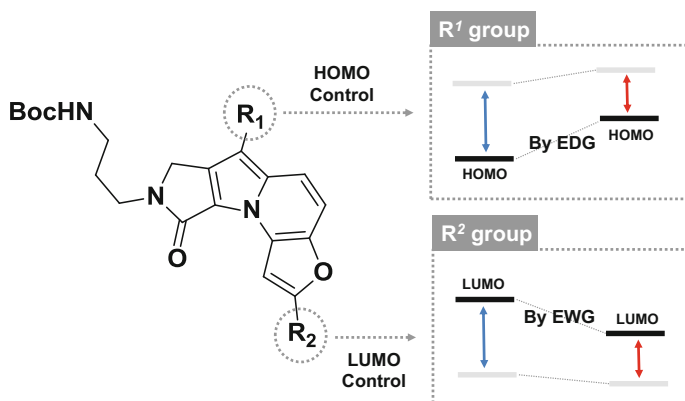
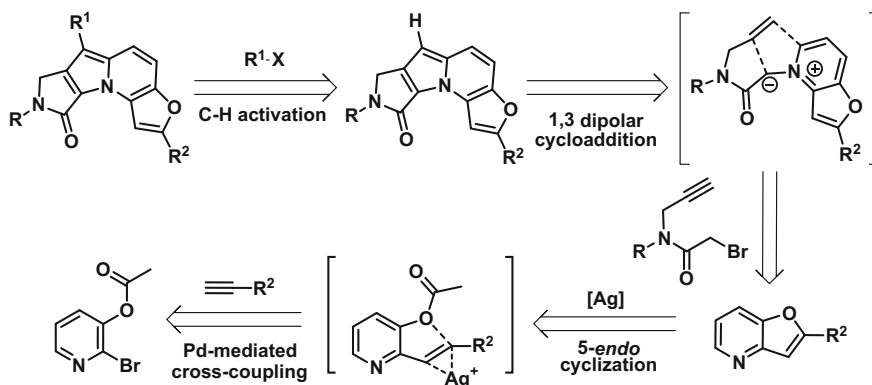


Fig. 4.3 Design principles to control the emission wavelength in furoindolizine system

4.2.2 Library Construction Based on a Novel Furo[3,2-*e*]Indolizine Scaffold

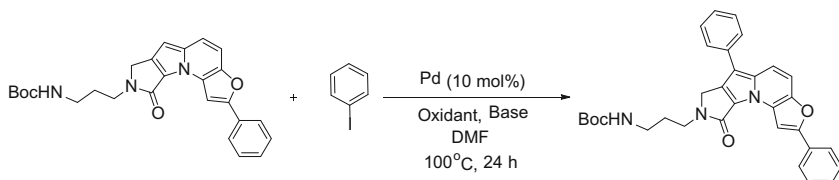
Based on the retrosynthetic analysis, the syntheses of the furo[3,2-*b*]pyridine derivatives [15] were a prerequisite for the fabrication of the furo[3,2-*e*]indolizine library (Scheme 4.1). The R²-group-containing terminal acetylene moiety was incorporated into 2-bromopyridin-3-yl acetate via Sonogashira coupling. After simple filtration of the resulting mixture, the silver-mediated cyclization allowed me to access the furo[3,2-*b*]pyridine derivatives in a facile manner. Then, the nucleophilic addition of furo[3,2-*b*]pyridine derivatives to alkyne-containing α -bromoamides yielded the furopyridinium salts as key intermediates. Without further purification, the resulting furopyridiniums were converted into furo[3,2-*e*]indolizine skeletons, aided by the treatment of DBU and CuI through a 1,3-dipolar cycloaddition. The R¹ functional



Scheme 4.1 Retrosynthetic analysis for the furoindolizine-based skeleton [R = (CH₂)₃NHBoc]

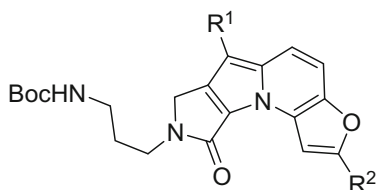
groups were introduced at the last stage of synthesis through direct C–H activation. After the optimization of reaction conditions (Table 4.3), the direct C–H activation of the furoindolizine core was successfully achieved through its thermal transformation in the presence of PdCl₂(PPh₃)₂, AgOAc, and KOAc at 100 °C in a 61 ~ 86% yield with a moderate substrate scope, except for the electron-rich furoindolizine system **16** (see Table 4.4) due to its instability.

Table 4.3 An optimization table for the palladium-mediated cross-coupling reaction on the furoindolizine-based core skeleton



Entry	Pd-Catalyst (10 mol %)	Oxidant (1.5 eq.)	Base (3.0 eq.)	Yield (%) ^a (NMR estimation)
1	Pd(PPh ₃) ₄	-	KOAc	48
2	Pd ₂ (dba) ₃	-	KOAc	51
3	PdCl ₂ (PPh ₃) ₂	AgOAc	KOAc	78
4	Pd(OAc) ₂	AgOAc	KOAc	40
5	Pd(TFA) ₂	AgOAc	KOAc	40
6	PdCl ₂ (PPh ₃) ₂	-	KOAc	49
7	PdCl ₂ (PPh ₃) ₂	Cu(OAc) ₂	KOAc	34
8	PdCl ₂ (PPh ₃) ₂	O ₂	KOAc	60
9	PdCl ₂ (PPh ₃) ₂	Oxone	KOAc	n.d.
10	PdCl ₂ (PPh ₃) ₂	AgOAc	-	38
11	PdCl ₂ (PPh ₃) ₂	AgOAc	KF	43
12	PdCl ₂ (PPh ₃) ₂	AgOAc	K ₂ CO ₃	23
13	PdCl ₂ (PPh ₃) ₂	AgOAc	Cs ₂ CO ₃	13

^aThe reaction yield was evaluated based on the peak integration of ¹H NMR spectra. *p*-Dimethoxybenzene was used as a reference reagent for ¹H NMR integration.

Table 4.4 A list of the compounds in the furoindolizine library with the values of their experimental and theoretical photophysical properties

# <i>cpd</i>	R ¹	R ²	λ_{abs}^a (nm)	f^b	\mathcal{E}^c	E_{gap}^d (eV)	λ_{em}^e (nm)	Q.Y. ^e
01	H	H	355	0.2348	1.7E4	3.18	405	0.88
02	4-(CN)Ph	H	381	0.5467	2.2E4	2.90	453	0.69
03	Ph	H	372	0.3259	1.3E4	2.80	456	0.71
04	4-(NEt ₂)Ph	H	386	0.2737	1.2E4	2.47	514	0.54
05	H	4-(CN)Ph	415	0.6262	2.4E4	2.61	502	0.85
06	4-(CN)Ph	4-(CN)Ph	434	0.9179	3.2E4	2.40	527	0.86
07	Ph	4-(CN)Ph	436	0.7117	2.5E4	2.34	533	0.80
08	4-(NEt ₂)Ph	4-(CN)Ph	459	0.5137	1.9E4	1.98	630	0.10
09	H	Ph	391	0.5929	2.6E4	2.82	457	0.83
10	4-(CN)Ph	Ph	413	0.9641	3.9E4	2.60	491	0.83
11	Ph	Ph	410	0.6955	2.5E4	2.53	499	0.80
12	4-(NEt ₂)Ph	Ph	424	0.5454	1.9E4	2.20	560	0.33
13	H	4-(NMe ₂)Ph	405	0.9299	3.8E4	2.82	471	0.86
14	4-(CN)Ph	4-(NMe ₂)Ph	431	1.1950	3.9E4	2.65	505	0.87
15	Ph	4-(NMe ₂)Ph	423	1.0864	3.7E4	2.59	501	0.83
16	4-(NEt ₂)Ph	4-(NMe ₂)Ph	N/A	0.8915	N/A	2.28	N/A	N/A

All experimental data were obtained in DCM condition. ^a Only the largest absorption maxima are shown.

^b Calculated oscillator strength values of the S₀-S₁ transition through TDDFT at the B3LYP/6-31G^{*} level. ^c Molar

absorption coefficient at the maximum absorption wavelength. ^d Calculated values of the energy gap between the S₀ and S₁ state based on the optimized geometry of first excited state through TDDFT at the B3LYP/6-31G^{*} level.

^e Excited at the maximum absorption wavelength.

4.2.3 Photophysical Property Analysis

Using this synthetic route, fifteen furoindolizine-based fluorescent compounds were constructed and their photophysical properties were measured, including their maximum absorption and emission wavelengths, molar absorptivity, and quantum yields (Table 4.4). Also the oscillator strength values (f values) of their S_0 - S_1 transitions were calculated via TD-DFT calculations. Particularly, special interests directed toward the relationship between experimental molar absorptivity and the computable f values, calculated on the basis of the ground-state-optimized geometry. Another theoretical value, the energy gap between the S_0 and S_1 states, was obtained through TD-DFT calculations to examine the predictable tendency of the emission-spectrum changes compared with the observed emission wavelengths.

In terms of the molar absorptivity, the major enhancement was achieved through the additional π -conjugated systems at the R^2 position, in accordance with the trends predicted by their oscillator strength values (Fig. 4.4). Any aryl moiety at the R^2 position ensured the decent enhancement of the molar absorptivity, especially in the case of an electron-donating dimethylaminophenyl moiety (Fig. 4.4c, right). For the R^1 position, however, effective enhancement of the molar absorptivity was achieved only via the incorporation of a 4-cyanophenyl group (Fig. 4.4c, left). In fact, a negligible change of the molar absorptivity or even its reduction was

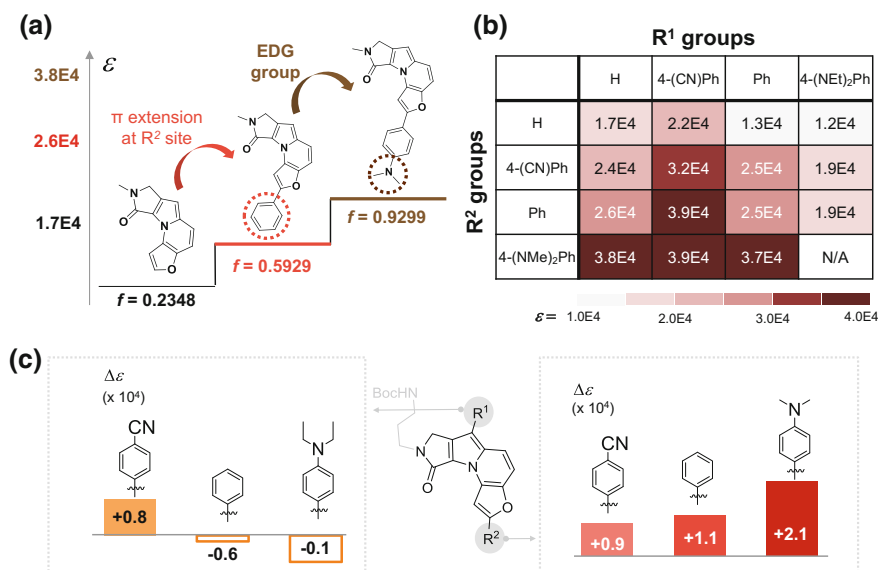


Fig. 4.4 Absorption-related photophysical properties of the furoindolizine library. **a** Schematic graph for the changes in oscillator strength values along with molar absorptivity upon structural modification. **b** A colored table of the molar absorptivity of synthesized compounds. The darker colors represent higher molar absorptivity. **c** The average changes in the molar absorptivity upon the introduction of aryl substituents at the R^1 and R^2 positions in comparison with hydrogen

observed when incorporated either a phenyl or aniline moiety at the R¹ position. These contrasting events could possibly be attributed to the different effects of R¹ and R² groups on overlap efficiency between HOMO and LUMO [16]; an EDG at the R¹ position caused a localization of the electron density into the R¹ phenyl group in the HOMO, resulting in a lower spatial overlap between HOMO and LUMO (Fig. 4.5a). An EDG at the R² position, however, extended their spatial overlap via a delocalization of the electron density into the furoindolizine core itself, allowing for efficient electron transition via light absorption (Fig. 4.5b). Furthermore, the relationship between the observed molar absorptivity (ϵ) and the

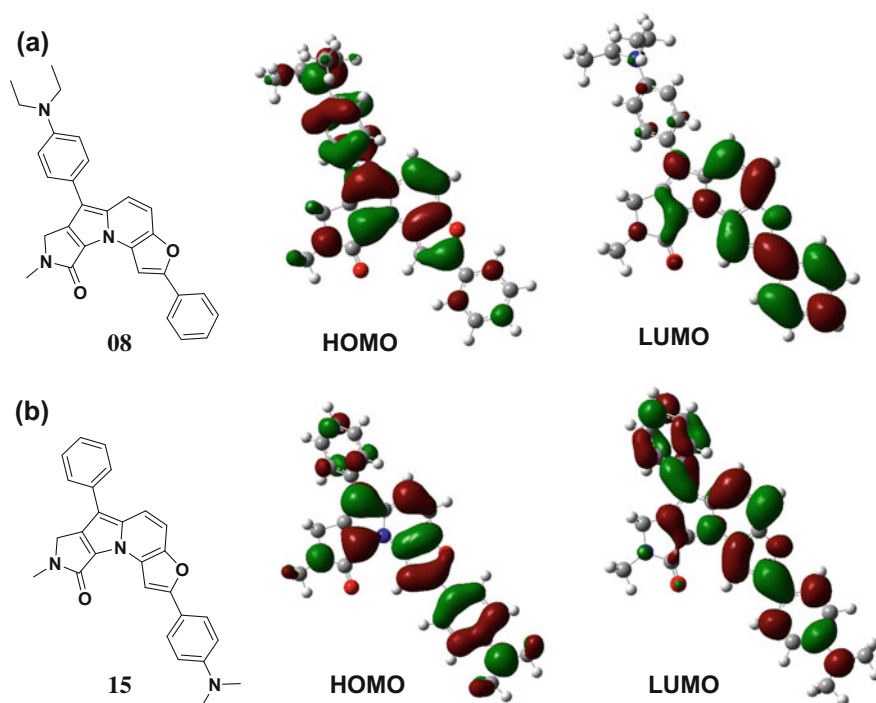


Fig. 4.5 Chemical structures and HOMO and LUMO electron density distribution for **a** R¹ EDG (08) and **b** R² EDG (15), calculated through DFT at the B3LYP/6-31G(d) level

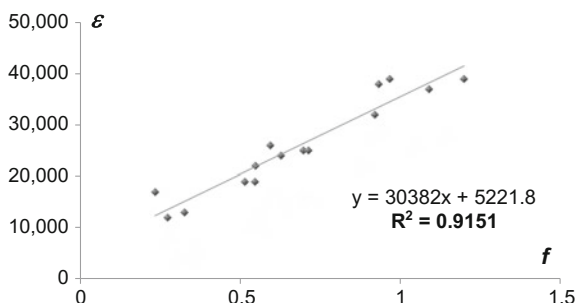
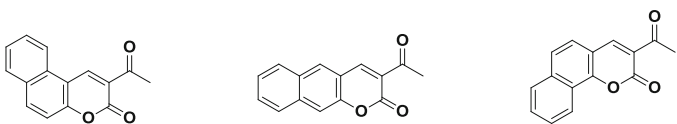


Fig. 4.6 A scattered plot of oscillator strength values and molar absorption coefficients

calculated oscillator strength value (f) was investigated. Surprisingly, a good linear relationship between ϵ and f was determined ($r^2 = 0.92$, Fig. 4.6), suggesting both the effectiveness of the design strategy and the predictability of molar absorptivity. The predictability of molar absorptivity was also confirmed with the calculated f values in different organic fluorophores including coumarin [17a] and BODIPY [17b,c] (Figs. 4.7 and 4.8). Next, through the systematic comparison of emission related properties, interesting patterns were observed in the furoindolizine system. As shown in Table 4.4 and Fig. 4.9, the longer emission wavelengths were



f	425 nm $f=0.0000$ 369 nm $f=0.2532$ 321 nm $f=0.0548$	401 nm $f=0.0202$ 387 nm $f=0.0000$ 334 nm $f=0.4606$	380 nm $f=0.1505$ 377 nm $f=0.0000$ 318 nm $f=0.1583$
ϵ	382 nm 15,100	337 nm 22,500	390 nm 8,600

Fig. 4.7 The calculated oscillator strength values for $S_0 \rightarrow S_1$, $S_0 \rightarrow S_2$ and $S_0 \rightarrow S_3$ (from top to bottom) using DFT/TDDFT at the B3LYP/6-31G(d) level and reported molar absorption coefficients for benzocoumarin derivatives

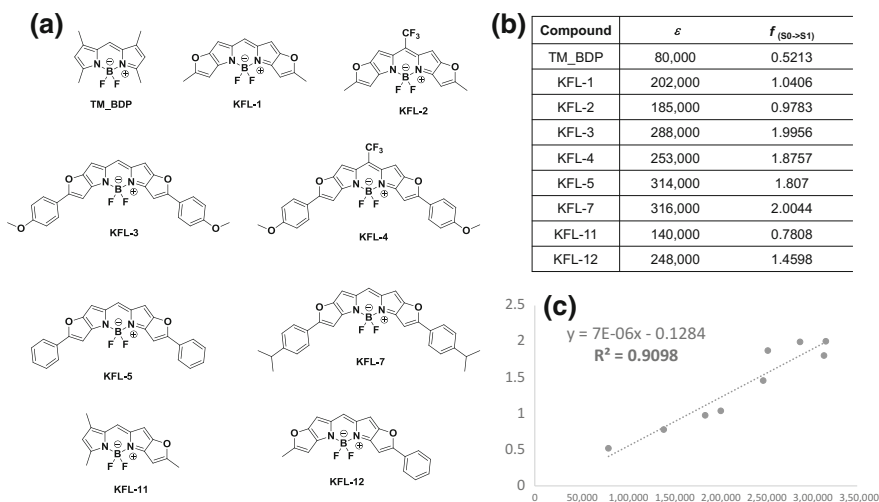


Fig. 4.8 The relationship between the reported molar absorption coefficients and the calculated oscillator strength values for representative BODIPY derivatives. **a** Chemical structures of representative BODIPY derivatives. **b** A table for reported molar absorption coefficients of BODIPY derivatives and the corresponding calculated oscillator strength values for the $S_0 \rightarrow S_1$ transition. **c** A scattered plot of oscillator strength values and molar absorption coefficients of BODIPY derivatives

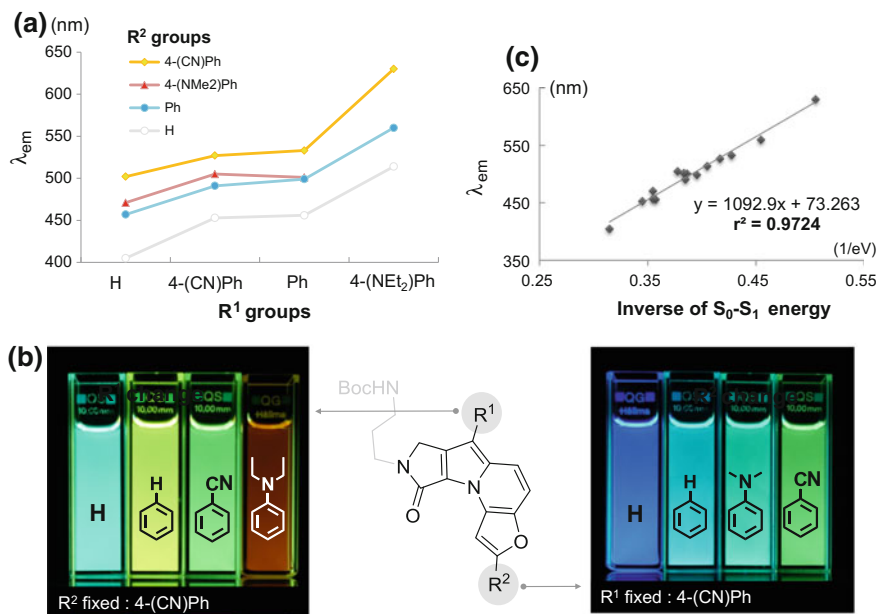


Fig. 4.9 **a** Emission-wavelength changes depending on the R¹ and R² functional groups. **b** Photographic images of the fluorescence emission colors of the representative compounds, irradiated at 365 nm. **c** A scatter plot of the inverse of the S₀-S₁ energy gap versus the maximum emission wavelength

observed when the furoindolizine compounds were equipped with an EDG at the R¹ and an EWG at the R² position. For example for compounds sharing the same R¹ group, the change from a hydrogen to a 4-cyanophenyl group at the R² position caused a ~ 90 nm bathochromic shift in the emission wavelength (Fig. 4.9a). A more drastic bathochromic shift (over 110 nm on average) was observed in the case of 4-diethylaminophenyl moiety at the R¹ position, which was expected as a result of initial design hypothesis. In addition, molecules covering a full visible-color range were successfully constructed with the furoindolizine library, spanning from 405 to 630 nm (Fig. 4.9b). Moreover, the excellent correlation of the theoretical S₀-S₁ energy gap with the experimental emission wavelength ($r^2 = 0.97$) was observed, suggesting the feasibility of the emission-wavelength tuning of the furoindolizine analogues via simple calculations (Fig. 4.9c).

4.2.4 Rational Design of Novel Furoindolizine-Based Fluorescent Compounds and Bioapplication

As a proof of concept, an attention was directed toward the rational design of novel fluorescent molecules displaying desired photophysical properties, including emission wavelengths and enhanced molar absorptivity. In previous reports, SF09, SF16, and SF20 were the brightest fluorophores that matched the fluorescence-filter sets for blue, green, and orange, respectively [10b]. On the basis of these SF analogues, brighter fluorescent compounds using the furoindolizine-based core skeleton were pursued. In fact, the brightness (*B*) of a fluorescence compound can be quantified by its molar absorptivity multiplied by its quantum yield. Therefore, the novel furoindolizine analogues were designed to possess enhanced molar absorptivity with the desired emission wavelengths, matched for each filter set. As shown in Fig. 4.10a, a set of fluorophores (**17**, **18**, and **19**) were designed and synthesized with high accuracy, on the basis of computable *f* values and E gap. It was verified that the

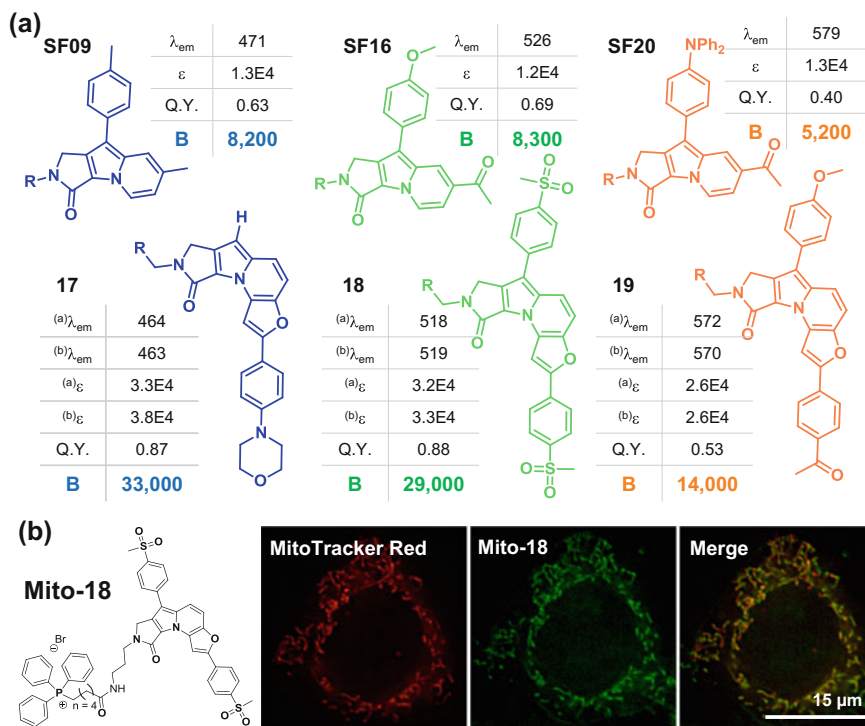


Fig. 4.10 a Rational design of novel furoindolizine-based fluorophores (**17**, **18**, and **19**) for each filter set of blue, green, and orange, respectively, with enhanced brightness in comparison with original SF analogues (SF09, SF16, and SF20). ^(a)Estimated values; ^(b)Observed values. [R = (CH₂)₂NHBoc] b Chemical structure of **Mito-18** and fluorescent live cell images in HeLa human cervical cancer cells stained by MitoTracker Red and **Mito-18**

brightness of the newly designed organic fluorophores exhibited 4.0-, 3.5-, and 2.7-fold enhancements in blue-, green-, and orange-spectral areas, respectively. To demonstrate the applicability of newly developed furoindolizine-based fluorescent materials in biological systems, a mitochondria probe, **Mito-18**, were designed via incorporation of triphenylphosphonium moiety at the N8 linker site. As shown in Fig. 4.10b, **Mito-18** exhibited an excellent sensitivity and selectivity toward mitochondria, confirmed by merged image with MitoTracker Red in live cell conditions, suggesting a reasonable solubility and stability of furoindolizine analogues as potential monitoring tools in the biomedical research.

4.3 Conclusion

In this chapter, a rational design strategy for the improvement of molar absorptivity of organic fluorophores was suggested guided by computable oscillator strength value. Using this strategy, an unprecedented furo[3,2-*e*]indolizine-based fluorescent core skeleton was successfully discovered from Seoul-Fluor with enhanced molar absorptivity. Through the synthesis of a series of furoindolizine analogues, it was clearly showed that the computable values, such as the oscillator strength values and the theoretical S_0-S_1 energy gap, can serve as excellent guideline for predicting the photophysical properties, such as the molar absorptivity and the emission wavelength. Moreover, the design capability was demonstrated by the rational discovery of three fluorescent dyes having significantly enhanced brightness, and their emission was matched with each fluorescent filter set for practical bioapplication. It is expected that this design strategy can be usefully applied to development of unexplored organic fluorophores and light-harvesting materials with desirable photophysical properties.

4.4 Experimental Section

4.4.1 General Information

a. Basic characterization

^1H and ^{13}C NMR spectra were recorded on an Agilent 400-MR (Agilent Technologies) and Varian Inova-500 (Varian Associates), and chemical shifts were measured in ppm downfield from internal tetramethylsilane (TMS) standard. Multiplicity was indicated as follows: s (singlet); d (doublet); t (triplet); q (quartet); m (multiplet); dd (doublet of doublet); dt (doublet of triplet); br s (broad singlet), br

d (broad doublet) etc. Coupling constants were reported in Hz. Low resolution mass spectrometry (LRMS) was obtained by LC/MS system, Finnigan MSQ_{plus} Surveyer (Thermo Scientific) or 6120 Quadrupole LC/MS (Agilent Technologies). High resolution mass spectrometry (HRMS) of furoindolizine fluorescence compounds was further confirmed by Ultra High Resolution ESI Q-TOF mass spectrometer (Bruker).

b. Absorption and fluorescence related properties

Absorption spectra and molar absorption coefficient at the absorption maxima of furoindolizine fluorescence compounds were measured by UV-VIS spectrophotometer UV-1650PC (Shimadzu, Japan). Emission spectra was measured by Cary Eclipse Fluorescence spectrophotometer (Varian Associates) and absolute quantum yield was measured by QE-2000 (Otsuka Electronics).

c. Chemical and bio reagents

3-Bromopropylamine hydrobromide, di-*tert*-butyl dicarbonate, propargyl amine, triethylamine (TEA), bromoacetyl bromide, 1,8-diazabicyclo[5.4.0]undec-7-ene (DBU), copper(I) iodide (CuI), furo[3,2-*b*]pyridine, 2-phenylfuro[3,2-*b*]pyridine, iodobenzene, 4-iodobenzonitrile, 4-iodoanisole, 4-bromophenyl methyl sulfone, palladium acetate (PdOAc), bis(triphenylphosphine)palladium(II) dichloride (PdCl₂(PPh₃)₂), silver acetate (AgOAc), potassium acetate (KOAc), tetrabutylammonium fluoride (TBAF) solution, silver trifluoromethanesulfonate, and all terminal alkyne derivatives were purchased from Sigma-Aldrich, Tokyo Chemical Industry Co., Ltd or Acros, and used without further purification. The progress of reaction was monitored using thin-layer chromatography (TLC) (silica gel 60, F₂₅₄ 0.25 mm), and components were visualized by observation under UV light (254 and 365 nm) or by treating the TLC plates with anisaldehyde, KMnO₄, and ninhydrin followed by heating. Solvents were purchased from commercial vendors and used without further purification. Cell culture reagents including fetal bovine serum, culture media, and antibiotic-antimycotic solution were purchased from GIBCO. MitoTracker Red CMXRos was purchased from Molecular Probes. The culture dish and glass-bottom dish were purchased from CORNING.

d. Quantum mechanical calculations

All quantum mechanical calculations were performed in Gaussin09 W. The ground state structures of furoindolizine compounds, Seoul-Fluor derivatives, and benzocoumarin derivatives were optimized using density functional theory (DFT) at the B3LYP/6-31G* level. The oscillator strength values were calculated through time dependent density functional theory (TD-DFT) with the optimized structures of the ground state. The Energy gap between the S₀-S₁ states of furoindolizine analogues were calculated based on the optimized structure of the first-excited state to compare with experimental emission properties. Calculation for BODIPY derivatives were performed in the Materials Studio[®] 4.2 program (Accelrys Software, Inc.) at the GAA/PBE/DNP level in DMol3 to reduce the calculation cost.

e. Fluorescence microscopy

Fluorescence microscopy studies were carried with DeltaVision Elite imaging system (GE Healthcare) equipped with a sCMOS camera. Objective lenses are supported by Olympus IX-71 (Olympus) inverted microscope equipped with Plan APO 60X/Oil (PLAPON60 × O), 1.42 NA, WD 0.15 mm. DeltaVision Elite uses a solid state illumination system, InSightSSI fluorescence illumination module. Four-color standard filter set (GE Healthcare, 52-852113-003) was used to detect fluorescence signals.

4.4.2 *Experimental Procedure for Live Cell Fluorescence Image*

1. Cell culture

HeLa cell line (human cervical carcinoma cells) was obtained from American Type Culture Collection (ATCC). HeLa cells were cultured in RPMI 1640 (GIBCO) supplemented with heat-inactivated 10% (v/v) fetal bovine serum (FBS, GIBCO) and 1% (v/v) antibiotic-antimycotic agent (GIBCO). HeLa cell line was maintained in humidified atmosphere of 5% CO₂ and 95% air at 37 °C, and cultured in 100 mm cell culture dish (CORNING).

2. Mitochondria staining experiment with Mito-18 and MitoTracker Red

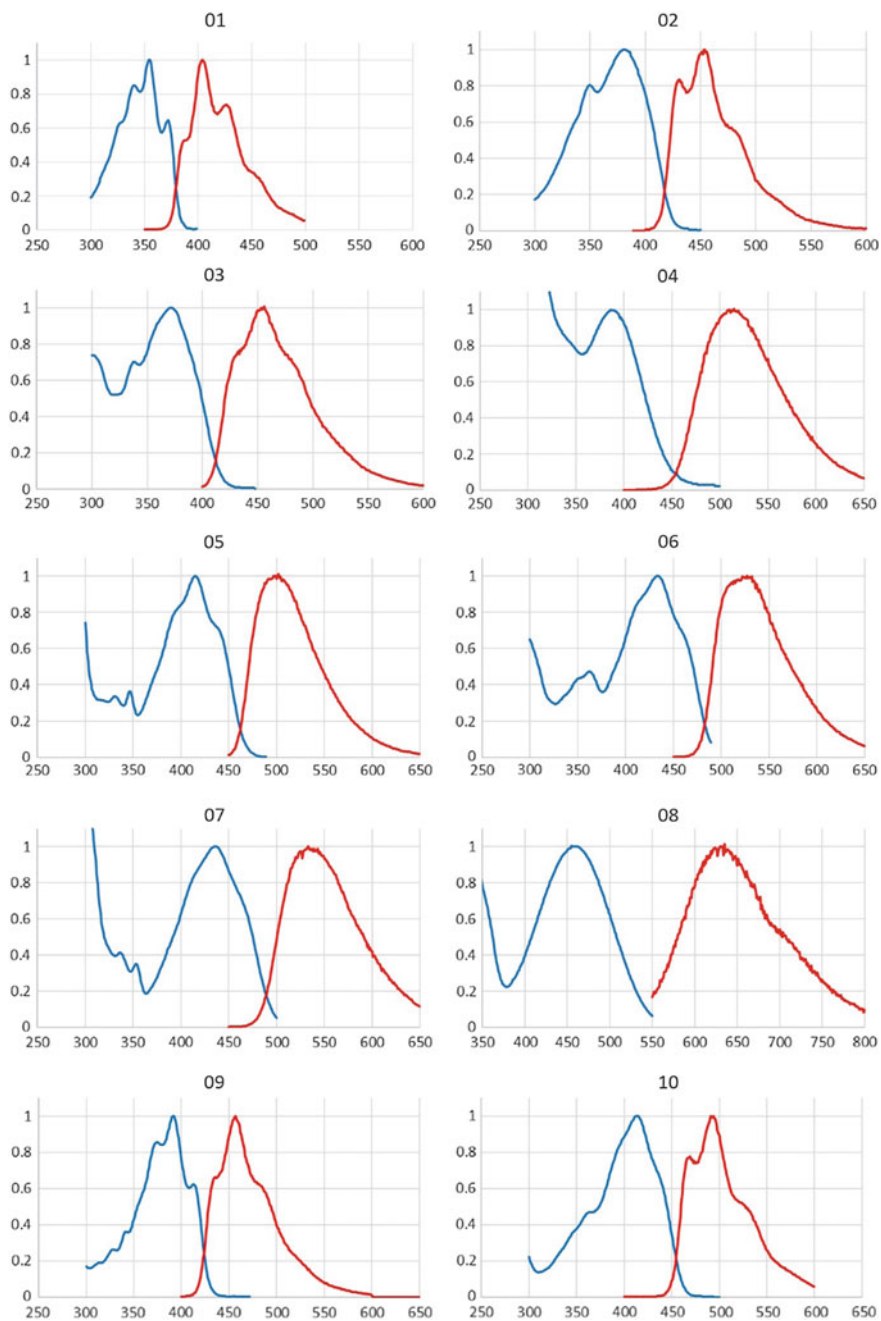
HeLa cells were seeded on cover glass bottom dish and incubated at 5% CO₂, 37 °C for overnight. Cells are treated with 20 μM **Mito-18** in media for 1 h. After 1 h, 20 nM MitoTracker Red CMXRos (Life Technologies) was added to cells, and incubate for 30 min. After the treatment, dyes were washed with PBS buffer for 3 times and then fluorescence images were taken by fluorescence microscopy under PBS buffer with DeltaVision Elite imaging system (GE Healthcare) equipped with 60X/1.42 NA oil lens. Fluorescence signal of each probes were obtained using FITC filter (**Mito-18**, Ex; 475 nm with 28 nm bandwidth, Em; 525 nm with 48 nm bandwidth) and Cy5 filter (MitoTracker Red CMXRox, Ex; 632 nm with 22 nm bandwidth, Em; 670 nm with 34 nm bandwidth).

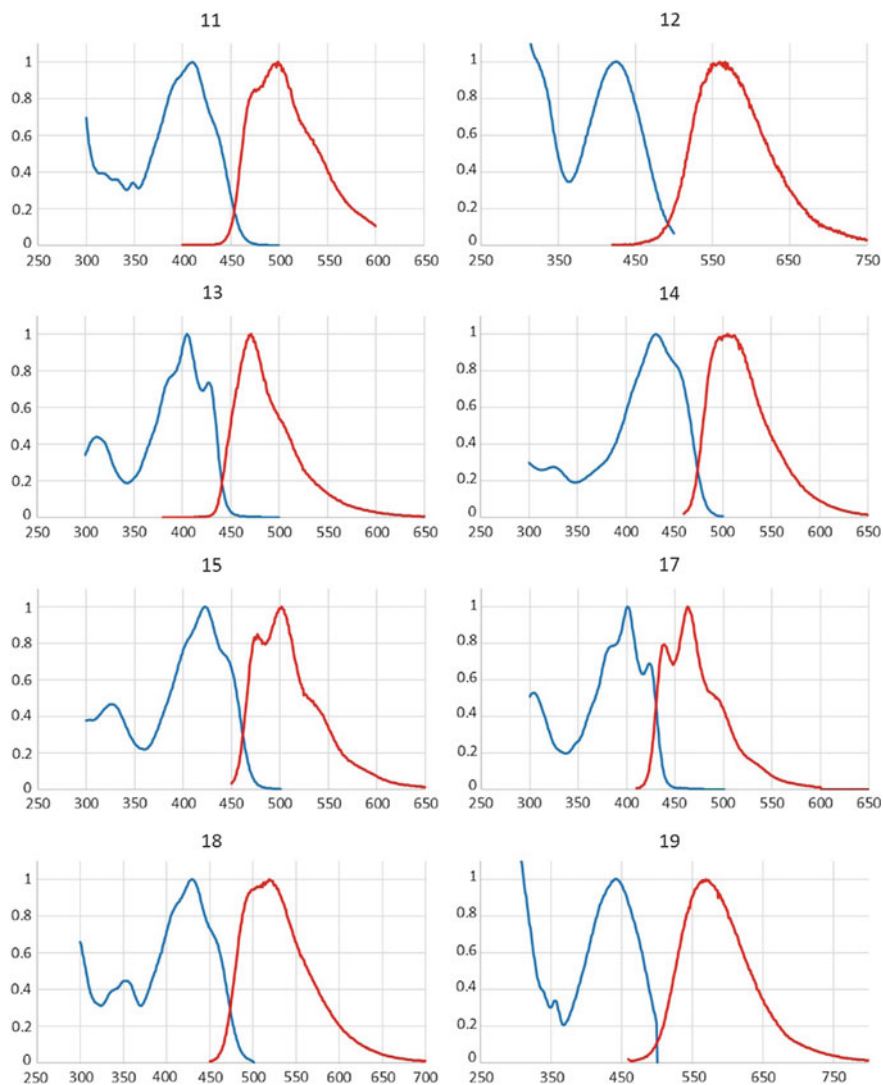
Absorption and emission spectra of all furoindolizine compounds

- Horizontal axis: wavelength (nm)
- Vertical axis: normalized intensity (a.u.)

Left blue line: absorption spectra

Right red line: emission spectra





4.4.3 Computational Results of Furoindolizine Analogues

# cpd	Electronic transition	Energy (eV)	f (oscillator strength)
01	$S_0 \rightarrow S_1$	3.7316 eV 332.26 nm	$f = 0.2348$
	$S_0 \rightarrow S_2$	4.1879 eV 296.06 nm	$f = 0.0420$
	$S_0 \rightarrow S_3$	4.7567 eV 260.65 nm	$f = 0.0001$
02	$S_0 \rightarrow S_1$	3.3275 eV 372.60 nm	$f = 0.5467$
	$S_0 \rightarrow S_2$	3.7156 eV 333.68 nm	$f = 0.0712$
	$S_0 \rightarrow S_3$	4.0517 eV 306.00 nm	$f = 0.0142$
03	$S_0 \rightarrow S_1$	3.4905 eV 355.21 nm	$f = 0.3259$
	$S_0 \rightarrow S_2$	4.0271 eV 307.87 nm	$f = 0.0706$
	$S_0 \rightarrow S_3$	4.2297 eV 293.13 nm	$f = 0.1535$
04	$S_0 \rightarrow S_1$	3.2084 eV 386.44 nm	$f = 0.2737$
	$S_0 \rightarrow S_2$	3.8527 eV 321.81 nm	$f = 0.0593$
	$S_0 \rightarrow S_3$	4.0629 eV 305.16 nm	$f = 0.0159$
05	$S_0 \rightarrow S_1$	2.9199 eV 424.62 nm	$f = 0.6262$
	$S_0 \rightarrow S_2$	3.8066 eV 325.71 nm	$f = 0.1642$
	$S_0 \rightarrow S_3$	4.0519 eV 305.99 nm	$f = 0.0621$
06	$S_0 \rightarrow S_1$	2.8076 eV 441.61 nm	$f = 0.9179$
	$S_0 \rightarrow S_2$	3.4494 eV 359.43 nm	$f = 0.2282$
	$S_0 \rightarrow S_3$	3.7989 eV 326.37 nm	$f = 0.0862$
07	$S_0 \rightarrow S_1$	2.7515 eV 450.61 nm	$f = 0.7117$
	$S_0 \rightarrow S_2$	3.7433 eV 331.21 nm	$f = 0.1957$
	$S_0 \rightarrow S_3$	3.8626 eV 320.99 nm	$f = 0.1392$
08	$S_0 \rightarrow S_1$	2.4405 eV 508.02 nm	$f = 0.5137$
	$S_0 \rightarrow S_2$	3.2408 eV 382.57 nm	$f = 0.3306$
	$S_0 \rightarrow S_3$	3.5917 eV 345.20 nm	$f = 0.1929$
09	$S_0 \rightarrow S_1$	3.2300 eV 383.85 nm	$f = 0.5929$
	$S_0 \rightarrow S_2$	3.9430 eV 314.44 nm	$f = 0.0602$
	$S_0 \rightarrow S_3$	4.3047 eV 288.02 nm	$f = 0.0179$
10	$S_0 \rightarrow S_1$	3.0152 eV 411.20 nm	$f = 0.9641$
	$S_0 \rightarrow S_2$	3.4429 eV 360.11 nm	$f = 0.0539$
	$S_0 \rightarrow S_3$	3.8750 eV 319.96 nm	$f = 0.0503$
11	$S_0 \rightarrow S_1$	3.0455 eV 407.11 nm	$f = 0.6955$
	$S_0 \rightarrow S_2$	3.8669 eV 320.63 nm	$f = 0.0636$
	$S_0 \rightarrow S_3$	3.9850 eV 311.12 nm	$f = 0.2064$
12	$S_0 \rightarrow S_1$	2.8039 eV 442.18 nm	$f = 0.5454$
	$S_0 \rightarrow S_2$	3.6142 eV 343.05 nm	$f = 0.2764$
	$S_0 \rightarrow S_3$	3.7556 eV 330.13 nm	$f = 0.0947$
13	$S_0 \rightarrow S_1$	3.1553 eV 392.94 nm	$f = 0.9299$
	$S_0 \rightarrow S_2$	3.7940 eV 326.79 nm	$f = 0.0179$
	$S_0 \rightarrow S_3$	4.0536 eV 305.86 nm	$f = 0.0444$

(continued)

(continued)

# cpd	Electronic transition	Energy (eV)	f (oscillator strength)
14	$S_0 \rightarrow S_1$	2.8613 eV 433.32 nm	$f = 1.1950$
	$S_0 \rightarrow S_2$	3.2935 eV 376.45 nm	$f = 0.1272$
	$S_0 \rightarrow S_3$	3.6195 eV 342.55 nm	$f = 0.0098$
15	$S_0 \rightarrow S_1$	3.0058 eV 412.48 nm	$f = 1.0864$
	$S_0 \rightarrow S_2$	3.6786 eV 337.04 nm	$f = 0.0622$
	$S_0 \rightarrow S_3$	3.8175 eV 324.78 nm	$f = 0.1140$
16	$S_0 \rightarrow S_1$	2.8657 eV 432.65 nm	$f = 0.8915$
	$S_0 \rightarrow S_2$	3.5335 eV 350.89 nm	$f = 0.3607$
	$S_0 \rightarrow S_3$	3.7179 eV 333.48 nm	$f = 0.0784$
17	$S_0 \rightarrow S_1$	3.1616 eV 392.15 nm	$f = 0.9272$
	$S_0 \rightarrow S_2$	3.8097 eV 325.44 nm	$f = 0.0533$
	$S_0 \rightarrow S_3$	4.0779 eV 304.04 nm	$f = 0.0608$
18	$S_0 \rightarrow S_1$	2.8862 eV 429.58 nm	$f = 0.8972$
	$S_0 \rightarrow S_2$	3.6101 eV 343.43 nm	$f = 0.2309$
	$S_0 \rightarrow S_3$	3.8490 eV 322.12 nm	$f = 0.0618$
19	$S_0 \rightarrow S_1$	2.6442 eV 468.90 nm	$f = 0.6753$
	$S_0 \rightarrow S_2$	3.5330 eV 350.93 nm	$f = 0.0000$
	$S_0 \rightarrow S_3$	3.6495 eV 339.73 nm	$f = 0.2998$

4.4.4 Prediction of Photophysical Properties for 17, 18 and 19

1. From Fig. 4.6

The equation for ε estimation = $30382f + 5221.8$
(f : calculated oscillator strength values)

2. From Fig. 4.9c

The equation for λ_{em} estimation = $1092.9x + 73.263$,
(x : calculated $1/eV$)

	f (calculated oscillator strength values for $S_0 \rightarrow S_1$)	Estimated ε	x (calculated $1/eV$)	Estimated λ_{em}
17	0.9272	33,392	0.357935	464 nm
18	0.8972	32,480	0.406835	518 nm
19	0.6753	25,738	0.456496	572 nm

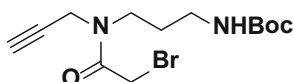
4.4.5 Synthetic Procedure and Compound Characterization

Preparation of *tert*-butyl (3-(prop-2-yn-1-ylamino)propyl)carbamate was conducted through the previous synthetic report.²

Preparation of *tert*-butyl (3-(2-bromo-*N*-(prop-2-yn-1-yl)acetamido)propyl)carbamate

To a stirred solution of bromoacetyl bromide (2.0 equiv.) in anhydrous CH₂Cl₂ (0.1 M) at -78 °C under argon, added dropwise a *tert*-butyl (3-(prop-2-yn-1-ylamino)propyl)carbamate (1 equiv.) and 3 equiv. of triethylamine (TEA) in CH₂Cl₂ (0.1 M) over a period of 1 h. The solution was stirred at -78 °C for 2 h. When the reaction was completed checked by TLC, saturated NaHCO₃(aq) was added to the solution and the organic material was extracted with CH₂Cl₂. The combined organic extracts were dried over Na₂SO₄(s), and concentrated *in vacuo* after filtration. The residue was purified by silica-gel flash column chromatography to afford the desired product. (Transparent oil, Y: 83%).

tert-Butyl (3-(2-bromo-*N*-(prop-2-yn-1-yl)acetamido)propyl)carbamate



¹H NMR (2:1 rotamer ratio, asterisks denote minor rotamer peaks, 400 MHz, CDCl₃) δ 5.23 (br s, 1H), 4.76* (br s, 1H), 4.23* (d, *J* = 2.0 Hz, 2H), 4.14 (d, *J* = 2.0 Hz, 2H), 3.96 (s, 2H), 3.89* (s, 2H), 3.56–3.52 (m, 2H), 3.56–3.52* (m, 2H), 3.23–3.18* (m, 2H), 3.13–3.09 (m, 2H), 2.38 (br s, 1H), 2.26* (br s, 1H), 1.94–1.88* (m, 2H), 1.79–1.73 (m, 2H), 1.45* (s, 9H), 1.44 (s, 9H); ¹³C NMR (100 MHz, CDCl₃) δ 167.5, 166.4*, 156.2, 79.1, 78.2*, 78.0, 73.7, 72.6*, 45.9*, 44.2, 38.2, 38.0*, 37.1, 34.9*, 29.3*, 28.5, 28.5*, 27.6, 26.1, 25.9*; LRMS (ESI) *m/z* calcd for C₁₃H₂₂BrN₂O₃ [M + H]⁺: 333.08; Found: 332.92.

General procedure for preparation of furopyridine derivatives

(a) Terminal alkyne derivatives required to prepare various furopyridine derivatives were commercially available, except 1-(4-ethynylphenyl)ethanone and 4-(4-ethynylphenyl) morpholine, which were synthesized by reported procedure.^{3,4}

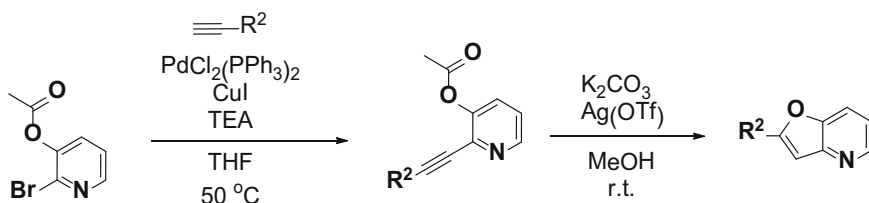
(b) Preparation of 2-bromopyridin-3-yl acetate was conducted refer to the reported synthetic procedure.⁵

²Angew. Chem. Int. Ed. **2014**, 53, 1346–1350.

³J. Am. Chem. Soc. **2006**, 128, 12370–12371.

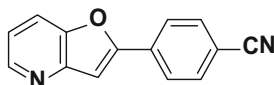
⁴Chem. Comm. **2003**, 17, 2146–2147.

⁵ACS Med. Chem. Lett. **2014**, 5, 1284–1289.



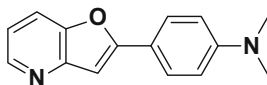
To a suspension of 2-bromopyridin-3-yl acetate (1.0 equiv.), PdCl₂(PPh₃)₂ (3 mol%), and CuI (6 mol%) in THF (0.1 M), in the presence of TEA (15.0 equiv.), was added a terminal alkyne derivative (2.0 equiv.) under argon atmosphere with vigorous stirring at 50 °C. After the reaction was completed checked by TLC, the resulting solution was filtered through Celite and concentrated *in vacuo*. After that, to the solution of filtered residue in MeOH (0.1 M), were added potassium carbonate (3.0 equiv.) and silver triflate (10 mol%) with stirring at room temperature. When the reaction was completed checked by TLC, brine was added to the solution and the organic material was extracted with ethyl acetate. The combined organic extracts were dried over Na₂SO₄(s), and concentrated under reduced pressure after filtration. The residue was purified by silica-gel flash column chromatography to afford the desired furopyridine derivatives.

4-(Furo[3,2-*b*]pyridin-2-yl)benzonitrile

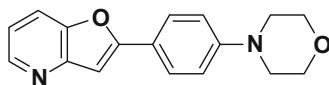


Yield: 45%; ¹H NMR (400 MHz, CDCl₃) δ 8.59 (d, *J* = 4.4 Hz, 1H), 8.00 (d, *J* = 8.4 Hz, 2H), 7.81 (d, *J* = 8.4 Hz, 1H), 7.77 (d, *J* = 8.8 Hz, 2H), 7.37 (s, 1H), 7.28 (dd, *J* = 4.4, 8.4 Hz, 1H); ¹³C NMR (100 MHz, CDCl₃) δ 157.1, 148.6, 148.4, 146.9, 133.8, 132.8, 125.7, 120.0, 118.6, 118.4, 112.7, 105.4; LRMS (ESI) *m/z* calcd for C₁₄H₉N₂O [M + H]⁺: 221.07; Found: 220.88.

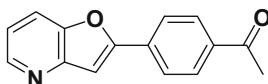
4-(Furo[3,2-*b*]pyridin-2-yl)-*N,N*-dimethylaniline



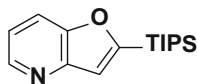
Yield: 77%; ¹H NMR (400 MHz, CDCl₃) δ 8.46 (br s, 1H), 7.75 (d, *J* = 8.8 Hz, 2H), 7.66 (d, *J* = 8.0 Hz, 1H), 7.09 (dd, *J* = 4.6, 8.2 Hz, 1H), 6.97 (s, 1H), 6.74 (d, *J* = 8.8 Hz, 2H), 3.00 (s, 6H); ¹³C NMR (100 MHz, CDCl₃) δ 161.0, 151.2, 150.0, 147.7, 145.6, 126.7, 117.7, 117.5, 117.0, 112.0, 99.0, 40.3; LRMS (ESI) *m/z* calcd for C₁₅H₁₅N₂O [M + H]⁺: 239.12; Found: 238.98.

2-(4-Morpholinophenyl)furo[3,2-*b*]pyridine

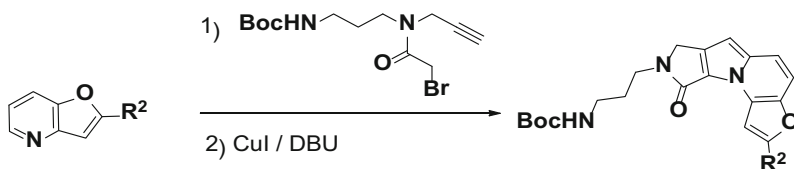
Yield: 63%; ^1H NMR (400 MHz, CDCl_3) δ 8.48 (d, $J = 4.0$ Hz, 1H), 7.81 (d, $J = 9.2$ Hz, 2H), 7.71 (d, $J = 8.0$ Hz, 1H), 7.15 (dd, $J = 4.6, 8.2$ Hz, 1H), 7.05 (s, 1H), 6.98 (d, $J = 8.8$ Hz, 2H), 3.89 (t, $J = 4.8$ Hz, 4H), 3.27 (t, $J = 5.0$ Hz, 4H); ^{13}C NMR (100 MHz, CDCl_3) δ 160.2, 152.1, 149.7, 147.9, 145.9, 126.7, 121.0, 118.2, 117.4, 115.1, 100.4, 66.8, 48.5; LRMS (ESI) m/z calcd for $\text{C}_{17}\text{H}_{17}\text{N}_2\text{O}_2$ $[\text{M} + \text{H}]^+$: 281.13; Found: 281.03.

1-(4-(Furo[3,2-*b*]pyridin-2-yl)phenyl)ethanone

Yield: 54%; ^1H NMR (400 MHz, CDCl_3) δ 8.57 (br s, 1H), 8.06 (d, $J = 8.0$ Hz, 2H), 7.98 (d, $J = 8.0$ Hz, 2H), 7.80 (d, $J = 8.4$ Hz, 1H), 7.35 (s, 1H), 7.28–7.24 (m, 1H), 2.65 (s, 3H); ^{13}C NMR (100 MHz, CDCl_3) δ 197.3, 158.2, 148.6, 148.5, 146.5, 137.4, 133.8, 129.1, 125.4, 119.6, 118.3, 104.6, 26.8; LRMS (ESI) m/z calcd for $\text{C}_{15}\text{H}_{12}\text{NO}_2$ $[\text{M} + \text{H}]^+$: 238.09; Found: 238.1.

2-(Triisopropylsilyl)furo[3,2-*b*]pyridine

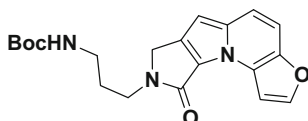
Yield: 90%; ^1H NMR (500 MHz, acetone- d_6) δ 8.52 (dd, $J = 1.3, 4.8$ Hz, 1H), 7.91 (d, $J = 8.5$ Hz, 1H), 7.32 (d, $J = 1.0$ Hz, 1H), 7.28 (dd, $J = 4.5, 8.5$ Hz, 1H), 1.50–1.44 (m, 3H), 1.22–1.13 (m, 18H); ^{13}C NMR (125 MHz, acetone- d_6) δ 166.0, 151.3, 149.0, 146.7, 120.4, 119.8, 118.4, 18.9, 11.7; LRMS (ESI) m/z calcd for $\text{C}_{16}\text{H}_{26}\text{NOSi}$ $[\text{M} + \text{H}]^+$: 276.18; Found: 276.2.

General procedure for preparation of furoindolizine-based core skeletons

To a solution of *tert*-butyl (3-(2-bromo-*N*-(prop-2-yn-1-yl)acetamido)propyl)-carbamate (1.2 equiv.) in acetonitrile (0.1 M), was added a furopyridine derivative (1.0 equiv.), and the solution was stirred at 80 °C overnight. After the complete

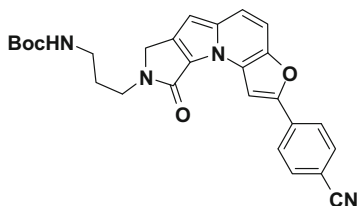
consumption of starting materials, copper iodide (1.0 equiv.) was added to a reaction mixture followed by slow addition of 1,8-diazabicycloundec-7-ene (DBU) (3.0 equiv.) at room temperature with vigorous stirring. When the reaction was completed checked by TLC, the resulting mixture was filtered through the short bed of silica gel and concentrated *in vacuo*. The residue was purified by silica-gel flash column chromatography to afford the desired furoindolizine-based core skeletons. Some furopyridine derivatives used different metal sources instead of copper iodide; AgOTf was used in the case of R² = 4-(acetyl)Ph group, and Ag₂O was used in the case of R² = 4-(NMe₂)Ph and 4-(morpholino)Ph.

***tert*-Butyl (3-(9-oxo-7*H*-furo[3,2-*e*]pyrrolo[3,4-*b*]indolizin-8(9*H*)-yl)propyl)carbamate (01)**



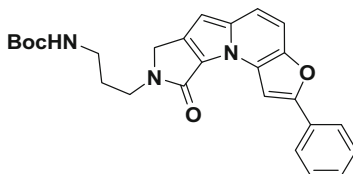
Yield: 19%; ¹H NMR (400 MHz, CDCl₃) δ 7.85 (d, *J* = 2.0 Hz, 1H), 7.62 (d, *J* = 2.4 Hz, 1H), 7.29–7.23 (m, 2H), 6.45 (s, 1H), 5.44 (br s, 1H), 4.35 (s, 2H), 3.66 (t, *J* = 6.2 Hz, 2H), 3.17 (q, *J* = 6.1 Hz, 2H), 1.86–1.79 (m, 2H), 1.44 (s, 9H); ¹³C NMR (100 MHz, CDCl₃) δ 162.2, 156.2, 143.3, 143.1, 138.4, 135.8, 125.7, 121.6, 114.3, 109.7, 104.8, 94.9, 79.0, 46.6, 40.1, 37.4, 28.9, 28.5; HRMS (ESI) *m/z* calcd for C₂₀H₂₃N₃NaO₄ [M + Na]⁺: 392.1581; Found: 392.1581.

***tert*-Butyl (3-(2-(4-cyanophenyl)-9-oxo-7*H*-furo[3,2-*e*]pyrrolo[3,4-*b*]indolizin-8(9*H*)-yl)propyl)carbamate (05)**



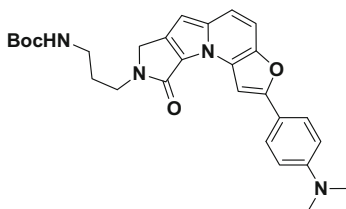
Yield: 49%; ¹H NMR (400 MHz, CDCl₃) δ 8.19 (s, 1H), 7.92 (d, *J* = 8.8 Hz, 2H), 7.68 (d, *J* = 8.8 Hz, 2H), 7.35 (d, *J* = 9.6 Hz, 1H), 7.26 (d, *J* = 8.8 Hz, 1H), 6.51 (s, 1H), 5.36 (br s, 1H), 4.40 (s, 2H), 3.68 (t, *J* = 6.4 Hz, 2H), 3.21 (br d, *J* = 5.6 Hz, 2H), 1.87–1.84 (m, 2H), 1.46 (s, 9H); ¹³C NMR (100 MHz, CDCl₃) δ 162.1, 156.2, 151.8, 143.9, 138.3, 136.1, 133.9, 132.7, 127.1, 124.7, 122.3, 118.9, 115.9, 111.3, 109.2, 102.1, 95.9, 79.2, 46.8, 40.3, 37.6, 29.1, 28.6; HRMS (ESI) *m/z* calcd for C₂₇H₂₆N₄NaO₄ [M + Na]⁺: 493.1846; Found: 493.1847.

tert-Butyl (3-(9-oxo-2-phenyl-7H-furo[3,2-e]pyrrolo[3,4-b]indolizin-8(9H)-yl)propyl)carbamate (09)



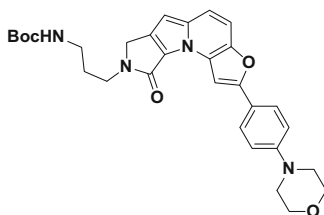
Yield: 35%; ^1H NMR (400 MHz, CD_2Cl_2) δ 8.08 (s, 1H), 7.92 (d, $J = 7.2$ Hz, 2H), 7.47 (t, $J = 7.6$ Hz, 2H), 7.38–7.31 (m, 3H), 6.51 (s, 1H), 5.50 (br s, 1H), 4.37 (s, 2H), 3.65 (t, $J = 6.2$ Hz, 2H), 3.13 (q, $J = 6.3$ Hz, 2H), 1.83–1.76 (m, 2H), 1.44 (s, 9H); ^{13}C NMR (100 MHz, CDCl_3) δ 162.3, 156.3, 154.4, 142.9, 138.6, 136.0, 130.1, 128.9, 128.6, 127.5, 124.7, 121.6, 114.1, 109.4, 99.4, 95.1, 79.1, 46.7, 40.3, 37.6, 29.0, 28.6; HRMS (ESI) m/z calcd for $\text{C}_{26}\text{H}_{27}\text{N}_3\text{NaO}_4$ [$\text{M} + \text{Na}$] $^+$: 468.1894; Found: 468.1893.

tert-Butyl (3-(2-(4-(dimethylamino)phenyl)-9-oxo-7H-furo[3,2-e]pyrrolo[3,4-b]indolizin-8(9H)-yl)propyl)carbamate (13)



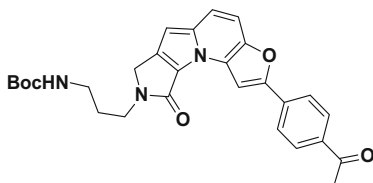
Yield: 26%; ^1H NMR (400 MHz, CDCl_3) δ 7.87 (s, 1H), 7.78 (d, $J = 9.2$ Hz, 2H), 7.25 (d, $J = 6.4$ Hz, 1H), 7.19 (d, $J = 9.6$ Hz, 1H), 6.77 (d, $J = 8.8$ Hz, 2H), 6.42 (s, 1H), 5.40 (br s, 1H), 4.36 (s, 2H), 3.67 (t, $J = 6.2$ Hz, 2H), 3.19 (br d, $J = 5.6$ Hz, 2H), 3.03 (s, 6H), 1.85–1.82 (m, 2H), 1.45 (s, 9H); ^{13}C NMR (100 MHz, CDCl_3) δ 162.4, 156.3, 155.8, 150.7, 142.0, 138.9, 136.1, 128.1, 126.1, 121.1, 118.3, 112.5, 112.2, 109.4, 96.4, 94.5, 79.1, 46.7, 40.4, 40.3, 37.5, 29.1, 28.6; HRMS (ESI) m/z calcd for $\text{C}_{28}\text{H}_{32}\text{N}_4\text{NaO}_4$ [$\text{M} + \text{Na}$] $^+$: 511.2316; Found: 511.2317.

tert-Butyl (3-(2-(4-morpholinophenyl)-9-oxo-7H-furo[3,2-e]pyrrolo[3,4-b]indolizin-8(9H)-yl)propyl)carbamate (17)



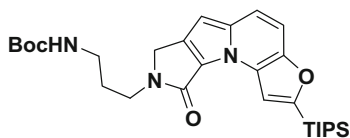
Yield: 22%; ^1H NMR (400 MHz, CDCl_3) δ 7.94 (s, 1H), 7.81 (d, $J = 8.4$ Hz, 2H), 7.28–7.21 (m, 2H), 6.96 (d, $J = 8.4$ Hz, 2H), 6.44 (s, 1H), 5.38 (br s, 1H), 4.37 (s, 2H), 3.89 (t, $J = 4.6$ Hz, 4H), 3.67 (t, $J = 6.4$ Hz, 2H), 3.25 (t, $J = 4.6$ Hz, 4H), 3.20 (q, $J = 5.9$ Hz, 2H), 1.87–1.81 (m, 2H), 1.45 (s, 9H); ^{13}C NMR (100 MHz, CDCl_3) δ 162.4, 156.3, 155.0, 151.4, 142.4, 138.8, 136.1, 127.9, 126.0, 121.6, 121.3, 115.3, 113.2, 109.4, 97.5, 94.7, 79.1, 66.9, 48.7, 46.7, 40.3, 37.6, 29.1, 28.6; HRMS (ESI) m/z calcd for $\text{C}_{30}\text{H}_{34}\text{N}_4\text{NaO}_5$ $[\text{M} + \text{Na}]^+$: 553.2421; Found: 553.2421.

***tert*-Butyl (3-(2-(4-acetylphenyl)-9-oxo-7H-furo[3,2-*e*]pyrrolo[3,4-*b*]indolizin-8(9H)-yl)propyl)carbamate**



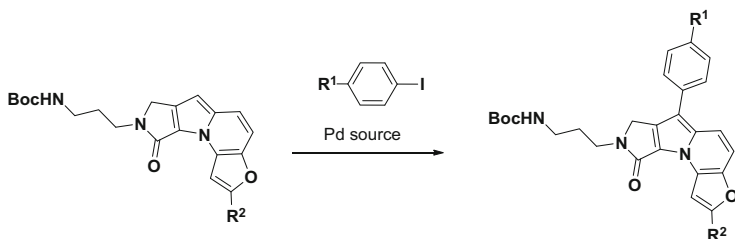
Yield: 29%; ^1H NMR (400 MHz, CDCl_3) δ 8.07 (s, 1H), 7.92 (d, $J = 8.4$ Hz, 2H), 7.84 (d, $J = 8.0$ Hz, 2H), 7.26 (d, $J = 9.6$ Hz, 1H), 7.20 (d, $J = 9.2$ Hz, 1H), 6.42 (s, 1H), 5.41 (br s, 1H), 4.33 (s, 2H), 3.66 (t, $J = 6.2$ Hz, 2H), 3.21 (br d, $J = 6.0$ Hz, 2H), 2.59 (s, 3H), 1.87–1.84 (m, 2H), 1.46 (s, 9H); ^{13}C NMR (100 MHz, CDCl_3) δ 197.2, 162.0, 156.2, 152.7, 143.5, 138.3, 136.1, 135.9, 133.9, 128.9, 127.1, 124.2, 121.9, 115.2, 109.1, 101.3, 95.6, 79.2, 46.7, 40.3, 37.6, 29.0, 28.5, 26.6; LRMS (ESI) m/z calcd for $\text{C}_{28}\text{H}_{30}\text{N}_3\text{O}_5$ $[\text{M} + \text{H}]^+$: 488.22; Found: 488.2.

***tert*-Butyl (3-(9-oxo-2-(triisopropylsilyl)-7H-furo[3,2-*e*]pyrrolo[3,4-*b*]indolizin-8(9H)-yl)propyl)carbamate**



Yield: 70%; ^1H NMR (400 MHz, CDCl_3) δ 8.07 (s, 1H), 7.29–7.23 (m, 2H), 6.44 (s, 1H), 5.31 (br s, 1H), 4.35 (s, 2H), 3.67 (t, $J = 6.4$ Hz, 2H), 3.19 (q, $J = 6.1$ Hz, 2H), 1.88–1.83 (m, 2H), 1.48–1.40 (m, 12H), 1.17–1.15 (m, 18H); ^{13}C NMR (100 MHz, CDCl_3) δ 162.3, 160.0, 156.3, 146.9, 138.6, 135.7, 126.4, 121.8, 115.2, 114.1, 110.0, 94.8, 79.1, 46.6, 40.3, 37.7, 29.0, 28.5, 18.7, 11.2; LRMS (ESI) m/z calcd for $\text{C}_{29}\text{H}_{44}\text{N}_3\text{O}_4\text{Si}$ $[\text{M} + \text{H}]^+$: 526.31; Found: 526.3.

Procedure for preparation of R¹ group embedded furoindolizine compounds (Pd coupling reaction)



Preparation of *N,N*-diethyl-4-iodoaniline was conducted through the reported procedure.⁶

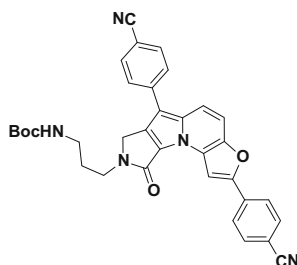
For general iodo-aryl moieties

Condition A. To a solution of a furoindolizine-based core skeleton in dimethylformamide (0.1 M), were added a iodo-aryl derivative (2.0 equiv.), bis(triphenylphosphine)palladium(II) dichloride ($\text{PdCl}_2(\text{PPh}_3)_2$, 10 mol%), silver acetate (1.5 equiv.), and potassium acetate (3.0 equiv.), and the solution was stirred at 100 °C overnight. When the reaction was completed checked by TLC, the reaction mixture was filtered through the short bed of silica gel and concentrated *in vacuo*. The residue was purified by silica-gel flash column chromatography to afford the desired products. (** at isolated yield indicates 10 mol% of $\text{PdCl}_2(\text{PPh}_3)_2$ was applied additionally to completely convert the starting materials)

For *N,N*-diethyl-4-iodoaniline and 1-iodo-4-methoxybenzene

Condition B. To a solution of a furoindolizine-based core skeleton in dimethylformamide (0.1 M), were added a iodo-aryl derivative (2.0 equiv.), palladium acetate (20 mol%), and potassium acetate (3.0 equiv.), and the solution was stirred at 80 °C overnight. When the reaction was completed checked by TLC, the reaction mixture was filtered through the short bed of silica gel and concentrated *in vacuo*. The residue was purified by silica-gel flash column chromatography to afford the desired products.

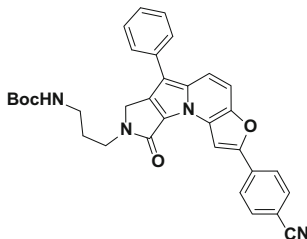
tert-Butyl (3-(2,6-bis(4-cyanophenyl)-9-oxo-7*H*-furo[3,2-*e*]pyrrolo[3,4-*b*]indolizin-8(9*H*)-yl)propyl)carbamate (06)



⁶*Helv. Chim. Acta* **2010**, *93*, 587–594.

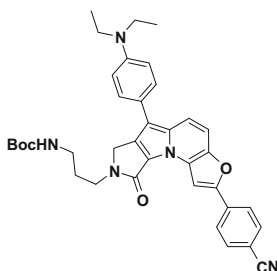
Yield: 80%^{**}; $^1\text{H NMR}$ (400 MHz, CDCl_3) δ 8.29 (s, 1H), 7.96 (d, 8.8 Hz, 2H), 7.76–7.65 (m, 7H), 7.43 (d, $J = 9.6$ Hz, 1H), 5.24 (br s, 1H), 4.57 (s, 2H), 3.73 (t, $J = 6.6$ Hz, 2H), 3.23–3.20 (m, 2H), 1.91–1.88 (m, 2H), 1.45 (s, 9H); $^{13}\text{C NMR}$ (100 MHz, CDCl_3) δ 161.7, 156.2, 152.8, 144.2, 139.3, 135.1, 134.9, 133.6, 133.1, 132.8, 127.7, 127.6, 125.0, 122.8, 119.1, 118.7, 114.3, 111.9, 111.0, 109.6, 109.4, 102.1, 79.4, 47.0, 40.6, 37.7, 29.1, 28.6; HRMS (ESI) m/z calcd for $\text{C}_{34}\text{H}_{29}\text{N}_5\text{NaO}_4$ $[\text{M} + \text{Na}]^+$: 594.2112; Found: 594.2111.

***tert*-Butyl (3-(2-(4-cyanophenyl)-9-oxo-6-phenyl-7*H*-furo[3,2-*e*]pyrrolo[3,4-*b*]indolizin-8(9*H*)-yl)propyl)carbamate (07)**



Yield: 61%; $^1\text{H NMR}$ (500 MHz, CDCl_3) δ 8.24 (s, 1H), 7.92 (d, $J = 8.5$ Hz, 2H), 7.68 (d, $J = 9.0$ Hz, 3H), 7.56 (d, $J = 7.0$ Hz, 2H), 7.50–7.47 (m, 2H), 7.34–7.29 (m, 2H), 5.33 (br s, 1H), 4.53 (s, 2H), 3.71 (t, $J = 6.5$ Hz, 2H), 3.21 (br d, $J = 6.0$ Hz, 2H), 1.88–1.86 (m, 2H), 1.45 (s, 9H); $^{13}\text{C NMR}$ (100 MHz, CDCl_3) δ 162.0, 156.2, 152.1, 144.2, 134.8, 134.4, 134.3, 133.8, 132.7, 129.3, 127.6, 127.3, 126.6, 124.8, 122.0, 118.9, 115.1, 111.5, 111.4, 109.7, 102.2, 79.3, 47.0, 40.5, 37.6, 29.1, 28.6; HRMS (ESI) m/z calcd for $\text{C}_{33}\text{H}_{30}\text{N}_4\text{NaO}_4$ $[\text{M} + \text{Na}]^+$: 569.2159; Found: 569.2160.

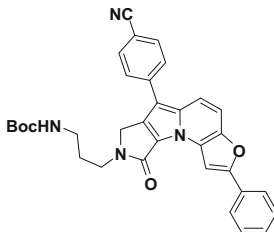
***tert*-Butyl (3-(2-(4-cyanophenyl)-6-(4-(diethylamino)phenyl)-9-oxo-7*H*-furo[3,2-*e*]pyrrolo[3,4-*b*]indolizin-8(9*H*)-yl)propyl)carbamate (08)**



Yield: 27%; $^1\text{H NMR}$ (400 MHz, CDCl_3) δ 8.20 (s, 1H), 7.91 (d, $J = 8.4$ Hz, 2H), 7.67 (d, $J = 8.4$ Hz, 2H), 7.64 (d, $J = 10.0$ Hz, 1H), 7.41 (d, $J = 9.2$ Hz, 2H), 7.22 (d, $J = 10.0$ Hz, 1H), 6.79 (d, $J = 8.8$ Hz, 2H), 5.37 (br s, 1H), 4.49 (s, 2H), 3.70 (t, $J = 6.4$ Hz, 2H), 3.42 (q, $J = 7.0$ Hz, 4H), 3.20 (br d, $J = 5.6$ Hz, 2H), 1.87–1.84 (m, 2H), 1.45 (s, 9H), 1.22 (t, $J = 7.0$ Hz, 6H); $^{13}\text{C NMR}$ (100 MHz, CDCl_3) δ 162.2, 156.3, 151.7, 146.6, 144.2, 134.4, 134.0, 133.7, 132.7, 128.7,

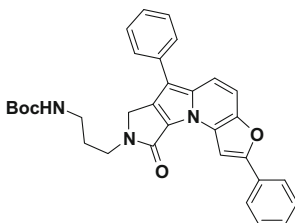
127.2, 124.7, 121.6, 121.0, 119.0, 115.6, 112.3, 112.2, 111.2, 108.7, 102.3, 79.3, 47.0, 44.6, 40.5, 37.6, 29.1, 28.6, 12.8; HRMS (ESI) m/z calcd for $C_{37}H_{40}N_5O_4$ $[M + H]^+$: 618.3075; Found: 618.3077.

***tert*-Butyl (3-(6-(4-cyanophenyl)-9-oxo-2-phenyl-7*H*-furo[3,2-*e*]pyrrolo[3,4-*b*]indolizin-8(9*H*)-yl)propyl)carbamate (10)**



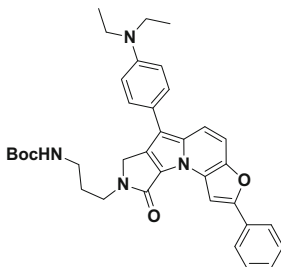
Yield: 81%; 1H NMR (400 MHz, $CDCl_3$) δ 8.06 (s, 1H), 7.83 (d, $J = 8.0$ Hz, 2H), 7.69 (d, $J = 8.0$ Hz, 2H), 7.61–7.55 (m, 3H), 7.44 (t, $J = 7.6$ Hz, 2H), 7.38–7.34 (m, 2H), 5.30 (br s, 1H), 4.49 (s, 2H), 3.70 (t, $J = 6.2$ Hz, 2H), 3.22 (br d, $J = 6.0$ Hz, 2H), 1.90–1.86 (m, 2H), 1.45 (s, 9H); ^{13}C NMR (100 MHz, $CDCl_3$) δ 161.7, 156.2, 155.3, 143.1, 139.6, 135.3, 134.8, 132.9, 129.6, 129.1, 129.0, 128.0, 127.2, 124.8, 122.2, 119.3, 112.5, 111.1, 108.8, 108.6, 99.3, 79.3, 47.0, 40.5, 37.7, 29.1, 28.6; HRMS (ESI) m/z calcd for $C_{33}H_{30}N_4NaO_4$ $[M + Na]^+$: 569.2159; Found: 569.2158.

***tert*-Butyl (3-(9-oxo-2,6-diphenyl-7*H*-furo[3,2-*e*]pyrrolo[3,4-*b*]indolizin-8(9*H*)-yl)propyl)carbamate (11)**



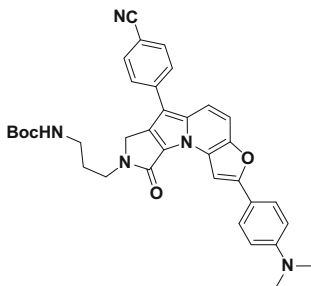
Yield: 67%; 1H NMR (400 MHz, $CDCl_3$) δ 8.13 (s, 1H), 7.90 (d, $J = 7.2$ Hz, 2H), 7.61 (d, $J = 9.6$ Hz, 1H), 7.56 (d, $J = 8.0$ Hz, 2H), 7.49–7.43 (m, 4H), 7.37–7.28 (m, 3H), 5.37 (br s, 1H), 4.50 (s, 2H), 3.69 (t, $J = 6.2$ Hz, 2H), 3.21 (br d, $J = 6.4$ Hz, 2H), 1.87–1.83 (m, 2H), 1.45 (s, 9H); ^{13}C NMR (100 MHz, $CDCl_3$) δ 162.2, 156.3, 154.7, 143.1, 135.1, 134.7, 134.4, 130.0, 129.2, 129.0, 128.8, 127.7, 127.5, 126.3, 124.8, 121.4, 113.3, 110.7, 110.0, 99.5, 79.2, 46.9, 40.4, 37.6, 29.0, 28.6; HRMS (ESI) m/z calcd for $C_{32}H_{31}N_3NaO_4$ $[M + Na]^+$: 544.2207; Found: 544.2207.

***tert*-Butyl (3-(6-(4-(diethylamino)phenyl)-9-oxo-2-phenyl-7H-furo[3,2-*e*]pyrrolo[3,4-*b*]indolizin-8(9H)-yl)propyl)carbamate (12)**



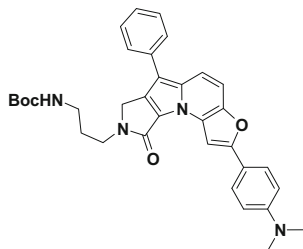
Yield: 30%; ^1H NMR (400 MHz, CDCl_3) δ 8.12 (s, 1H), 7.91 (d, $J = 8.4$ Hz, 2H), 7.59 (d, $J = 10.0$ Hz, 1H), 7.47–7.41(m, 4H), 7.36–7.32 (m, 1H), 7.27–7.25 (m, 1H), 6.79 (d, $J = 8.4$ Hz, 2H), 5.42 (br s, 1H), 4.48 (s, 2H), 3.69 (t, $J = 6.2$ Hz, 2H), 3.41 (q, $J = 7.0$ Hz, 4H), 3.20 (br d, $J = 5.6$ Hz, 2H), 1.86–1.83 (m, 2H), 1.45 (s, 9H), 1.22 (t, $J = 7.0$ Hz, 6H); ^{13}C NMR (100 MHz, CDCl_3) δ 162.4, 156.3, 154.3, 146.4, 143.2, 134.7, 133.7, 130.2, 128.9, 128.7, 128.6, 127.6, 124.7, 121.4, 120.9, 113.8, 112.4, 111.3, 109.1, 99.6, 79.2, 46.9, 44.6, 40.4, 37.6, 29.0, 28.6, 12.8; HRMS (ESI) m/z calcd for $\text{C}_{36}\text{H}_{41}\text{N}_4\text{O}_4$ [$\text{M} + \text{H}$] $^+$: 593.3122; Found: 593.3121.

***tert*-Butyl (3-(6-(4-cyanophenyl)-2-(4-(dimethylamino)phenyl)-9-oxo-7H-furo[3,2-*e*]pyrrolo[3,4-*b*]indolizin-8(9H)-yl)propyl)carbamate (14)**



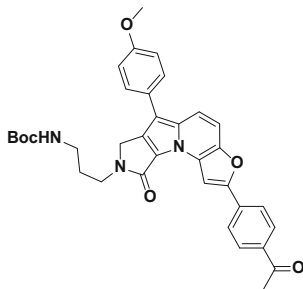
Yield: 86%; ^1H NMR (400 MHz, CDCl_3) δ 7.92 (s, 1H), 7.77 (d, $J = 9.2$ Hz, 2H), 7.71 (d, $J = 8.4$ Hz, 2H), 7.64 (d, $J = 8.8$ Hz, 2H), 7.55 (d, $J = 10.0$ Hz, 1H), 7.40 (d, $J = 10.0$ Hz, 1H), 6.76 (d, $J = 9.2$ Hz, 2H), 5.29 (br s, 1H), 4.53 (s, 2H), 3.71 (t, $J = 6.4$ Hz, 2H), 3.21 (q, $J = 6.1$ Hz, 2H), 3.05 (s, 6H), 1.90–1.86 (m, 2H), 1.44 (s, 9H); ^{13}C NMR (100 MHz, CDCl_3) δ 161.9, 157.0, 156.3, 151.0, 142.4, 140.0, 135.8, 135.0, 133.0, 128.9, 127.2, 126.4, 121.8, 119.4, 117.7, 112.2, 111.2, 110.8, 108.6, 108.0, 96.2, 79.3, 47.0, 40.5, 40.4, 37.7, 29.1, 28.6; HRMS (ESI) m/z calcd for $\text{C}_{35}\text{H}_{35}\text{N}_5\text{NaO}_4$ [$\text{M} + \text{Na}$] $^+$: 612.2581; Found: 612.2581.

***tert*-Butyl (3-(2-(4-(dimethylamino)phenyl)-9-oxo-6-phenyl-7*H*-furo[3,2-*e*]pyrrolo[3,4-*b*]indolizin-8(9*H*)-yl)propyl)carbamate (15)**



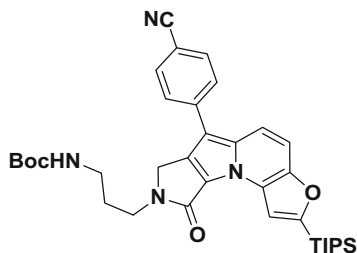
Yield: 81%^{**}; ¹H NMR (400 MHz, CDCl₃) δ 7.94 (s, 1H), 7.80 (d, *J* = 8.8 Hz, 2H), 7.59–7.56 (m, 3H), 7.47 (t, *J* = 7.8 Hz, 2H), 7.34–7.28 (m, 2H), 6.77 (d, *J* = 9.2 Hz, 2H), 5.38 (br s, 1H), 4.52 (s, 2H), 3.70 (t, *J* = 6.2 Hz, 2H), 3.21 (q, *J* = 6.0 Hz, 2H), 3.04 (s, 6H), 1.88–1.84 (m, 2H), 1.44 (s, 9H); ¹³C NMR (100 MHz, CDCl₃) δ 162.4, 156.3, 156.2, 150.8, 142.4, 135.5, 135.0, 134.5, 129.2, 128.5, 127.5, 126.2, 126.1, 120.9, 118.2, 112.2, 111.6, 110.1, 110.0, 96.4, 79.2, 46.9, 40.5, 40.4, 37.6, 29.0, 28.6; HRMS (ESI) *m/z* calcd for C₃₄H₃₇N₄O₄ [M + H]⁺: 565.2809; Found: 565.2807.

***tert*-Butyl (3-(2-(4-acetylphenyl)-6-(4-methoxyphenyl)-9-oxo-7*H*-furo[3,2-*e*]pyrrolo[3,4-*b*]indolizin-8(9*H*)-yl)propyl)carbamate (19)**



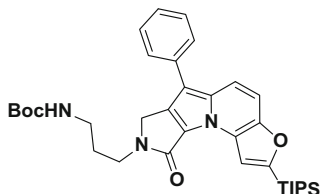
Yield: 17%; ¹H NMR (500 MHz, CD₂Cl₂) δ 8.28 (s, 1H), 8.04 (d, *J* = 8.5 Hz, 2H), 8.01 (d, *J* = 9.0 Hz, 2H), 7.66 (d, *J* = 10.0 Hz, 1H), 7.52 (d, *J* = 9.0 Hz, 2H), 7.35 (d, *J* = 10.0 Hz, 1H), 7.03 (d, *J* = 9.0 Hz, 2H), 5.45 (br s, 1H), 4.51 (s, 2H), 3.86 (s, 3H), 3.69 (t, *J* = 6.5 Hz, 2H), 3.16 (q, *J* = 6.2 Hz, 2H), 2.62 (s, 3H), 1.85–1.80 (m, 2H), 1.43 (s, 9H); HRMS (ESI) *m/z* calcd for C₃₅H₃₅N₃NaO₆ [M + Na]⁺: 616.2418; Found: 616.2417.

***tert*-Butyl (3-(6-(4-cyanophenyl)-9-oxo-2-(triisopropylsilyl)-7H-furo[3,2-*e*]pyrrolo[3,4-*b*]indolizin-8(9H)-yl)propyl)carbamate**



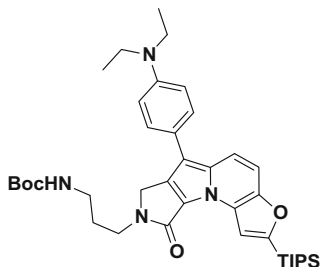
Yield: 78%; ^1H NMR (400 MHz, CDCl_3) δ 8.17 (s, 1H), 7.73 (d, $J = 8.8$ Hz, 2H), 7.66–7.62 (m, 3H), 7.45 (d, $J = 10.0$ Hz, 1H), 5.21 (br s, 1H), 4.54 (s, 2H), 3.71 (t, $J = 6.6$ Hz, 2H), 3.21 (br d, $J = 6.4$ Hz, 2H), 1.90–1.87 (m, 2H), 1.50–1.42 (m, 12H), 1.17 (d, $J = 7.2$ Hz, 18H); ^{13}C NMR (100 MHz, CDCl_3) δ 161.8, 161.6, 156.2, 147.2, 139.9, 135.3, 134.5, 133.0, 127.4, 127.0, 122.4, 119.3, 115.1, 112.5, 111.8, 108.8, 108.5, 79.2, 46.9, 40.5, 37.8, 29.0, 28.5, 18.7, 11.2; LRMS (ESI) m/z calcd for $\text{C}_{36}\text{H}_{47}\text{N}_4\text{O}_4\text{Si}$ [$\text{M} + \text{H}$] $^+$: 627.34; Found: 627.3.

***tert*-Butyl (3-(9-oxo-6-phenyl-2-(triisopropylsilyl)-7H-furo[3,2-*e*]pyrrolo[3,4-*b*]indolizin-8(9H)-yl)propyl)carbamate**



Yield: 84%^{**}; ^1H NMR (400 MHz, CDCl_3) δ 8.14 (s, 1H), 7.63 (d, $J = 10.0$ Hz, 1H), 7.57 (d, $J = 8.0$ Hz, 2H), 7.47 (t, $J = 7.8$ Hz, 2H), 7.34 (d, $J = 9.6$ Hz, 1H), 7.29 (t, $J = 8.0$ Hz, 1H), 5.30 (br s, 1H), 4.51 (s, 2H), 3.70 (t, $J = 6.6$ Hz, 2H), 3.20 (q, $J = 6.0$ Hz, 2H), 1.88–1.85 (m, 2H), 1.49–1.42 (m, 12H), 1.17 (d, $J = 7.2$ Hz, 18H); ^{13}C NMR (100 MHz, CDCl_3) δ 162.2, 160.5, 156.3, 147.1, 135.0, 134.9, 134.1, 129.2, 127.5, 126.7, 126.2, 121.5, 115.2, 113.2, 110.6, 110.4, 79.1, 46.8, 40.4, 37.7, 29.0, 28.5, 18.8, 11.2; LRMS (ESI) m/z calcd for $\text{C}_{35}\text{H}_{48}\text{N}_3\text{O}_4\text{Si}$ [$\text{M} + \text{H}$] $^+$: 602.34; Found: 602.3.

***tert*-Butyl (3-(6-(4-(diethylamino)phenyl)-9-oxo-2-(triisopropylsilyl)-7*H*-furo[3,2-*e*]pyrrolo[3,4-*b*]indolizin-8(9*H*)-yl)propyl)carbamate**

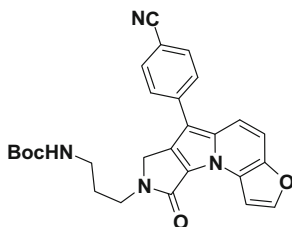


Yield: 32%; ^1H NMR (400 MHz, CD_2Cl_2) δ 8.12 (s, 1H), 7.60 (d, $J = 9.6$ Hz, 1H), 7.42 (d, $J = 8.8$ Hz, 2H), 7.29 (d, $J = 9.8$ Hz, 1H), 6.78 (d, $J = 9.2$ Hz, 2H), 5.47 (br s, 1H), 4.48 (s, 2H), 3.66 (t, $J = 6.6$ Hz, 2H), 3.40 (q, $J = 7.1$ Hz, 4H), 3.14 (q, $J = 6.1$ Hz, 2H), 1.84–1.78 (m, 2H), 1.49–1.42 (m, 12H), 1.21–1.18 (m, 24H); ^{13}C NMR (100 MHz, CD_2Cl_2) δ 162.4, 160.1, 156.3, 147.4, 146.7, 134.6, 133.7, 128.7, 126.6, 121.8, 121.5, 115.5, 114.0, 112.6, 111.3, 109.7, 78.9, 47.0, 44.8, 40.5, 37.7, 29.1, 28.5, 18.8, 12.8. 11.5; LRMS (ESI) m/z calcd for $\text{C}_{39}\text{H}_{57}\text{N}_4\text{O}_4\text{Si}$ $[\text{M} + \text{H}]^+$: 673.41; Found: 673.4.

General procedure for TIPS deprotection reaction (For 02, 03, and 04)

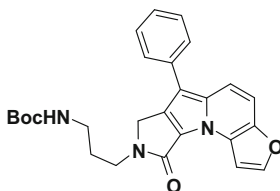
To a stirred solution of TIPS protected furoindolizine-based core skeleton in THF (0.1 M) at -40 °C, was slowly added tetrabutylammonium fluoride solution (1.0 M in THF, 1.5 equiv.) which was cooled down to -10 °C. Stirred reaction mixture was allowed to warm up to 0 °C for 1 h. When the reaction was completed checked by TLC, brine was added to the solution and the organic material was extracted with ethyl acetate. The combined organic extracts were dried over $\text{Na}_2\text{SO}_4(\text{s})$, and concentrated under reduced pressure after filtration. The residue was purified by silica-gel flash column chromatography to afford the desired product.

***tert*-Butyl (3-(6-(4-cyanophenyl)-9-oxo-7*H*-furo[3,2-*e*]pyrrolo[3,4-*b*]indolizin-8(9*H*)-yl)propyl)carbamate (02)**



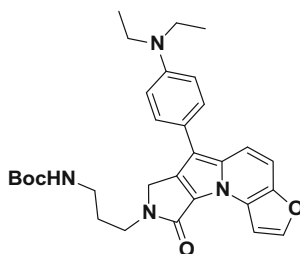
Yield: 82%; ^1H NMR (400 MHz, CD_2Cl_2) δ 7.91 (d, $J = 2.0$ Hz, 1H), 7.74 (d, $J = 8.4$ Hz, 2H), 7.71 (d, $J = 2.0$ Hz, 1H), 7.65 (d, $J = 8.4$ Hz, 3H), 7.41 (d, $J = 9.6$ Hz, 2H), 5.42 (br s, 1H), 4.51 (s, 2H), 3.66 (t, $J = 6.6$ Hz, 2H), 3.13 (q, $J = 6.5$ Hz, 2H), 1.85–1.78 (m, 2H), 1.41 (s, 9H); ^{13}C NMR (100 MHz, CD_2Cl_2) δ 161.9, 156.2, 144.6, 143.8, 139.9, 135.4, 135.1, 133.2, 127.6, 126.5, 122.7, 119.5, 113.3, 111.6, 109.1, 108.9, 105.1, 79.1, 47.1, 40.5, 37.6, 29.1, 28.5; HRMS (ESI) m/z calcd for $\text{C}_{27}\text{H}_{26}\text{N}_4\text{NaO}_4$ $[\text{M} + \text{Na}]^+$: 493.1846; Found: 493.1845.

tert-Butyl (3-(9-oxo-6-phenyl-7H-furo[3,2-e]pyrrolo[3,4-b]indolizin-8(9H)-yl)propyl)carbamate (03)



Yield: 99%; ^1H NMR (400 MHz, CD_2Cl_2) δ 7.89 (d, $J = 1.2$ Hz, 1H), 7.68 (d, $J = 1.6$ Hz, 1H), 7.65 (d, $J = 10.0$ Hz, 1H), 7.57 (d, $J = 8.4$ Hz, 2H), 7.47 (t, $J = 8.0$ Hz, 2H), 7.33–7.27 (m, 2H), 5.50 (br s, 1H), 4.49 (s, 2H), 3.66 (t, $J = 6.4$ Hz, 2H), 3.13 (q, $J = 6.1$ Hz, 2H), 1.83–1.76 (m, 2H), 1.42 (s, 9H); ^{13}C NMR (100 MHz, CD_2Cl_2) δ 162.2, 156.2, 144.0, 143.7, 135.1, 135.0, 134.6, 129.4, 127.7, 126.4, 126.2, 121.8, 113.8, 110.7, 110.5, 105.1, 79.0, 47.0, 40.4, 37.6, 29.1, 28.5; HRMS (ESI) m/z calcd for $\text{C}_{26}\text{H}_{27}\text{N}_3\text{NaO}_4$ $[\text{M} + \text{Na}]^+$: 468.1894; Found: 468.1896.

tert-Butyl (3-(6-(4-(diethylamino)phenyl)-9-oxo-7H-furo[3,2-e]pyrrolo[3,4-b]indolizin-8(9H)-yl)propyl)carbamate (04)



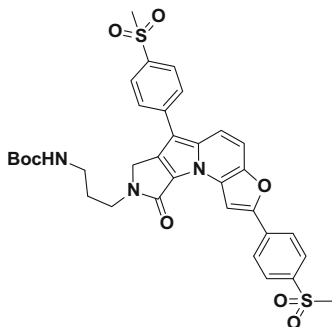
Yield: 99%; ^1H NMR (400 MHz, acetone- d_6) δ 7.90–7.88 (m, 2H), 7.67 (d, $J = 9.6$ Hz, 1H), 7.45 (d, $J = 9.2$ Hz, 2H), 7.34 (d, $J = 9.6$ Hz, 1H), 6.81 (d, $J = 8.8$ Hz, 2H), 6.14 (br s, 1H), 4.58 (s, 2H), 3.66 (t, $J = 6.4$ Hz, 2H), 3.43 (q, $J = 7.1$ Hz, 4H), 3.15 (q, $J = 6.4$ Hz, 2H), 1.90–1.83 (m, 2H), 1.40 (s, 9H), 1.18 (t,

$J = 7.0$ Hz, 6H); ^{13}C NMR (100 MHz, acetone- d_6) δ 162.2, 156.6, 147.2, 144.7, 144.0, 134.7, 134.6, 129.2, 126.2, 122.1, 122.0, 114.9, 113.1, 112.1, 109.8, 105.3, 78.5, 47.2, 44.9, 40.9, 38.3, 29.3, 28.6, 13.0; HRMS (ESI) m/z calcd for $\text{C}_{30}\text{H}_{37}\text{N}_4\text{O}_4$ $[\text{M} + \text{H}]^+$: 517.2809; Found: 517.2809.

Procedure for preparation of 18

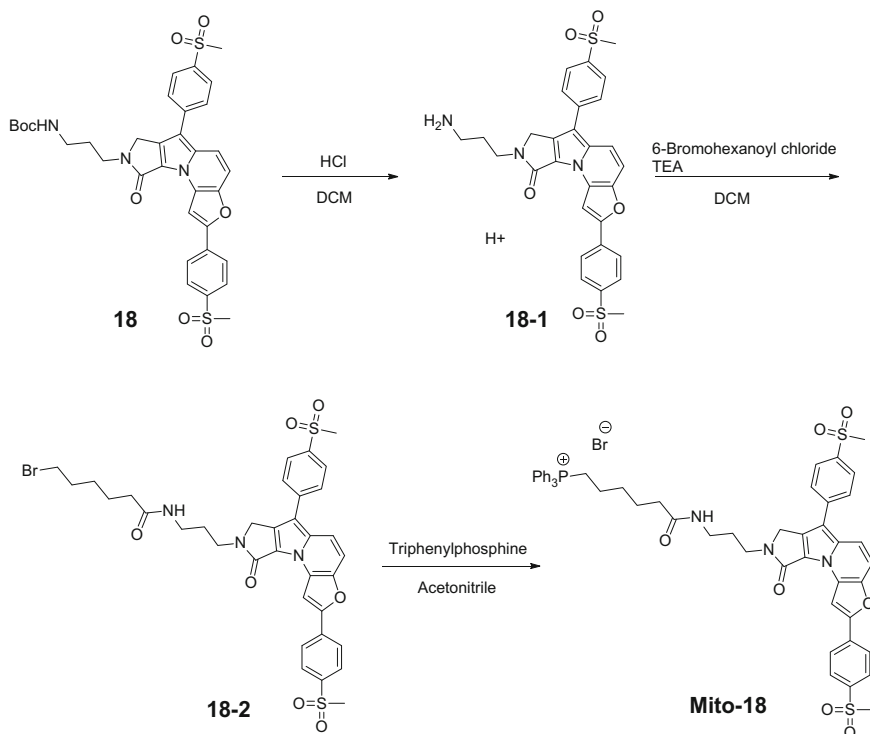
To a solution of **01** (1.0 equiv.) in dimethylformamide (0.1 M), were added 4-bromophenyl methyl sulfone (10.0 equiv.), bis(triphenylphosphine)palladium(II) dichloride (20 mol%), silver acetate (1.5 equiv.) and potassium acetate (3.0 equiv.), and the solution was stirred at 100 °C. When the reaction was completed checked by TLC, the reaction mixture was filtered through the short bed of silica gel and concentrated *in vacuo*. The residue was purified by silica-gel flash column chromatography to afford **18**.

tert-Butyl (3-(2,6-bis(4-(methylsulfonyl)phenyl)-9-oxo-7H-furo[3,2-*e*]pyrrolo[3,4-*b*]indolizin-8(9H)-yl)propyl)carbamate (18)



Yield: 26%; ^1H NMR (400 MHz, CDCl_3) δ 8.31 (s, 1H), 8.05–7.99 (m, 6H), 7.75–7.70 (m, 3H), 7.43 (d, $J = 9.6$ Hz, 1H), 5.24 (br s, 1H), 4.57 (s, 2H), 3.73 (t, $J = 6.6$ Hz, 2H), 3.23–3.18 (m, 2H), 3.13 (s, 3H), 3.11 (s, 3H), 1.92–1.89 (m, 2H), 1.45 (s, 9H); ^{13}C NMR (100 MHz, CDCl_3) δ 161.7, 156.2, 152.7, 144.2, 140.3, 140.0, 137.7, 135.2, 135.0, 134.6, 128.5, 128.2, 127.7, 127.6, 125.2, 122.8, 114.3, 111.0, 109.4, 102.2, 79.4, 47.0, 44.8, 44.7, 40.6, 37.7, 29.1, 28.6; HRMS (ESI) m/z calcd for $\text{C}_{34}\text{H}_{35}\text{N}_3\text{NaO}_8\text{S}_2$ $[\text{M} + \text{Na}]^+$: 700.1758; Found: 700.1759.

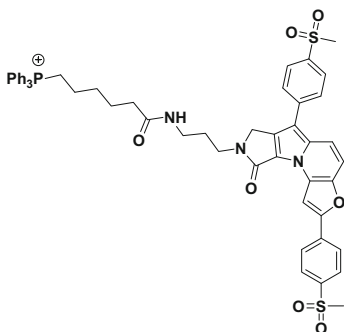
Procedure for preparation of Mito-18



To a solution of compound **18** in DCM (0.1 M) was added a 10% v/v of hydrochloric acid (HCl), and the solution was stirred overnight at room temperature. After full consumption of starting material, the solution was diluted with DCM and washed with sodium bicarbonate solution. The organic layer was extracted with DCM, dried over sodium sulfate and filtered through a cotton plug. The resulting solution was evaporated under reduced pressure to afford **18-1**. LRMS (ESI) m/z calcd for $C_{29}H_{28}N_3O_6S_2$ $[M + H]^+$: 578.14; Found: 578.1.

After that, 6-Bromohexanoyl chloride (1.5 equiv.) was slowly added to a stirred solution of **18-1** with TEA (3.0 equiv.) in DCM (0.1 M) at room temperature and the solution was stirred for 6 h. After **18-1** was fully consumed, the solvent was removed, and crude mixture was dissolved in acetonitrile (0.1 M) followed by addition of triphenylphosphine (3.0 equiv.). The mixture was stirred under reflux condition for 2 days. The crude product was purified by reverse-phase-HPLC to afford a desired **Mito-18**. [HPLC solvents consist of water containing 0.1% TFA (trifluoroacetic acid) for solvent A, and acetonitrile containing 0.1% TFA for solvent B]

(6-((3-(2,6-bis(4-(methylsulfonyl)phenyl)-9-oxo-7H-furo[3,2-*e*]pyrrolo[3,4-*b*]indolizin-8(9*H*)-yl)propyl)amino)-6-oxohexyl)triphenylphosphonium (Mito-18)



Yield: 24% (overall yield over 3 steps); ^1H NMR (400 MHz, $\text{DMSO-}d_6$) δ 8.26 (s, 1H), 8.08 (d, $J = 8.4$ Hz, 2H), 8.04 (d, $J = 8.4$ Hz, 2H), 8.00 (d, $J = 8.0$ Hz, 2H), 7.94–7.84 (m, 7H), 7.80–7.69 (m, 13H), 4.73 (s, 2H), 3.61–3.51 (m, 4H), 3.29 (s, 3H), 3.27 (s, 3H), 3.13–3.08 (q, $J = 6.5$ Hz, 2H), 2.06–2.03 (m, 2H), 1.81–1.76 (m, 2H), 1.51–1.47 (m, 6H); LRMS (ESI) m/z calcd for $\text{C}_{53}\text{H}_{51}\text{N}_3\text{O}_7\text{PS}_2$ $[\text{M}]^+$: 936.29; Found: 936.2.

References

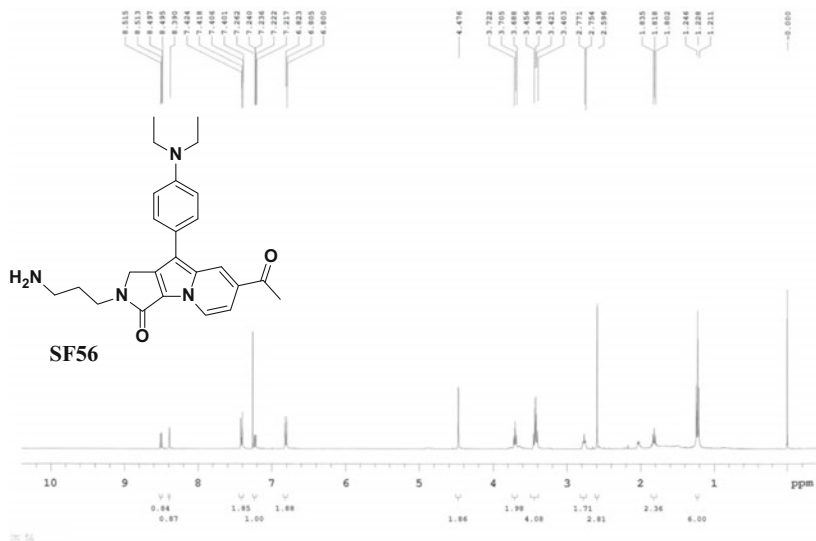
- (a) Valeur B (2001) *Molecular fluorescence: principles and applications*, Wiley-VCH Weinheim, pp 24–27. (b) Parson WW (2007) *Modern optical spectroscopy: with examples from biophysics and biochemistry*, Springer-Verlag, Berlin Heidelberg, p 3, p 91, p 126
- (a) Wang P, Klein C, Humphry-Baker R, Zakeeruddin SM, Grätzel M (2005) *J Am Chem Soc* 127:808–809. (b) Gao F, Wang Y, Shi D, Zhang J, Wang M, Jing X, Humphry-Baker R, Wang P, Zakeeruddin SM, Grätzel M (2008) *J Am Chem Soc* 130:10720–10728. (c) Chen H, Huang H, Huang X, Clifford JN, Forneli A, Palomares E, Zheng X, Zheng L, Wang X, Shen P, Zhao B, Tan S (2010) *J Phys Chem C* 114:3280–3286. (d) Jiang X, Karlsson KM, Gabrielsson E, Johansson EMJ, Quintana M, Karlsson M, Sun L, Boschloo G, Hagfeldt A (2011) *Adv Funct Mater* 21:2944–2952
- (a) Melinger JS, Pan Y, Kleiman VD, Peng Z, Davis BL, McMorro D, Lu M (2002) *J Am Chem Soc* 124:12002–12012. (b) Yu Q, Liu S, Zhang M, Cai N, Wang Y, Wang P (2009) *J Phys Chem C* 113:14559–14566. (c) Lin Y, Cheng P, Liu Y, Shi Q, Hu W, Li Y, Zhan X (2012) *Org Electron* 13:673–680
- (a) Chen J, Burghart A, Derecskei-Kovacs A, Burgess K (2000) *J Org Chem* 65:2900–2906. (b) Zhao W, Carreira EM (2006) *Chem Eur J* 12:7254–7263. (c) Goeb S, Ziessel R (2007) *Org Lett* 9:737–740. (d) Karton-Lifshin N, Albertazzi L, Bendikov M, Baran PS, Shabat D (2012) *J Am Chem Soc* 134:20412–20420. (e) Nakanishi K, Fukatsu D, Takaishi K, Tsuji T, Uenaka K, Kuramochi K, Kawabata T, Tsubaki K (2014) *J Am Chem Soc* 136:7101 – 7109
- (a) Kim E, Park SB (2009) *Chem Asian J* 4:1646–1658. (b) Kobayashi H, Ogawa M, Alford R, Choyke PL, Urano Y (2010) *Chem Rev* 110:2620–2640. (c) Yun S-W, Kang N-Y, Park S-J, Ha H-H, Kim YK, Lee J-S, Chang Y-T (2014) *Acc Chem Res* 47:1277–1286

6. (a) Lavis LD, Raines RT (2008) *ACS Chem Biol* 3:142–155. (b) Lavis LD, Raines RT (2014) *ACS Chem Biol* 9:855–866
7. Hilborn RC (1982) *Am J Phys* 50:982–986
8. (a) Evans RC, Douglas P, Burrow HD (2013) *Applied photochemistry*, Springer-Verlag, p 60. (b) Ji S, Yang J, Yang Q, Liu S, Chen M, Zhao J (2009) *J Org Chem* 74:4855–4865. (c) Zhang X, Xiao Y, Qi J, Qu J, Kim B, Yue X, Belfield KD (2013) *J Org Chem* 78:9153–9160
9. (a) Sahu H, Panda AN (2013) *Macromolecules* 46:844–855. (b) Sand AM, Liu C, Valentine AJS, Mazziotti DA (2014) *J Phys Chem A* 118:6085–6091
10. (a) Kim E, Koh M, Ryu J, Park SB (2008) *J Am Chem Soc* 130:12206–12207. (b) Kim E, Koh M, Lim BJ, Park SB (2011) *J Am Chem Soc* 133:6642–6649. (c) Lee Y, Na S, Lee S, Jeon NL, Park SB (2013) *Mol Biosyst* 9:952–956. (d) Choi EJ, Kim E, Lee Y, Jo A, Park SB (2014) *Angew Chem* 126: 1370–1374; *Angew Chem Int Ed* 53:1346–1350. (e) Kim E, Lee Y, Lee S, Park SB (2015) *Acc Chem Res* 48: 538–547
11. (a) Kim E, Lee S, Park SB (2012) *Chem Commun* 48:2331–2333. (b) Choi EJ, Park SB (2015) *Org Biomol Chem* 13:5202–5208
12. (a) Lim J-L, Chirayil S, Thummel RP (1991) *J Org Chem* 56:1492–1500. (b) Liang Y, Zhang P, Yang S, Tao Z (2013) *J Chem (2013) Adv Energy Mater* 3: 600–605. (c) Dang D, Xiao M, Zhou P, Zhong J, Fan J, Su N, Xiong W, Yang C, Wang Q, Wang Y, Pei Y, Yang R, Zhu W (2015) *Eur J Org Chem* 4:820–827. (d) Kato S-I, Furuya T, Nitani M, Hasebe N, Ie Y, Aso Y, Yoshihara T, Tobita S, Nakamura Y (2015) *Chem Eur J* 21:3115–3128. (e) Huang J-D, Chai S, Ma H, Dong B (2015) *J Phys Chem C* 119:33–44
13. (a) Umezawa K, Nakamura Y, Makino H, Citterio D, Suzuki K (2008) *J Am Chem Soc* 130:1550–1551. (b) Umezawa K, Matsui A, Nakamura Y, Citterio D, Suzuki K (2009) *Chem Eur J* 15:1096–1106
14. Higashiguchi K, Matsuda K, Asano Y, Murakami A, Nakamura S, Irie M (2005) *Eur J Org Chem* 1:91–97
15. (a) Chartoire A, Comoy C, Fort Y (2008) *Tetrahedron* 64:10867–10873. (b) Jasselin-Hinschberger A, Comoy C, Chartoire A, Fort Y (2015) *Eur J Org Chem* 11:2321–2331
16. (a) Cai D, Marques MAL, Milne BF, Nogueira F (2010) *J Phys Chem Lett* 1:2781–2787. (b) Liu X, Xu Z, Cole JM (2013) *J Phys Chem C* 117:16584–16595
17. (a) Murata C, Masuda T, Kamochi Y, Todorki K, Yoshida H, Nohta H, Yamaguchi M, Takadate A (2005) *Chem Pharm Bull* 53:750–758. (b) Umezawa K, Nakamura Y, Makino H, Citterio D, Suzuki K (2008) *J Am Chem Soc* 130:1550–1551. (c) Umezawa K, Matsui A, Nakamura Y, Citterio D, Suzuki K (2009) *Chem Eur J* 15:1096–1106

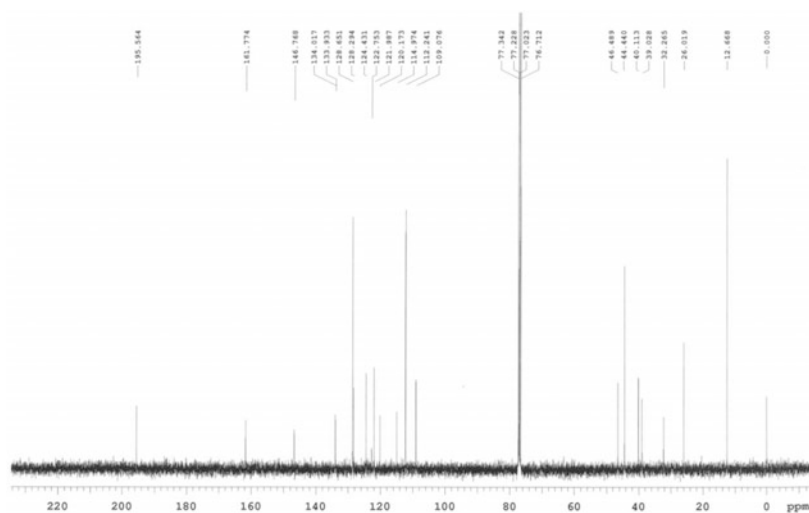
Appendix

NMR spectra

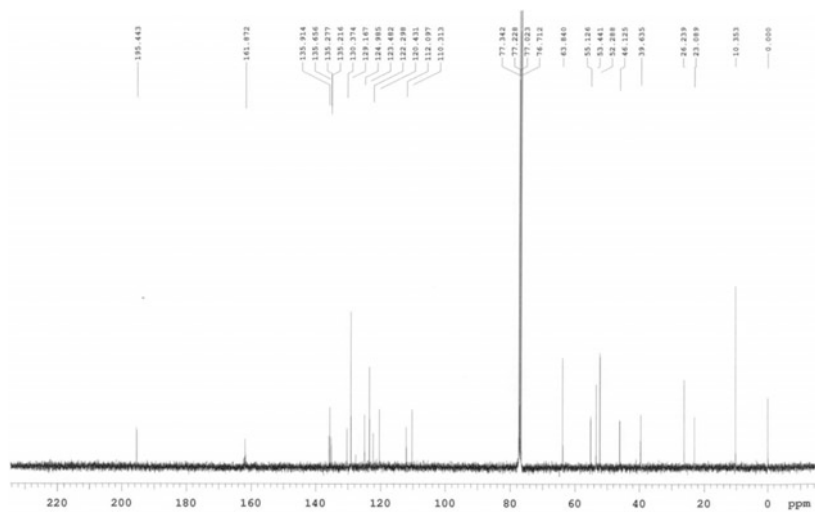
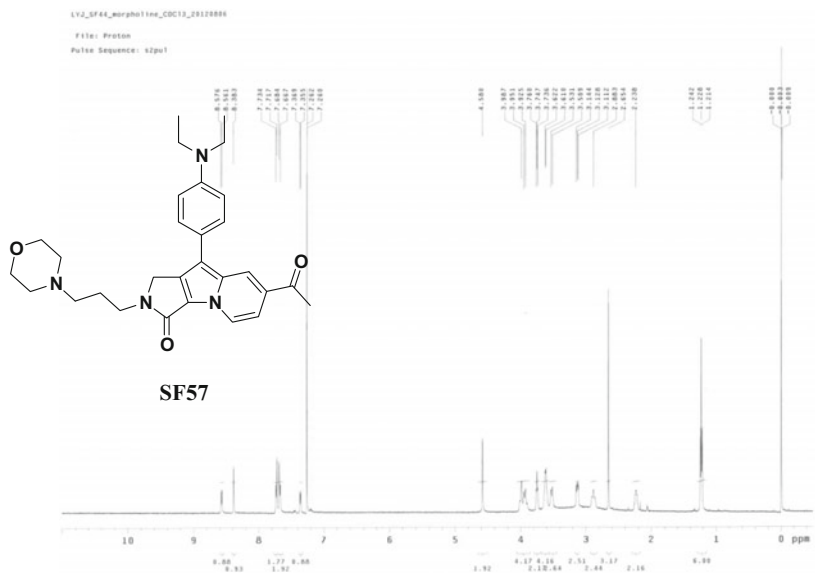
Chapter 2

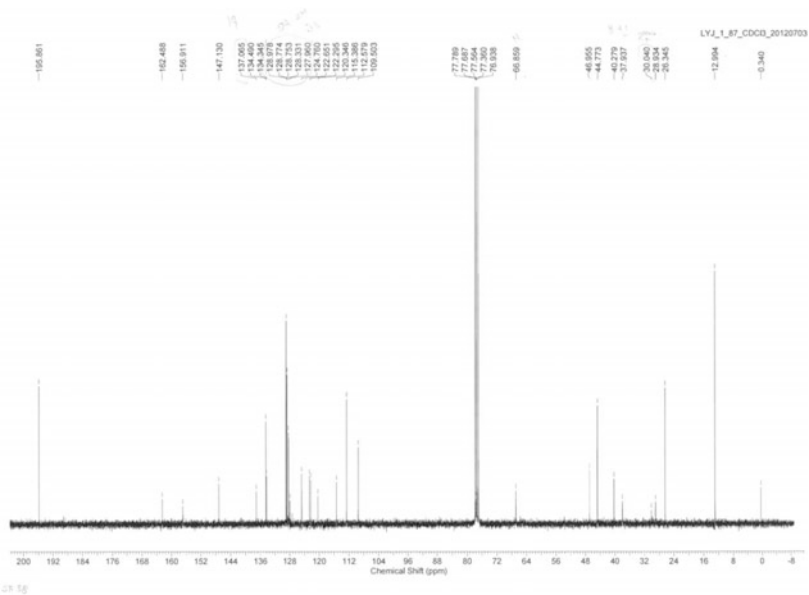
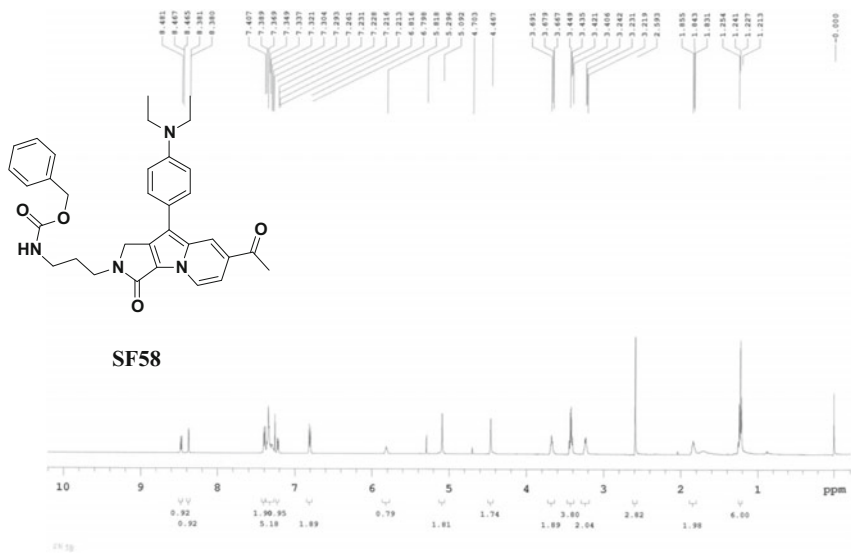


25 54

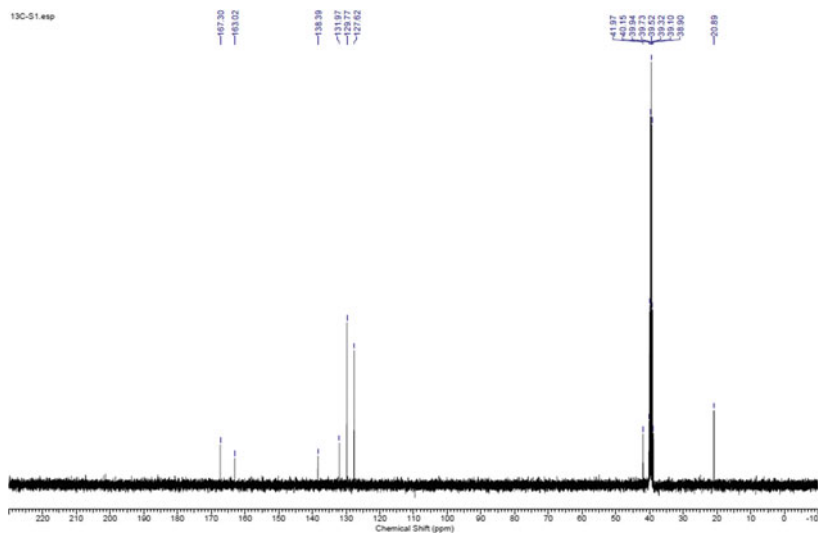
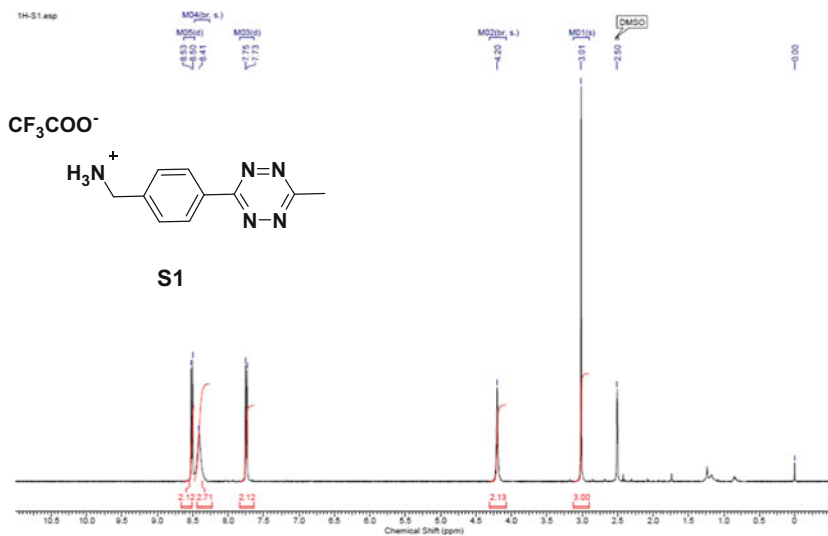


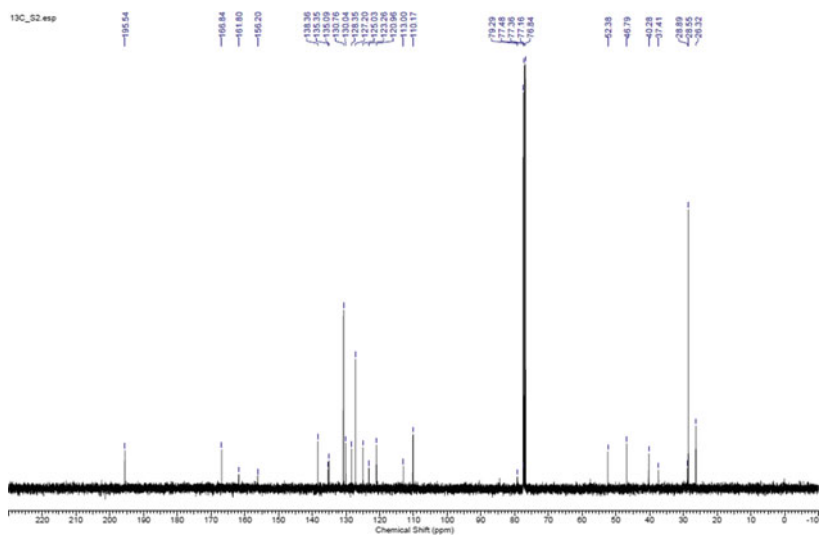
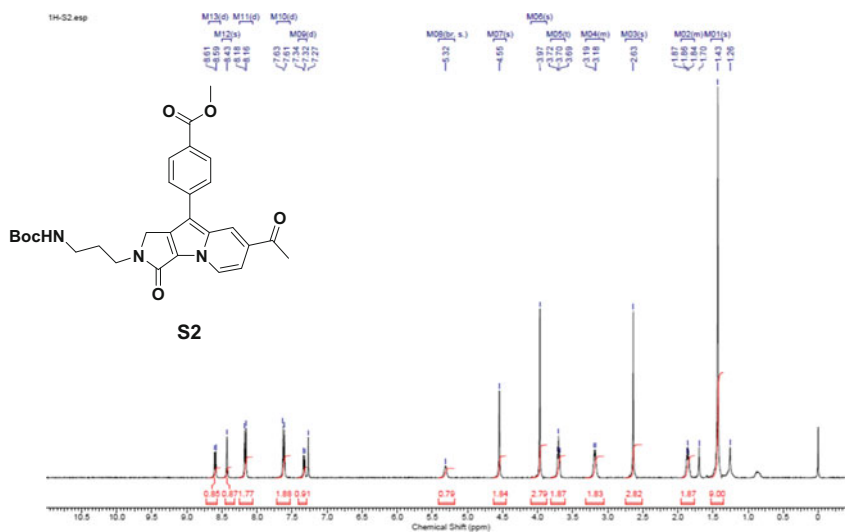
25 54

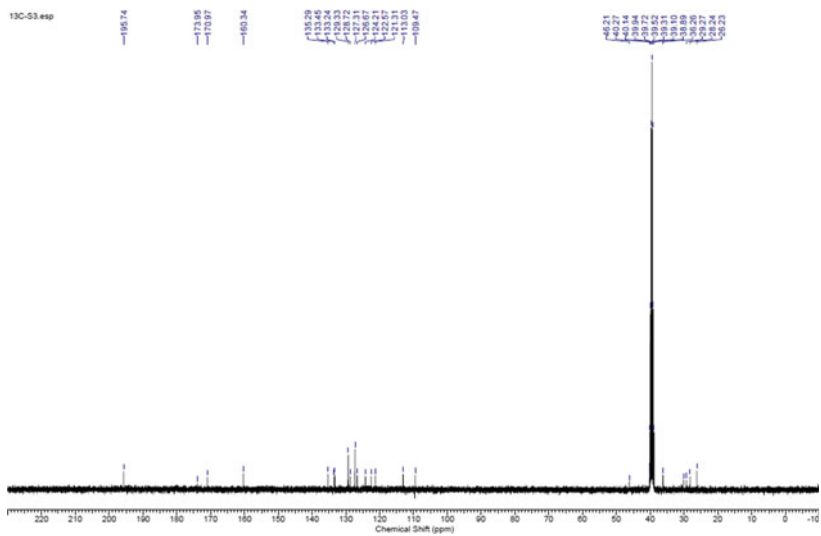
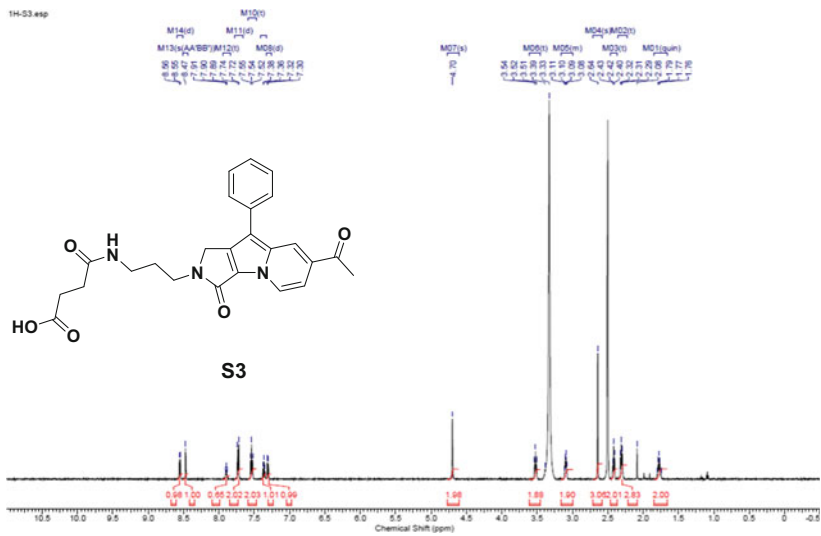


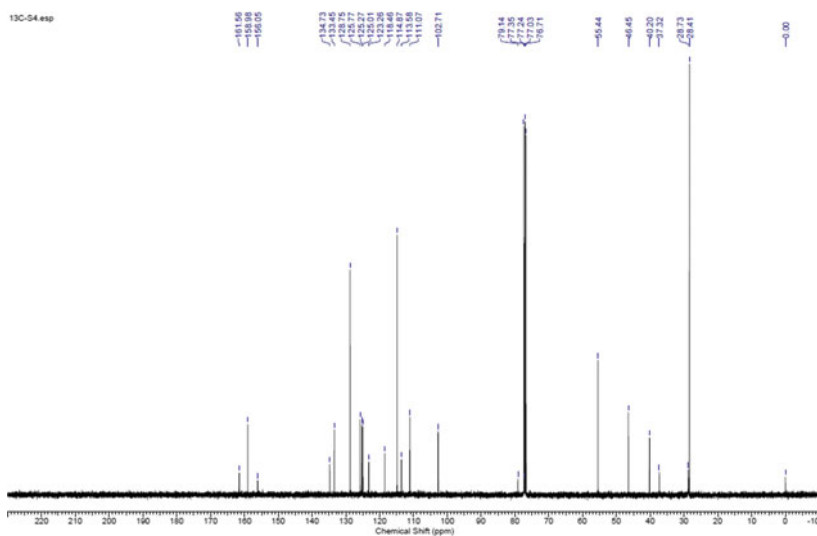
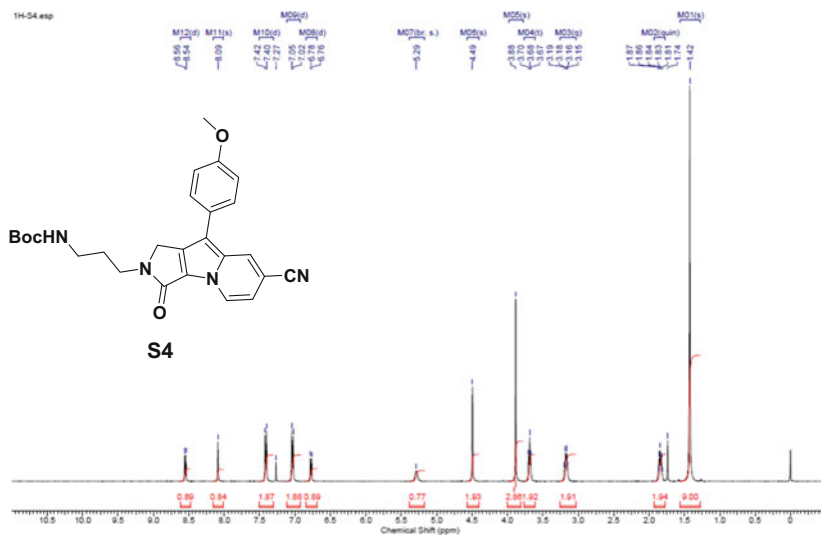


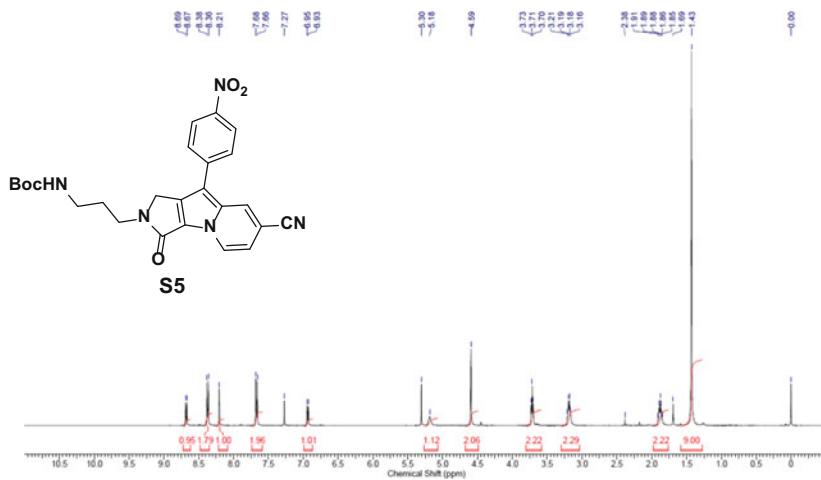
Chapter 3



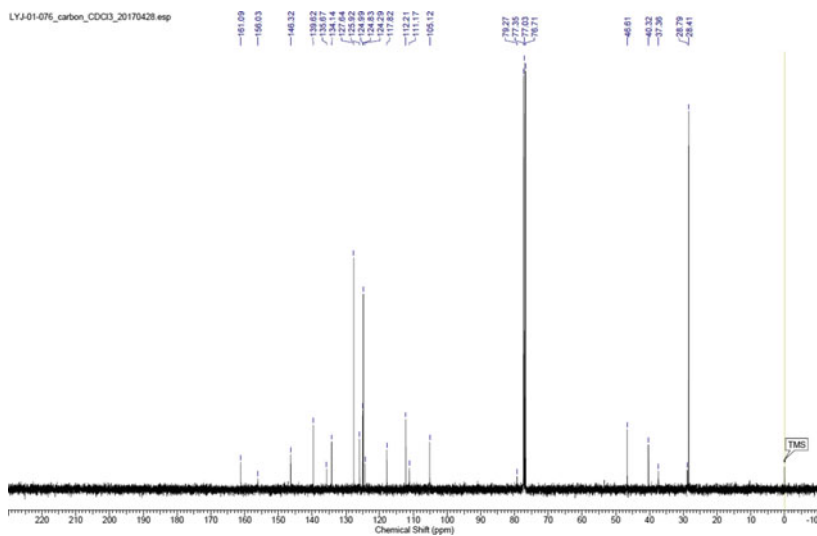


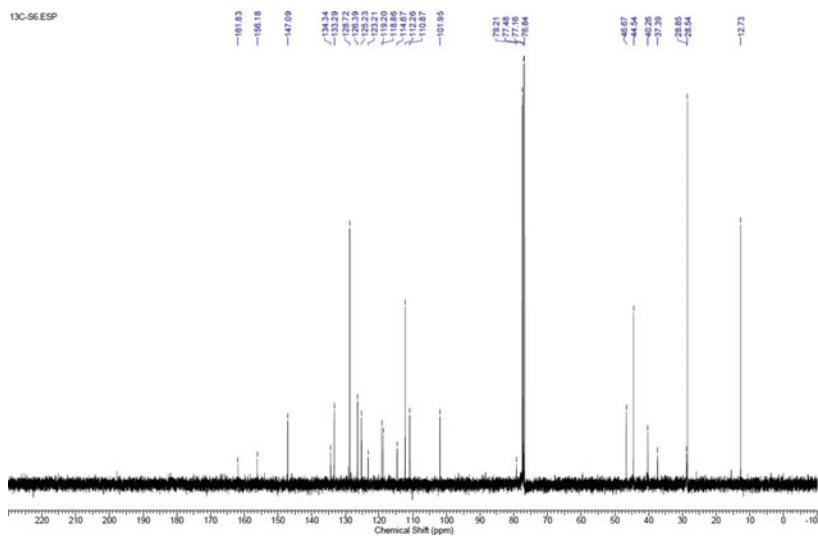
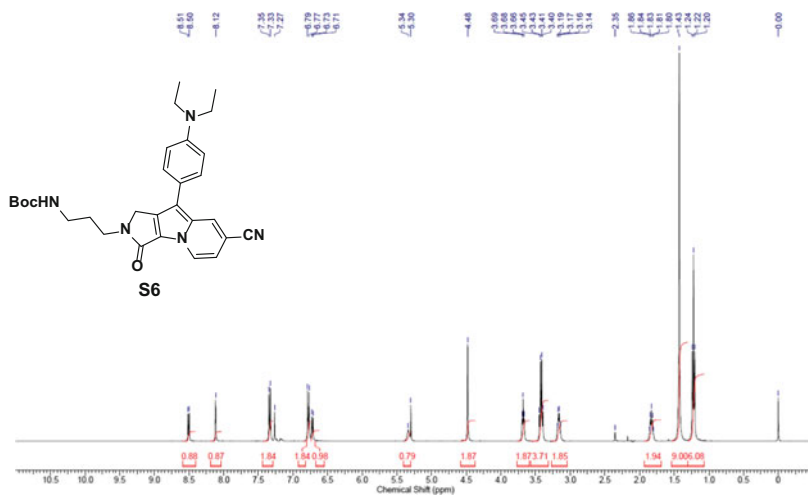


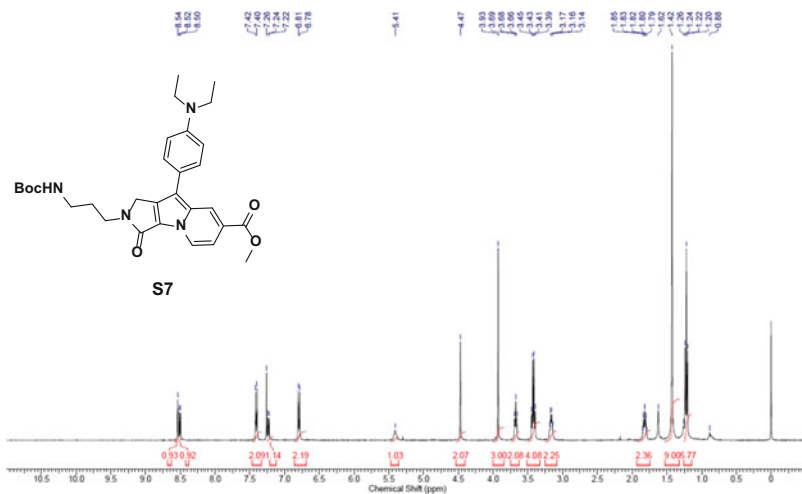




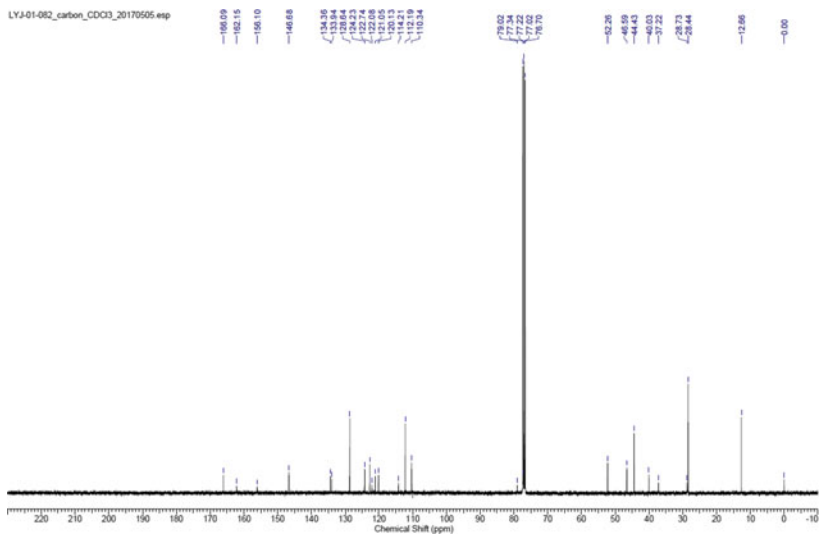
LYA-01-076_carbon_CDCl3_20170428_exp

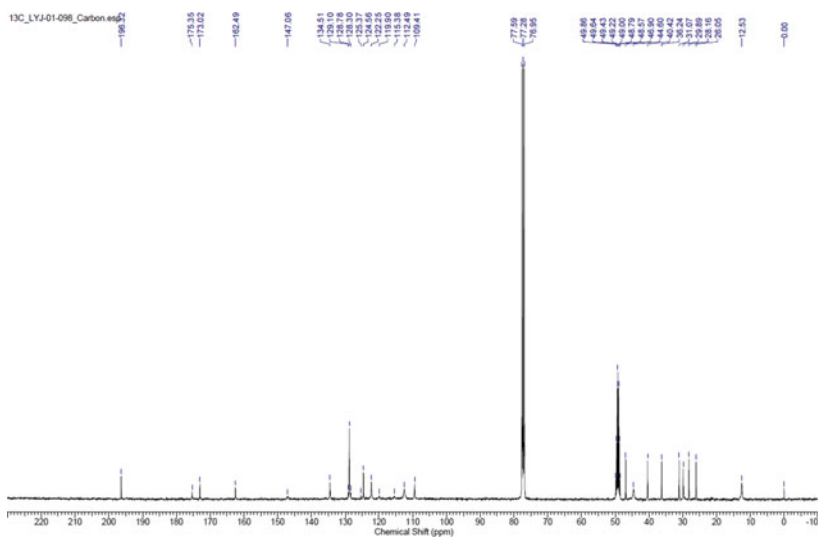
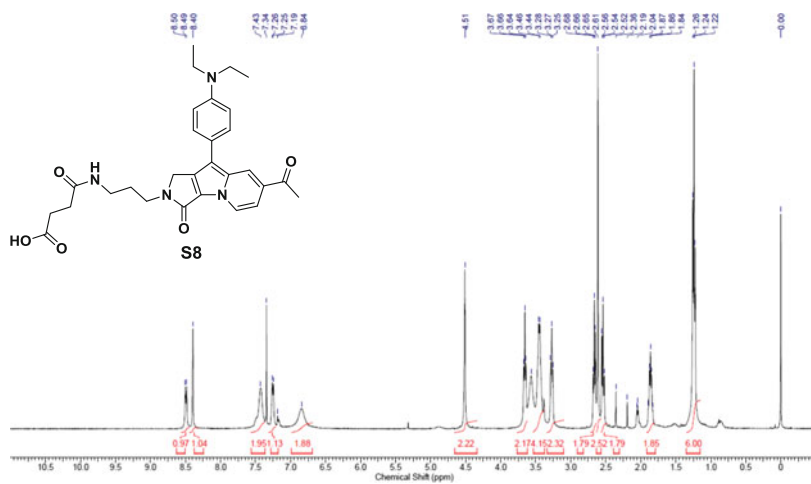


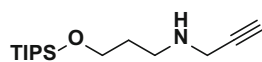




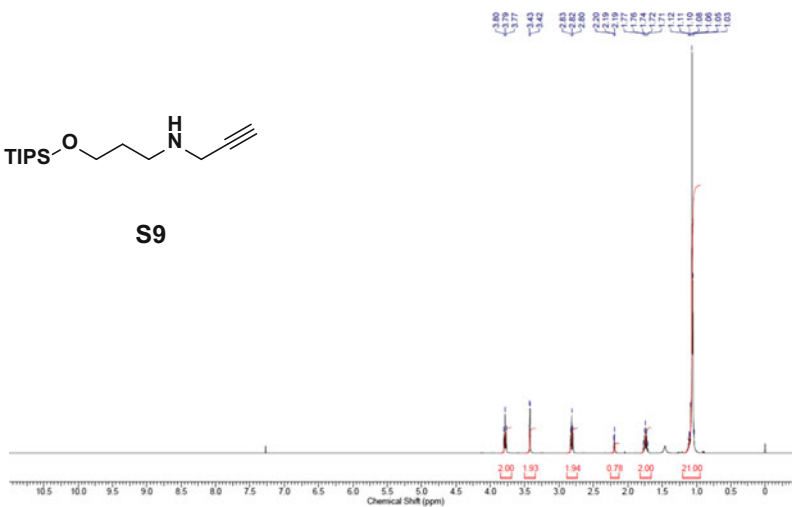
LYJ-01-082_carbon_CDCl3_20170505.esp



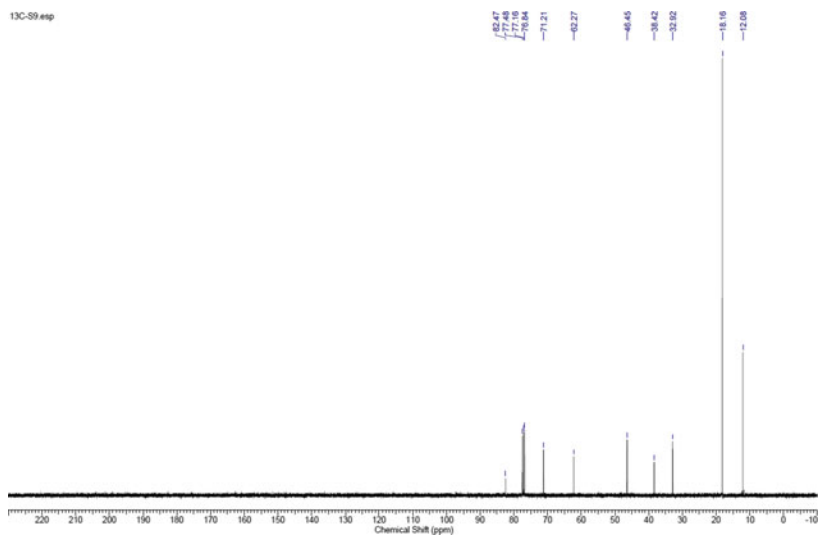


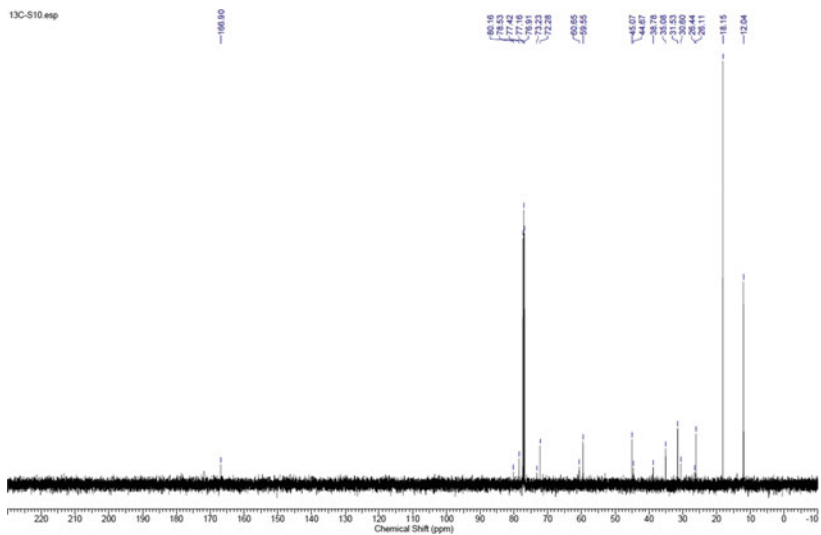
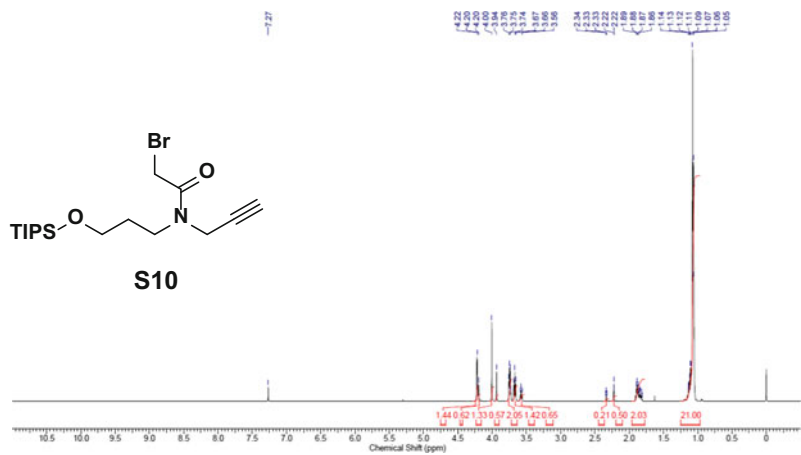


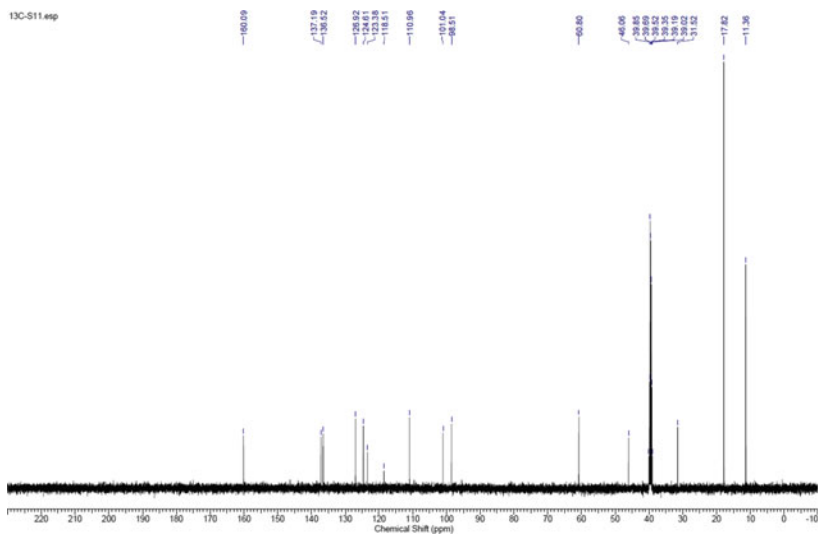
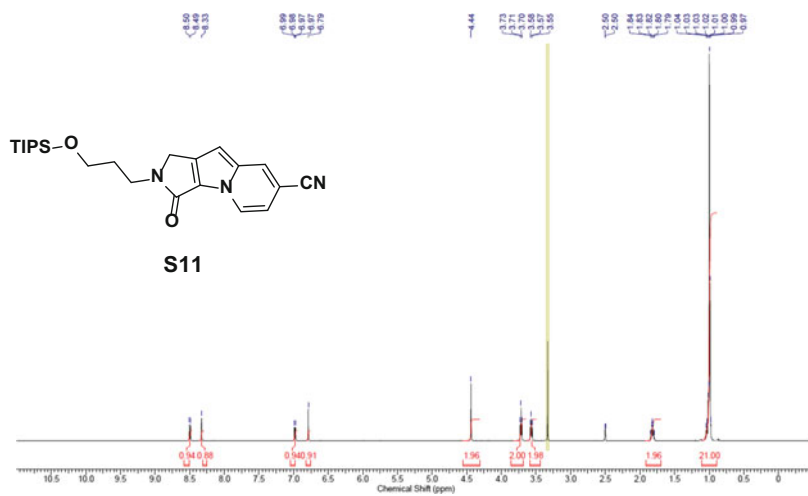
S9

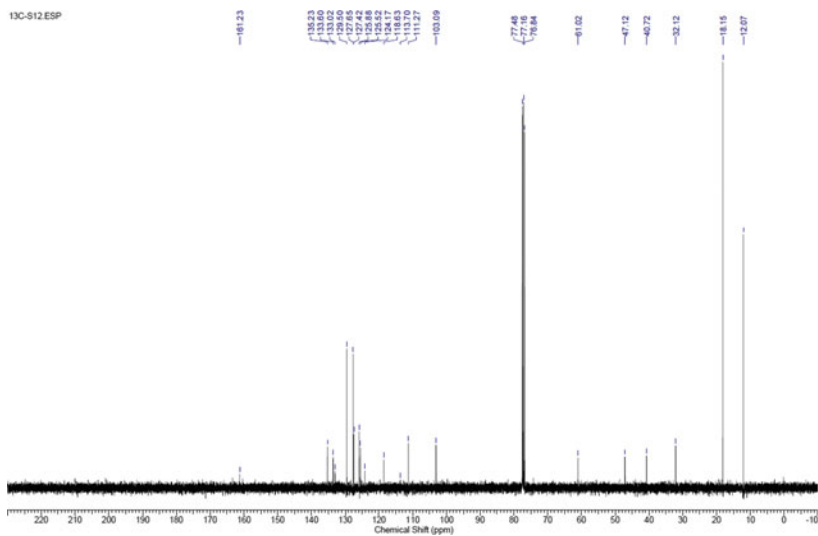
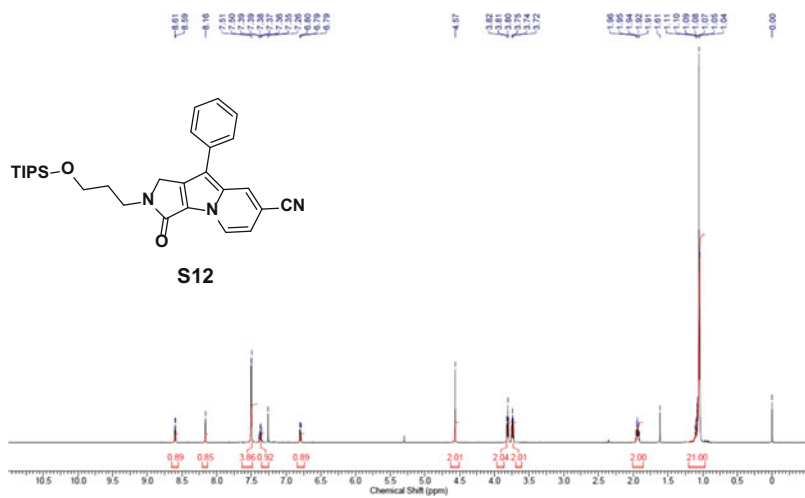


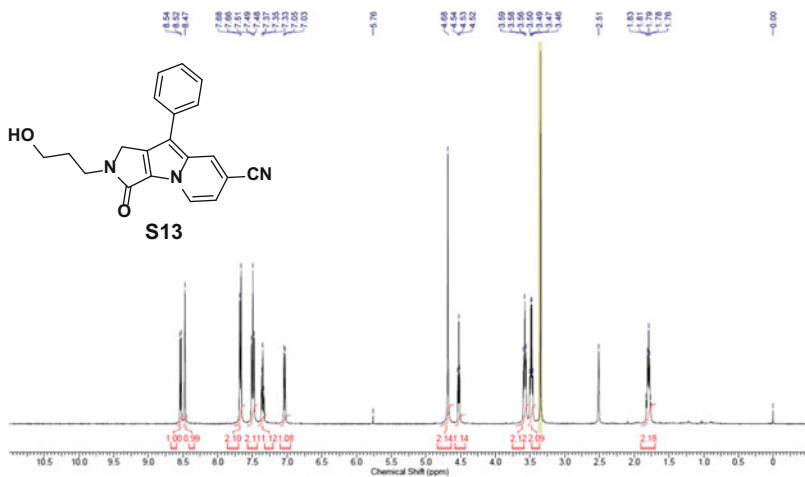
13C-S9.esp



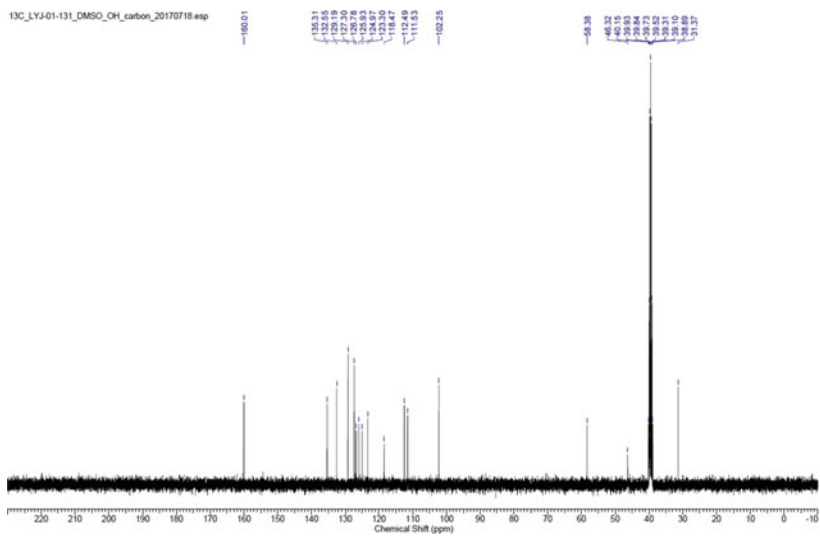


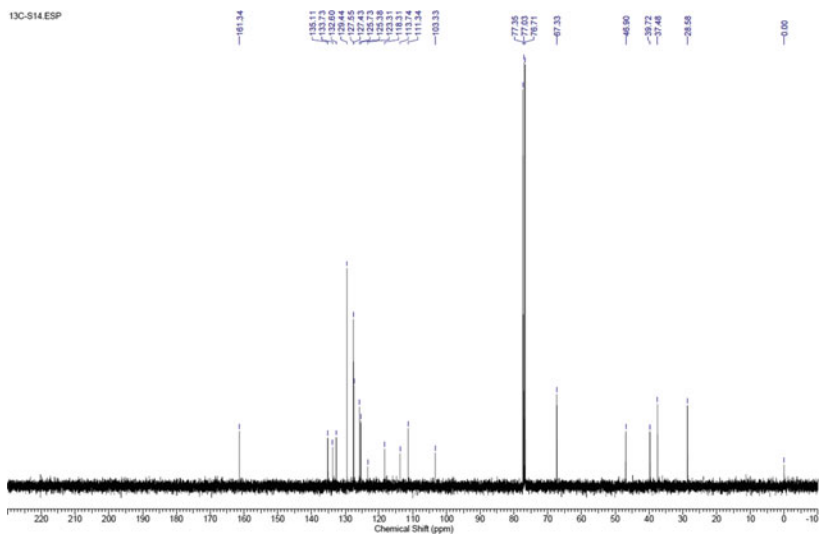
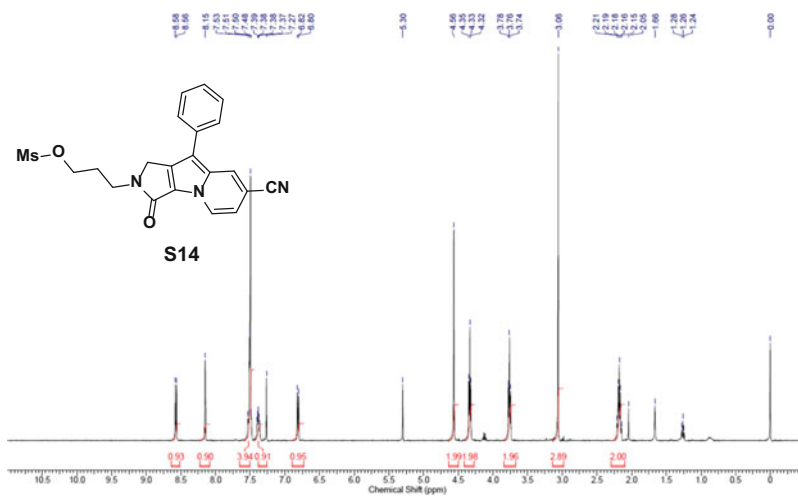


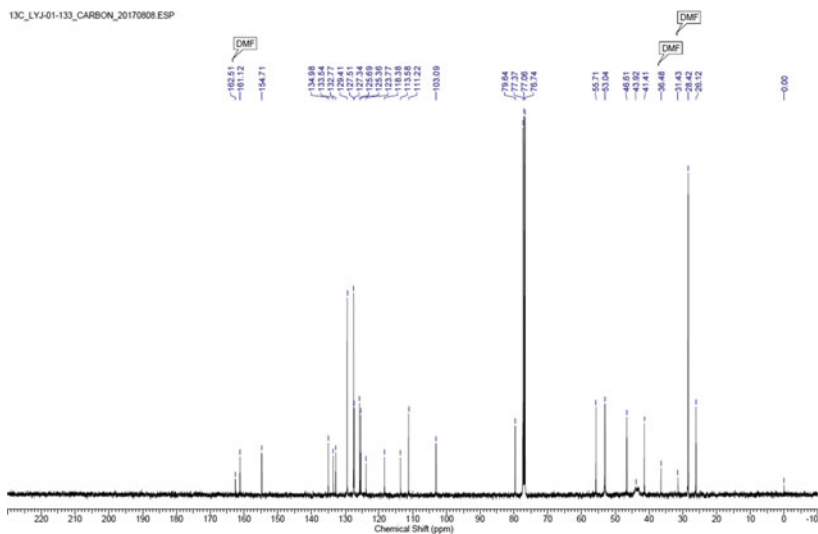
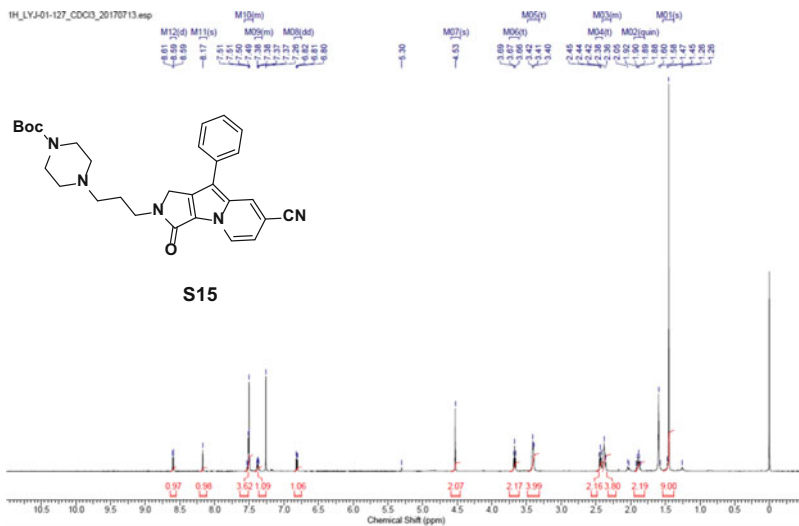


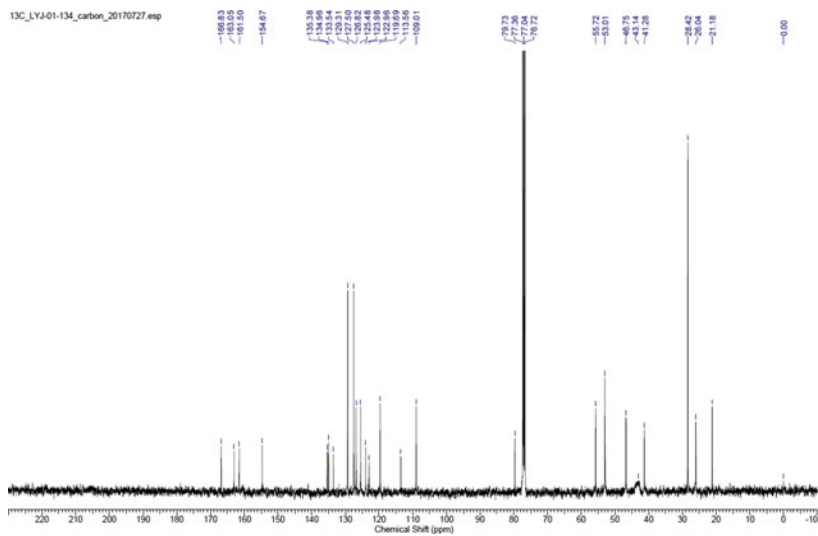
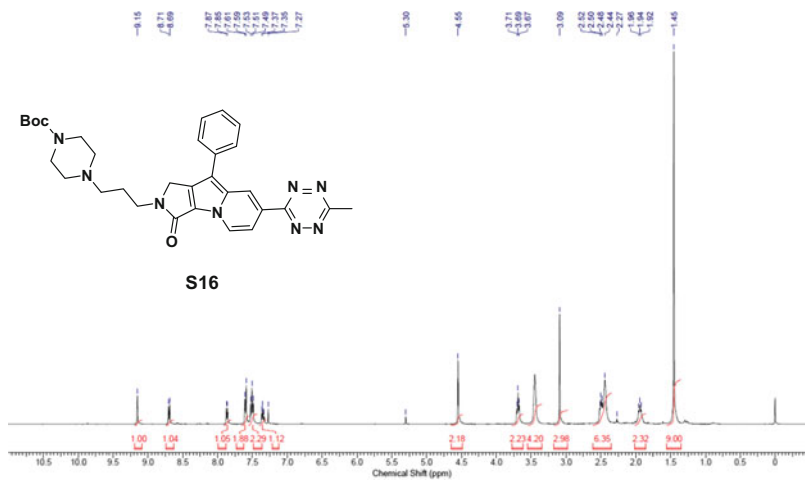


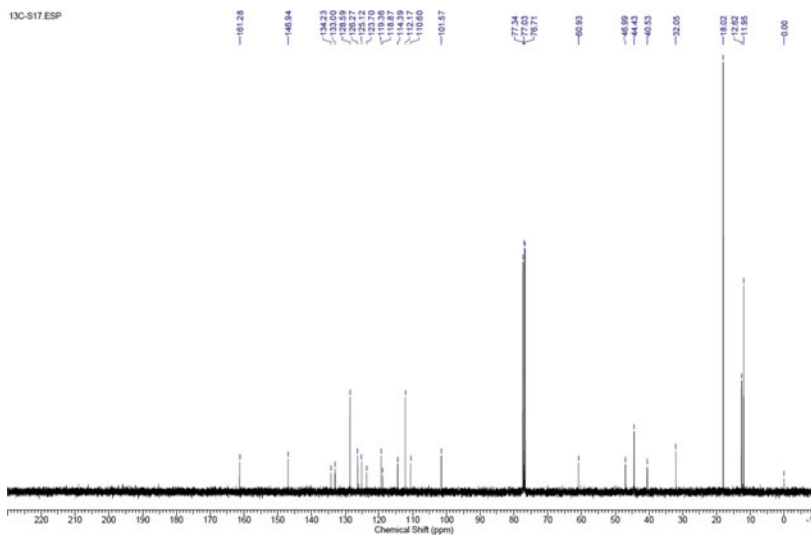
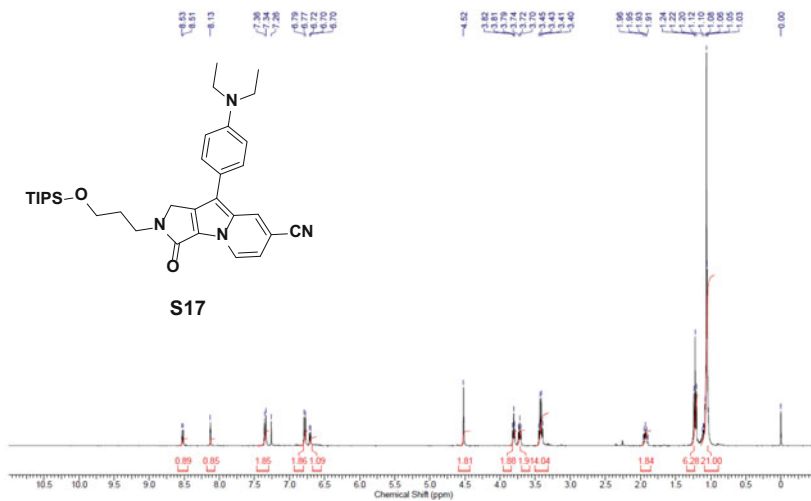
13C_LYJ-01-131_DMSO-d6_carbon_20170718.esp

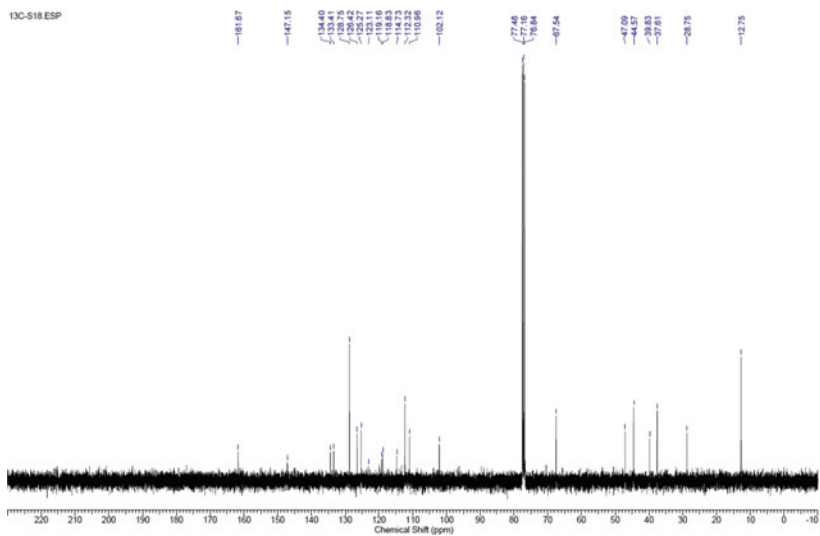
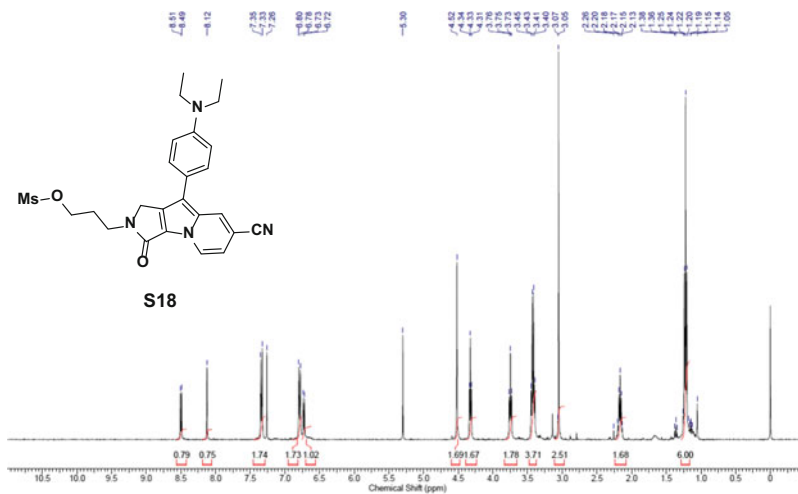


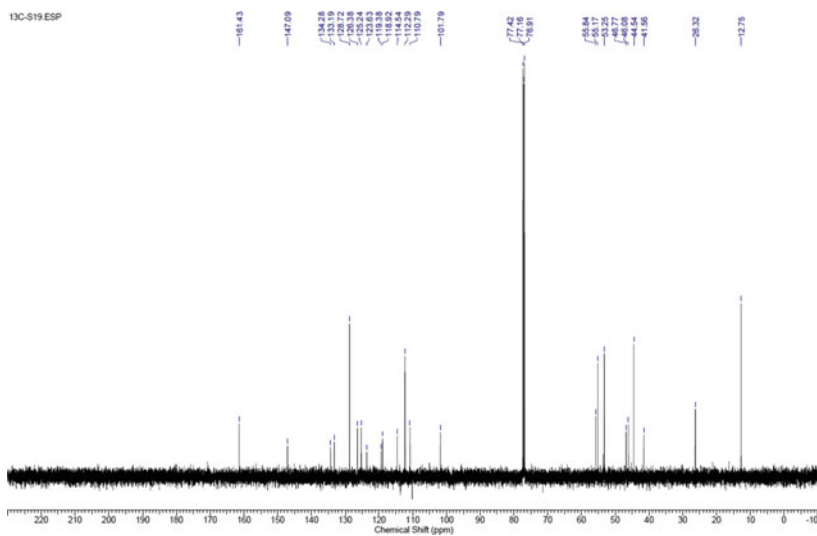
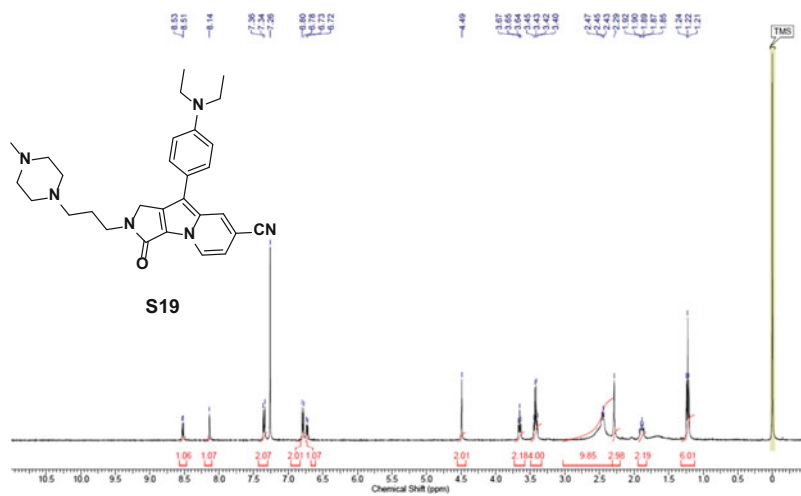


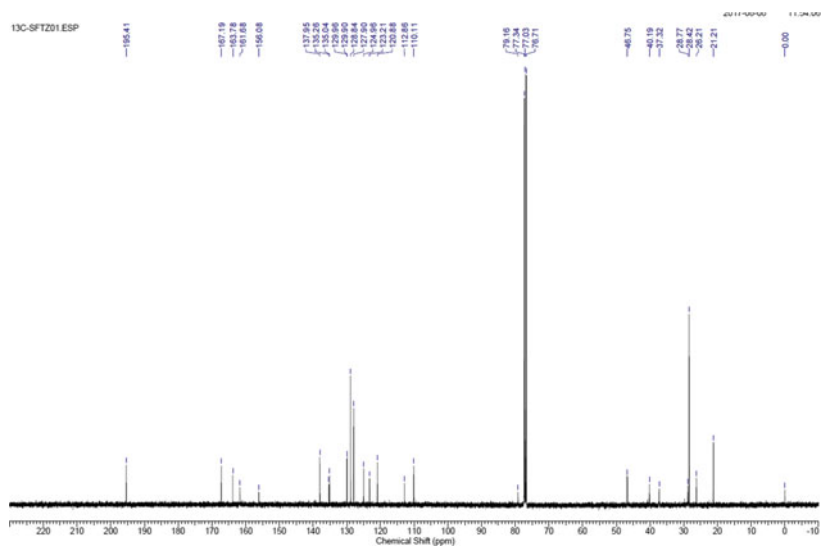
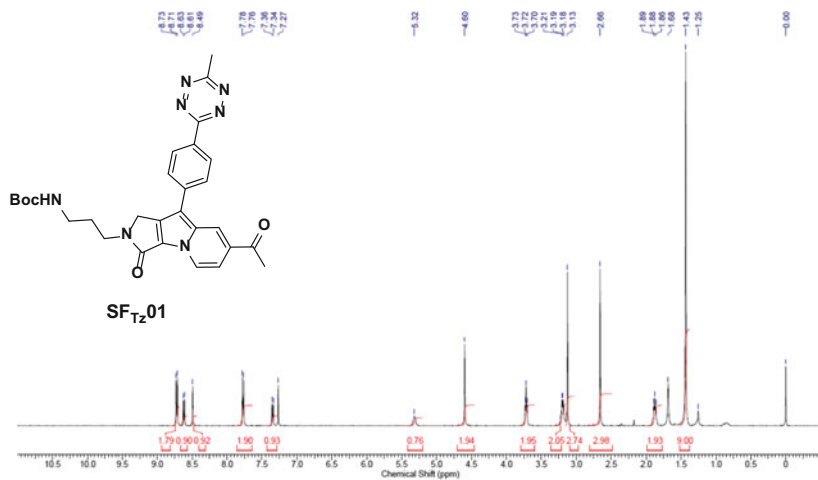


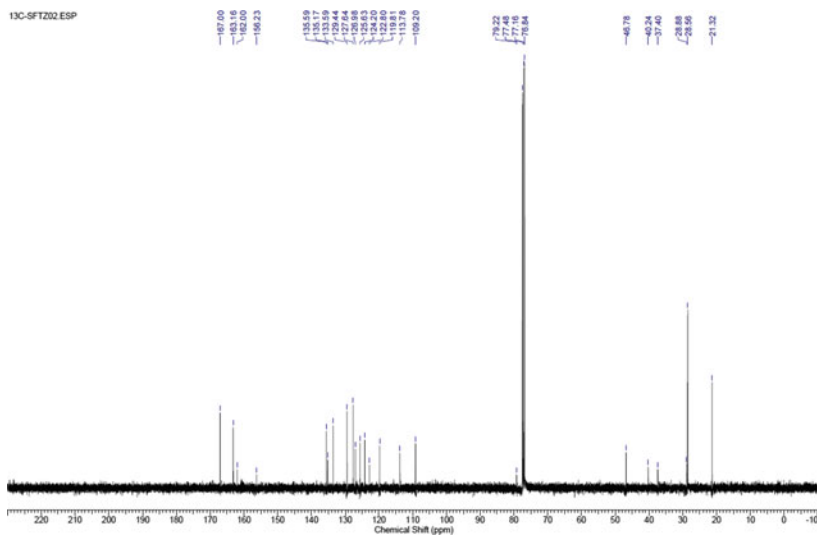
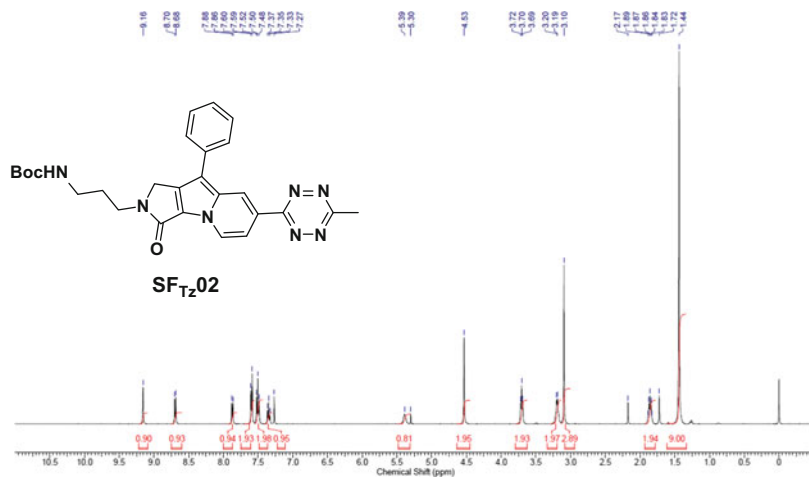


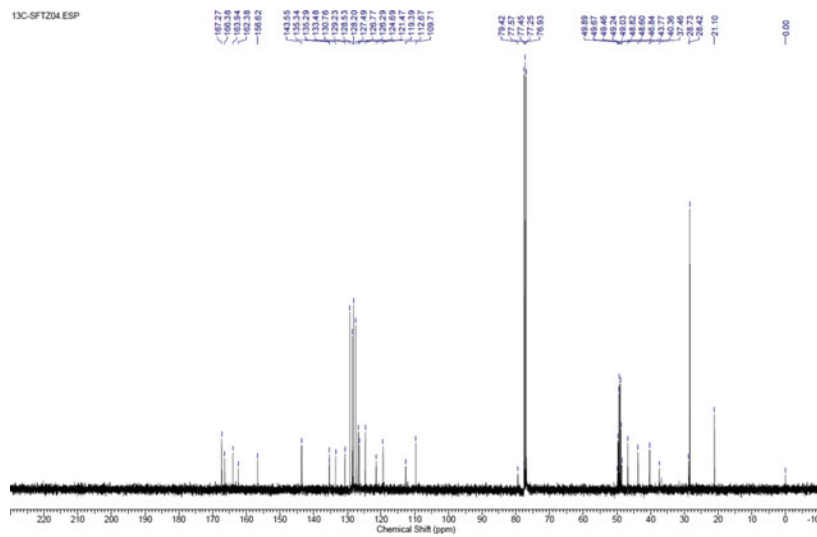
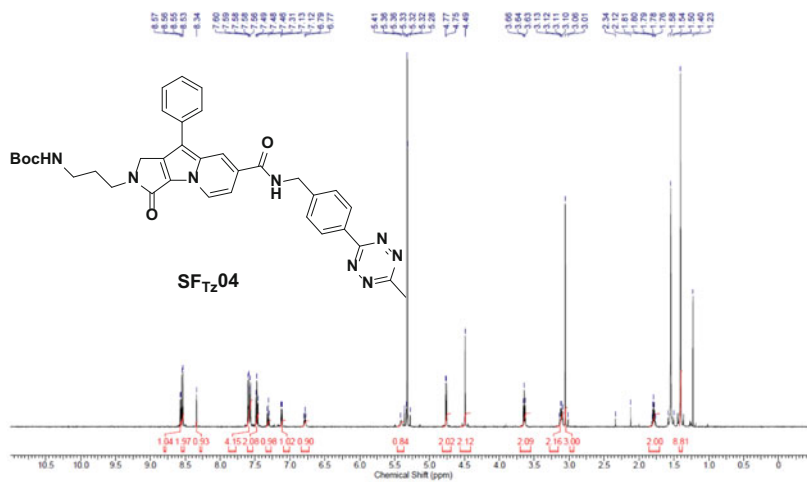


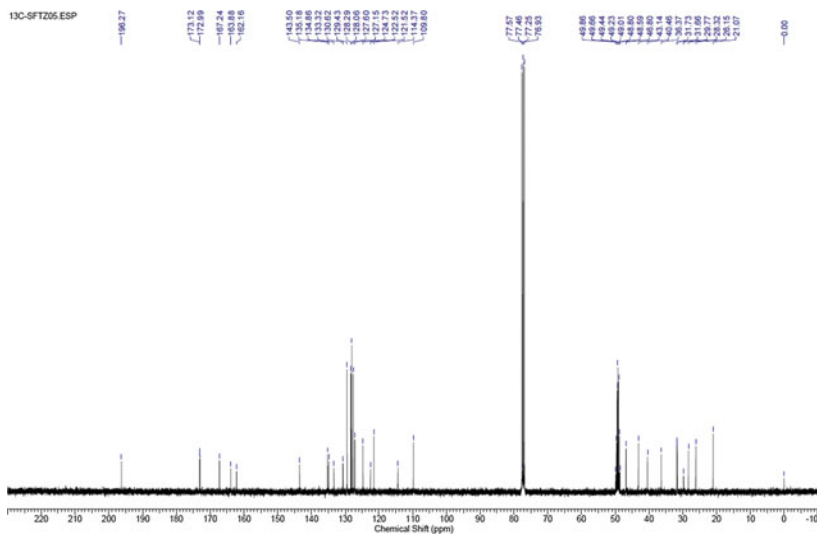
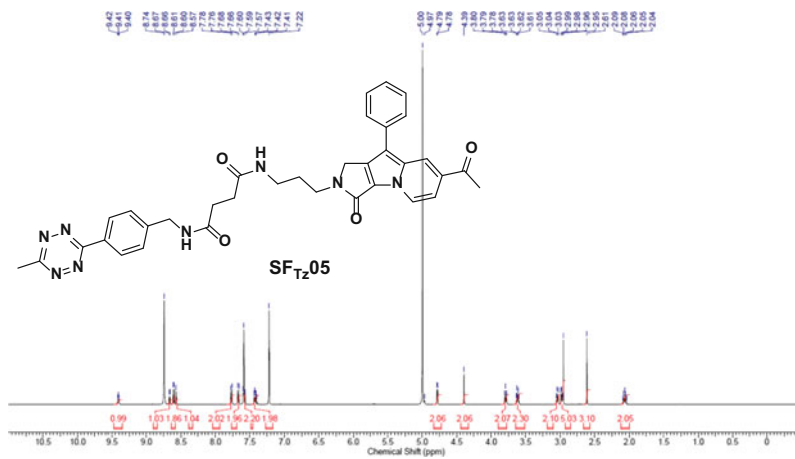


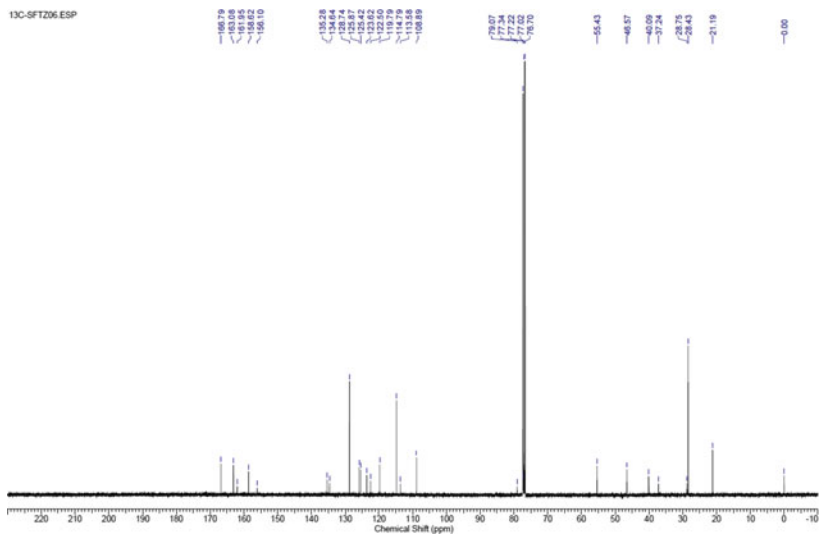
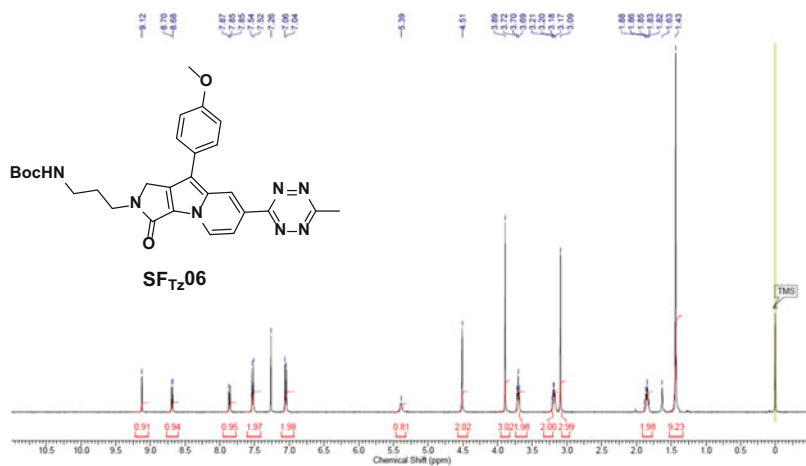


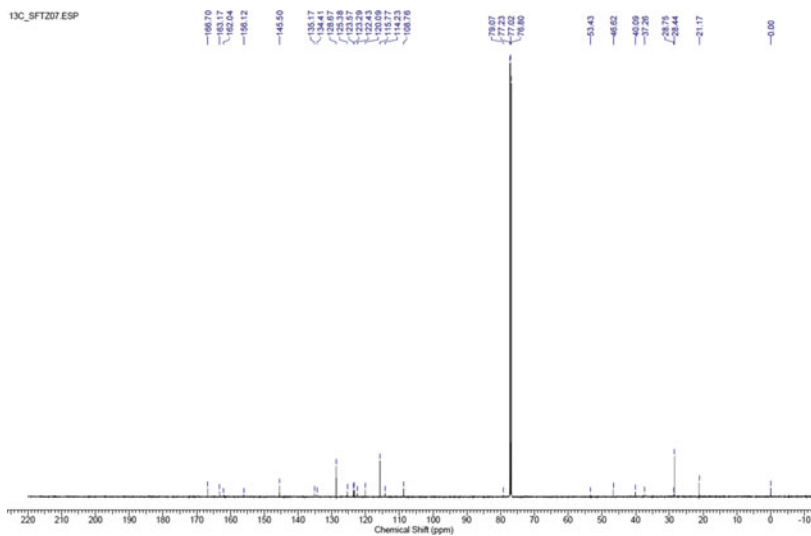
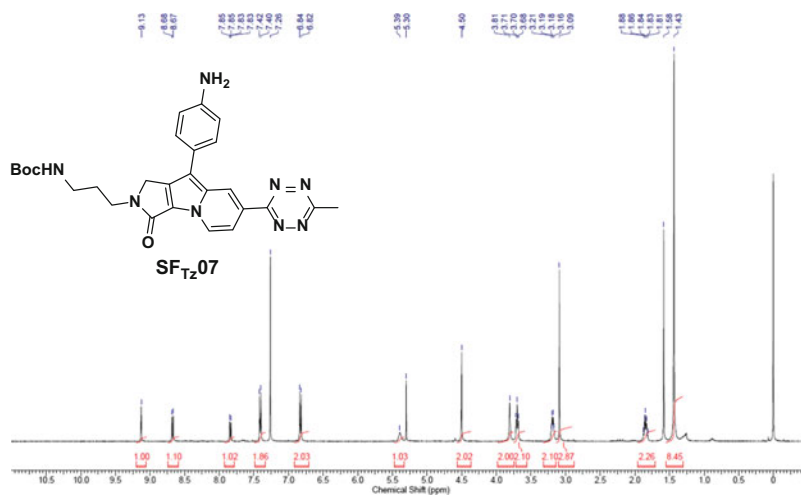


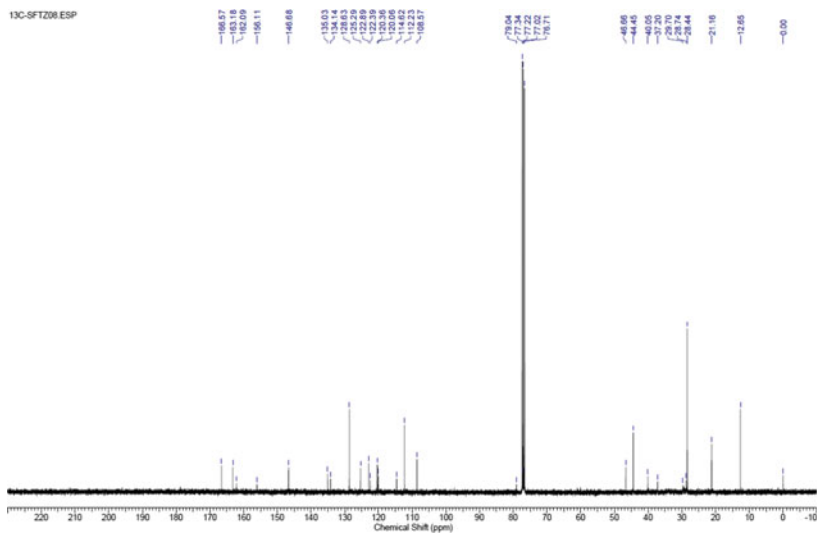
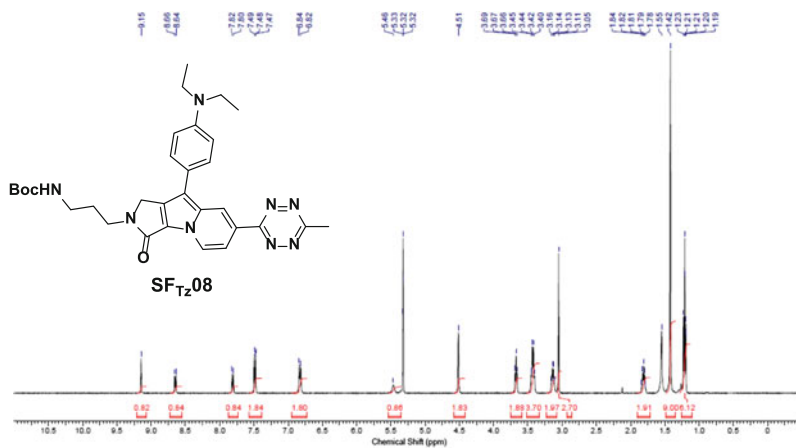


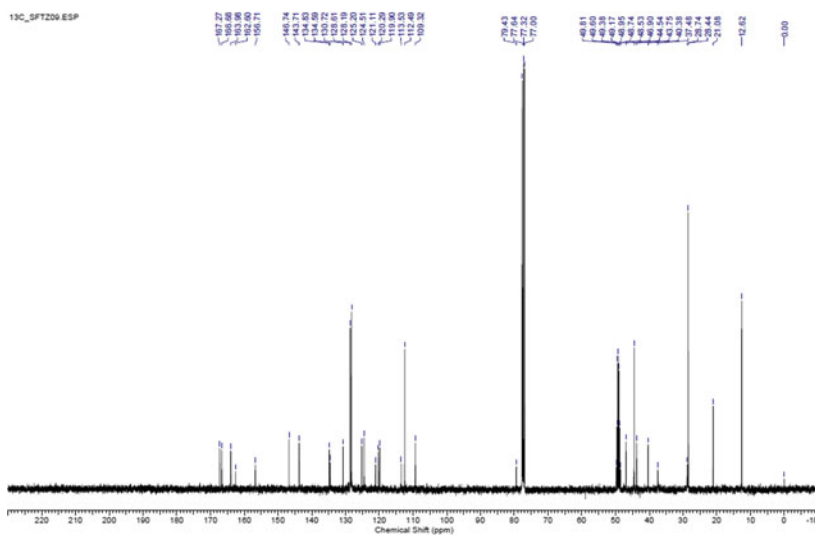
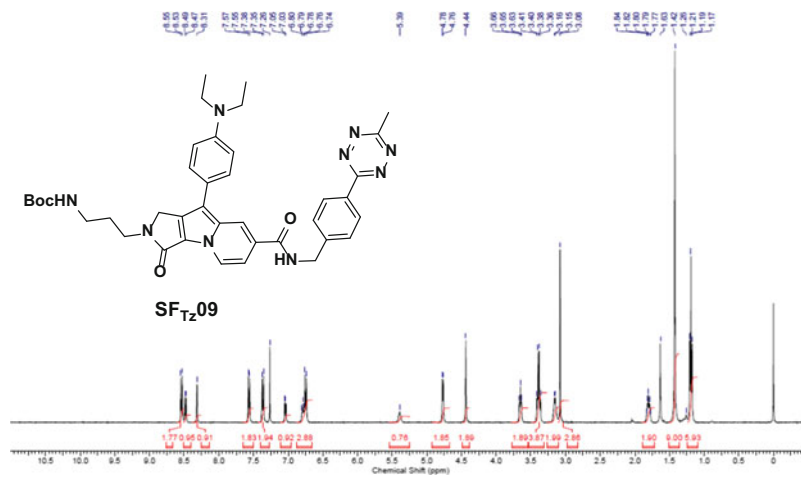


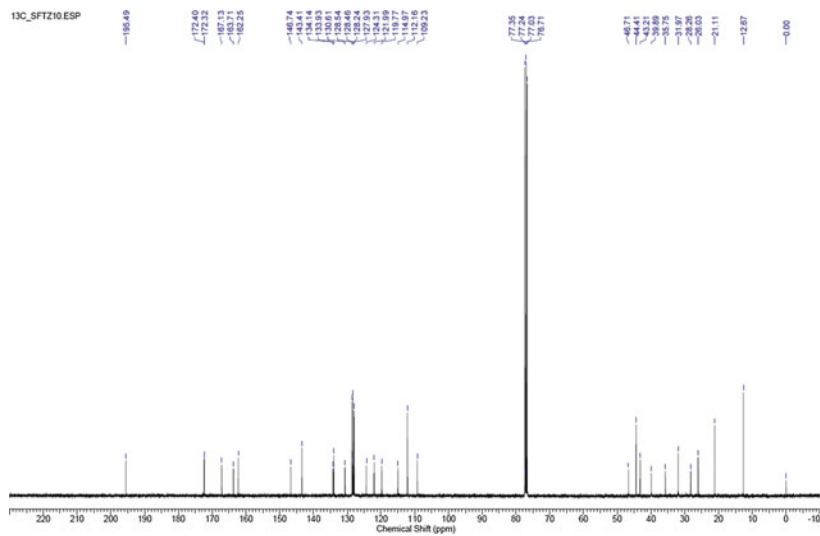
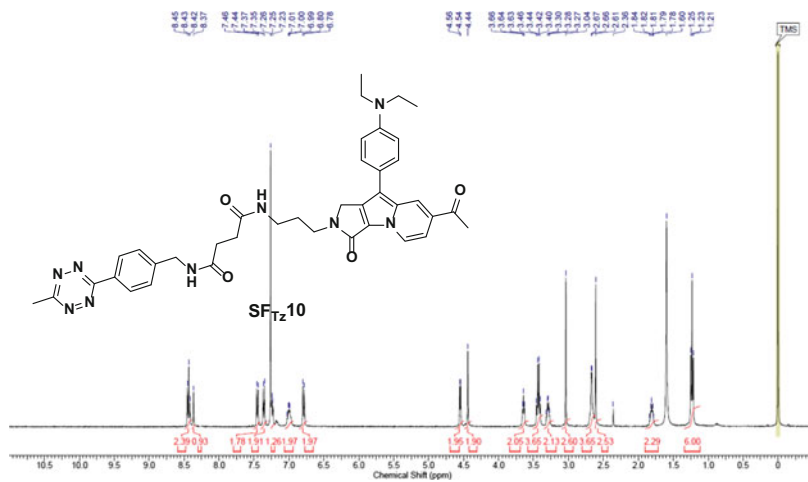


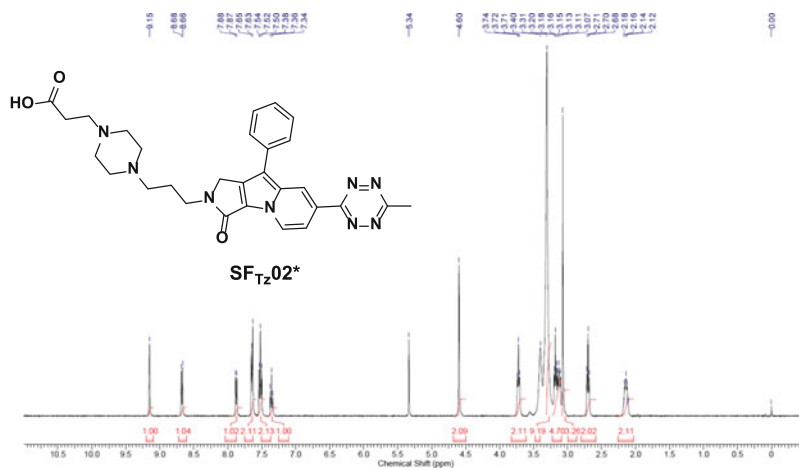




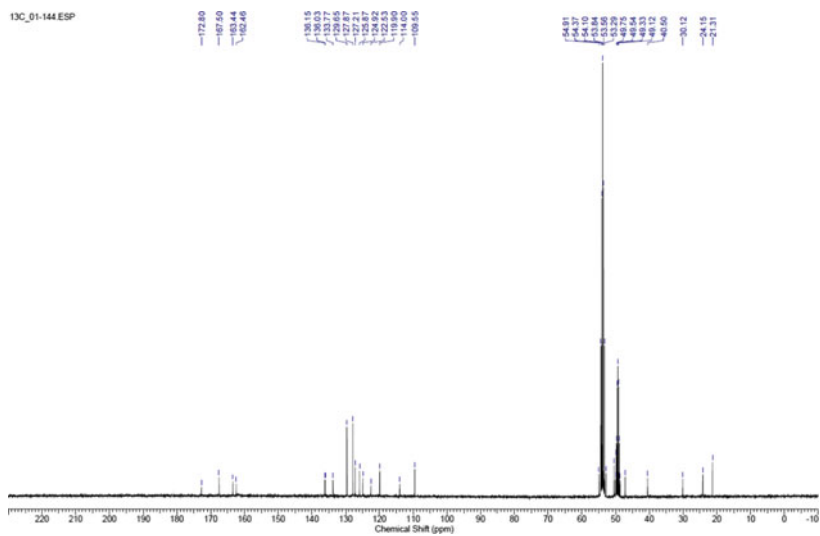


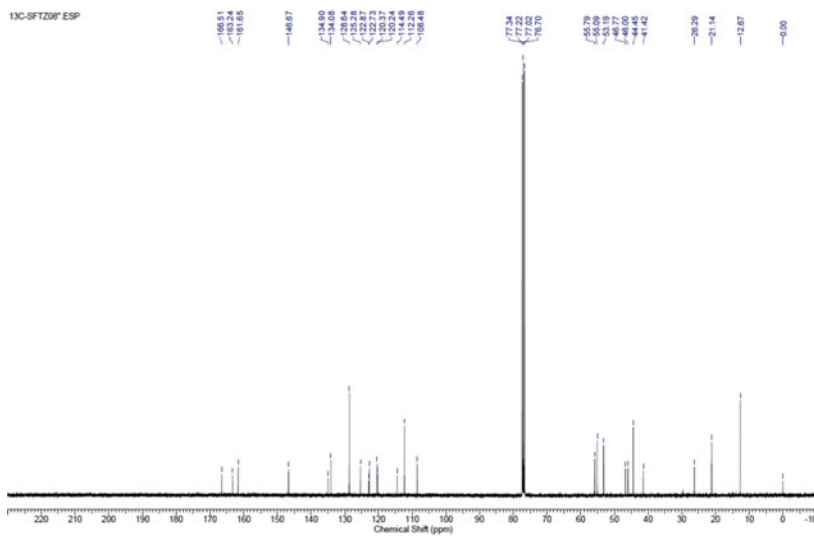
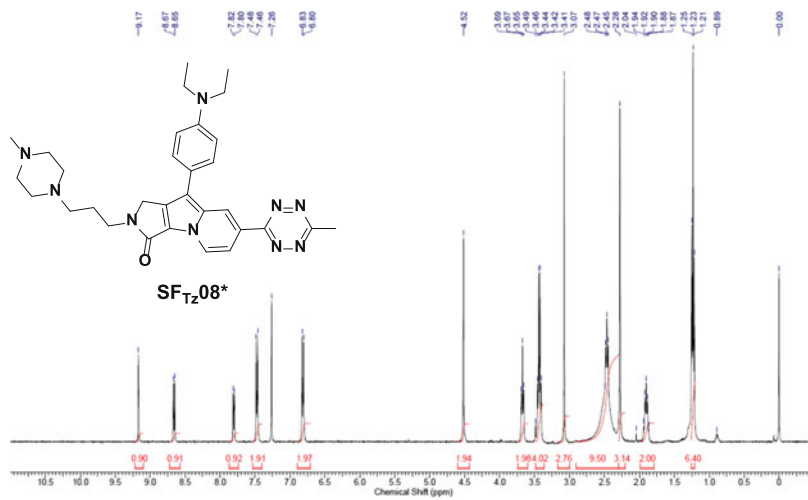






13C_01-144.ESP





Chapter 4

